Development of mid-IR Coherent Sources vis-à-vis Laser Assisted Aerodynamic Studies

by

M Bhaskara Sai Prasad

(Enrolment No: PHYS01201304015)

Bhabha Atomic Research Centre,

Mumbai - 400085, India.

A thesis submitted to the
Board of Studies in Physical Sciences
In partial fulfillment of requirements
for the Degree of

DOCTOR OF PHILOSOPHY

of

HOMI BHABHA NATIONAL INSTITUTE

May 2019

Homi Bhabha National Institute

Recommendations of the PhD Viva Voce Committee

As members of the viva-voce committee, we certify that we have read the dissertation prepared by **M B Sai Prasad** entitled **"Development of mid-IR coherent sources vis-à-vis laser assisted aerodynamic studies"** and recommend that it may be accepted as fulfilling the thesis requirement for the award of Degree of Doctor of Philosophy in Physical Sciences.

Chairman: Dr. D J Biswas, RRF, BARC		Date: 16/08/2019
Guide: Dr. J Padma Nilaya, SO(H), BARC		Date: 16/08/2019
External Examiner: Dr. Dinesh K Pandya, IIT Jammu		Date: 16/08/2019.
Member 1: Dr Alok K Ray, OS, BARC		Date: 16/08/2019
Member 2: Dr. Rekha Rao, SO(H), BARC		Date: 6/8/2019.
Member 3: Dr. Aniruddha Kumar, SO(G), AFFF, BARC		Date: 16-8-19

Final approval and acceptance of this thesis is contingent upon the candidate's submission of the final copies of the thesis to HBNI.

I hereby certify that I have read this thesis prepared under my direction and recommend that it may be accepted as fulfilling the thesis requirement.

Date: 05/09/2019

Place: BARC, Mumbai

Signature

Guide & Convener

(J.PADMA NILAYA)

STATEMENT BY AUTHOR

This dissertation has been submitted in partial fulfillment of requirements for an advanced degree at Homi Bhabha National Institute (HBNI) and is deposited in the Library to be made available to borrowers under rules of the HBNI.

Brief quotations from this dissertation are allowable without special permission, provided that accurate acknowledgement of source is made. Requests for permission for extended quotation from or reproduction of this manuscript in whole or in part may be granted by the Competent Authority of HBNI when in his or her judgment the proposed use of the material is in the interests of scholarship. In all other instances, however, permission must be obtained from the author.

M Bhaskara Sai Prasad

DECLARATION

I hereby declare that the investigation presented in the thesis has been carried out by me. The work is original and has not been submitted earlier as a whole or in part for a degree / diploma at this or any other Institution / University.

M Bhaskara Sai Prasad

List of Publications Arising From the Thesis

Published in Journals

1. "Second Harmonic Conversion of the 10 μm emissions of Pulsed and CW-CO_2 Lasers in $ZnGeP_2$", J. Padma Nilaya, **M. B. Sai Prasad**, Sunil Daga, Tatsat Dwivedi, S. Das, U. Chatterjee, and D. J. Biswas, *Laser Physics*, 2014, 24, 105403.

2. "Generation of continuously tunable 5 μm coherent radiation by second harmonic conversion of the emission of a multi-atmosphere TE CO_2 laser in $AgGaSe_2$", J Padma Nilaya, **M. B. Sai Prasad** and D. J. Biswas, *Laser Physics*, 2014, 24, 085401.

3. "Low-Jitter Synchronous Operation of Two Spark Gap Driven Laser Pulsers", **M. B. Sai Prasad**, Sunil Daga, Tatsat Dwivedi, J. Padma Nilaya, D. J. Biswas; *Optics & Laser Technology*, 2015, 65, 76-78.

4. "Cryogenically cooled CW electric discharge CO laser operated with CO_2 laser mixture", **M. B. Sai Prasad**, Tatsat Dwivedi, J P Nilaya, Shailesh Kumar, D. J. Biswas; *Laser Physics*, 2018, 28, No. 12, 125002.

5. "Practical techniques to homogenize the feed gas mixture and enhance the laser-jet interaction time in laser assisted aerodynamic separation studies", **M. B. Sai Prasad**, J. Padma Nilaya, Ayan Ghosh, A. K. Nayak, Vijendra Singh, A. K. Kalburgi, and D. J. Biswas, *Review of Scientific Instruments*, 2019, 90, 045121.

Communicated to Journals

1. "Advantage of Multi-step Vibrational Excitation in Laser Assisted Aerodynamic Separation of Sulfur Isotopes and a Novel Method of Estimating the Separation Efficiency of the Process", **M. B. Sai Prasad**, J. Padma Nilaya, Ayan Ghosh, D. J. Biswas, *Chemical Physics*.

Published in Conferences

1. "Characterization of SF_6-Ar Gas Jet by a Line Tunable CW-CO_2 laser", **M. B. Sai Prasad**, Atul Tak, Ayan Ghosh, Sunil Daga, J. Padma Nilaya, Tatsat Dwivedi, Goutam Chakraborty, R. C. Das, Shailesh Kumar, A. K. Nayak, D. J. Biswas, A. K. Das, L. M. Gantayet, **Jan 2014**, *National Laser Symposium-22*, Manipal University of Technology, Manipal.

2. "Development of a continuously tunable mid-IR source and its applications in laser assisted aerodynamic isotope separation", D. J. Biswas, J. P. Nilaya, **M. B. Sai Prasad**, Sunil Daga, G. Chakraborty, Ayan Ghosh, R. C. Das, A. Tak, A. K. Nayak, 2014, *Kiran*, 25, 61.

3. "Generation of discretely tunable 5 μm coherent radiation by SH conversion of the emission of a pulsed and CW-CO_2 laser in $ZnGeP_2$ crystal", J. Padma Nilaya, **M. B. Sai Prasad**, Sunil Daga, Tatsat Dwivedi, D. J. Biswas, Jan 2014, *National Laser Symposium-22*, Manipal University of Technology, Manipal.

4. "Enhancement of second harmonic generation efficiency of CO_2 laser emission in $AgGaSe_2$ by utilizing an external multi-pass cavity", J. Padma Nilaya, **M. B. Sai Prasad**, D. J. Biswas, Jan 2014, *National Laser Symposium-22*, Manipal University of Technology, Manipal.

5. "Low-Jitter Synchronous Operation of Two Spark Gap Driven Laser Pulsers", **M. B. Sai Prasad**, Sunil Daga, Tatsat Dwivedi, J. Padma Nilaya, D. J. Biswas, Jan 2014, *National Laser Symposium-22*, Manipal University of Technology, Manipal.

6. "Evidence of isotope selective absorption in Di-methyl Stannane-Helium binary gas jet using a continuously tunable 5 μm coherent source", **M. B. Sai Prasad**, S. Daga, A. Ghosh, G. Chakraborty, T. Dwivedi, A. Tak, R. C. Das, J. P. Nilaya, S. Kumar, A. K. Nayak, D. J. Biswas, A. K. Das, L. M. Gantayet, Dec 2014, *National Laser Symposium-23*, S. V. University, Tirupati.

7. "Demonstration and characterization of Sulfur enrichment through laser assisted aerodynamic separation process in SF_6-Ar binary gas mixture", **M. B. Sai Prasad**, J. Padma Nilaya, Ayan Ghosh, A. K. Nayak, D. J. Biswas, Dec 2015, *National Laser Symposium-24*, RRCAT, Indore.

8. "Evidence of enhancement of separation factor in Sulfur isotope enrichment through laser assisted aerodynamic separation process in SF_6-Ar binary gas mixture due to Multi- photon absorption", **M. B. Sai Prasad**, Ayan Ghosh, J. Padma Nilaya, A. K. Nayak, D. J. Biswas, Dec 2015, *National Laser Symposium-24*, RRCAT, Indore.

9. "Estimation of separation factor in laser assisted aerodynamic separation process of sulfur isotopes by absorption method", J. Padma Nilaya, Ayan Ghosh, **M. B. Sai Prasad**, A. K. Nayak, D. J. Biswas, Dec 2015, *National Laser Symposium-24*, RRCAT, Indore.

10. "Observation of multi-line lasing in the 5 μm region from a LN_2 cooled cw-CO_2-N_2-He gas discharge tube enclosed in a non-dispersive cavity", Tatsat Dwivedi, **M. B. Sai Prasad**, J. Padma Nilaya, Shailesh Kumar, 2016, *National Laser Symposium-25*, KIIT University, Bhubaneswar.

11. "Towards extending the interaction between the laser beam and the jet in laser assisted aerodynamic separation", J. Padma Nilaya, **M. B. Sai Prasad**, A. Ghosh, D. J. Biswas, A. K. Kalburgi1, C. Yadav, Vijendra Singh and A. K. Nayak, 2017, *National Laser Symposium-26*, BARC, Mumbai.

12. "Experimental Estimation of nozzle and Skimmer Throughputs in Laser Assisted Nozzle Separation Process", **M. B. Sai Prasad**, J. P. Nilaya, A. Ghosh, D. J. Biswas, A. K. Kalburgi, M. P. Sharma, G. Babu, V. Nataraju, A. K. Nayak, 2017, *National Laser Symposium-26*, BARC, Mumbai.

M Bhaskara Sai Prasad

Dedicated to

My Loving Parents

&

Respected Teachers

Acknowledgments

I express my sincere gratitude to my guide, Dr. J. Padma Nilaya, for her able guidance and stimulating discussions at every stage of the work reported in this thesis. Without her share of commitment, responsibility, painstaking efforts and critical reviewing, this work would not have been what it is. Her perseverance at work inspires me a lot and will continue to.

I sincerely thank my mentor, Dr. D. J. Biswas, for generating the quantum of work reported in the thesis. Some of the work reported herein is sheerly the outcome of his bright ideas. His excitement at having results drives my curiosity endlessly. He is an excellent teacher who taught the fundamentals of laser physics for which I shall be ever grateful.

I am grateful to Dr. L. M. Gantayet, who introduced to us the field of laser assisted aerodynamic separation. His knowledge and deep understanding of the subject has driven me to learn some new things in physics.

I thank from the bottom of my heart, all my doctoral committee members, Dr. D J Biswas, Dr. Alok K Ray, Dr. J. Padma Nilaya, Dr. Rekha Rao, Dr. Aniruddha Kumar & Dr. A K Nayak, for sitting through and lending a patient ear hearing out all my seminars and the yearly progress reviews. The insightful comments and suggestions have been invaluable and helped in making me see the light of this day and write my thesis. My added thanks go to Dr. Aniruddha Kumar for making it every time all the way from Tarapur to Mumbai to attend my doctoral committee meetings.

I thank my colleague, Tatsat Dwivedi, who keeps my day ticking with news snippets with a wonderful mind of his own. I have to be honest and admit that, if not for the work that we did together on CO laser, this thesis would be an incomplete. In this regard, thanks are due to Dr. Shailesh Kumar too. And to my other colleague, Goutam Chakraborty, who with his

wit and humour makes my day enjoyable at work. To Dr. A. K. Pulhani, Dr. V. S. Rawat, Dr. G. Sridhar and my batch mate Jinesh Thomas too, for constantly enquiring about the progress of my PhD and motivating.

My sincere thanks reach out to A. K. Kalburgi, Head, ChTD, and his colleagues including Shri. Vijendra Singh, MDD, for the numerous scientific discussions, for allowing us to borrow some of the crucial equipment/components that helped in conducting our experiments seamlessly. I would like to thank, V. Nataraju, Head, Mass Spectrometry Section, and his group members, in particular, Gonde Babu, for the mass spectrometric analysis of our samples.

I thank my other colleagues, Mr. Atul Tak, Ayan Ghosh, Dr. R. C. Das and Sunil Daga, who have contributed their part scientifically at some stage or the other. Thanks to Mr. Dinesh Khopkar for making the AutoCAD drawings of the various systems fabricated during the course of our experimental work. I extend my thanks to the workshop staff, especially, Lalit Kanthe, for easing our efforts by lending technical help in setting up of the experimental systems.

I express my sincere gratitude to Dr. B K Nayak, Dean, Physical Sciences for his unstinted support and encouragement that helped me to pace my submission. Thanks are due also to Dr. Saibal Basu, former Dean, Physical Sciences.

I am ever grateful to R K Rajawat, Head, L&PTD & AD, BTDG, for his constant support and encouragement. His cheerfulness and positivity simply rubs.

My sincere thanks to Prof. Dinesh Kant Pandya and Prof. Milan Trtica for agreeing to be the reviewers and patiently going through the quantum of work reported herein thus leading to their constructive suggestions.

Big thanks go out to my two finest friends, Praveen & Venkat, who make my life beautiful outside office, day in day out. They are always around for me anytime and are just like family.

Thanks to my college friend, Srinrusimham Amarvadi, who is the reason for my landing at IITM; for believing in my success more than I did. Thanks to Makkapati Ravi Kiran & Sarath Chandra who are true reflections of simplicity. Thanks also go to my several good old friends who have supported me directly or indirectly.

I cannot imagine my current position without the education provided by my excellent teachers and shall ever remain indebted to them.

I thank all my family members; my loving and affectionate mother, my father, who always takes great pride in me, my father-in-law, Dr. G S N Sastry, who enquires more about me and the progress of my PhD than he does his daughter; my brothers, my caring sister and their families. Special thanks go out to my loving and caring wife, Madhu Salini, who understands and takes great care of me and supports me tirelessly. Endless thanks to them all for sharing my pains. And to my cute little boy, Somasekhar, who brightens my every single day and is the source of my strength.

Table of Contents

Homi Bhabha National Institute

Name of the Student: M Bhaskara Sai Prasad

Name of the Constituent Institution: BARC, Mumbai

Enrolment No. : PHYS01201304015

Title of the Thesis: Development of mid-IR Coherent Sources vis-à-vis Laser Assisted Aerodynamic Studies.

Board of Studies: Physical Sciences

SYNOPSIS

(Limited to 10 pages in double spacing)

Ever since Theodore Maiman operated the first laser in 1960, it fired the imagination of scientists in many countries towards using it to shrink the size of the usually huge industrial enrichment plants. The reason behind this is the extraordinary purity of laser light that could be easily exploited to selectively excite the rarer isotope leading to its straightforward separation from the abundant species. The approach based on this simple concept has been extensively researched over last many decades in the form of Molecular Laser Isotope Separation (MLIS) [1] although with limited success primarily owing to the requirement of extremely intense laser source. The other approach that has gained momentum over the last decade or so basically combines isotope selective laser excitation with an existing separation scheme viz., aerodynamic separation [2] that takes advantage of the difference in the masses of the two isotopes. This laser assisted aerodynamic scheme [3, 4] has established its clear advantage over the classical MLIS scheme.

It is well known that when an isotopic gaseous mixture expands through an orifice, the heavier species tends to concentrate near the jet centerline while the lighter one moves outwardly. This thus presents a possibility of separating the heavier and lighter species. The efficiency of the separation of isotopes through this process understandably depends on their relative mass difference. The conventional aerodynamic separation can thus be very effective in separating lighter isotopes e.g., hydrogen and deuterium. The enrichment factor that is achievable under this scheme for heavier isotopes with negligible relative mass difference, on the other hand, will be too small to have any practical utility. This drawback can be overcome by shining the expanding jet with an appropriate coherent beam of light [3]. It is well known that polyatomic molecules seeded in an inert carrier gas subjected to supersonic nozzle expansion communicate with the low temperature bath provided by the monatomic carrier gas resulting in the relaxation of their various degrees of freedom. As the gas cools, the molecules in the jet form Van der Waals clusters. Selective laser excitation of one of the isotopes prevents it from forming clusters thereby giving rise to a larger mass difference between the excited isotope and the non-resonant isotope that continue to form clusters, resulting in a much wider spatial separation between them [3, 4 and 5]. Diluting the molecular isotopic mixture in a buffer gas like Argon further enhances the overall separation efficiency as now the possibility of transferring the vibrational excitation from the resonant to the non-resonant species through collisions reduces drastically [3, 4 and 5].

Unlike the case of MLIS that follows the multi-photon dissociation route, the requirement on the intensity of the laser source is much less stringent here, thereby making this process accessible to even continuous wave (CW) laser sources that are capable of generating much less power. CO_2 laser that operates in the mid-infrared region and tunable over 9 to 11 μm region, albeit discretely, is the most attractive choice to impart the selective vibrational excitation to the rarer isotopic species either directly or by way of converting its emission into

other wavelengths through non-linear or optical pumping routes. The discrete tunability of the parent laser, sometimes, however, comes in the way of resonant excitation as the possibility of exact coincidence between absorption centre of the resonant isotopic species and the emission centre of the coherent source is extremely rare. The possibility of continuous tunability of CO_2 laser emission is of great advantage in such cases. It is also sometimes imperative to carry out precursor spectroscopic studies before applying laser assisted aerodynamic separation scheme to certain isotopes of considerable importance, like tin. An appropriate working molecule of stannane, viz., alkyl stannanes are known to have a strong absorption feature lying in the 5 micron region. Continuous tunability of the 10 micron CO_2 laser can be directly imparted to the 5 micron emission generated by second harmonic (SH) process, thereby enabling such spectroscopic studies. Indigenous development of various coherent sources over the mid-IR region and employing them for isotope selective studies is the central theme of the work reported in this thesis. Discretely and continuously tunable mid-IR coherent sources encompassing both 5 and 10 micron regions of the electromagnetic spectrum that have been indigenously developed, form the basis of the chapters 2, 3, 4 of the thesis while their applications in isotope selective studies in conjunction with aerodynamic separation process constitute the remaining part of the thesis.

For convenience of presentation, the thesis has been divided into six chapters and a summary of the content of the thesis in a chapter wise manner is presented below.

Chapter 1: Introduction to the Thesis

In this introductory chapter, an overview of the various mid-IR laser sources in the 5, 10 & 16 μm regions have been discussed. The role of these sources in isotope selective excitation leading to their separation has been discussed. The very process of laser assisted aerodynamic separation has been discussed at length. An insight into the design criterion of nozzles,

skimmers, their fabrication etc., has been provided. A literature survey of the different aspects of gas dynamics viz., the compressible fluid flow, isentropic fluid flow, shocks in supersonic jets, jet diagnostics, clusters and cluster diagnostics in a supersonic expansion has also been presented.

Chapter 2: Continuous Tunable Emission from a Multi-atmosphere CO_2 Laser and the Prospect of Synchronized Operation of Two Pulsed CO_2 Lasers.

In this chapter, to begin with, the physics of CO_2 laser operation, its lasing action on various normal band transitions (P & R) at atmospheric pressure and the discrete nature of the emission lines have been discussed. The working principles of high pressure operation of the CO_2 laser that enable continuous tunability leading to the reduction in the dark region over its emission spectrum are too discussed. Operation at a high pressure (~ 10 atmospheres) results in the broadening of the gains on the neighboring ro-vibrational transitions to the extent that they merge with each other providing the prospect of a near continuous tunability over the 9 - 11 μm region. To this end, detailed characterization of a commercial multi-atmosphere CO_2 laser tuned from 10P (28) to 10P (32) in a continuous fashion has been demonstrated. This was possible by way of changing the Q of the cavity and the energy loading of the gain medium. These aspects are discussed in detail in this chapter.

Synchronized operation of a pulsed laser with an event assumes significance under certain conditions, e.g., oscillator-amplifier operation, multiplexing the operation of multiple lasers, spectroscopy studies viz., pump-probe experiments etc., necessitating simultaneous operation of more than one pulsed laser. Synchronized operation of two such lasers, therefore, means the simultaneous closure of the two switches that drive them. The jitter associated in this process, that essentially stems from the statistical variation in the formative time often hinders the performance of such synchronized operation. A novel technique that employs, in addition

to the electrical coupling, UV coupling of the two switches, resulted in a better synchronization with reduced jitter in their operation. The coupled UV photons of appropriate energy pre-condition the inter-electrode gap reducing the formative time lag allowing the switch to close with a correspondingly reduced jitter. This finding, that has a bearing in applications where a number of spark gap driven lasers are to be operated in tandem, has also been elaborated.

Chapter 3. Generation of Continuously & Discretely Tunable Coherent Mid-IR Sources in the 5 μm region by Second Harmonic Conversion.

In this chapter, at the outset, some basic aspects of non-linear optics are discussed. A coherent source in the 5 μm region of the mid-infrared finds application in numerous fields of research including HR spectroscopy. As discussed earlier, most applications of a 5 μm coherent source will benefit greatly if the emission could be tuned continuously over this spectral range. Frequency doubling of a tunable CO_2 laser emission in suitable non-linear crystals is an attractive method but the emission is discrete. To this end, generation of continuously tunable 5 μm coherent source by SH conversion of the emission of multi-atmospheric TE CO_2 laser using $AgGaSe_2$ Crystal has been reported. The performance has been characterized with regard to energy and power conversion efficiency. The excellent phase and amplitude synchronization of the SH emission with the pump pulse could be observed by studying the temporal profile of the pump and the corresponding SH emission. The mode beating of the pump that is also reflected in the SH emission provides signature of the instantaneous nature of the SH generation process. Further, the results of the generation and characterization of discretely tunable coherent 5 μm radiation by SH conversion of emission of both CW & TEA (Transverse Excitation Atmospheric) CO_2 lasers using a $ZnGeP_2$ crystal too has been studied and elaborated. The energy and peak power conversion efficiencies have been measured and

compared for both cases. The SH output as a function of CO_2 partial pressure too has been studied for the case of TEA CO_2 laser operation.

Chapter 4. Development of a Cryo-cooled CW Electric Discharge CO laser by Employing CO_2 Laser gas mixture.

One aspect of CO_2 laser that has hitherto remained experimentally unexplored is its emission spectrum when the gain cell is subjected to LN_2 temperature (77 K) conditions, understandably, owing to the freezing of the CO_2 gas at such low temperatures. The emission characteristics of a free running CW-CO_2 laser when its gain cell is cooled to LN_2 temperature have been studied for the first time and the results are elaborated here. These findings are very significant as they establish that the multi-line laser emission in 5 μm region originates from CO molecules that are formed inherently as a discharge product through the dissociation of CO_2 gas in the CO_2-N_2-He discharge mixture thus dispensing with the need to handle extraneous toxic CO gas for lasing action. The laser yielded a maximum of ~8 Watt power for a current of ~5 mA at 20 KV discharge voltage under the free running conditions. That, CO laser, providing coherent radiation spanning 4 to 6 μm serves as a useful source for spectroscopic studies is well understood.

Chapter 5: Application of 10 μm Source for SF_6 Enrichment by Laser Assisted Aerodynamic Process.

Experimental results demonstrating the enrichment of $^{34}SF_6$ when the emission of a CW-CO_2 laser is made to interact with a supersonically cooled SF_6-Ar binary gas jet have been presented. A single longitudinal mode (SLM), tunable, indigenously developed line tunable CW-CO_2 laser, capable of delivering up to 14 W output was employed for these studies. The separation efficiency has been studied as a function of the molar concentration of SF_6 in the

gas mixture and the stagnation pressure. Separation factors exceeding '2' under certain parameter conditions have been obtained.

Further to this work, the advantage of a red-shifted excitation source in enhancing the enrichment efficiency has also been experimentally demonstrated. To this end, in the first set of experiments, the CW-CO_2 laser was tuned to emit on the 10P (16) line known to have a strong overlap with the ν_3 absorption feature of $^{32}SF_6$ (cross-section, σ, at 947.7 cm^{-1} is ~3.072 x 10^{-17} cm^2) [6]. The separation factor α, was measured to be ~1.45. In the next set of experiments, when the laser beam was tuned to the 10P (20) line (cross-section, σ, at 944.2 cm^{-1} is ~2 x 10^{-18} cm^2) [5], the corresponding separation factor was found to be ~1.63. This enhancement owes its origin to the efficient multi-photon excitation possible here due to the red-shifted nature of the incident radiation. The details pertaining to this work are reported in this chapter. A novel way of estimation of separation factor by absorption method has been conceived wherein the knowledge of the absorption cross-section of the molecule for the incident laser line is rendered irrelevant. The separation factor obtained by this technique is seen to corroborate with mass spectroscopic measurements.

Chapter 6: Application of Continuously Tunable 5 µm Source in Isotope Selective Studies in Aerodynamic Gas Jets.

Isotope selective absorption studies in the Di-Methyl Stannane-He binary jet have been carried out by employing the indigenous continuously tunable 5 µm source. Estimation of isotopic shifts of fundamental vibrational frequencies of alkyl stannanes was first carried out using the *ab-initio* density functional theory (DFT) methods. The experimentally measured shift in the absorption peaks for the two isotopes that were measured was found to be in line with the theory.

This was followed by undertaking the study pertaining to homogenization of the process and buffer gas mixture that is an essential prerequisite for the aerodynamic expansion. The time taken for homogenization of the process and the buffer gas can be much too long in particular for a heavier process gas. This creates an experimental hindrance when the process and the buffer gases cannot be mixed apriori owing to the process gas being radiological/toxological. The necessity to vary the ratio of the mixing during experimentation can further multiply the complexity. In the light of all the above, it is essential to ensure that the feed gas, as it is fed to the nozzle, is a homogenous mixture of the process gas and the buffer gas. To this end, practical methods of homogenization of feed and buffer gas mixture were carried out and the results discussed. The nozzle & skimmer throughputs for a 150 micron nozzle, 1 mm skimmer diameter were measured experimentally as estimation of skimmer throughput theoretically is not straightforward.

In another study, a method of enhancement of the laser-jet interaction time for efficient laser assisted aerodynamic separation has been attempted. A pulsed laser capable of providing intensities in the range of hundreds of kW/cm^2 to MW/cm^2 is often required in case of certain molecules (owing to poor cross-sections) for efficient isotope selective photo-excitation. Since the laser is pulsed, ideally the nozzle jet stream should also be in the pulsed mode. However, the fastest pulsed valve available commercially has a typical opening time of several hundreds of microseconds, much too long compared to the duration of the laser emission resulting in very negligible fraction of the molecules in the jet actually interacting with the laser beam. This thereby results in dilution of any enrichment that might have occurred during the laser-jet interaction period. To this end, a novel method of re-circulating the gas through the nozzle time and again so as to enable its interaction with the laser was envisaged that eventually led to an increase in the laser-jet interaction time by a factor of ~‘20’.

References:

1. Molecular Laser isotope Separation, ***Los Alamos Science***, 1982, 3, No. 1, 1-33.

2. Separation of the isotopes of uranium by the separation nozzle process, E W Becker, K. Bier, W. Bier, R. Schütte, D. Seidel, ***Angewandte Chemie***, *International Edition*, 6, No.6, 1967, 507-518.

3. Laser Assisted Aerodyanmic Separation, H Van den Bergh, ***Laser and Optoelectronik***, 1985, 3, 263-273.

4. Isotopically Selective Condensation and Infrared Laser Assisted Gas Dynamic Isotope Separation, J.M.Zellweger, J.M.Philippoz, P.Melinon, R.Monot and H. Van den Bergh, ***Physical Review Letters***, 1984, 52, No. 7, 522.

5. Separation of isotopes by laser-assisted retardation of condensation (SILARC), Jeff W Eerkens, ***Laser and Particle Beams***, 1998, 16, No. 2, 295-316.

6. R. V. Ambartzumian, Yu. A. Gorbkhov, V. S. Letokhov, G. N. Makarov, *Soviet Physics-JETP Letters*, 1975, 21, 171.

Table of Figures

List of Tables

Chapter 1: Introduction to the Thesis

1.1. Background

Ever since Theodore Maiman operated the first laser in 1960, it fired the imagination of scientists in many countries towards using it to shrink the size of the usually huge industrial enrichment plants. The reason behind this is the extraordinary purity of laser light that could be easily exploited to selectively excite the rarer isotope leading to its straightforward separation from the abundant species. Two approaches based on this simple concept viz., atomic vapor laser isotope separation (AVLIS) [1.1, 1.2] and molecular laser isotope separation (MLIS) [1.3] have been extensively researched over last many decades but have not established themselves as viable alternatives to the conventional experimental methods. Another laser based approach [1.5, 1.6] that has gained momentum over the last decade or so basically combines isotope selective laser excitation with an existing separation scheme viz., aerodynamic separation [1.4] that takes advantage of the difference in the masses of the two isotopes. This laser assisted aerodynamic scheme [1.5, 1.6] has established its clear advantage over the classical MLIS scheme in terms of power requirement from the laser. It is well known that when an isotopic gaseous mixture expands through an orifice, the heavier species tends to concentrate near the jet centerline while the lighter one moves outwardly [1.5]. This thus presents a possibility of separating the heavier component from the lighter species. The efficiency of the separation of isotopes through this process understandably depends on their relative mass difference. The conventional aerodynamic separation can thus be very effective in separating lighter isotopes e.g., hydrogen and deuterium with large relative mass difference. The enrichment factor that is achievable under this scheme for heavier isotopes with negligible relative mass difference, on the other hand, will be too small to have any practical utility [1.7]. However, it is known that polyatomic molecules seeded in an inert carrier gas subjected to supersonic nozzle expansion communicate with the low temperature

bath provided by the monatomic carrier gas resulting in the relaxation of their various degrees of freedom [1.8, 1.9] viz., vibrational, rotational and the translational. Thus, as the gas cools, the molecules in the jet form Van der Waals clusters with themselves (homo) and as well as with carrier atoms (hetero) [1.5, 1.6, 1.8 & 1.9]. Selective laser excitation of one of the isotopes is known to prevent it from forming clusters, thereby giving rise to a larger mass difference between the excited isotope and the non-resonant isotope that continue to form clusters, resulting in a much wider spatial separation between them. The intrinsic advantage derived from the repression of condensation of the laser excited isotopic molecule in the expanding gas jet [1.10, 1.11] makes it compatible for enriching certain heavy isotopes of strategic interest [1.12, 1.13] and has therefore gained attention of late [1.14-1.19]. Thus while spatial separation of the heavier and lighter streams primarily take place under the influence of pressure gradient between the local pressure of the expanding continuum stream and the background gas in the expansion chamber [1.5, 1.6, 1.10], diluting the molecular isotopic mixture in a buffer gas like Argon further enhances the overall separation efficiency as now the possibility of transferring the vibrational excitation from the resonant to the non-resonant species through collisions reduces drastically thereby reducing the scrambling reactions [1.5, 1.6, 1.10]. Unlike the case of MLIS, where, a single molecule needs to absorb tens of photons sequentially to reach the dissociation limit, the requirement on the intensity of the laser source is much less stringent here, as the excitation of the fundamental vibrational level would suffice in preventing cluster formation, thereby making this process accessible [1.11] to even continuous wave (CW) laser sources that generate much less power. Laser assisted aerodynamic separation process thus has established itself as a superior alternative to MLIS that is based on classical multi-photon dissociation route.

CO_2 laser that operates in the mid-infrared region and tunable over 9 to 11 μm region, albeit discretely, is the most attractive option to impart the selective vibrational excitation to the

isotopic species of choice either directly or by way of converting its emission into other wavelengths through non-linear or optical pumping routes. However, more often than not, the discrete tunability of the parent laser sometimes comes in the way of resonant excitation, as the possibility of exact coincidence between absorption centre of the desired isotopic species and the emission line centre of the coherent source is extremely rare. The possibility of continuous tunability of the coherent sources is of great advantage in such cases. It is also sometimes imperative to carry out precursor spectroscopic studies before applying laser assisted aerodynamic separation scheme to certain isotopes of strategic importance or otherwise, like Sn, Mo, U etc. Indigenous development of coherent sources emitting over the 5 and 10 μm wavelengths of the mid-infrared (mid-IR) region of the electromagnetic spectrum and employing them for isotope selective studies is the central theme of the work reported in this thesis.

1.2. Motivation

The first demonstration of dramatic enhancement of enrichment factor upon combining laser with aerodynamic separation made use of a discretely tunable CO_2 laser that fortuitously had reasonable overlap with the absorption centre of the desired isotope, $^{32}SF_6$, the working molecule [1.5, 1.6]. However, the possibility of exact coincidence between the absorption centre of the desired isotopic species and the emission centre of the coherent source is rare as discussed above. A case in point is ^{124}Sn. Its importance as a detector element in neutrino-less double beta decay experiments is well-recognized [1.20, 1.21]. Organo-tin compounds with their Sn-H stretching frequency (fundamental ν_3 mode) lying in the region of 1800-1900 cm^{-1} have a good absorption feature in the 5 μm spectral region that can be reached only by frequency doubling of the emission of a continuously tunable CO_2 laser [1.22, 1.23]. This requirement further lent a boost to the activity of developing a 5 μm coherent source. Hence, development of both discretely and continuously tunable coherent sources in the 10 μm

region followed by employing them as pump sources for extending the wavelength to other regions in mid-IR, viz., 5 μm, by way of non-linear processes forms the important thrust of the work.

Secondly, homogenization of the process and buffer gas mixture is an essential prerequisite for carrying out the aerodynamic expansion process. The time taken for homogenization can however be much too long when a heavier process gas and/or higher stagnation pressures are involved [1.24]. The problem gets compounded when the process and the buffer gases cannot be mixed a priori owing to the process gas being radiological/toxic. The necessity to vary the ratio of the gases in the mixture during experimentation too can further multiply the complexity. In the light of all the above, it is essential to ensure that the feed gas, as it is fed to the nozzle, is a homogenous mixture of the process gas and the buffer gas. To this end, a simple practical method of homogenization of the feed and buffer gas mixture have been conceived, developed and demonstrated. Further, often, the poor absorption cross-section of certain molecules warrants usage of a pulsed laser that is capable of providing very high intensities, in the range of few 10's of MW/cm^2 to 100's of GW/cm^2. Since the laser is pulsed, to avoid dilution, the nozzle jet stream should also be in the pulsed mode, for efficient laser assisted aerodynamic separation process. However, the fastest valves available commercially have typical opening times of several hundreds of microseconds, much too long compared to the duration of the laser emission (typically ~few 100's of nsec) resulting in very negligible fraction of the molecules in the jet actually interacting with the laser beam. This thereby results in dilution of any enrichment that might have occurred during the laser-jet interaction period. A method to mitigate this problem and increase the laser-jet interaction time has been elegantly demonstrated as part of this work.

1.3. Scope of the Present Work

Development and characterization of tunable Mid-IR coherent sources operating in both the 5 & 10 μm regions of the electromagnetic spectrum and their applications in laser assisted aerodynamic process leading to isotope selective studies forms the main thrust of the dissertation work. In this regard, a continuously tunable coherent 5 μm source has been developed by Second Harmonic (SH) conversion of the emission of a multi-atmospheric Transverse Excitation (TE) CO_2 laser in $AgGaSe_2$ (AGS) non-linear crystal. In addition, generation of discretely tunable 5 μm source from a $ZnGeP_2$ (ZGP) crystal by SH conversion of the emission of indigenously developed Continuous Wave (CW) and Transverse Excitation Atmosphere (TEA) CO_2 lasers has also been reported. The indigenously developed sources have been used in the isotope selective studies of sulfur and tin. The aforementioned coherent sources have also been employed in isotope selective studies of certain isotopes of strategic interest, the details of which though are not being reported here in the thesis. Further, coherent multi-line lasing in the 5 μm region from CO gain medium formed in a CO_2-N_2-He discharge when cooled to LN_2 conditions has been accomplished for the first time and has been reported. In another work, an elegant practical method to reduce the time required for homogenization of feed and buffer gas mixture, a pre-requisite for any aerodynamic separation process been demonstrated. Furthermore, a novel method to increase the laser-jet interaction time leading to reduction in dilution, and, in turn, enhancement in the efficiency of separation, has been reported.

1.4. Plan of the Thesis

For convenience of presentation, the thesis has been divided into six chapters and the contents of the work in the chapter-wise manner are presented briefly as below.

The introductory chapter (chapter 1) conveys the main objective, motivation, and, the scope of the thesis. A brief introduction to mid-IR coherent sources and their utilities in the context

of the present work have also been enunciated. Further, the various aspects of supersonic free-jets and aerodynamic nozzle expansion have been deliberated upon in detail in this chapter.

In **chapter 2**, to begin with, the physics of CO_2 laser, its lasing action in the atmospheric pressure region on various normal band transitions (P & R) and the discrete nature of the emission lines at this pressure have been discussed. A detailed characterization of a TE multi-atmosphere CO_2 laser towards obtaining continuous tunability has been carried out.

The results of generation of continuously tunable coherent 5 μm source by SH conversion of the emission of the multi-atmospheric TE CO_2 laser by using an $AgGaSe_2$ crystal and its characterization with regard to energy and power conversion efficiency forms the essence of **chapter 3**. Further, the results obtained on generation of discretely tunable coherent 5 μm radiation by SH conversion of emission of both CW & TEA (Transverse Excitation Atmospheric) CO_2 lasers using a $ZnGeP_2$ crystal, the characterization of the generated SH output w.r.t. energy and power conversion efficiency and the characterization as a function of CO_2 partial pressure for the case of TEA CO_2 laser operation have been presented.

Emission characteristics of a free-running CW-CO_2 laser when its gain cell is subjected to LN_2 temperature has been studied for the first time and the results elaborated in **chapter 4**. These findings are very significant as they establish multi-line laser emission in the 5 μm region originating from CO molecules that are formed inherently in the discharge through the dissociation of CO_2 in the CO_2-N_2-He gas mixture, thus dispensing with the need for extraneous use of toxic CO gas for lasing action.

In **chapter 5**, the experimental demonstration of the enrichment of $^{34}SF_6$ when the emission of a CW-CO_2 laser was made to interact with a supersonically cooled SF_6-Argon binary gas jet by laser assisted aerodynamic separation scheme has been described. An indigenously

developed, line tunable, single longitudinal mode CW-CO_2 laser, capable of delivering up to 14 W output on TEM_{00} output was employed for these studies. The separation efficiency has been studied as a function of the molar concentration of SF_6 in the gas mixture and the stagnation pressure. Further to this work, the advantage of a red-shifted excitation source in enhancing the enrichment efficiency has also been experimentally demonstrated. This enhancement owes its origin to the efficient multi-photon excitation possible here due to the red-shifted nature of the incident radiation. The intricate details pertaining to this work are reported in this chapter. Also, a novel way of estimation of separation factor by an absorption method has been elegantly conceived wherein the knowledge of the absorption cross-section of the molecule for the incident laser line is rendered irrelevant. The separation factor obtained by this technique was seen to corroborate with the mass spectrometric measurements.

In **chapter 6**, isotope selective excitation studies in the Di-Methyl Stannane-Helium (DMS-He) binary gas jet have been carried out by employing the indigenously developed continuously tunable 5 μm source. The experimentally measured shift in the absorption peaks for case of two of the isotopes of this molecule was measured and found to be in line with that estimated theoretically. Following this, a novel and simple method of homogenization of feed and buffer gas mixture, conceived in our lab, was carried out and the results elaborated. A method of enhancement of the laser-jet interaction time for reducing dilution and thereby enhancing the efficiency of the process too has been reported. This involves re-circulating the feed gas mixture time and again through a nozzle leading to an increase in the laser-jet interaction time by a factor of ~20.

To the end, a summary of the entire work reported in the thesis, has been presented under the head **'General Conclusions'**.

1.5. An Overview of Mid-IR Coherent Sources

Molecular lasers operating in the mid-IR spectral region of the electromagnetic spectrum spanning from ~2-25 μm finds several applications encompassing the fields of physics, chemistry, biology, and medicine [1.25-1.27]. The most important example of this category by far, is the CO_2 laser emitting over 9-11 μm region in a discrete manner which uses transitions between vibrational levels of the ground electronic state [1.28]. Invented by C K N Patel in 1964, these lasers are capable of producing high peak powers ranging from kW to 100's of MW and intensities ranging from few 10's of MW/cm^2 to several 100's of GW/ cm^2 and possess wide tuning range. Among its several applications, one important area is in the separation of isotopes. The high power densities available from this laser facilitate, understandably, higher molecular excitation rates thereby annulling the poorer absorption cross-sections that are inherent to some of the molecules [1.11]. Further, though CO_2 laser provides numerous transitions spanning over 9-11 micron region, there are several strategic molecules whose absorption features do not directly overlap with any of these lines. This limitation can be overcome by optically pumping an appropriate medium by the CO_2 laser radiation which results in the generation of new coherent sources at other frequencies [1.29-1.37]. A host of such generated coherent sources emits near 5, 12 & 16 micron wavelengths regions, to name a few, and are widely tunable. These lasers pumped by CO_2 laser can be employed for selective excitation of the fundamental, overtone or combination band regions of appropriate isotopes including those that are of strategic interest [1.38-1.40]. A case in point is in the isotope separation of uranium. The 10 μm emission from a CO_2 laser undergoes rotational Raman scattering in the para-H_2 medium generating coherent radiation at 16 μm wavelength [1.31-1.33] and has been the work horse in nuclear industry for carrying uranium isotope separation in its molecular form [1.3]. CF_4 laser operating in the 16 μm region too has been used for isotope selective multi-photon dissociation of UF_6 [1.38]. The

NH_3 [1.35, 1.36] laser that operates in the 12 μm region has overlapping feature with the tritium isotope in certain molecular form [1.39]. This laser has been recognized as an important source for the removal of tritium from contaminated light and heavy water in fission reactors [1.41, 1.42]. Other noteworthy and versatile means of producing optical output in the mid-IR region are from, the CO gas medium in the 4-6 μm region [1.29], non-linear optical parametric frequency conversion in the 2-20 μm region [1.43-1.46], semiconductor diode lasers (e.g., quantum cascade lasers) [1.47-1.49], optical fibers [1.34] etc. With their broad tunability and substantial output power, these are extensively used in mid-IR spectroscopy [1.34].

1.6. An Overview of Supersonic Nozzle Expansion

Gases of interest seeded in an inert carrier gas and subjected to supersonic nozzle expansion communicate with the low temperature bath provided by the monatomic carrier gas via two

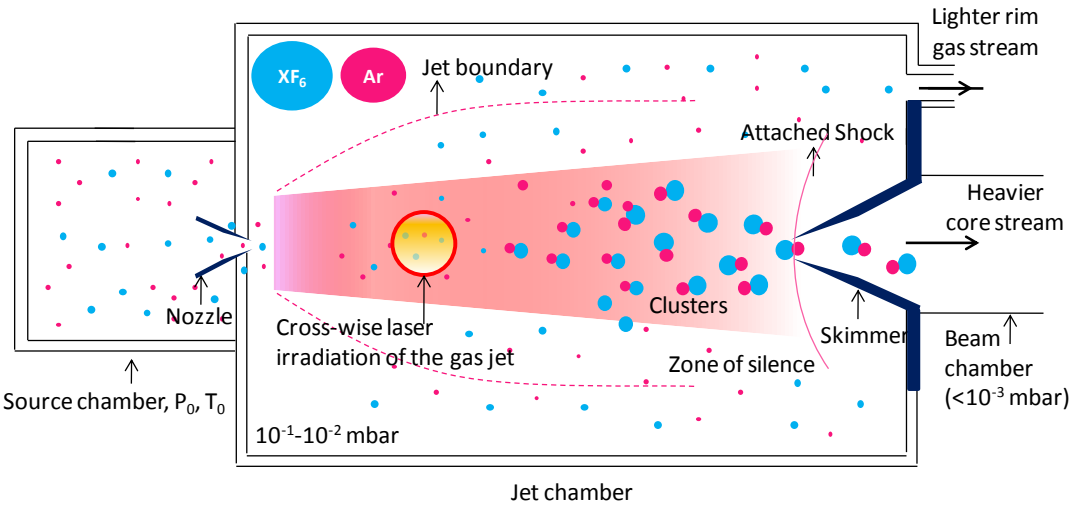

Figure 1. 1. Schematic of the supersonic nozzle expansion from a stagnation source. The gas expands isentropically into the expansion chamber and a skimmer placed at a suitable upstream location inside the zone of silence skims the central portion of the jet into the beam chamber. An attached bow shock enables the gas to be skimmed in its free stream condition. Also shown is the selective laser excitation at a suitable downstream distance towards inhibiting cluster formation of the excited isotope with the buffer gas.

body collisions resulting in the relaxation of their translational, vibrational and rotational degrees of freedom [1.8, 1.9]. The extremely low temperature bath promotes formation of weakly bound Van der Waals clusters in the jet. Selective condensation repression of a desired isotope in such dynamically cooled jets by infrared vibrational excitation assumes significance in realizing isotope enrichment [1.11]. Hence, knowledge of various parameters viz., temperature, pressure, number density, velocity, Mach number etc., in the flow field of such supersonic jets is very crucial. The flow properties can be accurately predicted using analytical expressions for isentropic fluid flow [1.50-1.52]. To this end, various terms encountered in supersonic flow viz., continuum regime, free-molecular Regime, Mach number, stagnation temperature, static temperature, dynamic temperature, stagnation pressure, static pressure, dynamic pressure, axial velocity, shocks etc., are discussed herein. Further, various properties of a continuum free-jet have been elaborated. The schematic of nozzle expansion from a source at (P_o, T_o) through a nozzle/orifice into an expansion chamber maintained at a background pressure P_b is shown in figure 1.1. The expansion being adiabatic, the velocity of the flow increases at the expense of internal energy of the fluid and hence the random thermal energy is converted into directed kinetic energy of the flow resulting in the reduction of the local gas temperature [1.51]. The substantial cooling associated with the isentropic expansion reduces the local sound speed in the expanding gas medium too, thereby increasing the Mach number in the supersonic flow [1.52]. In the continuum region of the flow, collisions occur with sufficient frequency for equilibrium to be maintained between the various degrees of freedom throughout the expansion process. However, at some point in the expansion, the collision frequency drops to such a low value that a particular degree of freedom (translational, rotational or vibrational) may fall out of equilibrium. This is the beginning of transition from continuum to free-molecular flow that results in collision free environment and freezing of flow parameters [1.50]. To be noted that,

the rotational relaxation occurs more readily than vibrational, and, translational energy exchange occurs even more readily than rotational relaxation. Hence $T_{tr} < T_{rot} < T_{vib}$ [1.50]. Thus, there exists a certain region in the expansion regime called the 'zone of silence' (figure 1.1) where the fluid properties are just right to exploit them for isotope selective studies, or, for that matter, in spectroscopy [1.50].

1.6.1. Compressible and incompressible Fluid Flow

Sound propagates in a medium with speed that depends on the bulk compressibility of the medium. The less compressible the medium, the higher the speed of sound. Thus, speed of sound is a convenient reference speed, when a flow is involved. Consider the flow of air around an object moving at a certain speed. If the speed of the flow (which is the speed of the object itself) is much less compared to the speed of sound (330 m/s at normal atmosphere conditions) in the medium, the medium behaves as if it were incompressible. However, if the flow velocity becomes comparable to the speed of sound, compressibility effects sets in and become prominent necessitating compressible flow properties to be applied to the medium. In actual, the speed of sound itself can vary from one point to another in the flow and so the velocity at each point has to be compared with the local sound speed at that point. This ratio is called the Mach number [1.52]. The Mach number, defined as speed at any point in the fluid (υ) to the local sound velocity (a), is given by,

$$M = \upsilon/a. \qquad [1.1]$$

All fluids are compressible to some extent or the other. The medium is said to be compressible if there is a certain change in density, $\Delta\rho$, for a given change in pressure, ΔP. A quantitative criterion [1.52] to understand the compressibility effects in a fluid flow, i.e., to know whether a medium behaves as compressible or incompressible, is as follows.

$$\text{We have, } \frac{\Delta\rho}{\rho} = \frac{1}{\rho}\frac{\Delta\rho}{\Delta P}\,\Delta P;\ \text{where, } a = \sqrt{\frac{\Delta P}{\Delta\rho}} \qquad [1.2]$$

From Bernoulli's equation for steady flow,

$$\Delta P \propto \rho \upsilon^2 \qquad [1.3]$$

Rearranging the terms in equation 1.2 gives,

$$\frac{\Delta\rho}{\rho} = \frac{1}{\rho}\frac{\Delta\rho}{\Delta P}\Delta P = \frac{\upsilon^2}{a^2} = M^2 \qquad [1.4]$$

$$\text{Or,} \frac{\Delta\rho}{\rho} = M^2 \qquad [1.5]$$

It is customary to assume that the flow is incompressible if the change in density is less than 10% of the mean value, which happens if M < 0.3. So compressibility effects become significant when Mach number exceeds 0.3 [1.52] which is the case in aerodynamic expansion from a nozzle. Thus, fluid flow from a nozzle is treated as compressible flow.

1.6.2. Thermodynamics of Isentropic Nozzle Flow

Consider a flow of a fluid through some volume element, say, a nozzle, as shown in figure 1.2. A nozzle is a device that increases the velocity of a fluid at the expense of pressure. When both the K.E. and P.E. of the fluid flow are negligible (case of low speed flows with no change in elevation), then, enthalpy represents the total energy of the fluid, given by,

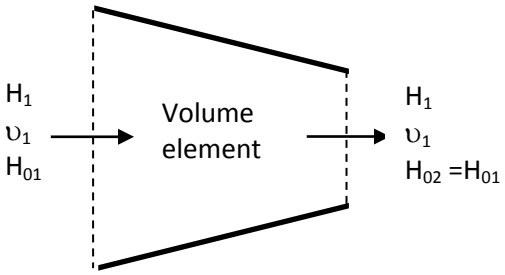

Figure 1.2. Steady flow of a fluid through an adiabatic nozzle.

$$H = U + PV \text{ (internal energy + flow energy)} \qquad [1.6]$$

For high speed flows, the P.E. of the fluid is still negligible, but the K.E. is not. In such cases, it is convenient to combine the enthalpy and the K.E. of the fluid into a single term called stagnation (or total) enthalpy, H_o, defined as

$H_0 = H + ½ m\upsilon^2$, [1.7]

where, H is the static enthalpy.

For the expanding flow, the energy balance equation reads, $E_{in} = E_{out}$

$\Rightarrow H_1 + ½ m\upsilon_1^2 = H_2 + ½ m\upsilon_2^2$ [1.8]

Or, $H_{01} = H_{02}$

If the fluid were brought to a complete stop in an adiabatic manner, the velocity at state 2 would be 0 and equation 1.8 would read,

$H_1 + ½ m\upsilon_1^2 = H_2 = H_{02}$ [1.9]

The stagnation state is a theoretical state in which the fluid flow is brought into a complete motionless condition in an isentropic process (a process which is both adiabatic and reversible). The various properties of the fluid in the stagnation state are called stagnation properties. As can be seen, during a stagnation process, the K.E. of the fluid is converted to enthalpy (internal energy plus flow energy) that results in an increase in the fluid temperature (internal energy) and pressure.

Rewriting equation 1.7 in terms of specific enthalpy,

$h_o = h + ½ \upsilon^2$ [1.10]

Where, the specific enthalpy, h (= H/m), represents the energy of a flowing fluid stream per unit mass and h_o is the stagnation enthalpy per unit mass. The quantity, h_o, is a constant along any streamline. Substituting for 'h' in terms of 'C_p' and 'T' in equation 1.10 yields,

$$C_p T_o = C_p T + \frac{\upsilon^2}{2} \quad [1.11]$$

$$\text{Or, } T_o = T + \frac{\upsilon^2}{2C_p}; \qquad [1.12]$$

T_o is called the stagnation temperature and it represents the temperature that the fluid would attain when it is brought to rest adiabatically. The term $\frac{\upsilon^2}{2C_p}$ in the above equation corresponds to the temperature rise during such a process and is called the dynamic temperature [1.51]. On the similar lines, one can define the static and dynamic components of pressure [1.51].

We now derive the isentropic relations for compressible fluid flow. The assumptions made in deriving these equations are inviscid (high speed flows), isentropic continuum flow [1.51]. In the continuum flow, collisions occur with sufficient frequency that there exists local thermodynamic equilibrium between all the degrees of freedom.

We know, the speed of sound,

$$a = \sqrt{\gamma R' T} \Rightarrow T = \frac{a^2}{\gamma R'}, \qquad [1.13]$$

where, R' is the particular gas constant, given by,

$R' = \frac{R}{M}$, R, being the universal gas constant, M the molecular mass and γ, is the specific heat ratio of the gas/gas mixture.

$$\text{Also, } \gamma = \frac{C_p}{C_v}\ ;\ R = C_p - C_v \qquad [1.14]$$

$$\Rightarrow C_P = \frac{\gamma R}{\gamma - 1}\ ,\ C_\upsilon = \frac{R}{\gamma - 1} \qquad [1.15]$$

Substituting the above expressions in equation 1.12 yields,

$$\frac{T_o}{T} = 1 + \frac{\gamma - 1}{2}\frac{\upsilon^2}{a^2} \qquad [1.16]$$

$$\frac{T_o}{T} = 1 + \frac{\gamma - 1}{2}M^2 \qquad \left[\frac{\upsilon}{a} = M\right] \qquad [1.17]$$

$$\frac{P_o}{P} = \left(\frac{T_o}{T}\right)^{\gamma/\gamma-1}; \qquad [1.18]$$

$$\frac{\rho_o}{\rho} = \frac{n_o}{n} = \left(\frac{T_o}{T}\right)^{1/\gamma-1} \qquad [1.19]$$

Once M is known, all other thermodynamic parameters in the flow field can be evaluated.

1.6.3. Free-Jet Expansion

When a gas expands isentropically from a source at higher stagnation pressure into a chamber maintained at vacuum through a nozzle or an orifice such that the Knudsen number, Kn = (λ/d) is << 1 i.e., λ <<D, where 'λ' is the mean free path (source chamber), 'd' the characteristic dimension (here the nozzle diameter), the flow is referred to as free-jet as the gas expands free of the containing nozzle walls. Figure 1.3 shows the features of a free-jet expansion from a convergent (axisymmetric) nozzle under isentropic conditions. The gas starts from a negligibly small velocity inside the nozzle called the stagnation state (P_0, T_0) (M=0) and with an imposed pressure difference, (P_0-P_b), accelerates as the area decreases toward the source exit. The flow may reach sonic speed (Mach number = 1), at the nozzle exit, provided the pressure ratio, $\frac{P_0}{P_b}$, equals a certain critical value, G = $((\gamma+1)/2))^{\gamma/(\gamma-1)}$, which is less than 2.1 for all gases [1.50], where, γ, is the specific heat ratio. If the pressure ratio is less than this critical value, the flow will be subsonic with exit pressure 'P_e' equal to 'P_b', without any

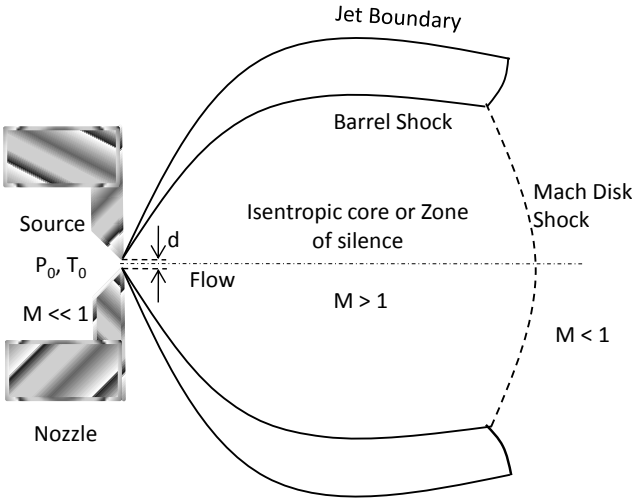

Figure 1.3. Continuum free-jet expansion from a nozzle at stagnation (P_o, T_o).

further expansion [1.50, 1.51]. As $\frac{P_0}{P_b}$ increases beyond this critical ratio, the flow becomes sonic at the source exit and the exit pressure, P_e, becomes independent of P_b, and equals $P_e = P^* = P_o\left(\frac{2}{\gamma+1}\right)^{\gamma/\gamma-1}$. Since the pressure at the exit, P_e, now exceeds P_b, the flow is said to be under-expanded and a subsequent expansion occurs as the flow attempts to meet the necessary boundary condition imposed by the ambient pressure, P_b.

I. e., $P_e = \begin{cases} P_b \text{ for } P_b \geq P^* \\ P^* \text{ for } P_b < P^* \end{cases}$ [Refer to figure 1.4]

Thus, a convergent nozzle accelerates subsonic flows with M < 1. For sufficient nozzle pressure ratio, the flow will reach sonic velocity at the narrowest point (nozzle throat). In this situation, the nozzle is said to be chocked and the Mach number equals 1. Increasing the nozzle pressure ratio further will not increase the Mach number beyond unity at the throat, but downstream (i.e., external to the nozzle), the flow is free to expand to supersonic velocities (M > 1). At the throat of the nozzle where M = 1, the parameters, T^*, P^* and ρ^*, referred to as chocked flow conditions and are arrived at by substituting M = 1 in equation 1.17, 1.18 and 1.19 respectively,

$$\frac{T^*}{T_o} = \frac{2}{\gamma+1} \qquad (1.20)$$

$$\frac{P^*}{P_o} = \left(\frac{2}{\gamma+1}\right)^{\gamma/\gamma-1} \qquad [1.21]$$

$$\frac{\rho^*}{\rho_o} = \frac{n^*}{n_o} = \left(\frac{2}{\gamma+1}\right)^{1/\gamma-1} \qquad [1.22]$$

It is obvious from equation 1.20, that, in order to obtain supersonic free-jet expansion, the pressure ratio, $\frac{P_o}{P_b}$, should exceed $\left(\frac{\gamma+1}{2}\right)^{\gamma/\gamma-1}$ [1.50]. The maximum mass flow rate occurs at the throat of the nozzle given by, $\dot{m} = D.C.\,\rho^* A^* \upsilon^*$, where, D.C. is the discharge coefficient

(defined as the ratio of the actual discharge to the theoretical discharge) at the nozzle exit which is typically ~0.82 for most gases [1.53].

Supersonic flow has two characteristics that make the expansion interesting. First, unlike subsonic flow, in a supersonic flow, as the flow area increases, the velocity too increases, so that M becomes greater than 1, beyond the exit. Second, a supersonic flow cannot sense downstream conditions. This is crucial feature caused by that fact that information propagates at the speed of sound whereas fluid moves much faster i.e., M > 1. Thus, the flow does not know about the prevailing boundary condition, P_b, and M continues to increase [1.50]. The gas thus over-expands to a pressure which is much lower than the background pressure, but, yet at some point in the flow, it must adjust to the background conditions. The resulting dilemma is resolved by the formation of shock waves; the Mach disk shock normal to the jet centerline and the barrel shock at the sides (figure 1.3) [1.50]. Shock waves reduce the Mach number to subsonic values to meet the boundary conditions, and once M < 1, the flow can adjust to background conditions. I.e., the isentropic properties of the flow are frittered and the pressure and the temperature of the gas in the flow increase. Shocks are very thin, non-isentropic regions of large density, pressure, temperature and velocity gradients. A detailed account of shocks in supersonic jets is presented as below.

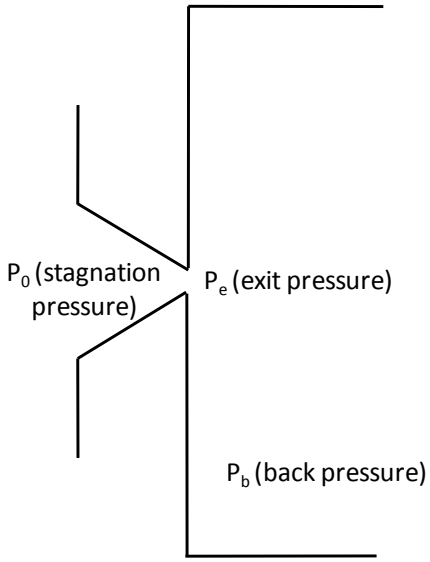

Figure 1. 4. Expansion of gas from stagnation, P_o, into a background at P_b, P_e is the pressure at the nozzle exit.

1.6.4. Shocks in Supersonic Jets

Shock or a shock wave is a type of propagating disturbance. When an object (or disturbance) moves faster than the information about it can be propagated into the surrounding fluid, fluid

near the disturbance cannot react or 'get out of the way' before the disturbance arrives resulting in a shock wave [1.54]. I.e., shock wave forms when the speed of a fluid changes by more than the speed of sound as in the case of supersonic flow. At the region where this occurs, sound waves travelling against the flow reach a point where they cannot travel any further upstream and the pressure progressively builds up in that region rapidly resulting in a high pressure shock wave. Like an ordinary wave, a shock wave carries energy as it propagates through the medium. Shock wave is characterized by an abrupt nearly discontinuous change in pressure, temperature & density of the medium that results in increase of entropy. The properties change almost instantaneously and the abruptness of change in features of the medium can be viewed as a phase transition. The thickness of the shock waves in air is of the order of mean free path of the gas molecules at that place which is ~200 nm and resembles a line or a plane. Shock wave is also formed in the supersonic free-jet expansion if it is interfered by either a solid object, like, say, a skimmer, whose characteristic dimension (its orifice diameter) is greater than the local mean free path or by the residual background gas in the expansion chamber.

1.6.5. Design Criterion of Nozzle and Skimmer

As mentioned earlier, a nozzle is a specially shaped tube through which fluid flows; a device that increases the velocity of a fluid at the expense of pressure. The typical aspect ratio, L/D, of a nozzle is ~2 to 3, where L is the length of the nozzle and D is the diameter at the throat (exit end) of the nozzle (figure 1.5).

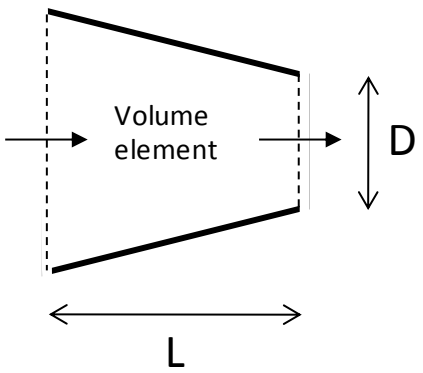

Figure 1.5. A nozzle with an aspect ratio L/D.

A skimmer (figure 1.6) is a hollow truncated cone with an orifice at its apex. It separates the expansion chamber with high background density from the beam chamber at lower pressure achieved by means of differential pumping. Since it is placed in a supersonic stream, it will

give rise to a bow shock as shown in figure 1.1. To be noted, in order to use the skimmer in the continuous regime, the internal angle ($\theta_{internal}$) of the skimmer should be as large as possible to minimize the interference of the background molecules that are reflected off the walls of the skimmer with the skimmed gas in the form of beam (where the supersonic flow properties are intact) and the maximum external cone angle ($\theta_{external}$) of the skimmer must be less than a certain critical value for a particular Mach number, for the bow shock to be an attached one which would enable the gas in that region to be skimmed in its free-stream condition without frittering any of the advantages of the supersonic jet [1.9]. Since the thickness of shock is of the order of a few free-stream mean free paths, the molecules of the gas passing through the shock will undergo at least a few collisions in passing from free-stream to post-shock state. So, if the diameter of the skimmer inlet is of the order of a free-stream mean free path, one can expect that the shock will be an attached one, and the gas reaching the inlet would not have undergone all the collisions that degrade it to the post-shock conditions. Therefore, a skimmer of diameter of the order of the free-stream mean free path is a convenient design criterion. While a maximum internal angle of 50° would suffice, it has been found experimentally that if the external cone angle is 60° or less, all bow shock waves at the entrance of the skimmer at which Mach number is 6 will be attached [1.9]. In order to preserve the cooling produced in the supersonic expansion, the expanding gas should not be allowed to be scattered from the background gas in the expansion chamber which would reheat the supersonic jet and would ultimately randomize the directed flow. Therefore the discharge from the nozzle should be pumped away quite fast to maintain low background pressure in the expansion chamber.

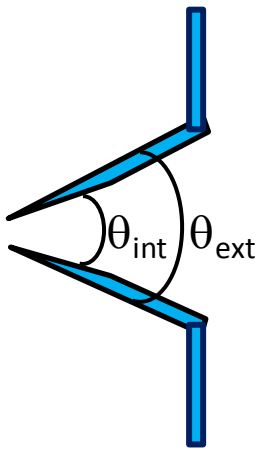

Figure 1.6. Skimmer with its $\theta_{internal}$ and $\theta_{external}$ indicated.

However, in a supersonic nozzle expansion, when we need to work with high background pressures of say ~0.1 mbar that can involve a shock structure, the skimmer must be placed upstream of the mach disk in the continuum region of the flow as shown in figure 1.1 for skimming or extracting the beam. I.e., the free-jet needs to be skimmed well before the Mach disk. To be noted, significant separation (spatially) of the heavier and the lighter streams occurs within the first few diameters in the flow where the pressure gradients (between the expanding gas and the background pressure maintained by the pump) are strong [1.5].

The mach disk location in terms of nozzle diameters is given by the expression, $\frac{x_M}{D} = 0.67\sqrt{\frac{P_0}{P_b}}$ [1.50], where x_M the Mach disk location from the nozzle exit and 'D' is the diameter of the nozzle. P_o, P_b, have their usual meanings as discussed earlier. The location of the Mach disk is the region where the normal shock raises the local pressure in the jet to the background pressure P_b. The width (or diameter) of the Mach disk at the front and the barrel shock at the sides are of the order of $0.5x_M$, $0.75x_M$ within an error of ± 25% [1.50] respectively. Further, the terminal Mach number, M_T, is given by, $M_T = 133\,[P_0 D]^{0.4}$, where P_0 is the source or stagnation pressure and D is the diameter of the nozzle.

The variation of Mach number with, x, the distance from the nozzle exit along the jet centerline is given by the following relations for different cases of axial downstream distance.

In the region of free-jet expansion, the variation of Mach number, M, as a function of distance from the orifice, along the flow axis, can be computed by the formulae [1.50] as below. Once M is known all other flow parameters in the supersonic jet can be computed.

$$M = 1.0 + A\left(\frac{x}{D}\right)^2 + B\left(\frac{x}{D}\right)^3 \text{ for } 0 < \left(\frac{x}{D}\right) < 1 \qquad [1.23]$$

$$M = \left(\frac{x}{D}\right)^{\gamma-1/j}\left[C_1 + C_2\left(\frac{x}{D}\right) + C_3\left(\frac{x}{D}\right)^2 + C_4\left(\frac{x}{D}\right)^3\right] \text{ for } (x/D) > 0.5 \qquad [1.24]$$

Where, x is distance from the orifice, D is diameter of the orifice, A, B, C_1, C_2, C_3, and C_4 are constants. Values of these constants are given in table 1.1 [1.50].

Source	j	γ	C_1	C_2	C_3	C_4	A	B
3D	1	5/3	3.232	-0.7563	0.3937	-0.0729	3.337	-1.541
3D	1	7/5	3.606	-1.742	0.9226	-0.2069	3.190	-1.610
3D	1	9/7	3.971	-2.327	1.326	-0.311	3.609	-1.950

Table 1.1. Centerline Mach number correlations for case of axisymmetric expansion (3D). Values are given for different values of heat capacity ratio (γ) of the gases of interest.

$$M = \left[A\left(\frac{x-x_0}{D}\right)^{\gamma-1} - \frac{\frac{1}{2}\left(\frac{\gamma+1}{\gamma-1}\right)}{A\left(\frac{x-x_0}{D}\right)^{\gamma-1}}\right] \qquad \left(\frac{x}{D}\right) > \left(\frac{x}{D}\right)_{min} \qquad [1.25]$$

Where, $\frac{x_0}{D}$, A are constants specific to γ, the specific heat ratio of the gas, as given in the table 1.2 [1.50].

1.6.6. Transition from Continuum to Molecular Regime

In the continuum regime, collisions occur with sufficient frequency for equilibrium to be maintained throughout the expansion process. However, at some point in the expansion, the collision frequency drops to such a low value that a particular degree of

γ	$\frac{x_0}{D}$	A	$\left(\frac{x}{D}\right)_{min}$
1.67	0.075	3.26	2.5
1.40	0.40	3.65	6
1.29	0.85	3.96	4

Table 1.2. Centerline Mach number correlations for axisymmetric flow. Values are given for different values of heat capacity ratio (γ) of the gases of interest.

freedom may fall out of equilibrium. This is the beginning of transition from continuum to free-molecular flow that results in collision-free environment. This is referred to as Rarefaction. Properties in the absence of these further collisions are said to be frozen.

The different flow regimes in the jet are classified according to the degree of rarefaction occurring in the jet and is defined by the Knudsen number, $Kn = \lambda/d$, where 'λ' is the local mean free path and 'd', the characteristic dimension. If, $Kn < 0.01$, the flow is said to be in the continuum or viscous regime. If, $0.01 < Kn < 0.1$, the flow is said to be in the slip regime (departure of species velocity from the mass average velocity) and for, $Kn > 10$, it is in the free-molecular regime.

1.6.7. Some Important Aspects of Free-Jet Expansion & Cluster Criteria

At any point in the flow, $h_o = h + \frac{1}{2} \upsilon^2$, where h_o, the stagnation enthalpy, is a constant along any streamline. As the gas expands and cools, the local (or static) enthalpy decreases and the mean velocity increases. In nozzle expansion, as a result of binary collisions between the monatomic carrier gas and the seed molecular gas, the random thermal energy (that includes the internal energy in the form of rotational & vibrational energy) of the molecules gets converted into directed kinetic energy of the flow and thus the temperature of the seed molecular gas falls. Further, P, ρ, too fall. The substantial cooling associated with supersonic expansion reduces the local sound speed of the expanding gas tremendously resulting in increasing M as velocity increases. The degree of cooling in a free-jet depends on the total number of two body collisions that occur during the expansion, which is proportional to the product of the stagnation number density and nozzle diameter (P_oD) [1.55]. Cluster formation requires 3-body collisions and is proportional to P_o^2D. Thus, the ratio of 3-body to 2-body collisions is proportional to stagnation pressure (or number density). By controlling the expanding conditions such that $\left(\frac{P_0}{D}\right)$ is minimum and (P_oD) is constant, one can obtain in

principle, any degree of cooling without any clustering [1.55]. Except when Helium is used as the carrier gas, clustering effects usually takes place for $(P_oD) > 10\ \text{torr} - \text{cm}$ [1.8] (helium, owing to its low boiling point does not undergo clustering easily). Reasonable free-jet continuum properties are obtained for $(P_oD) > 1\ \text{torr} - \text{cm}$. Below this value, the nozzle viscous effects become important, discharge coefficient decreases and the expansion does not remain in the continuum regime beyond a few nozzle diameters [1.8]. Since the cross-sections for elastic collisions are larger than those for collision-induced rotational transitions, which are still larger than those for vibrational transitions, the translational cooling, which means the narrowing of velocity distribution will be more effective than the rotational or vibrational cooling. In general, $T_{trans} < T_{rot} < T_{vib} < T_o$ [1.50].

1.7. Conclusions

In this chapter, the objective, motivation and scope of the work carried out in this dissertation have been discussed. A brief introduction to mid-IR coherent sources and an overview of supersonic nozzle expansion have been deliberated upon.

1.8. References

1.1. Laser Isotope Separation in Atomic Vapor, P. A. Bokhan, et al, Wiley-VCH (Reprint 2006).

1.2. Laser isotope separation of uranium, P. Ramakoteswara Rao, Current Science, 85(5), 615 (2003).

1.3. Molecular Laser Isotope Separation, Los Alamos Science, 3, No. 1, 1-33 (1982).

1.4. Separation of the Isotopes of Uranium by the Separation Nozzle Process, E W Becker, K. Bier, W. Bier, R. Schütte, D. Seidel, Angewandte Chemie, International Edition, 6, No.6, 507-518 (1967).

1.5. Laser Assisted Aerodynamic Separation, H Van den Bergh, Laser and Optoelectronik, 3, 263-273 (1985).

1.6. Isotopically Selective Condensation and Infrared Laser Assisted Gas Dynamic Isotope Separation, J M Zellweger, J M Philippoz, P Melinon, R Monot and H Van den Bergh, Physical Review Letters, 52, No. 7, 522 (1984).

1.7. ASP Separation Technology for Isotope and Gas Separation. Ronander E, Strydom H J, Viljoen J, Paper presented at the 12th International Workshop on Separation Phenomena in Liquids and Gases, Paris, France (2012).

1.8. Molecular Beams from Nozzle Sources, James B Anderson; Molecular Beams & Low density gas dynamics, Editor: Peter P Wegener, Publisher New York : M. Dekker, Series Gas dynamics, 4, 1-91 (1974).

1.9. Introduction to Molecular gas dynamics Giovanni Sanna, Giuseppe Tomassetti, Imperial College Press (2005).

1.10. Isotope Separation by Selective Laser-Assisted Repression of Condensation in Supersonic Free Jets, Jeff W Eerkens, Jaewoo Kim, AIChE Journal, 56 (9), 2331-2337 (2010).

1.11. Separation of Isotopes by Laser-Assisted Retardation of Condensation (SILARC), Jeff W Eerkens, Laser and Particle Beams, 16, No. 2, 295-316 (1988).

1.12. SILEX Uranium Enrichment, SILEX Annual Report, http://www.silex.com.au (2014).

1.13. Low Energy Methods of Molecular Laser Isotope Separation, G N Makarov, Physics-Uspekhi, 58 (7), 670-700, Physics Institute of the Russian Academy of Sciences (2015).

1.14. Hecht J, Laser Isotope Separation: Laser Uranium Enrichment Returns from the dead, Laser Focus World, 47 (10), 18 (2011).

1.15. Broad W J, Laser Advances in Nuclear Fuel Stir Terror Fear, New York Times, http://www.nytimes.com/2011/08/21/science/earth/21laser.html (2011).

1.16. V M Apatin, V N Lokhman, G N Makarov, N D D Ogurok, E A Ryabov, Journal of Exptl. and Theoretical Phys. 125, 531 (2017).

1.17. V M Apatin, V N Lokhman, G N Makarov, N D Ogurok, E A Ryabov, Quant. Electron 48, 157 (2018).

1.18. V N Lokhman, G N Makarov, A L Malinovskii, A N Petin, D G Poydashev and E A Ryabov, Laser Phys. 28, 105703 (2018).

1.19. V M Apatin, G N Makarov, N D Ogurok, A N Petin, and E A Ryabov, Joural of Exptl. and Theoretical Phys. 127, 244 (2018).

1.20. J Dawson, Nuclear Physics. A, 799, 167 (2008).

1.21. J Dawson et al., Physical Review C 78, 035503 (2008).

1.22. Feasibility study of neutrino-less double beta decay in ^{124}Sn, Vandana Nanal, Proceedings of the DAE Symp. on Nucl. Phys. 55, 114 (2010).

1.23. H Kimmel, C R Dillard, Spectrochimica Acta Part A: Molecular Spectroscopy 24, Issue 7, 909 (1968).

1.24. D C McKean, A R Morrisson, P W Clark, Spectrochimica Acta Part A: Molecular Spectroscopy 41, Issue 12, 1467 (1985).

1.25. Mid-Infrared Laser Applications in Spectroscopy, Frank K. Tittel, Dirk Richter and Alan Fried, Topics Appl. Phys., 89, 445–516, Springer-Verlag, Berlin Heidelberg (2003).

1.26. Mid-Infrared Laser Applications in Medicine and Biology, Ronald W. Waynant, Ilko K. Ilev and Israel Gannot, Phil. Trans. Royal Society London A, 359, 635–644 (2001).

1.27. Kincade K and Anderson S, Laser Focus World, 44, 74-95 (2008).

1.28. Interpretation of CO_2 Optical Maser Experiments, C. K. N. Patel, Phys. Rev. Lett., 12, 588 (1964).

1.29. Laser Oscillation on X1Σ+ Vibrational-Rotational Transitions of CO, C K N Patel and R J Kerl, Appl. Phys. Lett., 5, 81 (1964).

1.30. Characteristics of a CO Laser, Mani L Bhaumik, IEEE Journal of Qunatum Electronics, QE-8, No. 52 (1972).

1.31. A CO_2 Laser Pumped Para- H_2 Raman laser, Hideo Tashiro, Katsumi Midorikawa, Keigo Nagasaka, Susumu Namba, Rev Laser Eng (1985).

1.32. Stimulated Rotational Raman scattering from Para-H_2 Pumped by a CO_2 TEA laser, P Rabinowitz, A Stein, R Brickman, and A Kaldor, Optics Letters, 3 (4), 147-148 (1978).

1.33. 16 μm Generation by CO_2-pumped Rotational Raman scattering in H_2, Robert L Byer and W R Trutna, Optics Letters, 3 (4) (1978).

1.34. T Y Chang, in: Non-linear Infrared Generation: Y R Shen (ed.), Springer-Verlag, Berlin (1977).

1.35. Laser Action at 12.812 μm in Optically Pumped NH_3, T Y Chang and J D McGee, Appl. Phys. Letters, 28, 526 (1976).

1.36. High-power Efficient Optically Pumped NH_3 Laser Tunable over the Range 770–890 cm^{-1}, B. I. Vasil'ev et al, Soviet Journal of Quantum Electronics, 10 (1), 64-68 (1980).

1.37. A Z Grasiuk, V S Letokhov and V V Lobko, Progress in Quantum Electron. 6, 245-293 (1980).

1.38. J A Horsley et al, IEEE Journal of Quantum electronics, QE 16, 413 (1980).

1.39. V G Averin et al, Sov. J. Quant. Electron, 13, 189 (1983).

1.40. Spectral Considerations in the Laser Isotope Separation of Uranium Hexafluoride, J W Eerkens, Applied physics 10 (1), 15 (1976).

1.41. F Magnotia and I P Hermann, J. Chem. Phys. 81, 2363 (1984).

1.42. A K Nayak, S K Sarkar, D J Biswas, K V S Rama Rao and J P Mittal, Applied Physics B, 53, 246 (1991).

1.43. Kung A H, Proc. SPIE, 2379, 163 (1995).

1.44. Mirov S B et al, Proc. SPIE, 3491, 1082–88 (1998).

1.45. Herb R L, US Patent 4200808 (1980).

1.46. Pulsed Mid-IR Optical Parametric Oscillators, Konstantin Vodopyanov, 144-183, in Solid-State Mid-Infrared Laser Sources, Edited by Irina T Sorokina, Konstantin L Vodopyanov in Topics in Applied Physics, Springer Series, Volume 89 (2003).

1.47. Quantum cascade laser, J Faist et al., Science, 264, 553 (1994).

1.48. Continuous wave operation of a mid-infrared semiconductor laser at room temperature, M Beck et al., Science 295, 301 (2002).

1.49. Lu Q Y, Bai Y, Bandyopadhyay N, Slivken S and Razeghi M, Appl. Phys. Lett. 98, 181106 (2011).

1.50. Free-Jet Sources by D. R. Miller in Atomic and Molecular Beam Methods Vol I, Ed. G D Scoles (Oxford: Oxford University Press), 14-53 (1988).

1.51. Thermodynamics of High-speed Gas flow In Thermodynamics by Yunus A Cengel, Tata McGraw Hill (2004).

1.52. Fundamentals of Gas Dynamics, V Babu, Ane's Student Edition (2011).

1.53. Experimental Determination of the Discharge Coefficients for Critical Flow through an Axisymmetric Nozzle S. P. Tang and J. B. Fenn, AIAA Journal, 16 (1) 41-46 (1978).

1.54. https://www.wikilectures.eu/w/Shock-wave.

1.55. Supersonic Beam Sources by Michael D Morse in Atomic Molecular & Optical Physics: Atoms & molecules, Ed. by Dunning F B, Randan G Hulet, 29B (1st edition), 21-47 (1996).

Chapter 2: Continuous Tunable Emission from a Multi-atmosphere CO_2 Laser and the Prospect of Synchronized Operation of Two Pulsed CO_2 Lasers

2.1. Introduction

CO_2 laser [2.1-2.3] that operates in the mid-infrared region and tunable over 9 to 11 μm is the most attractive choice to impart vibrational excitation to the rarer isotopic species in its molecular form either directly or by way of converting its emission into another wavelength through non-linear [2.4] or optical pumping routes [2.5-2.7]. However, as discussed in the introduction chapter, more often than not, the exact coincidence between the absorption centre of the desired isotopic species and the emission centre of the coherent source is very rare warranting the need for a continuously tunable source. High pressure operation (typically ~8-10 bar) of a Transversely Excited (TE) CO_2 laser provides the prospect of its near continuous tunable operation over the 9-11 μm region by way of eliminating the dark regions in its emission spectrum. When such a laser source is used as a pump for generating coherent emission in other regions of mid-IR, following nonlinear routes, its continuous tunability gets automatically translated to the generated coherent radiation. To this end, we operated a multi-atmospheric CO_2 laser and obtained continuous tunability over most of its emission region. This was possible by way of judiciously changing the Q of the cavity together in combination with the energy loading of the gain medium. Parametric characterization and various aspects of continuous tunability have been discussed in detail herein. However, prior to that, the physics of CO_2 laser operation, its lasing action on various normal band transitions of P & R branches at atmospheric pressure conditions and the discrete nature of the emission lines shall be discussed.

Synchronized operation of a pulsed laser with an event may assume significance under certain conditions, e.g., operation of an oscillator and an amplifier, multiplexing the operation of several lasers, laser spectroscopy studies viz., pump-probe experiments, CARS (Coherent Anti-Stokes Raman Spectroscopy) etc., requiring the simultaneous operation of more than one pulsed laser. The operation of a pulsed gas laser involves switching of energy stored in a capacitor into the laser load by means of a high voltage, high current, fast switch, e.g., a spark gap. Synchronized operation of two such lasers, therefore, means the synchronization of the switching of the two sparks gaps that drive them. This is generally achieved by triggering the two spark gaps electrically from a common trigger source [2.8, 2.9] or triggering one by deriving an electrical impulse from the closure of the other [2.10]. In both these cases, the jitter in the closure of the switches that essentially stems from the statistical variation in the formative time hinders the performance [2.11]. A novel technique that employs, in addition to the electrical coupling, UV coupling of the two switches, resulted in a better synchronization with reduced jitter in their operation. The UV photons of appropriate energy pre-condition the inter-electrode gap reducing the formative time lag allowing the switch to close with a correspondingly reduced jitter. This finding, that has a bearing in applications where a number of spark gap driven lasers are to be operated in tandem, has been elaborated too in the later section of this chapter.

2.2. Basic Principles of CO_2 Laser Operation

CO_2 laser emitting in the 9-11 μm wavelength region was invented in 1964 by C K N Patel [2.2]. It is a versatile and important and coherent source in the mid-infrared region of the electromagnetic spectrum, with applications in industrial, medical and scientific fields. The operational characteristics of CO_2 laser are well understood and extensively documented in literature [2.1-2.3]. This laser is recognized as the most powerful laser in the mid-infrared region because of its high quantum efficiency (40%) and efficient pumping method. Carbon

dioxide, Helium and Nitrogen gases are the constituents of the gas mixture with CO_2 acting as the lasing gain medium. The laser, usually excited by an electrical gas discharge, can be operated in both CW and pulsed modes and is tunable discretely, emitting over a number of lines in the 9-11 μm region covering the vast 9R, 9P, 10R & 10P bands [2.3]. The characteristics of this laser are briefly summarized below.

2.2.1. Lasing Action in CO_2 Molecule

CO_2 is a linear, tri-atomic, symmetric molecule possessing three fundamental modes of viz., symmetric, bending (degenerate) and asymmetric stretching denoted by vibrational quantum

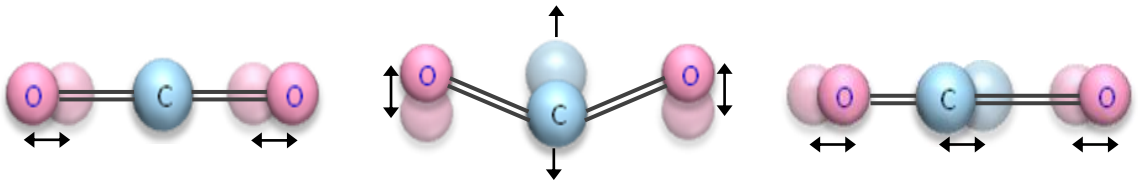

Symmetric stretchmode Bending mode Asymmetric stretchmode

Figure 2.1. Fundamental vibrational modes of CO_2 molecule.

number (n_1, n_2, n_3) respectively, as shown in figure 2.1.

Thus, the vibrational level energy of the CO_2 molecule is given by,

$$E_{vib} = \left(n_1 + \tfrac{1}{2}\right) h\nu_1 + \left(n_2 + \tfrac{1}{2}\right) h\nu_2 + \left(n_3 + \tfrac{1}{2}\right) h\nu_3$$

Where ν_1, ν_2, ν_3 are the resonant frequencies of the three modes respectively.

2.2.2. Normal Band Transitions in CO_2 Molecule

The CO_2, N_2 molecules in the lasing gas mixture are excited by collisions with accelerating electrons in the discharge thereby populating the higher ro-vibrational states. The energy level diagram of the CO_2 laser is shown in figure 2.2. Lasing action in CO_2 molecules occurs between the first anti-symmetric stretching mode, (001), and symmetric stretching mode, (100), resulting in emission on 10 μm band centered around 10.4 μm (figure 2.2).

Radiative transition from (001) to (020) is also possible owing to the (020) level being in Fermi resonance with the (100), resulting in the emission on 9 μm band. Due to higher emission probability at longer wavelengths, 10 μm band transitions are generally stronger than 9.6 μm transitions by a factor of 10.

2.2.3. The rotational spectrum of a CO_2 laser

The vibrational state of the molecule is further sub-divided into a whole series of rotational levels (figure 2.3). These levels are also quantized and denoted by rotational quantum number 'J'. The sum of population of all the rotational levels is equal to the corresponding vibrational level population. The population distribution among the various levels is governed by Maxwell-Boltzmann statistics. Population, N_J, in J^{th} level is given as,

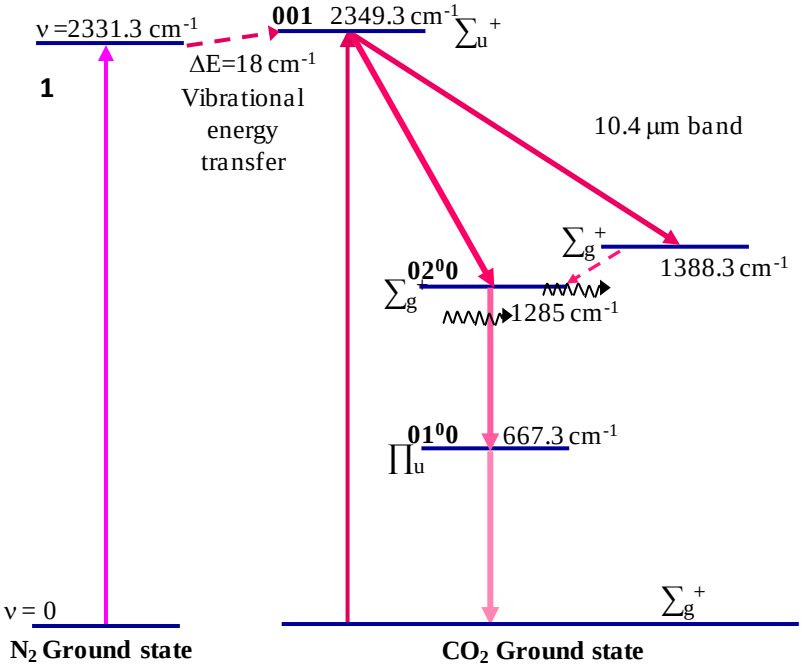

Figure 2.2. The relevant energy levels of CO_2 molecules that participate in the lasing process. The first vibrational level of N_2 molecule that is at near resonance with the upper laser level of CO_2 provides selective excitation. Direct excitation of CO_2 to its upper laser level too is shown.

$$N_J = N_0(2J+1)\frac{hcB}{kT}\exp^{-E_j/kT}$$

Where, N_0 is the ground vibrational level population

k = Boltzmann constant

B = Rotational constant

h = Plank constant

c = velocity of light

T = absolute temperature

E_J = Energy of the J^{th} rotational level

The energy difference between the adjacent rotational levels is much smaller than kinetic energy (kT) of the molecules at room temperature (0.025 eV). Thus, any disturbance in the population of the rotational energy levels is rapidly thermalized by collisions, and so, the Boltzmann distribution among the energy levels is maintained (the rotational thermalization time is considerably shorter than the vibrational level life time involving radiative and collisional relaxation). The rotational level, J_{max}, having the maximum population can be readily derived from the above equation as,

$$J_{max} = \left(\frac{kT}{2hcB}\right)^{1/2} - \frac{1}{2}$$

It can be shown that, for room temperature operation, J_{max} = 19, has the highest population in the (001) upper laser level. While 'even' J levels are absent in the Σ_u^+ state (001), 'odd' levels are absent in the lower lasing states, Σ_g^+ [(100) and (020)] due to symmetry considerations. As a result, laser transition can be obtained on the R branch ($\Delta J = -1$) and P branch ($\Delta J = +1$) while the Q branch ($\Delta J = 0$) is absent for the symmetric CO_2 molecule. Lasing action can be obtained from more than hundreds' of rotational lines in 9-11μm range for both bands. However, an overlap with a hot band transition (R(23) line of the hot band (01^11)-(11^10)) [2.12] in addition to higher population inversion compared to other lines, makes the 10P(20) line dominant in the absence of any dispersive element in the cavity.

2.2.4. Excitation Mechanism for Population Inversion

The population inversion and thus the optical gain in the active medium of CO_2 laser is achieved generally by means of electrical glow discharge. The accelerated electrons in the glow discharge collide with molecules and lose a part of their kinetic energy. The energy from electrons gets transformed into vibrational excitation energy of molecules. Primarily, two mechanisms are operative to realize population inversion in the CO_2 medium.

1. Direct electron collision.
2. Resonant energy transfer from N_2 molecule (shown in figure 2.2).

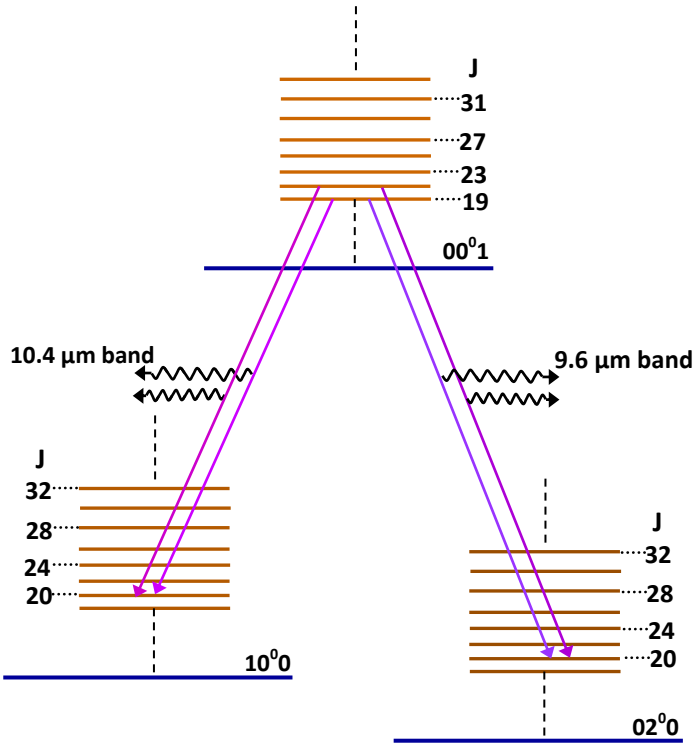

Figure 2.3. Details of rotational structures of CO_2 vibrational levels and a few rotational vibrational transitions of both 9µm and 10µm bands are shown here. Symmetry considerations do not allow even rotational levels in the 001 level while odd ones are absent in 100 and 020 levels.

2.2.4.1. Direct electron collision

When a gaseous medium is subjected to a properly tuned electrical discharge, CO_2 molecule in the ground state gets excited to the upper laser level through inelastic collisions with the electrons in the discharge.

$$CO_2\,(000) + e^-\,(KE) \rightarrow CO_2\,(001) + e\text{-}\,(\text{less KE})$$

The cross-section of such an electron collision induced excitation process for (001) level is larger than that for either (100) or (020) levels as the former transition is also optically

allowed. The direct electron-impact can also lead to excitation of higher order asymmetric modes ($00n_3$). The CO_2 molecule relaxes rapidly from these upper states to the (001) level though the resonant collision of the following type,

CO_2 (00n) + CO_2 (000) $\rightarrow$ CO_2 (00n-1) + CO_2 (001)

CO_2 (002) + CO_2 (000) $\rightarrow$ 2CO_2 (001)

2.2.4.2. Resonant energy transfer from N_2 molecule

Nitrogen is an important constituent of the laser gas composition which also gets excited by electronic collision during electrical discharge. The excitation of vibrational level of N_2 by slow electrons is a very efficient process with relatively high excitation cross-section.

N_2 (n = 0) + e^- (KE) $\rightarrow$ N_2 (n) + e^- (less KE)

The cross-section of the excitation to the individual vibrational levels is a sensitive function of electron energy and appreciably high up to n=8, that facilitates efficient CO_2 excitation.

CO_2 (000) + N_2 (n)$\rightarrow$ CO_2 (001) + N_2 (n-1) $\pm$ ΔE

More detailed description of the role of this gas is dealt in section 2.2.5 below.

2.2.5. Role of Gases Used in CO_2 Laser Operation

Generally, in CO_2 laser, the gas mixture of CO_2, N_2 and He in an appropriate ratio is used, that plays a significant role in determining the temporal shape and output power of the laser. While CO_2 is the active gain medium, the role of the other gases are as elaborated below.

2.2.5.1. Role of N_2

As discussed in section 2.2.4.2, N_2 molecule with two atoms has only one vibrational degree of freedom. As the molecule is homo-nuclear and diatomic, it does not possess any permanent electric dipole moment and hence no radiative decay of the excited vibrational

states occurs. Thus, N_2 can store energy in its vibrational states very efficiently. More than 50% of all N_2 molecules can be excited to higher vibrational levels inside the gas discharge. The first excited vibrational state, n = 1 has nearly the same energy (291.4 meV) as upper laser level (001) of CO_2 molecule.

$N_2 (n = 1) + CO_2 (000) \rightarrow CO_2 (001) + N_2 (n = 0) - 18\ cm^{-1}$

Inelastic collision between CO_2 and N_2 leads to transfer of energy from one molecule to another and hence N_2 can excite CO_2 to its higher vibrational levels. The energy levels of N_2 are closely in resonance with the corresponding CO_2 vibrational levels up to $\upsilon = 4$ ($\Delta E < kT$) resulting in the excitation of CO_2 molecule to higher vibrational levels as indicated below. The probability of such transfer is enhanced because of the meta-stable nature of the vibrational levels of N_2 molecules.

$N_2 (n') + CO_2 (000) \rightarrow CO_2 (001) + N_2 (n'-1) \pm \Delta E$

$N_2 (n') + CO_2 (000) \rightarrow CO_2 (00n) + N_2 (n'-n) \pm \Delta E$

Rapid transition between (00n) to (001) levels of CO_2 molecules results in population inversion in CO_2 as shown below.

$CO_2 (00n) + CO_2 (000) \rightarrow CO_2 (001) + CO_2 (n-1) \pm \Delta E$

Thus, the (001) level of CO_2 molecule gets selectively populated in an electrical discharge, creating population inversion between (001) and (100) or (020) levels.

The decay of population from (001) to (100) or (020) is not favored optically, and the non-resonant nature of collisions that the species at (001) level undergoes, helps to maintain the inversion. Stimulated emission brings down population inversion from (001) to (100) giving rise to lasing on 10 μm band, or to (020) level, giving rise to lasing on the 9 μm band. The

relaxation of lower levels, (100) and (020), are very fast, as both are coupled to (010) levels by two near resonant collision processes as shown below.

$$CO_2\,(100) + CO_2\,(000) \rightarrow 2CO_2\,(010) + \Delta E_1$$

$$CO_2\,(020) + CO_2\,(000) \rightarrow 2CO_2\,(010) + \Delta E_2$$

The above two processes have high probability since both ΔE_1 andΔE_2 are much smaller than kT. The decay of (010) to the ground level is however slow. However, here, addition of Helium as buffer gas, helps depopulate the (010) level and thus removes the bottlenecking effect as discussed below.

2.2.5.2. Role of Helium

For efficient pumping and towards maintaining large inversion, the thermal population of lower vibrational level, (010), must be less, and, population should be available in the ground vibrational level of the CO_2 molecule for further excitation. Population in (010) level can relax only through V-T processes and hence presents a bottleneck. Helium plays an important role in population decay of (010) levels to (000) by vibrational-translational (V-T) relaxation. Therefore, the vibrational energy of CO_2 molecule is transferred to kinetic energy, i.e., to the translatory motion, of the He atom. In addition, the large thermal conductivity of Helium helps cool the gas while its low electron affinity facilitates discharge stability. Thus, He plays the dual role of transferring the heat from the discharge gas caused during electrical excitation as well as aiding in depopulating the (010) level of the CO_2 molecules to their ground state.

The working details of a flow-in flow-out type Direct Current (DC) excited CW-CO_2 laser that has been designed and developed in-house, operable at low pressures (~few mbar) for

realizing sulfur isotope separation by laser assisted aerodynamic separation process is discussed in section 5.2 of chapter 5.

2.3. Development of the Continuously Tunable 10 μm Coherent Source

As discussed, CO_2 laser can be used for isotope selective excitation either directly or by way of converting its emission into other wavelengths through non-linear or optical pumping routes [2.4-2.7]. However, the emission of the laser being discrete, the possibility of exact coincidence between the absorption centre of the resonant isotopic species and the emission centre of the coherent source is rather rare for most of the isotopes, viz., Sn, Mo, U etc., warranting the need for continuously tunable coherent sources in the mid-IR region. A case in point being ^{124}Sn. The importance of ^{124}Sn as detector element in neutrino-less double beta decay studies is well recognized. The organo-tin compounds with their Sn-H stretching frequency (fundamental ν_3 mode) lying in the region of 1800-1900 cm^{-1} have good absorption in the 5 μm spectral region that can be reached by frequency doubling of the emission of a CO_2 laser and thus can serve as suitable working molecule [2.13, 2.14] for carrying out isotope selective studies of tin. Continuous tunability of 5 μm radiation (generated by non-linear route) will be automatic, if the 10 μm emission of the CO_2 laser can be made continuously tunable.

2.3.1. Operation & Characterization of the Continuously Tunable 10 μm Source

In case of a CW-CO_2 laser, the relatively low operating pressure restricts the overall broadening of the laser transition to within several hundreds of MHz while the spacing between two adjacent ro-vibrational transitions is several tens of GHz [2.1-2.3]. Thus, a CW CO_2 laser, when tuned with a grating, emits on well separated frequencies spanning over 9 to 11 micron region [2.3]. The broadening of the transition in case of a conventional pulsed TEA CO_2 laser where the operating pressure is one atmosphere, on the other hand, can vary

between 4 to 5 GHz depending on the partial pressures of the constituent gases [2.1]. Thus**,** in this case too, there remains a significantly large frequency region between adjacent ro-vibrational transitions that is devoid of gain and hence lasing is not possible. This dark region in the emission feature of a CO_2 laser can be reduced by increasing the operating pressure that, in turn, increases the broadening of the gain. Figure 2.4a shows the schematic of the gain bandwidths (broadening ~4 GHz) corresponding to two ro-vibrational lines for case of a TEA CO_2 laser, with a dark region, in between, where the gain is simply absent. To be noted the wide dark region (~50 GHz) intermediate to the two gain profiles. Figure 2.4 b shows the schematic of the broadened gain profiles for the above two ro-vibrational lines at typically ~10 bar pressure operation (in blue). The typical broadening of ~40 GHz of the emission profiles at this pressure is apparent. Shown in the same figure in red is the resulting merged gain profile due to the superposition of the individual broadened profiles. Figure 2.5a shows the absence of lasing in the intermediate region in the emission spectrum of the high pressure (~10 bar) CO_2 laser owing to the loss line being high. Figure 2.5b shows the lasing action that is now possible in the dark region owing to reduction in the loss line achieved by way of increasing the Q of the cavity or the energy loading of the medium thereby resulting in continuous tunable operation. Figure 2.6 shows the actual gain profiles for CO_2 laser operation for case of a gas mixture of CO_2:N_2:He :: 1:1:25 at 1 bar (in blue) from 920 to 990 cm^{-1}. The existence of dark regions for 1 bar operating pressure resulting in discrete nature of emission is evident. Also shown in figure 2.6 (in red) is the gain profile in the intermediate dark region alone (not on line centers'), for case of 9.5 bar operation (for line centres', it is obviously high as is for the case for 1 bar operation). The net gain in the dark regions that now occurs for 9.5 bar operating pressure is evident and to be noted gain on any of the line centre understandably is going to be much higher for this case of 9.5 bar operation. Hence, for helium rich laser gas mixture, assuming ~6MHz/torr pressure broadening [2.15], it may

be readily seen that, an operating pressure of ~8-10 atmosphere results in a broadening of the gains on the neighbouring ro-vibrational transitions to the extent that they merge with each other, for both P and R branch transitions, providing the prospect of a continuous tunable coherent source over 9 to ~11 μm (figure 2.7). However, higher is the operating pressure, smaller is the glow to arc transition time [2.16] making it increasingly difficult to effect a glow discharge, an essential pre-requisite for efficient coupling of the stored electrical energy from the pulser circuit into the active medium. Therefore, multi-atmospheric pressure operation is effected by taking advantage of a very rapid discharge to ensure that the current pulse extinguishes before arcing can set in. This can be achieved in specially designed mini laser systems that inherently offer low discharge loop inductance [2.17]. Rapid discharge has been effected by magnetic pulse compression technique [2.18] too.

The CO_2 laser (HP-10, Par Systems) used towards obtaining continuous tunable output made use of magnetic pulse compression based rapid discharge to effect glow discharge in the multi-atmospheric pressure (total pressure ~ 9.5 bar; CO_2:N_2:He::1:1:25) operation of the laser. The 105 cm long resonator cavity comprised of a plane master grating (150 lines/mm) and a concave (7 m ROC) ZnSe output coupler. The duration of the laser pulse was typically ~200 nsec. Towards obtaining continuous tunability, the following observations have been made. As can be seen from figure 2.7, the P branch lines are more widely spaced as compared to the R branch lines and so at 8 bar operating pressure, the merging of the broadening is more complete for R branch lines (as can be seen, the gain > 1) as against P branch lines. However, to get a continuous and stable emission from the laser, the effective gain needs to be improved at the dip between two lines. For the given operating pressure, this can be done, both, by increasing the cavity Q, and, increasing the energy loading, in a judicious manner. Therefore in our case, the approach was first to fill the gas to a pressure of ~9.5 bar. Then by choosing an appropriate Q of the cavity (reflectivity of the output coupler), we obtained

specified energy at the line centre of a high gain line at low operating voltage. We then progressively increased the voltage so as to obtain reasonable output at the line dip leading to continuous tunability of the emission.

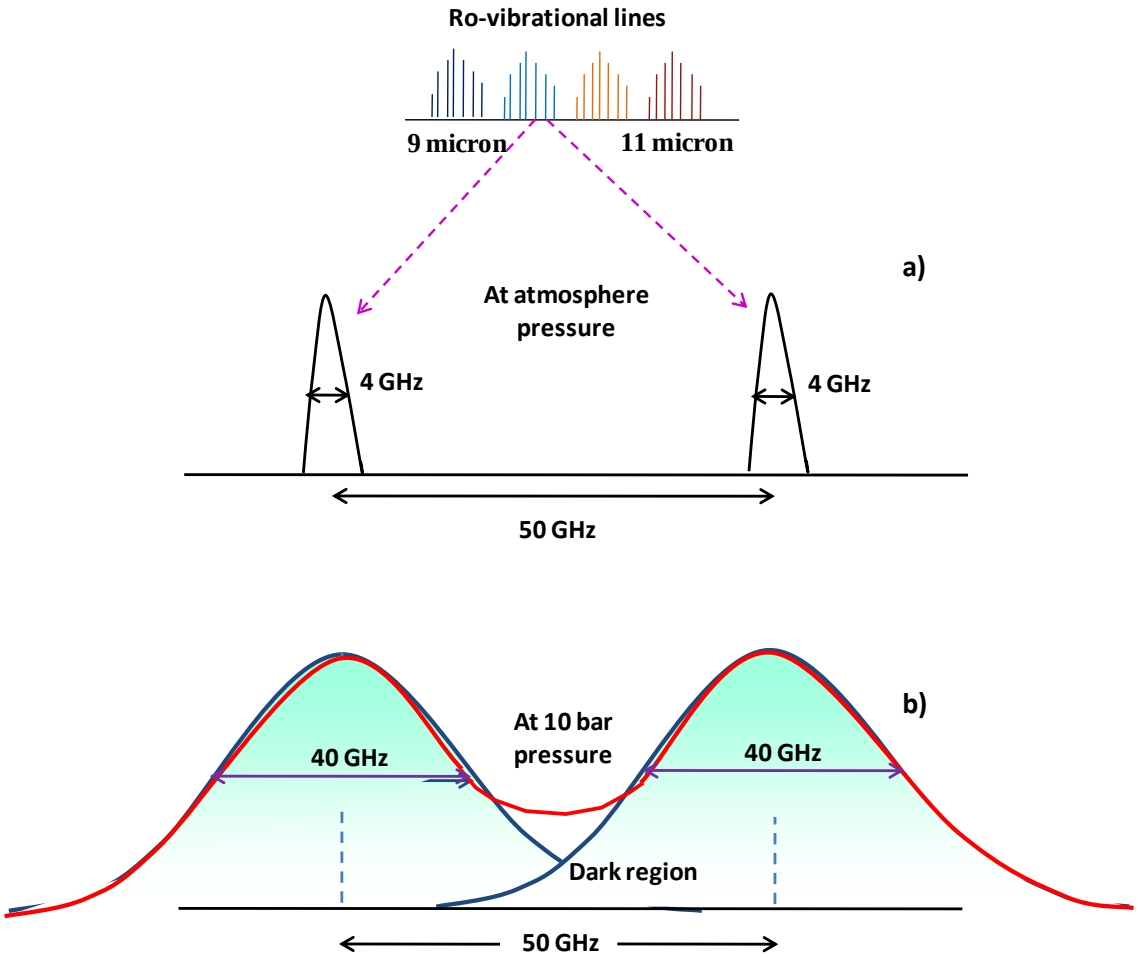

Figure 2.4 a. Schematic of the gain bandwidths (~4 GHz) corresponding to two ro-vibrational lines of a typical TE CO_2 laser for atmosphere pressure operation. To be noted the wide dark region (~50 GHz) intermediate to the two gain profiles. b. Schematic of the gain bandwidths for the two ro-vibrational lines of figure 2.4 a at 10 bar pressure operation (in blue). To be noted the broadenening (40 GHz) of the emission profiles at this pressure. Shown in red is the resulting merged gain profile due to the superposition of the individual broadened profiles.

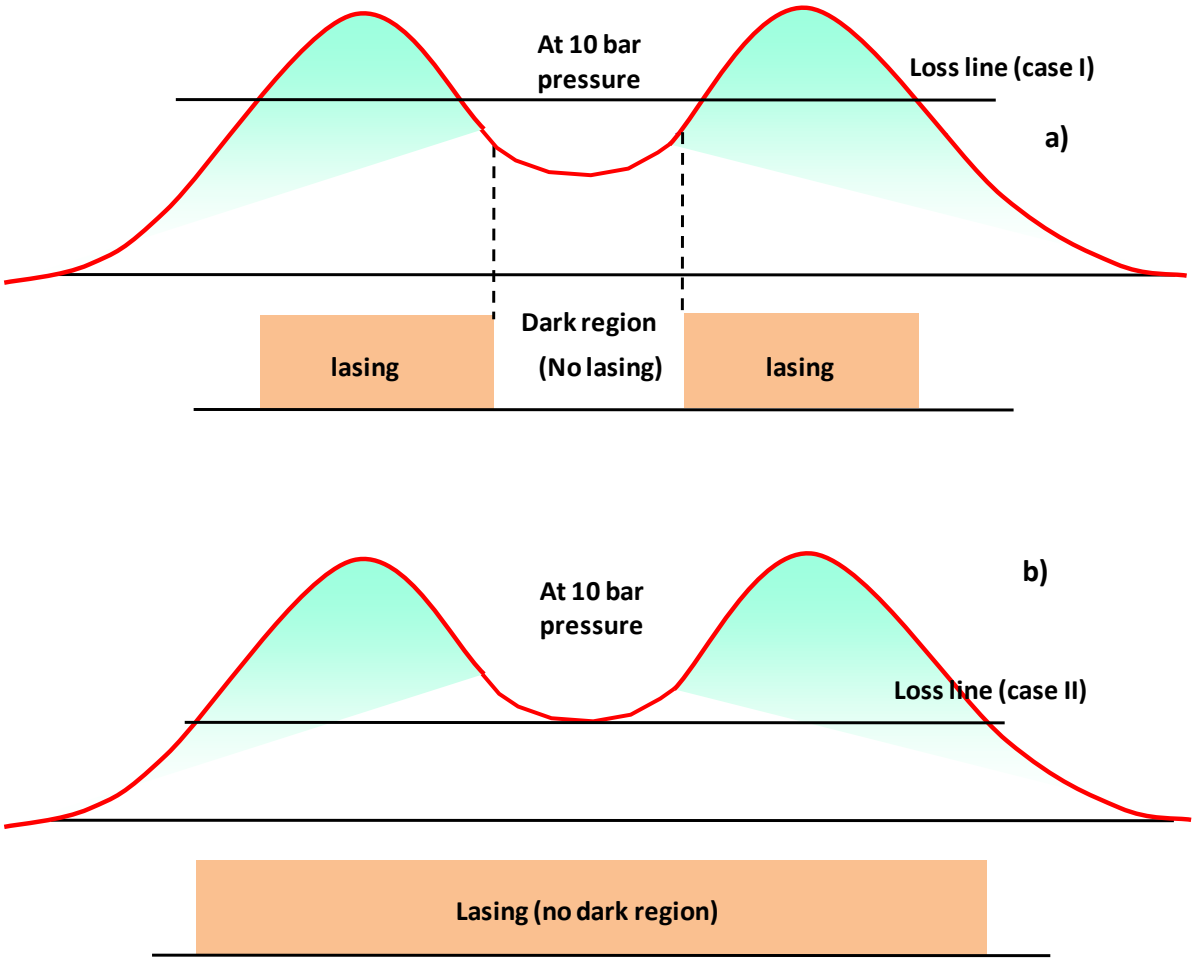

Figure 2.5 a. Discreteness in the laser emission spectrum due to the dark region owing to the loss line being high, in the high pressure operation of the CO_2 laser. b) Continuous tunability of the emission obtained owing to reduction in the loss line achieved by way of increasing the Q of the cavity and/or the energy loading of the medium.

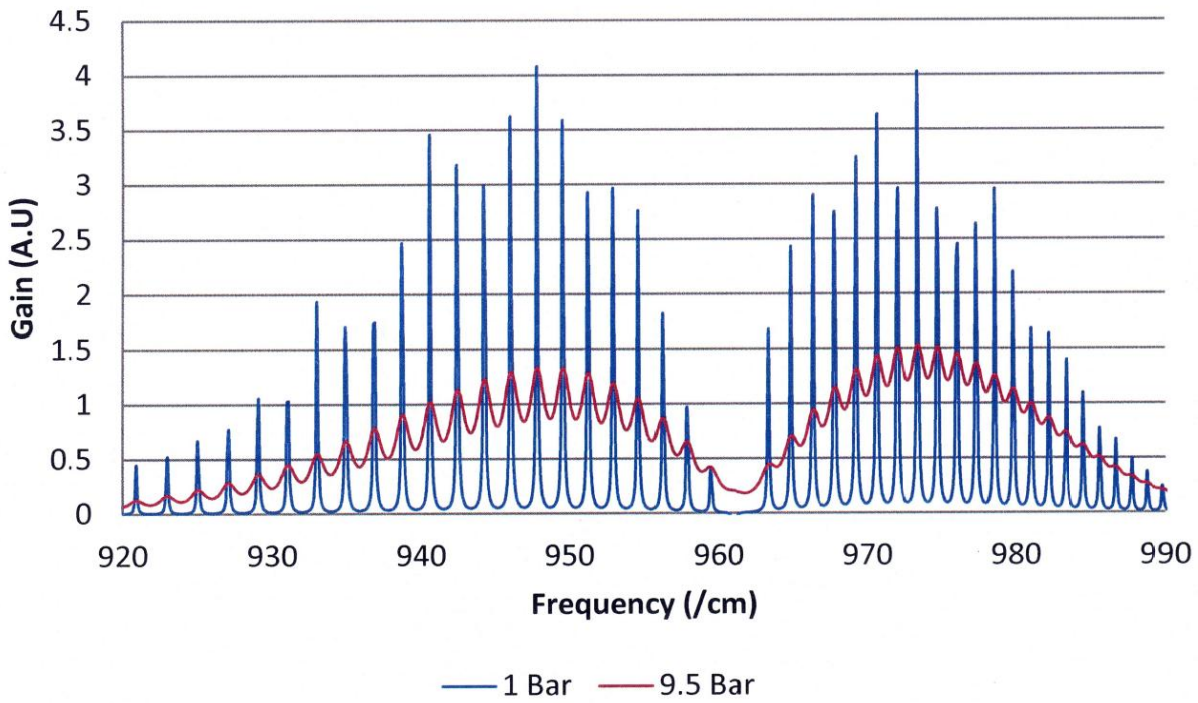

Figure 2.6. Relative gain for CO_2:N_2:He::1:1:25 mixture at 1 bar and 9.5 bar operation of a TE CO_2 laser.

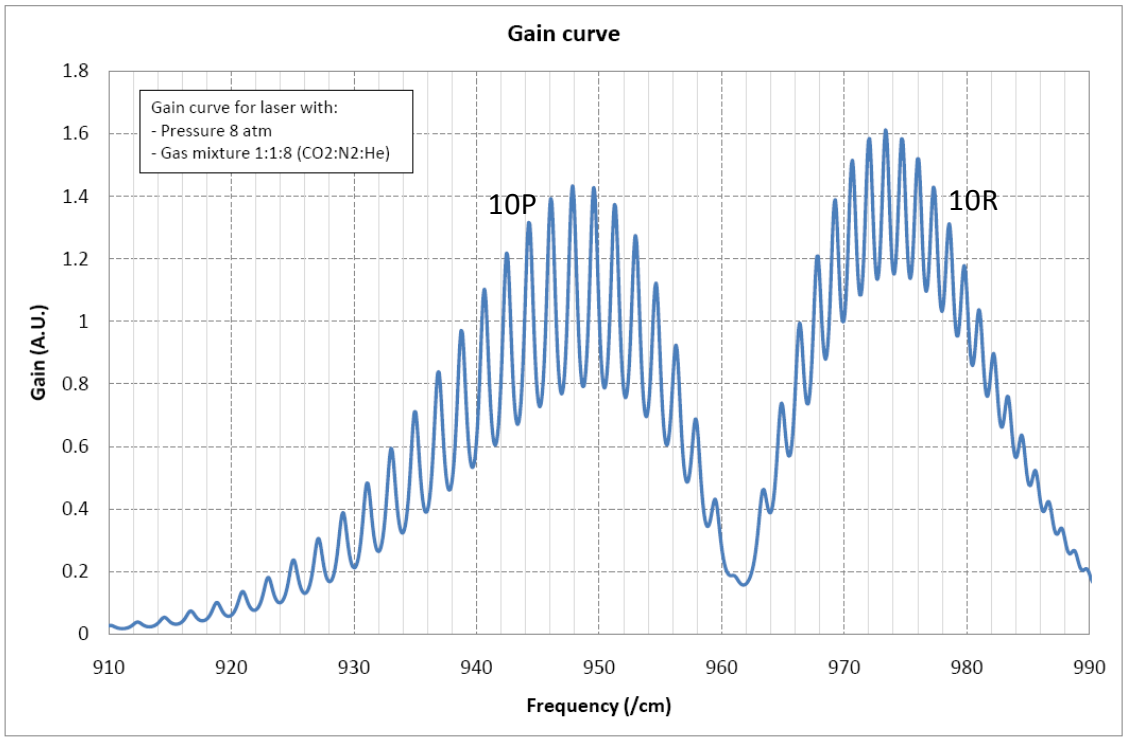

Figure 2.7. Theoretical gain on 10P and 10R branch lines of a TE CO_2 laser.

2.3.2. Continuous Wavelength Tuning

Continuous wavelength tuning leading to continuous emission from the laser with no intermediate dark region is shown in figures 2.8 & 2.9 for case of 10P and 9P emission respectively. The maximum obtainable output energy on the wavelengths intermediate to successive discrete transitions of the emission spectrum has been measured. While the grating could be continuously tuned, the output energy was measured, apart from the line centers', at 3 positions, between every two successive transitions starting from 10P(12) to 10P(20) & 9P(20) to 9P(28). That is, the output energy was first measured on the 10P(12) line centre, followed by measuring the energy at one-quarter, half and three-quarters all the way up to 10P(14). The energy measurements in such steps starting from 10P(12) all the way up to 10P(20) for case of 10P branch and similarly from 9P(20) to 9P(28) for case of 9P branch have been recorded and depicted in figure 2.8 & 2.9 respectively. A judicious interplay of the operation voltage and the Q of the resonator has resulted in near continuous tunability of the laser emission.

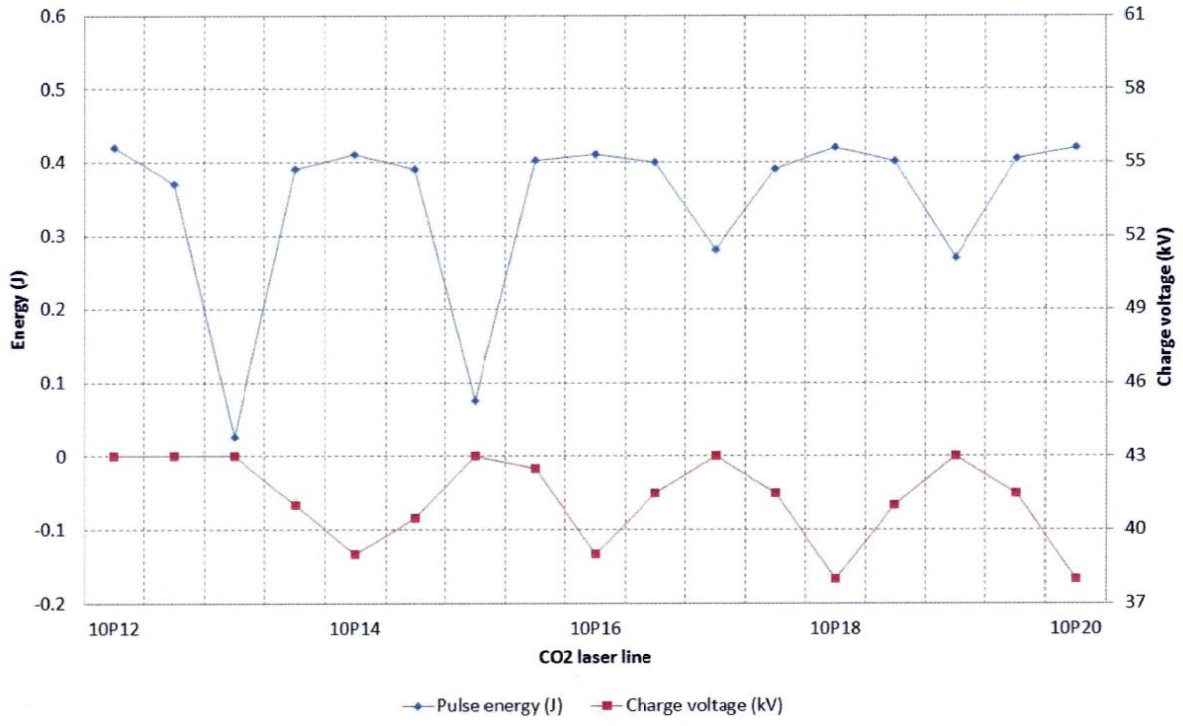

Figure 2.8. Continuous wavelength adjustment in the region between the 10P(12) and 10P(20) lines of the TE CO_2 laser (9.5 bar operation) for a gas mixture of CO_2:N_2:He::1:1:25, 60% output coupler.

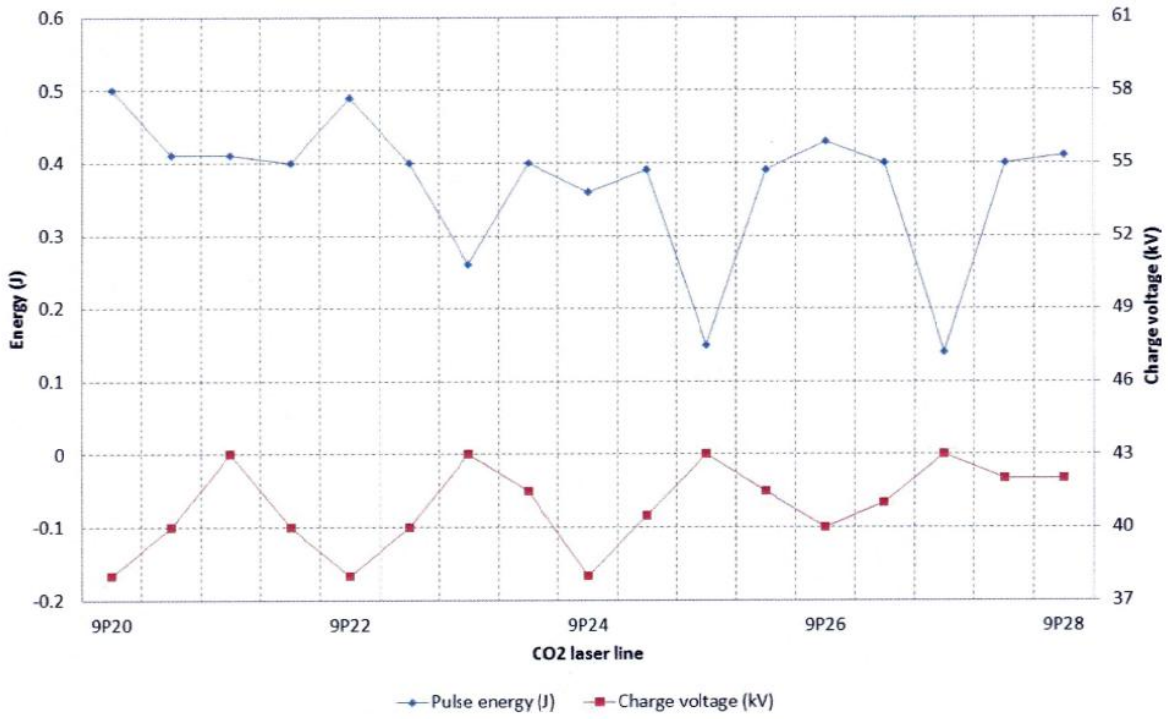

Figure 2.9. Continuous wavelength adjustment in the region between the 9P(20) and 9P(28) lines of the TE CO_2 laser (9.5 bar operation) for a gas mixture of CO_2:N_2:He::1:1:25, 65% output coupler.

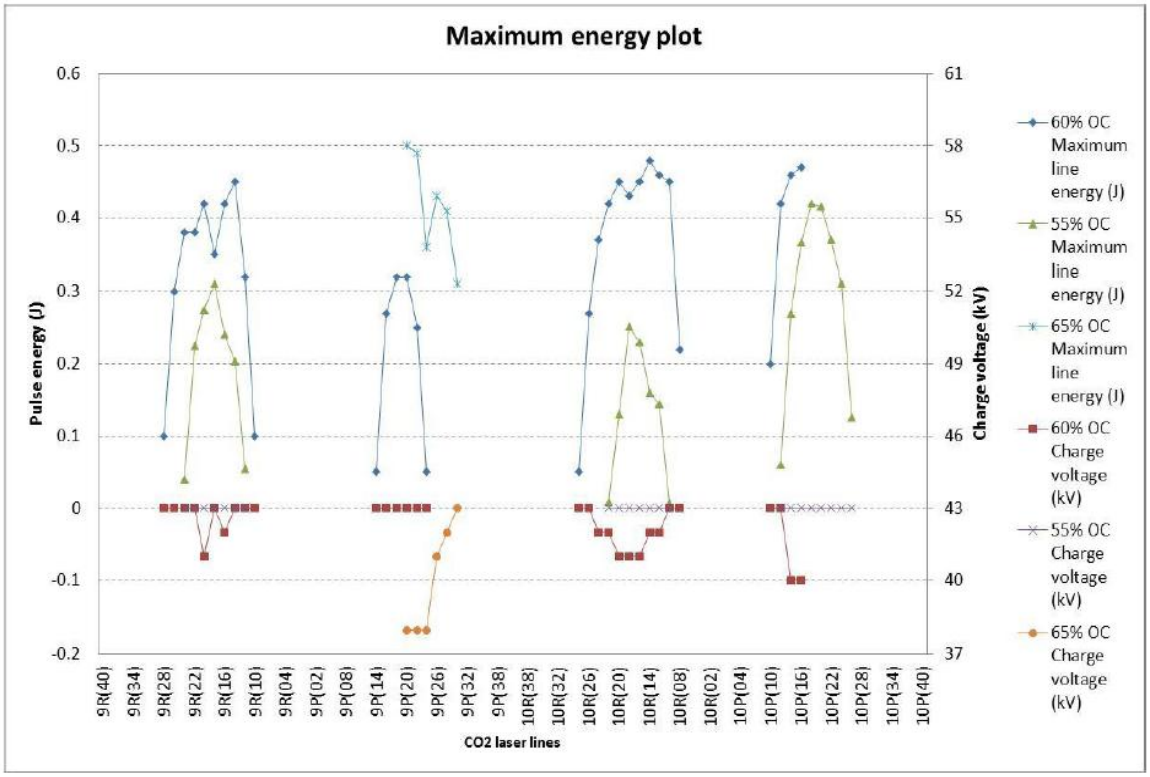

Figure 2.10. Plot of maximum output energy on different CO_2 laser lines spanning across 9R to 10P through 9P and 10R as a function of charging voltage in conjunction with reflectivity of the output coupler for CO_2:N_2:He::1:1:25 at 9.5 bar.

Figure 2.10 shows the detailed characterization of the laser carried out by way of studying the maximum obtainable output energy on different CO_2 laser lines covering from 9R to 10P region through 9P and 10R branches, as a function of charging voltage, coupled with reflectivity of the output coupler based on the afore-mentioned lines. As the grating was tuned to select the oscillating frequency, the reflectivity of the mirror was appropriately chosen so as to ensure that the gain at the chosen frequency exceeded the lasing threshold. It was possible to achieve continuous tunability across many of the P and R branch lines of both 9 and 10 μm bands in this manner. For e.g., to effect continuous tunability from 10P(20) to 10P(32) transitions, the reflectivity of the output coupler was gradually increased from 55% to 65% in steps of 5%). However, to be noted here that, increasing the Q of the cavity alone was not sufficient to give rise to lasing midway between two transitions where the gain exhibits a sharp dip. Appropriately increasing the charging voltage (from a minimum of 37 kV to a maximum of 43 kV in steps of 1 kV) and thus the gain of the system, in conjunction with changing the Q value of the cavity, was key to maintaining gain above lasing threshold in a continuous fashion that, in turn, led to achieving a near continuous tunability between the transitions (figure 2.10). The non-existence of any dark region in the lasing, as the grating was tuned from one line centre to the next, was the signature of continuous tunability between these two respective lines. As the grating was tuned in a vertical plane, the laser emitted on vertical polarization with output energy that varied depending on the gain above threshold value at that oscillating frequency and lied between a maximum of 400 mJ and a minimum of 100 mJ of energy per pulse for the above tuning range (figure 2.10).

2.4. Synchronized Operation of Two Pulsed Discharges

As discussed in the introduction section of this chapter, synchronous operation of two or more spark gaps is of utmost importance in applications pertaining to oscillator-amplifier operation or multiplexing the operation of two or more lasers in tandem. This is normally achieved by electrical coupling viz., capacitive [2.16] or inductive [2.16]. To this end, we have achieved for the first time to the best of our knowledge, that, in addition to the electrical coupling, UV coupling of the two switches results in a better synchronization with reduction in the jitter in their operation. In this configuration the jitter in the closure of the two switches has been found to reduce by ~100% under certain operating conditions. To be noted that UV coupling has been a time tested technique to achieve extended glow discharges by way of generating photoelectrons in the inter-electrode region [2.19]. In the past, such UV coupling has also been exploited to achieve simultaneous closure of mutually coupled parallel spark channels [2.20, 2.21] and the optical triggering of two self-switched TEA CO_2 lasers [2.22]. The schematic of the capacitively coupled pulser circuits used for this investigation is as depicted in figure 2.11. Capacitors C_1 and C_2 (10 nF each) charged to appropriate voltage are switched by SG_1 and SG_2 to discharge into their respective loads L_1 and L_2. In actual operation, L_1 and L_2 would represent two laser loads. However, for the sake of convenience, 50 Ω resistors have been used as loads. A single source has been used here to charge the two

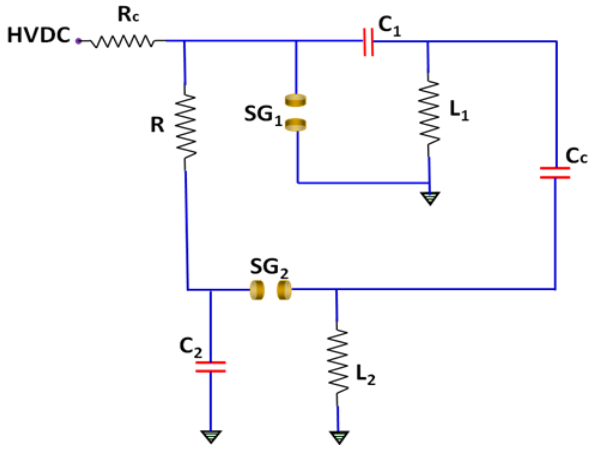

Figure 2.11. Schematic of the capacitively coupled pulser circuits. C_1 =C_2= 10 nF, Rc =100 MΩ, R = 20 KΩ , L_1=L_2= 50 Ω and C_c=1200 pF.

capacitors. The two pulsers are coupled electrically by means of a coupling capacitor C_c (1200 pF). Following the closure of one spark gap say SG_1, the coupling ensures enhancement of field across the electrodes of the second spark gap resulting in its closure. The delay between the switching of the two spark gaps was measured by collecting light originating from their closure through optical fibers judiciously so placed as to efficiently collect light following their closure, that in turn, triggered two separate optoelectronic circuits. This method of delay measurement is described in detail in the work by Aniruddha Kumar et al. [2.23]. The method is noise free, reliable and repeatable and importantly does away with the measurement of large pulse currents, making it ideal for such time delay measurements.

In the first set of experiments, the extent of delay and the associated jitter during the simultaneous closure of the two spark gaps SG_1 and SG_2 were studied as a function of ΔV, the difference in the self-breakdown voltages of the two gaps. This was achieved by setting the self-breakdown voltage of one of the spark gaps (say SG_1) to V (=18 KV), while varying

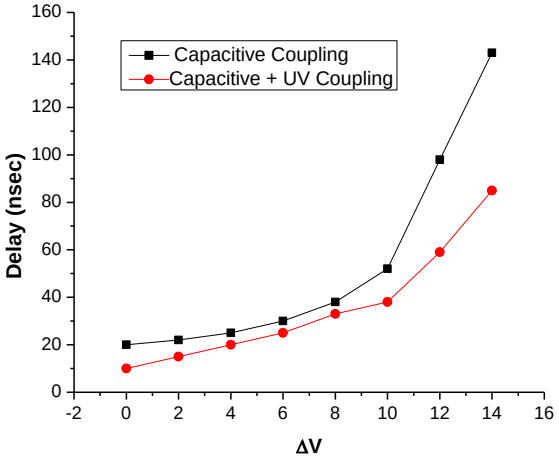

Figure 2.12. Delay in the closure of the two spark channels vs. the triggerable voltage range, ΔV.

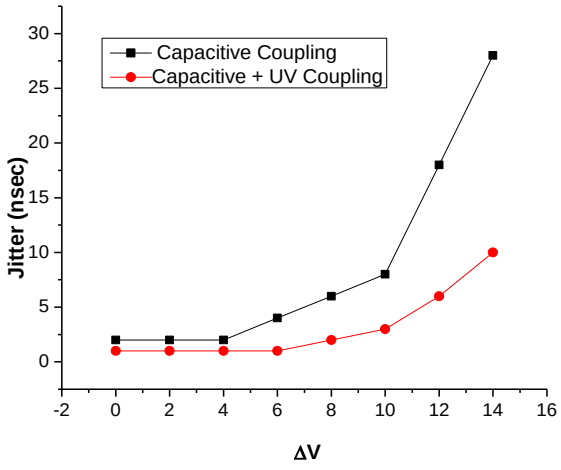

Figure 2.13. Jitter in the closure of the two spark channels vs. the triggerable voltage range, ΔV.

the self- breakdown voltage of the other (SG_2) by adjusting its inter-electrode gap. A high voltage probe (Tektronix, P6015A, 3.0 pF, 100 MΩ) was employed for measuring the breakdown voltage of the spark gap. In the beginning, ΔV was adjusted to be nearly zero and subsequently increased in small steps. It was ensured that the self-breakdown voltage of SG_2 always exceeded that of SG_1, for $\Delta V \neq 0$. In this configuration, once the voltage across SG_1 reaches its breakdown voltage 'V', the gap closes and the instantaneous voltage across SG_2 approaches twice the supply voltage, viz., 2V, due to the presence of coupling capacitor C_c in the circuit. SG_2 thus gets over-volted to a great extent causing its immediate closure resulting in a smaller delay and reduced jitter. The delay between the closure of the two gaps and the corresponding jitter was studied as a function of ΔV and has been shown graphically in figures 2.12, 2.13 respectively. The minimum delay found to occur for $\Delta V = 0$, was ~20 ns and the corresponding jitter < 5 ns for this case of capacitive coupling. Understandably, the delay and the associated jitter increased with increasing ΔV.

In the next set of experiments, the two gaps were placed in close vicinity of each other such that the UV photons emanating from the closure of one are coupled into the inter-electrode gap of the other, i.e., the two switches were now both capacitively as well as optically coupled. It is to be noted here that the coupling of UV radiation can be achieved either by placing the two spark gaps in close proximity of each other as has been done here or by using an UV silica optical fiber bundle as demonstrated in an earlier work [2.22]. Judicious care was taken to ensure that the fiber's ends were so placed that the light emanating from any of the spark gaps triggered the corresponding opto-electronic switch alone (particular to that particular fiber) in the delay measuring circuit. The delay and the corresponding jitter associated with the closure of the two spark gaps for this situation as a function of ΔV were measured and the dependence is depicted respectively in figures 2.12 and 2.13. It can be clearly seen that the delay and the associated jitter are lower when the switches are both

optically and electrically coupled as against the situation when they were only electrically coupled over the entire range of operation viz., ΔV= 0 to 16 KV. It is well known that UV photons of appropriate energy pre-condition the inter-electrode gap by way of creating photo-

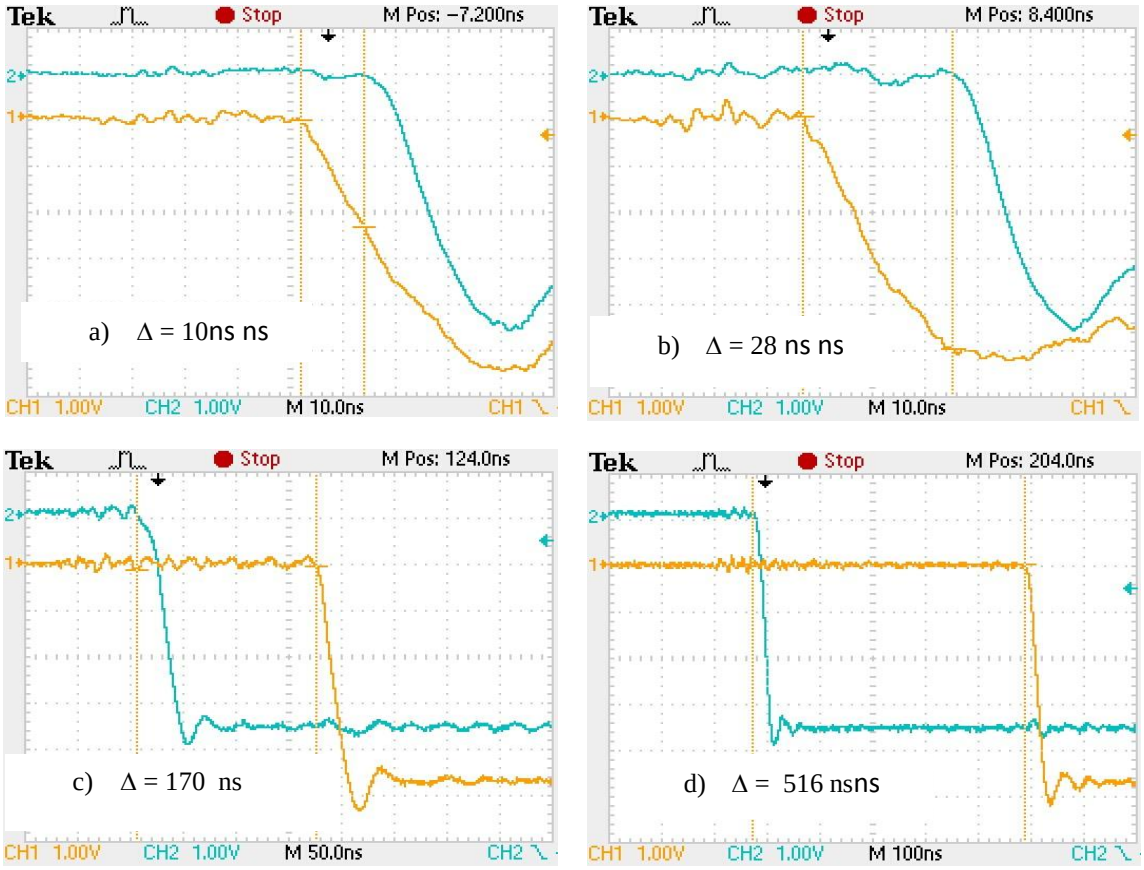

Figure 2.14. Measured delay in the closure of SG_1 and SG_2 for four different cases: (a) both electrically and UV coupled (Δ = 10 ns), (b) only electrically coupled (Δ = 28 ns), (c) only UV coupled (Δ = 170 ns), (d) no coupling (Δ =516 ns). As the optical fibre couples light onto the photo detector, the output of the delay measuring circuit switches from high to low.

electrons [2.19] that in turn reduces the formative time lag [2.24] allowing the switch to close with a better synchronization and correspondingly much reduced jitter.

In subsequent experiments, the delay and the corresponding jitter in the closure of the spark gaps were measured for the cases where the spark gaps were only UV coupled and also when no coupling of any sort existed between them. The oscilloscope traces of the switching

behavior of the delay measuring circuit for the above two cases, as well as the cases of optical-electrical coupling and only electrical coupling, studied earlier, are shown in figure 2.14 for the case when $\Delta V = 0$. Figure 2.14 (a) indicates the typical delay obtained in presence of both electrical and UV coupling that is found to be around 10 ns while in the absence of UV coupling, it is ~28 ns as can be seen in figure 2.14 (b). The associated jitter in the case of both electrical and UV coupling was measured to be as low as 1-2 ns while, that, in the case of only electrical coupling, the average measured jitter was found to be typically ~5 ns. For case of simple UV coupling, the delay is ~170 ns (figure 2.14(c)) and in the absence of any such coupling, it reached 500 ns (figure 2.14(d)). The jitter for these two cases understandably far exceeds several hundreds of nanoseconds as here SG_2 is never over-volted due to the absence of any electrical coupling.

2.5. Conclusions

Parametric characterization of a multi-atmosphere CO_2 laser, tuned in a continuous manner has been achieved. This was possible by way of judiciously changing the Q of the cavity together with the energy loading of the gain medium. Low-jitter synchronous operation of two spark gaps when they are optically coupled in addition to being electrically coupled has also been discussed. By judicious use of appropriate UV fiber bundles, efficient optical coupling can be possible that can facilitate synchronization of several spark gap switches in tandem.

2.6. References

2.1. Carbon Dioxide Laser, Advances in Quantum Electronics, D C Tyte, Ed. D W Goodwin, Academic Press, London (1970).

2.2. C K N patel, Physical Review, 136, A1187 (1964).

2.3. The CO_2 laser, W J Witteman, Springer Verlag, New York (1987).

2.4. T. Y. Chang, in: Non-linear Infrared Generation: Y. R. Shen (ed.), Springer-Verlag, Berlin (1977).

2.5. A CO_2 Laser Pumped Para- H_2 Raman laser, Hideo Tashiro, Katsumi Midorikawa, KeigoNagasaka, Susumu Namba, Rev Laser Eng (1985).

2.6. 16 μm Generation by CO_2-pumped Rotational Raman scattering in H_2, Robert L. Byer and W. R. Trutna, Optics Letters, 3 (4) (1978).

2.7. Laser Action at 12.812 μm in Optically Pumped NH_3, T. Y. Chang and J. D. McGee, Appl. Phys. Letters, 28, 526 (1976).

2.8. High-power, high-brightness master-oscillator power-amplifier copper laser system based on kinetically enhanced active elements, Daniel J W Brown, Michael J Withford, and James A Piper, IEEE Journal of Quant. Electron., 37(4), 518 (2001).

2.9. Discharge energy loading characteristics of a UV-preionized TEA CO_2 laser, Suzuki S, Ishibashi Y, Obara M, Fujioka T, Rev. Sci. Instruments, 53, 184-186 (1982).

2.10. Simple circuit to passively synchronize the pre-discharge and main discharge in a UV preionized TEA CO_2 laser, Shikarkhane N S, Nundy U, Chatterjee U K, Rev. Sci. Instruments, 56, 474-476 (1985).

2.11. High-power double-discharge TEA laser medium diagnostic, Girard C, Huguet M, Michon M., IEEE Journal of Quant. Electron., 9, 426-428 (1973).

2.12. Multiline CO_2 lasers and their uses, D J Biswas et al, Prog. Quant. Electron. 14, 1-61 (1990).

2.13. Feasibility study of neutrino-less double beta decay in ^{124}Sn, Vandana Nanal, Proceedings of the DAE Symp.onNucl. Phys., 55, 114 (2010).

2.14. H. Kimmel, C. R. Dillard, SpectrochimicaActa Part A: Molecular Spectroscopy 24, Issue 7, 909 (1968).

2.15. Duarte F J, Tunable Lasers Handbook (New York:Academic), Chapter 4, 77, (1966).

2.16. Biswas D J and Nilaya J P,Prog. Quantum Electron.26 1–63 (2002).

2.17. Marchetti S and Simili R, Optics and Laser Technology, 23, 31 (1991).

2.18. Nel J J, IEEE Xplore 21st Int. Pulse Modulator Symp., Costa Mesa, 63 (1994).

2.19. An efficient electrical CO_2 laser using preionization by ultraviolet radiation, Judd OP, Appl. Phys. Lett. 22, 95-96 (1973).

2.20. Switching of a TEA CO_2 laser with its own UV emitting parallel spark channels, Nilaya JP, Raote P, Patil G, Biswas, D J, Optics Express, 15, 129-136 (2007).

2.21. Simultaneous closure of multiple high voltage parallel spark channels without switch: A parametric study, Raote P, Patil G, Nilaya JP, Biswas D J, Appl. Phys. Lett, 93 (3), 031103 (2008).

2.22. Towards a triggerable switchless TEA CO_2 laser, Patil G C, Raote P, Sai Prasad M B, Nilaya J P, Biswas D J, Optics Communications, 284, 2189-2191 (2011).

2.23. A novel method of measuring the delay between pre-ionizing and main discharges in TE gas laser, Aniruddha Kumar, Bhatt R B, Biswas D J, Banerjee N S, Mokhriwale A, Nundy U, Meas. Sci. Technol., 12, 1739-1742 (2001).

2.24. A novel technique for synchronization of pre-ionizing and pumping currents for operation of high-pressure TEA CO2 lasers, Biswas D J, Chakera J A, Chatterjee U K, Meas. Sci. Technol. 4, 442-444 (1993).

Chapter 3: Generation of Continuously & Discretely Tunable Coherent Mid-IR Sources in the 5 μm Region by Second Harmonic Conversion

3.1. Introduction

Generation of coherent radiation in the mid-infrared region, in particular, in the 5 μm region, has received attention over the years owing to its utility in high resolution spectroscopy, metrology, trace gas detection, LIDAR, molecular isotope separation etc. As discussed in the previous chapter, one attractive method of developing these sources is through frequency doubling of CO_2 laser emission by establishing the condition of phase matching in suitable non-linear crystals viz., GaSe [3.1], $AgGaSe_2$ [3.2], $ZnGeP_2$ [3.3], $CdGeAs_2$ [3.4], $LiGaTe_2$ [3.5], $LiInSe_2$ [3.6] etc., and, to this end, search for new and more appropriate crystals continues to be an area of interest [3.7, 3.8]. Of these, frequency doubling in $AgGaSe_2$, $ZnGeP_2$, GaSe have emerged as attractive choices. Further, the existing continuously tunable sources around the 5 μm region [3.9] are based on either non-linear optical parametric frequency conversion processes [3.10-3.12] or quantum cascade diode lasers [3.13]. In the former case, which requires two [3.10, 3.11] or more [3.12] pump lasers in conjunction with non-linear crystal(s) to effect continuous tunability across 5 μm, the large line-width intrinsic to the solid state laser is carried on to the generated radiation rendering it unsuitable for applications like high resolution spectroscopy, isotope separation etc. Although mode hop free quantum cascade lasers have a narrow emission width, the tunability range offered by each diode is restricted, requiring the service of many diodes to effect continuous tunability across a respectable region. The only gas laser that is known to operate in the 5 μm region is the CO laser that is discretely tunable across this region [3.14] and no effort has thus far been expended, to the best of our knowledge, towards achieving continuous tunability of its

emission by increasing the operating pressure. Larger tunability coupled with narrow line-width and appreciable second harmonic (SH) output makes the frequency doubled CO_2 laser an attractive choice in this context and most applications of such a source will benefit greatly if the emission could be tuned continuously over this spectral range. To this end, generation of continuously tunable 5 μm coherent source by SH conversion of the emission of multi-atmospheric TE CO_2 laser using $AgGaSe_2$ crystal has been carried out and reported. The performance has been characterized with regard to energy and power conversion efficiency as well as the detection threshold pump intensities at which the onset and termination of the second harmonic conversion process has been observed. Further, the results of the generation and characterization of discretely tunable coherent 5 μm radiation by SH conversion of emission of both CW & TEA CO_2 lasers using a $ZnGeP_2$ crystal too has been studied and elaborated. The energy and peak power conversion efficiencies have been measured and compared in both the cases. The SH output as a function of CO_2 partial pressure too has been studied for the case of TEA CO_2 laser operation.

Before discussing our results on the 5 micron generation by non-linear processes, a brief introduction to the physics of second harmonic generation is presented below.

3.2. An Overview of Non-linear Optics

Polarization in a dielectric material can be approximated to be linearly proportional to the weak electric field associated with conventional incoherent light sources and is given by,

$P = \varepsilon_0 \chi^{(1)} E$, where, $\chi^{(1)}$ is the linear susceptibility of the medium.

However, with the advent of high intensity light sources in the form of lasers, it has been realized that, the material response can be more accurately described by the Taylor expansion of the material polarization, P, in terms of powers of applied electric field, E.

$P = \varepsilon_0(\chi^{(1)} E + \chi^{(2)} E^2 + \chi^{(3)} E^3 + \chi^{(4)} E^4 + \ldots)$, where $\chi^{(n)}$corresponds to the tensor of the nth order non-linear process. For practical applications that consider specific non-linear processes in well-defined directions, the tensor can be reduced to a single effective non-linear coefficient.

3.2.1. Second Harmonic Generation

For a harmonic input field $E = E_0 \sin \omega t$, the polarizability, considering up to the second order terms alone, may be expressed as,

$$P = \varepsilon_0(\chi^{(1)} E + \chi^{(2)} E^2)$$

$$P = \varepsilon_0(\chi^{(1)} E_0 \sin \omega t + \chi^{(2)} E_0^2 \sin^2 \omega t)$$

$$P = \varepsilon_0(\chi^{(1)} E_0 \sin \omega t + \chi^{(2)} E_0^2 (1-\mathrm{Cos}(2\omega t))/2)$$

Thus, it is evident that the non-linear polarization contains a component that emits at twice the frequency of the input light. Thus the input wave generates dipoles in the medium that radiate at twice the frequency of the input wave. It is essential that the induced dipoles emit in phase so that the generated light from various points of the dielectric medium gets added up constructively giving rise to a second harmonic beam. This is possible only if the input radiation oscillating at ω and the generated radiation oscillating at 2ω, travel in the same direction with same speed inside the dielectric medium. In other words, they are in phase during their entire journey inside the non-linear medium. In terms of photon picture, this phase matching condition basically implies that the momentum is conserved during the process of generation of a photon of 2ω from two photons of ω each. The consideration of natural frequency dispersion, i.e., the increase in the refractive index of a medium with increasing frequency, makes this seemingly impossible, as the fundamental and second harmonic waves are certainly expected to travel at different speeds.

3.2.2. Birefringence

When a beam of unpolarized light is incident on certain crystals, e.g., Quartz, Calcite, GaSe, $AgGaSe_2$, $ZnGeP_2$,KDP etc., then, in addition to the reflected beam, two refracted beams in place of a single one are observed. This phenomenon is called birefringence or double refraction. The unpolarized light, upon entering the crystal, splits into two plane polarized rays. One, the Ordinary 'o' ray, with vibrations perpendicular to the principal plane defined as the plane containing the optic axis and the normal to the incident surface, and, the other, extra-ordinary 'e' ray with vibrations in the principal plane. The crystal, therefore, resolves the light into two components by causing the two types of vibrations to travel in two distinct paths. This clearly means that the ordinary and the extraordinary components of light experience different refractive indices in the medium and hence will travel at different speeds. While the 'o' ray does not experience a change in refractive index with respect to the direction of propagation in the crystal, the 'e' beam sees a direction dependent refractive index. However, there exist certain directions inside the crystals called optic axes, along which the refractive indices of the ordinary and the extra-ordinary rays are equal, meaning that both of them travel with the same speed. The crystal that exhibits this

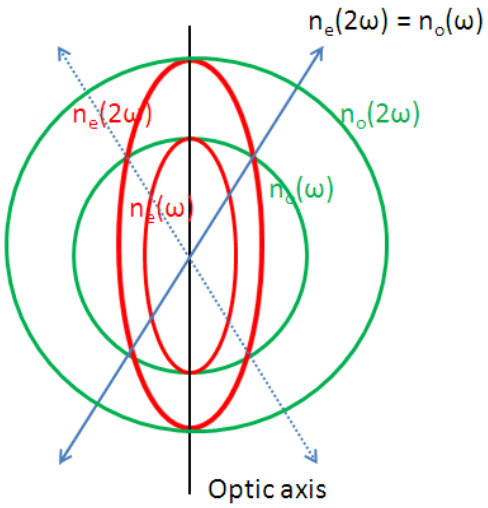

Figure 3.1. A case of negative uniaxial crystal where $n_e(\omega) < n_o(\omega)$. Phase matching directions are shown in blue arrows.

behavior in a one direction is called a uniaxial crystal while those with two optic axes are called biaxial crystals. Further the crystals for which $n_e < n_o$ are called negative crystals and those with $n_e > n_o$ are called positive crystals.

Figure 3.1 shows the refractive index for the 'o' and 'e' rays of frequencies ω and 2ω inside a negative uniaxial crystal. As can be seen, the refractive index for the 'e' ray of 2ω matches with that of 'o' ray of ω at an angle θ with respect to the optic axis along two symmetric directions with respect to the optic axis as indicated. Therefore if a pump beam, of frequency ω and polarization perpendicular to the principal plane, is made incident at an angle θ with respect to the optic axis of this crystal, phase matching conditions will be satisfied, resulting in the generation of second harmonic beam with a polarization orthogonal to the pump. Figure 3.2 shows the phase matching directions for a positive crystal. To be noted, the polarization, angle of incidence and incident frequency needs to be optimized to obtain phase matching conditions.

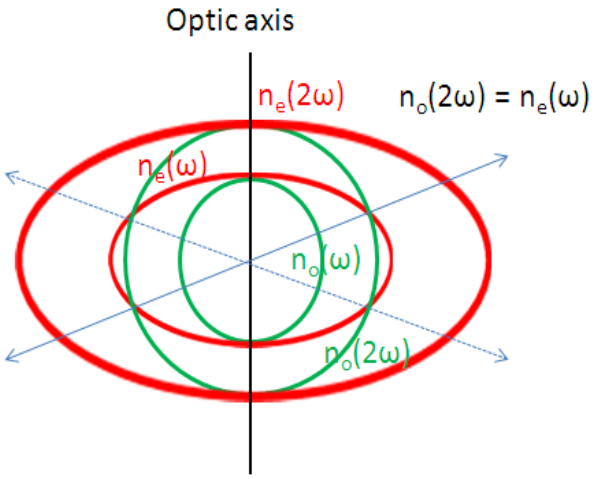

Figure 3.2. A case of positive uniaxial crystal where $n_e(\omega) > n_o(\omega)$. Phase matching directions are shown in blue arrows.

3.2.3. Cut angle of a Crystal

With prior knowledge of the phase matching angle for a particular wavelength, the crystal can be cut in such a way that, the incident radiation falling normally on the cut surface automatically makes the required angle with the optic axis satisfying the phase matching condition. This allows utilization of the entire length of the crystal for incident beam of cross-

section same as that of the crystal. Further, the normal angle of incidence also minimizes the reflection loss.

3.3. Generation of Continuously Tunable 5 µm Coherent source by SH Conversion of the Emission of Multi-atmospheric TE CO_2 laser using $AgGaSe_2$ Crystal

As discussed, frequency doubling of the CO_2 laser emission in GaSe, $AgGaSe_2$, $ZnGeP_2$ etc., have emerged as an attractive method of generating coherent radiation in the 5 µm region. Taking into consideration the non-linearity, damage threshold and transmission range, $AgGaSe_2$ and $ZnGeP_2$ have emerged as the most attractive choices for the generation of 5 µm coherent sources. The important properties of these two crystals [3.15] pertaining to this application are summarized in the table 3.1. The discrete ro-vibrational structure of a CO_2 molecule, as already discussed in detail in chapter 2, manifests itself in a frequency spacing between adjacent transitions of P branch as ~50 GHz and that of R branch as ~35 GHz in both 9 and10 µm bands [3.16]. CO_2 lasers, that operate in CW as well as pulsed conditions, can therefore be tuned, although discretely, to produce coherent emission spanning over 9 to 11 µm spectral region [3.16].

SH conversion of the CO_2 laser emission, therefore, yields a source of coherent radiation that also is discretely tunable over ~4.5 to ~5.5 µm region. Needless to say and as has been mentioned in the introduction section, most applications of a 5 µm coherent source will benefit greatly if the emission could be tuned continuously over this spectral range. To this end, it was our endeavor to generate continuously tunable 5 micron coherent radiation by SH conversion of the emission of a multi-atmosphere TE CO_2 laser in $AgGaSe_2$ crystal.

The continuous tunability of the SH has been successfully demonstrated over most of the frequency doubled spectral region of the pump laser where it could be near continuously

tuned by judiciously varying its gain in conjunction with the Q value of the resonator cavity as discussed in chapter 2. The extent of the continuous tunability was limited by the grating

Crystal and type	**Transmission range**	**Refractive index**			**Damage threshold @ 10.6 µm**	**Effective non-linearity**
		λ (µm)	**n_e**	**n_o**		
$ZeGeP_2$ Positive Uniaxial	0.74 -12 µm	10.6	3.1119	3.0725	> 1 kW/cm^2 for CW	75.4 pm/V
		5.3	3.1524	3.1141	> 1 GW/cm^2 for 2 ns pulse	
		1.06	3.2786	3.2324	>10 MW/cm^2 for 200 ns pulse	
$AgGaSe_2$ Negative Uniaxial	0.71-18 µm	10.6	2.5585	2.5915		33pm/V
		5.3	2.583	2.6140		
		1.06	2.6759	2.7005	>2 MW/cm^2 for 200 ns pulse	

Table 3.1. Some properties of birefringent crystals like AGS and ZGP.

resolution and its rotational step, in addition to the very low gain on transitions very close to the branch edges where threshold gain condition could not be met. At an arbitrarily chosen frequency of the pump laser, the second harmonic (SH) conversion process has been characterized with respect to the energy and power conversion efficiency as well as the detection threshold pump intensity required for the onset and termination of SH conversion.

Further, the observation of excellent temporal synchronization of the SH emission with the pump pulse is an experimental testimony to the instantaneous nature of the SH generation process.

The commercial continuously tunable CO_2 laser (HP-10, Par Systems) used for this investigation as stated in chapter 2, made use of magnetic pulse compressor based rapid discharge to effect glow discharge in the multi atmospheric pressure (total pressure ~ 9.5 bar; CO2:N2:He::1:1:25) operation of the laser. The 105 cm long resonator cavity comprised of a plane master grating (150 lines/mm) and a concave (7 m ROC) Zinc Selenide (ZnSe) output coupler. As the grating was tuned to select the oscillating frequency, energy loading and the reflectivity of the mirror were appropriately chosen so as to ensure that the gain at the chosen frequency exceeded the lasing threshold. It was possible to achieve continuous tunability across many of the P and R branch lines of both 9 and 10 µm bands in this manner.

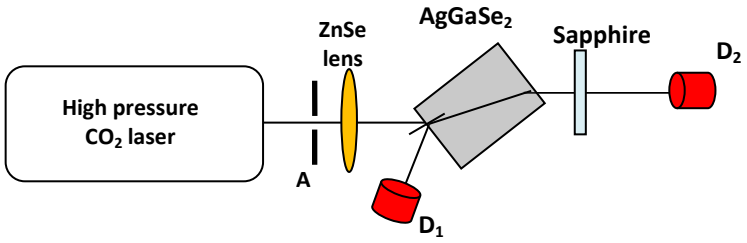

Figure 3.3. Schematic diagram of the experimental setup of second harmonic generation of the emission of a continuously tunable high pressure CO_2 laser. D_1 and D_2: energy/power detectors.

$AgGaSe_2$, a negative uniaxial crystal, is an appropriate non-linear medium to effect SH conversion of CO_2 laser emission as it offers high transmission for both pump and generated wavelengths and possesses moderate non-linearity. The $AgGaSe_2$ crystal (EKSMA Optics, Vilnius) used for this investigation had a cross-section 10 mm x 10 mm and thickness 15 mm. The schematic of the experimental set-up for SH conversion is shown in Figure 3.3 and the actual experimental set-up is shown in figure 3.4. As the CO_2 laser emission was on a vertical polarization, in order to effect Type I phase matching, the crystal was rotated in the

horizontal plane by mounting it on a suitable stage with provision of rotation along two orthogonal directions to optimize both θ and φ. The cut angle of the crystal is 69° that leads to satisfying the phase matching condition for second harmonic generation in case of normally incident 12 μm fundamental beam. To achieve phase matching condition in the present experiment, the angle of incidence of the pump beam with respect to the face normal of the crystal had to be adjusted appropriately and was measured to vary between 38° to 35.5° as the pump wavelength changed from 10P(28) line (10.6745 μm) to 10P(32) line (10.7186 μm) in steps of 0.0043 cm^{-1}. A 15 cm focal length AR (anti-reflection) coated ZnSe lens (refer to figure 3.3) was used to gently focus the pump beam onto the incident face of the crystal so as to achieve SH conversion by maintaining the optical flux inside the crystal well below its damage threshold. The Fresnel reflection of the pump beam from the incident face of the crystal was utilized to monitor both energy and temporal profile of the pump pulse by means of a pyroelectric joulemeter (Gentec ED 200) and a room temperature fast HgCdTe detector (Vigo Systems, PEML-3) respectively. The residual pump beam that emerged through the crystal along with the SH beam was completely blocked by a 4 mm thick sapphire plate (Crystran Ltd, UK) and the energy and temporal profile of the generated SH radiation were monitored along with that of the corresponding pump beam by making use of a sensitive pyroelectric Joulemeter (Gentec, ED 100) and a fast room temperature HgCdTe detector (Vigo Systems, PEML3) respectively.

In the first set of experiments, the continuous tunability of the multi-atmosphere CO_2 laser over the randomly chosen region of 10P(20) to 10P(32) was established. This was achieved by appropriately choosing the operating voltage and the cavity Q over this region as discussed in chapter 2. As the grating was continuously tuned to select pump frequency from one end of the emission spectrum to the other, the SH beam was detected all the while as the crystal was rotated in unison with the grating to ensure that phase matching condition stayed

satisfied for all the pump frequencies. Figure 3.5 depicts the measured SH output energy for nearly same input pump energy at wavelengths from ~5.337

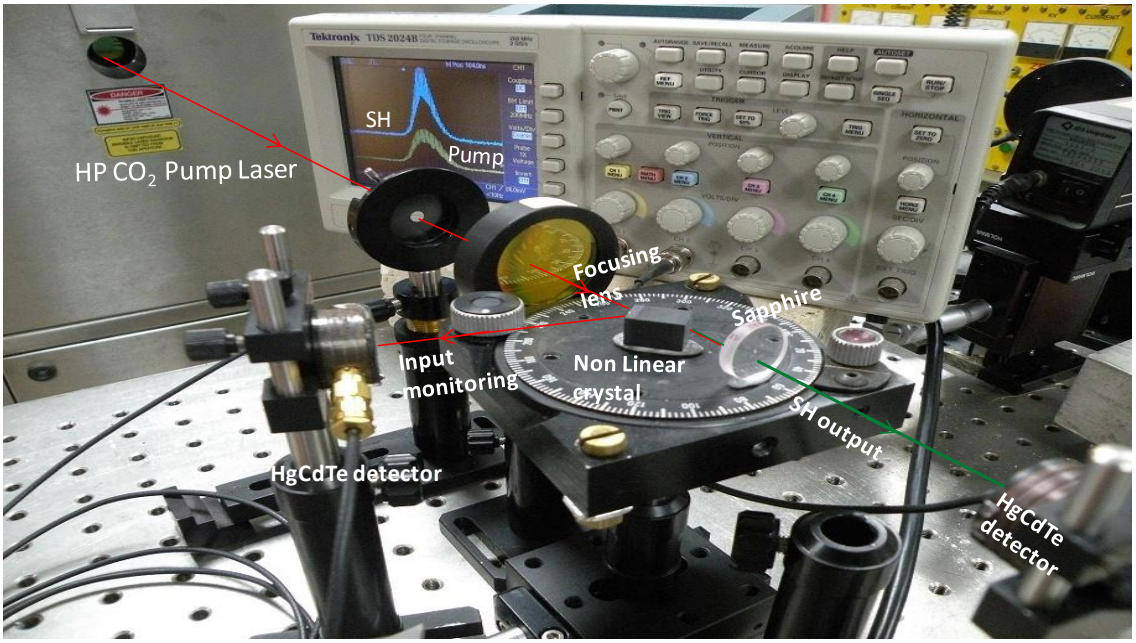

Figure 3.4. Set-up for the generation of continuously tunable coherent 5 micron source by SH conversion of the emission of the multi-atmospheric CO_2 pump laser.

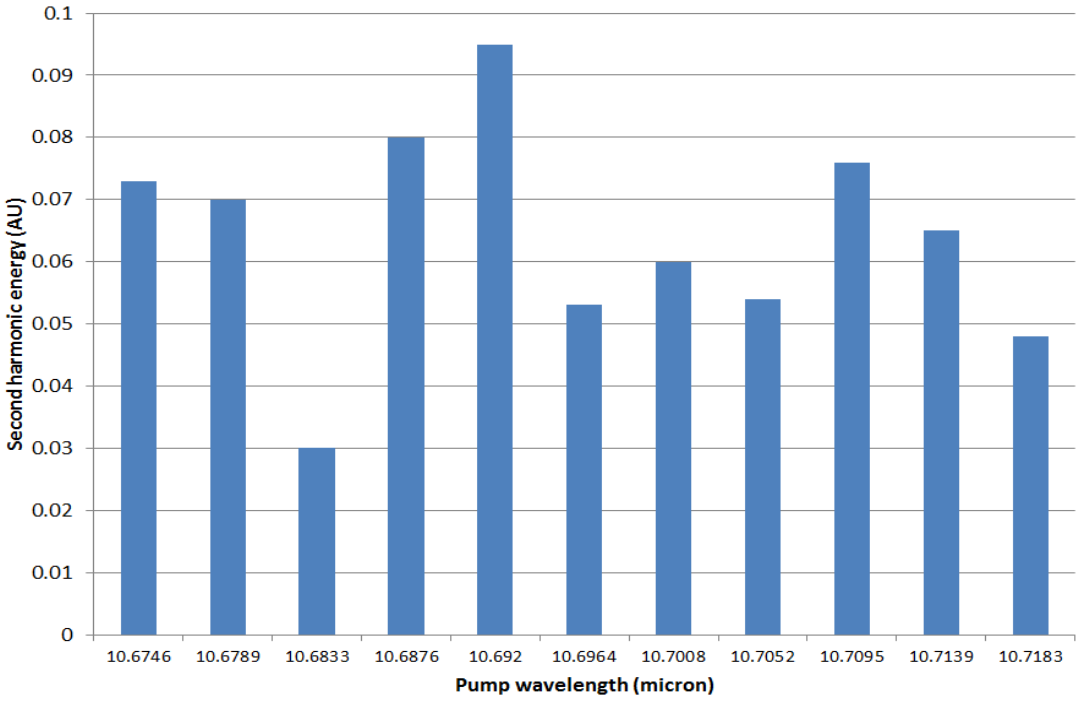

Figure 3.5. Measured SH energy at discrete pump emission wavelengths as the laser was tuned from 10P(28) to 10P(32) in a continuous fashion.

µm to 5.359 µm as the pump wavelength is tuned in steps of 0.0043 µm, decided by the resolution of the micrometer employed for tuning the grating, from 10P(28) line to 10P(32) line through the 10P(30) line. The reflectivity of the output coupler of the pump laser for this region of tuning was 65%. The reducing gain between the lines was compensated by increasing the operating voltage as described earlier. The origin of variation of the SH energy with frequency can be attributed to the following two factors. Firstly, it is not possible to obtain identical gain above threshold value in the pump laser for every frequency at which the measurement is being made owing to the discrete nature of gain (operating voltage) and Q value (reflectivity of the output coupler) variation. Secondly, the shot to shot variation in the temporal profile of the multi-longitudinal mode emission of the pump laser, that was inevitable for this cavity, as it did not make use of an invar spacer, has a direct bearing on the efficiency of the SH conversion, and, in turn, the measured SH energy. To be noted here is that, this behavior is qualitatively similar over the entire tuning range i.e. from 9R to 10P through 9P and 10R branches of the pump laser.

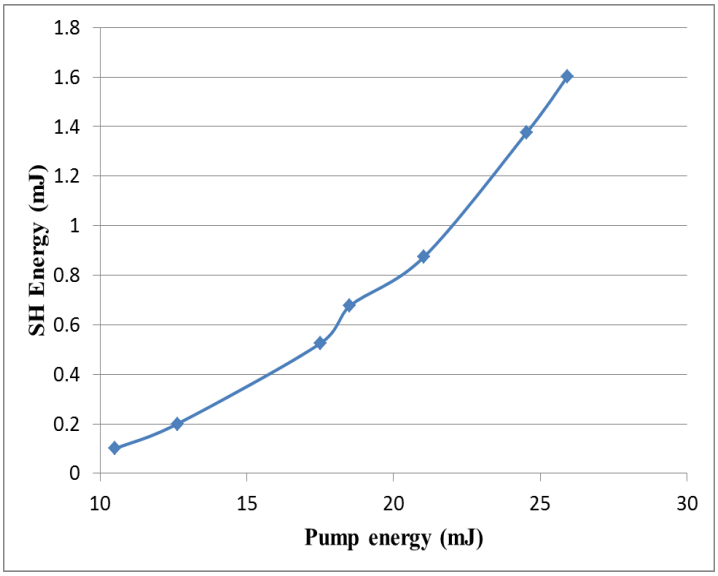

Figure 3.6. Dependence of the second harmonic output as a function of the input pump energy.

At this point, we fixed the pump frequency to an arbitrary value for further characterization of this continuously tunable 5 µm coherent source. Towards finding the efficiency of the SHG process, we recorded the SH output energy as a function of the energy in the fundamental beam at a particular frequency (figure 3.6). The parabolic dependence of the SH

energy on the input pump energy that is readily seen from this figure can be understood in the following manner. It is well known that for low pump intensities, the second harmonic conversion efficiency grows linearly with the pump intensity. Therefore, intensity of the SH beam bears a square proportionality with the pump intensity. While the simple ratio of output to input yields the external conversion efficiency, the internal conversion efficiency was estimated by taking into account the Fresnel refection losses of the pump and the SH beam respectively at the incident and the exit faces of the crystal, and also, the Fresnel reflection and absorptive losses, the SH beam suffers in the sapphire plate used for blocking the unabsorbed pump. The maximum internal conversion efficiency has thus been estimated from this figure as ~6.2%. For the above measurements, the pump energy was varied within a small range so as to ensure that the optical intensity at the crystal surface stayed well below its damage threshold. However, for sake of completeness we enhanced the incident intensity on the entrance face of the crystal to marginally below its rated optical damage threshold for a limited time and measured the maximum achievable internal SH conversion efficiency as ~15.6% for this system. This compares well with that reported by other researchers in $AgGaSe_2$ crystal for SH conversion at 5 micron coherent radiation albeit discretely in frequency [3.2, 3.17, 3.18].

Towards measuring the peak power SH conversion efficiency and the detection threshold intensity for the onset and sustenance of SH conversion process, we simultaneously monitored the pump pulse and the corresponding SH pulse temporally for an arbitrarily chosen pump pulse frequency and maintaining the exposure condition that yielded ~6% internal SH conversion efficiency. The temporal profiles of the pump pulse and the corresponding SH pulse as depicted in figure 3.7 clearly reveal the multimode nature of emission of the pump laser. However, for accurate estimation of power conversion and detection threshold intensity values, the power profiles captured in bandwidth limited mode

of oscilloscope operation were made use of (figure 3.8). Following the same considerations as in the case of energy conversion efficiency, the internal peak power SH conversion efficiency has been estimated as ~7%. As can be seen the peak power conversion efficiency marginally exceeds the energy conversion efficiency. Higher is the coherent field at the pump wavelength, better is its SH conversion. Since the peak power always far exceeds the average intra-pulse power of the pump beam in case of a gain switched TEA CO_2 laser, the power conversion efficiency is understandably greater than the energy conversion efficiency of the SH conversion process as also seen from the findings of many researchers [3.17-3.19]. However, the temporal profile of the high pressure laser clearly reveals the absence of the gain switched spike owing to its operation with a CO_2 lean gas mixture. As a result, the power conversion efficiency only marginally exceeds the energy conversion efficiency.

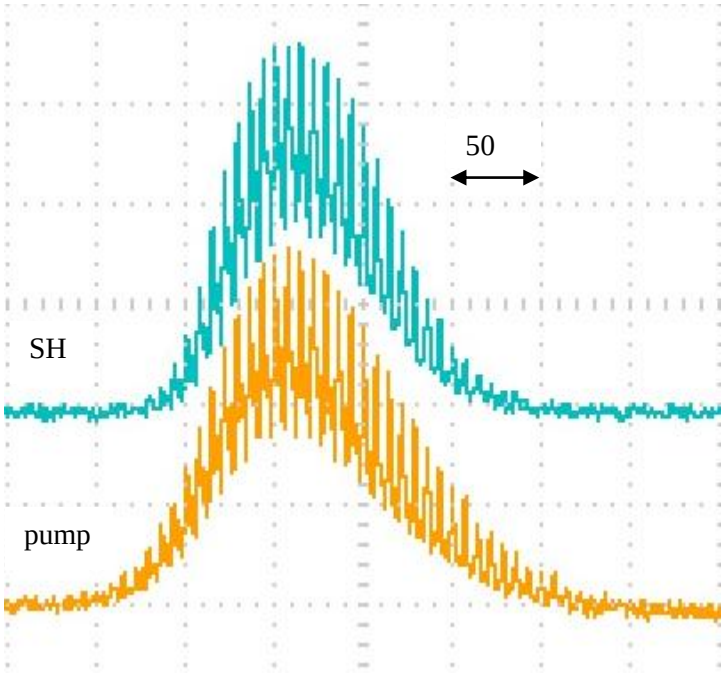

Figure 3.7. Temporal profiles of the pump (yellow) and the SH (green) pulses. The mode beating in the pump is also reflected in the SH emission. The absence of gain switched peak is apparent in the pump emission.

We next made use of temporal traces of pump and SH pulses of figure 3.8 to find out the detectable threshold pump intensity for the onset of SH conversion process. A careful inspection of this figure reveals that the onset of detection of SH generation occurs once the pump power builds up to ~10 kW that corresponds to a threshold pump intensity of ~145

kW/cm^2. This kind of measurements are highly error prone when a conventional pulsed TEA CO_2 laser is used as the pump source, as the gain switched spike causes the laser power to build up very rapidly which possibly explains the paucity of such information in literature. The pump pulse here, being totally devoid of the gain switched peak, allows accurate determination of the detectable threshold pump intensity for the detectable onset of SH generation process. Inherent high gain at high pressure operation has allowed operation with very low concentration of active molecules resulting in the dispensation of the gain switched peak. It can be also estimated from figure 3.8 that the detectable termination of the SH pulse too occurred for a pump intensity of ~145 kW/cm^2. This experimental study has thus clearly established for the first time, to the best of our knowledge, that, the threshold pump intensity for detection of SH generation and for its cessation is practically the same.

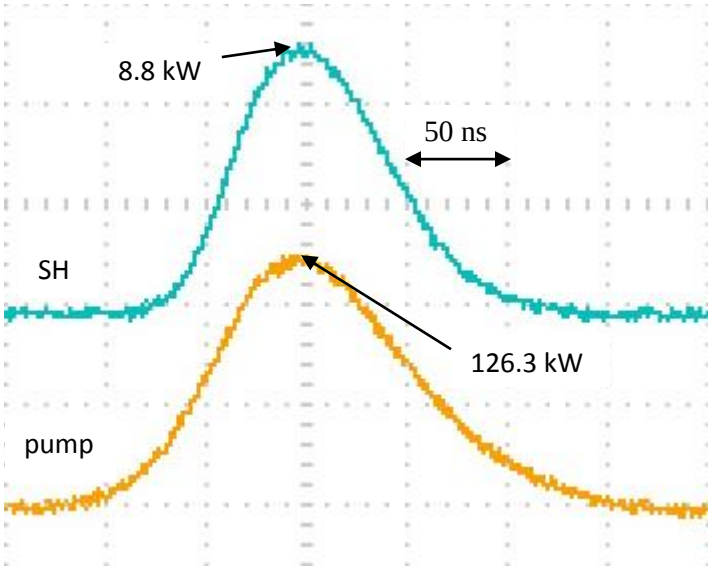

Figure 3.8. Temporal profiles of the pump (yellow) and the Second harmonic (green) pulses captured in the bandwidth limited mode of the oscilloscope.

We next undertook a more detailed study pertaining to the temporal synchronization of the generated SH pulse with the pump pulse. The richly modulated multimode pump pulse allowed an accurate comparison of the temporal evolution of the pump and the SH beam. For this study, the pump laser was operated under two different gains above threshold conditions resulting in its operation on 2 or 3 longitudinal modes. Time expanded temporal behaviour of

both the pump and SH pulses for these two conditions have been recorded respectively in the traces 'a' and 'b' of figure 3.9. The beating of the two oscillating longitudinal modes of the pump laser at a period of ~7 nsec that matches with the cavity round trip time is clearly evident in the top trace of figure 3.9 a. The corresponding SH pulse depicted in the lower trace of this figure clearly reveals its excellent synchronization with the pump pulse with respect to both amplitude and phase. Exactly similar behaviour in the case of operation of the pump laser with three longitudinal modes with a base period of 3.5 nsec can be seen in the traces of figure 3.9 b.

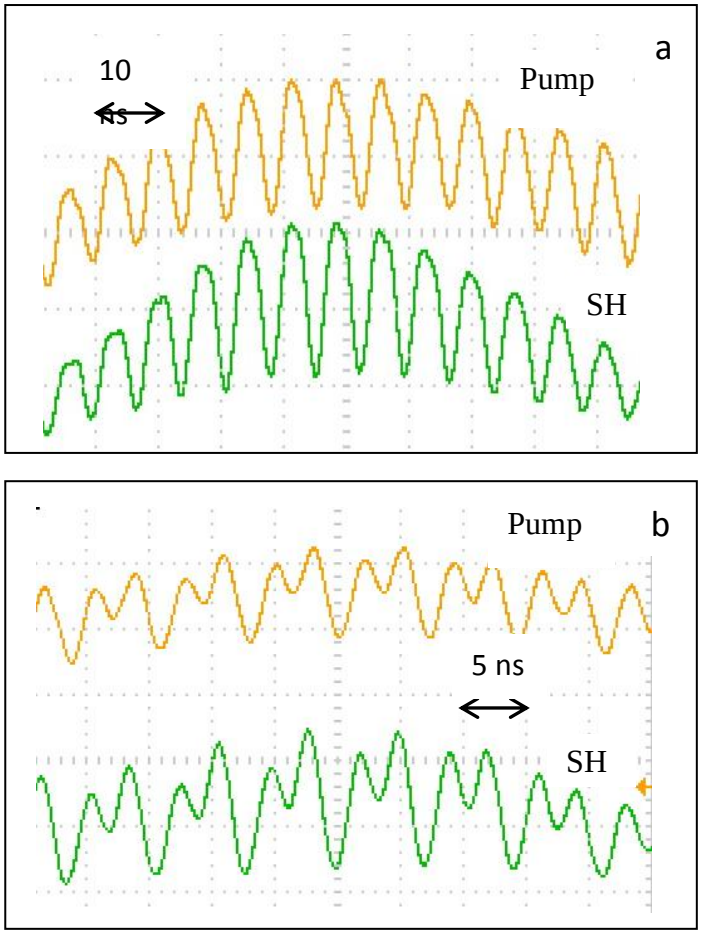

Figure 3.9. Temporal synchronization of the pump (yellow) and the SH (green) pulses in case of operation of the pump laser on a: 2 longitudinal modes b: 3 longitudinal modes.

3.3.1. Enhancement of Conversion Efficiency by way of a Multi-pass Cavity

$AgGaSe_2$ offers high transmission at both pump and generated wavelengths. However, its relatively low damage threshold limits the maximum intensity of the pump radiation to which it can be exposed and, in turn, the conversion efficiency [3.20] as a large fraction of the pump remains unutilized. We have increased the conversion efficiency by utilizing the unconverted

pump beam by way of constructing a multi-pass cavity external to the laser that contained the crystal.

The schematic of the experimental set up is shown in figure 3.10. An in-house built, He-free TEA CO_2 laser capable of delivering ~1 J of energy per pulse in the multi-transverse mode with a gas composition of CO_2:N_2 :: 2.5:3.5 and described, in detail, elsewhere [3.21], was

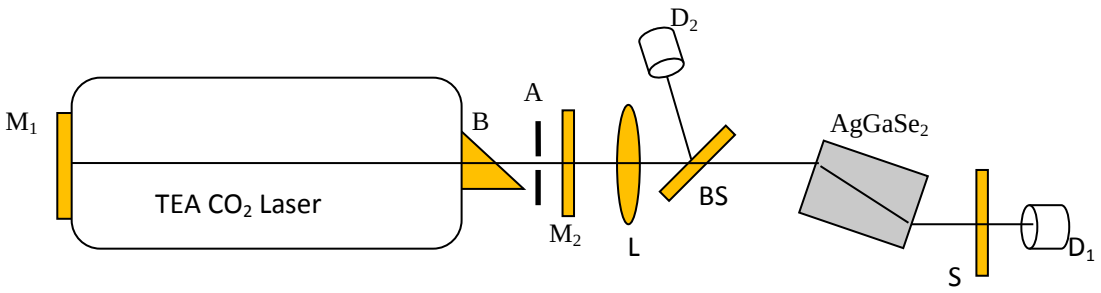

Figure 3.10. Schematic of the experimental set-up of single-pass second harmonic generation. M_1- gold coated mirror, M_2- 85% R mirror, B- Brewster Plate, A- Adjustable Aperture, L-lens of 25 cm focal length, BS- Beam splitter, S- Sapphire plate, D_1 and D_2 are the energy meters.

made to emit on vertical polarization and TEM_{00} mode with the help of intra-cavity ZnSe Brewster`s window and an aperture. In this mode of operation, the laser yielded a maximum of~160 mJ of energy per pulse on the 10P(20) line. The pump pulse had a typical ~200 nsec gain switched spike followed by a tail of ~1 µsec duration. The crystal was mounted in this case too on a stage equipped with provision of rotation in the horizontal and vertical planes for optimizing both θ and φ towards achieving type I phase matching with a vertically polarized fundamental beam. The cut angle of the crystal is 69^o that was originally meant to create phase matching condition for second harmonic generation in case of normally incident 12 µm fundamental beam, as mentioned earlier. The incident angle of the pump radiation at 10.4 µm to the entrance face of the crystal was adjusted to ~38° for achieving phase matching condition. A 25 cm focal length, AR coated ZnSe lens was used to gently focus the pump beam onto the crystal so as to achieve optimized second harmonic conversion by maintaining

the optical flux inside crystal below its damage threshold. The possibility of damage on the crystal surface was eliminated by adjusting the energy of the pump pulse so as to ensure that no glow was visible on the entrance face of the crystal. An ZnSe window (BS) AR coated @ 10 µm for normal incidence, when used at 45° angle of incidence, directed almost the entire pump beam towards the focusing lens reflecting only a small fraction towards pyroelectric detector D_2 (Gentec, ED 200) to monitor the pump energy. The residual pump beam that emerged through the crystal along with the second harmonic beam was blocked by a 3 mm thick sapphire plate and the energy of the generated second harmonic radiation were respectively monitored by a pyroelectric Joulemeter, D_1 (Gentec ED 200). Under most optimized condition, the maximum energy of SH beam was measured to be ~7.5 mJ giving rise to an external energy conversion efficiency of 7.5%. Taking into account the Fresnel reflection loss of the pump at the entrance face of the crystal and Fresnel reflection of the second harmonic beam at the exit face and its absorption and reflection losses in the Sapphire plate, the internal energy conversion efficiency is estimated as ~22.8% that compares well with those reported in the literature for similar pump pulse duration and crystal thickness [3.18, 3.22].

We next attempted to utilize the residual pump beam by constructing a Fabry-Perot cavity containing the crystal but external to the pump laser, the schematic of which is depicted in figure 3.11. The 85% reflective @ 10 µm plane output mirror (M_2) of the pump laser served as the rear mirror while a dielectric coated ZnSe mirror (M_3) of reflectivity 90% @ 10 micron and 50% @ 5 micron formed the front mirror (figure 3.11). The cavity was aligned by letting the residual pump beam reflected off mirror M_3 trace back its incident path through the aperture A_2. This arrangement allowed multiple passes of the pump beam through the crystal and generation of second harmonic beam, both, during its forward and return passes through it. Mirror M_3 allowed only 50% of the forward generated 5 micron beam to be coupled out

while the remaining is reflected back into the cavity. This, along with the unconverted pump and the second harmonic beam generated by the pump during its return path through the crystal is incident on the ZnSe beam splitter (BS) that is 30% reflective @ 5 µm at 45° angle of incidence. This enabled coupling of the return 5 micron beam out of the cavity as an additional second harmonic beam. Under most optimized conditions, the second harmonic energy conversion efficiency was estimated to be 11.25% after taking into account of the emergence of two 5 micron beams, one through mirror M_3 and the other, off ZnSe beam splitter, with a net gain of 50 % over the single pass case. It should be noted here that in our experiment only a fraction of the generated second harmonic has been coupled out of the cavity. Significant improvement in the performance of this multi-pass cavity is expected by replacing mirror M_3 with a dichroic mirror having ~100 % R @ pump wavelength and ~100 % transmission at 5 µm and the ZnSe beam splitter (BS) with another dichroic optics having

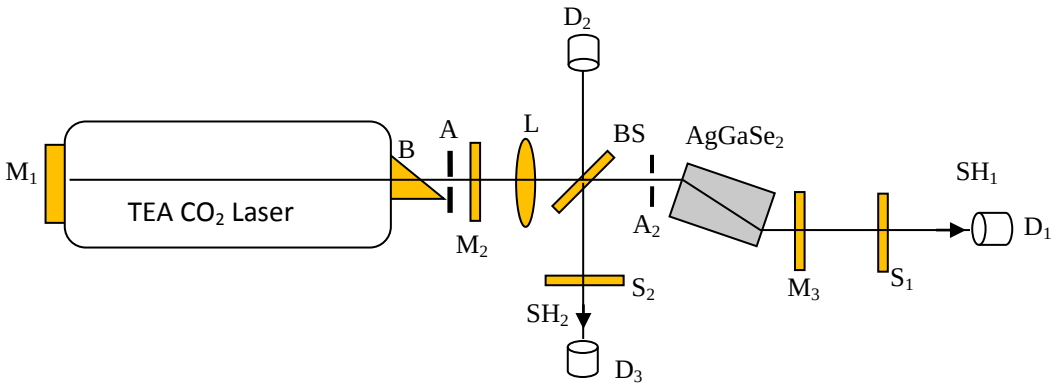

Figure 3.11. Schematic diagram of the experimental setup of multi-pass second harmonic generation. M_1- gold coated mirror, M_2- 85% R mirror, M_3 – 95%R @ 10 µm and 30%R @ 5 µm, B- Brewster Plate, A_1-Adjustable intra-cavity aperture, A_2-Adjustable aperture, L-25 cm f lens, BS-Beam splitter, S_1 and S_2 - Sapphire plates, D_1, D_2 and D_3energy meters.

~100 % transmission @ pump wavelength and ~100 % R at 5 micron at 45^{o} angle of incidence.

3.4. Generation of discretely Tunable Coherent 5 μm Radiation by SH Conversion of Emission of Pulsed and CW-CO_2 Lasers using ZGP crystal

$ZnGeP_2$ has gained importance as a non-linear material that possesses large non-linearity, relatively high damage threshold, and large angular and temperature tolerance with respect to phase matching conditions [3.23-3.24]. However, the usage of $ZnGeP_2$ has been generally restricted to the second harmonic generation (SHG) of CO_2 laser emission in the 9 μm region [3.25] owing to a strong absorption feature in the 10 μm region, overlapping with the 10P band. To be noted here that, high power generation capability of this crystal at and around 4.5 μm region has also been demonstrated of late [3.26]. Understandably therefore, the literature on the SHG at and around 5 μm region by $ZnGeP_2$ is scanty. There, however, exists a report on the frequency doubling of TEA CO_2 laser emission at 10.6 μm by a thick and annealed $ZnGeP_2$ [3.27] albeit at extremely high pump intensity running into several MW/cm^2. Laser absorption induced heating of the crystal has been shown to enhance the conversion efficiency. However, in order to satisfy phase matching condition, the CO_2 laser was required to be operated at unusually high repetition rate and generated extremely short pulses of tens of μJ energy. We present here, the results obtained in our laboratory, comparing the performance of a $ZnGeP_2$ crystal towards second harmonic conversion of the emission of both CW and pulsed TEA CO_2 lasers operating on the 10 μm band. To be noted that in contrast to [3.27], the second harmonic conversion of the emission of TEA CO_2 laser has been achieved for its conventional operation. We have chosen a R branch transition viz., 10R(16) line with 10.27 μm wavelength, that is somewhat removed from the 10P branch. A very satisfactory performance with regard to second harmonic (SH) conversion efficiency as observed even for a thin crystal clearly establishes the utility of $ZnGeP_2$ towards generation of a coherent source not only in the 4.5 μm but also in the 5 μm region of the mid-infrared. Experimental results comparing performance of this crystal when pumped alternately with

the emission of CW and TEA CO_2 lasers are discussed in this chapter. The performance has also been studied in detail as a function of the duration of the pump TEA CO_2 laser pulse.

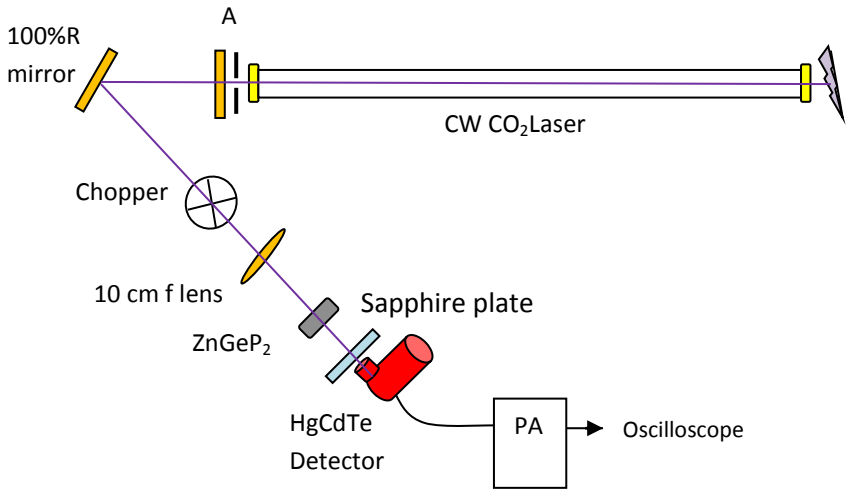

Figure 3.12. Schematic diagram of the experimental set-up for SH conversion of the emission of a CW-CO_2 laser.

A thin uncoated $ZnGeP_2$ crystal of cross-section 1 cm x 1 cm and thickness 3 mm was made use of for the frequency doubling of the emission of both pulsed and CW-CO_2 lasers, that were operated on the 10R(16) transition. The cut angle of the crystal is 71°, where it is automatically phase matched around 10P(14) transition for normal incidence. Considering the fact that $ZnGeP_2$ has vanishingly small effective non-linear coefficient for type-I phase matching in the 10P branch we have chosen to work with 10R(16) line for which the deviation of the angle of incidence with respect to the face normal to effect phase matching was experimentally found to be ~18°.

In the first set of experiments, the emission of an CW-CO_2 laser, developed in-house, and grating tuned to operate on the 10R(16) line, was made use of to effect SHG in the crystal. The schematic of the experimental set-up is as shown in figure 3.12. A 6 m concave master grating blazed at 10.6 µm and a 70% reflective plane output coupler separated by ~110 cm defined the resonator cavity. The rulings of the grating were so aligned as to result in emission on a horizontal polarization. An intra-cavity aperture 'A' allowed operation of the laser on a TEM_{00} mode producing ~2W CW power. An AR coated ZnSe lens of 10 cm focal length was used to enhance the intensity of the incident beam on the crystal to an appropriate value that was well below the damage threshold of the crystal. A liquid N_2 cooled HgCdTe photoconductive detector (Judson model: J15D14) in conjunction with a chopper of 50% duty cycle was used to detect the SH output. A 4 mm thick sapphire plate (Crystran Ltd, UK) was placed in front of the detector (as before) to completely block the unconverted pump beam that emerged along with the SH beam. The output of the detector was displayed on the oscilloscope after suitable amplification (Judson PA101).

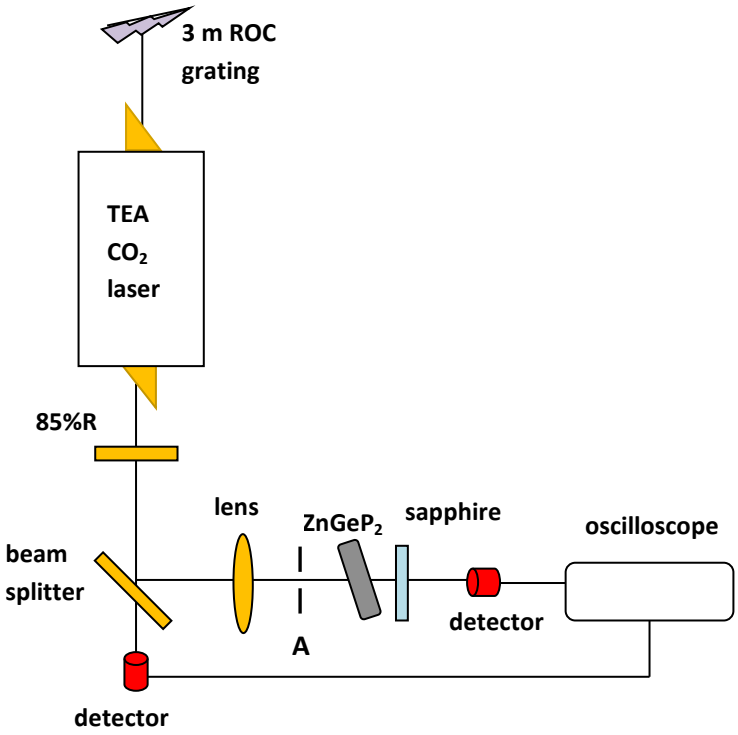

Figure 3.13. Schematic diagram of the experimental set up for SH conversion of the emission of a TEA CO_2 laser.

$ZnGeP_2$ is a positive, uniaxial crystal. In order to effect Type-I phase matching, as the CO_2 emission was on a horizontal polarization, the crystal too was rotated in the horizontal plane

by mounting it on a suitable stage with provision of rotation along two orthogonal directions to optimize both θ and φ. The SH output was observed when the external angle of incidence lied between 16° to 20° corresponding to an internal phase matching angle of 65.9° and 64.7° respectively with optimized performance being obtained for a phase matching angle of 65.3°. A maximum of 40 μW of SH CW output at 5.137 μm was measured. After accounting for the Fresnel reflection losses of the fundamental beam at the input face (~26%) of the crystal, and, the SH beam at the exit face (~26%), as well as, the Fresnel reflection and absorption losses in the 4 mm thick sapphire crystal for the SH beam (~44%), the internal conversion efficiency of the SH process can be estimated as 6.5×10^{-3}%. The value of pump intensity at which detection onset of SH generation occurs was measured by gradually increasing the power of the fundamental beam till the point where the SH signal just began to show up. This point was reached for an incident pump power of 0.96 W while the focussed spot diameter of the input beam on the crystal incident face was ~1.14 mm. Thus the pump intensity pre-requisite for the detection onset of SHG process can be estimated as ~94 W/cm^2.

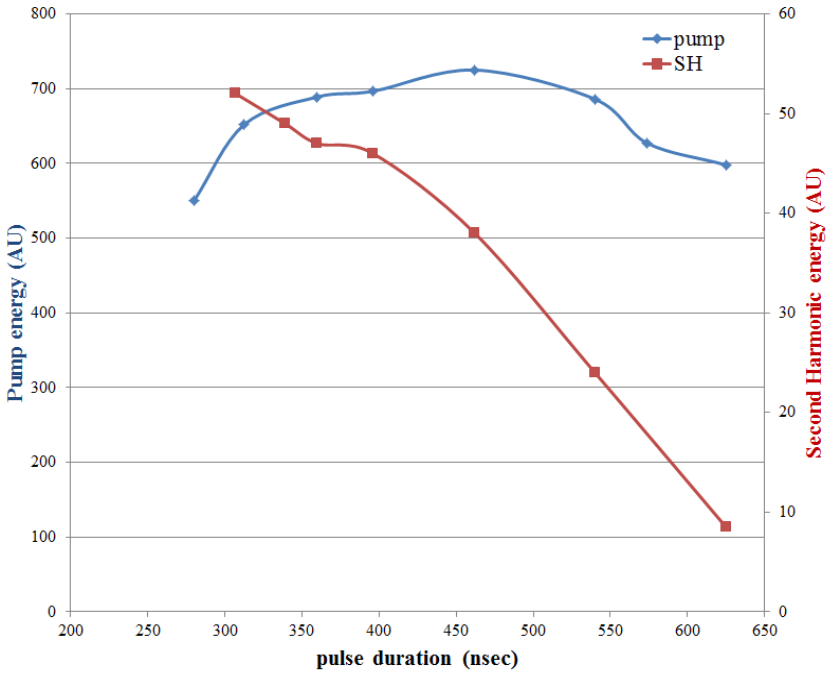

Figure 3.14. The dependence of the pump energy (blue) and the second harmonic energy (red) on the pump pulse duration.

In the next set of experiments, SH of the emission of an indigenous pulsed He-free TEA CO_2 laser [3.28] was generated and the corresponding experimental layout is as shown in figure

3.13. The pump laser cavity was defined by a 3 m concave grating blazed in the first order for 10 µm and an 85% reflective plane ZnSe output coupler spaced by ~88 cm. The grating was tuned to allow oscillation on the 10R(16) line yielding a maximum multimode energy output of ~375 mJ on parallel polarization as measured by a pyroelectric Joulemeter (Gentec, ED 200). A ZnSe beam splitter was used to direct ~98% of the emission towards an AR coated ZnSe lens of focal length 25 cm while the remaining was made use of to monitor the power profile of the pump with a room temperature fast HgCdTe detector (PEML3, Vigo Systems). The crystal was so located as to allow a gentle focusing of the pump radiation onto its incident face. An aperture 'A' was placed between the lens and the crystal to restrict the incident intensity to well below the surface damage threshold of the crystal, that was confirmed by the absence of any observable glow on the crystal surface. The measured energy incident on the crystal in this condition was ~100 mJ while the area of the beam incident on the crystal face was ~ 0.11 cm^2. The crystal was aligned as in the previous case and the optimized SHG occurredfor an external angle of incidence of ~18°, where the output on SH was measured to be ~0.875 mJ, giving rise to an external conversion efficiency of 0.875%. The 4 mm Sapphire plate was made use of as before, to block the unabsorbed pump beam completely. The SH pulse energy and the temporal pulse shapes were monitored respectively by a sensitive pyroelectric joule meter (Gentec, ED100) and a fast photo-detector (PEML3, Vigo systems). After accounting for the losses experienced by the pump and the SH beam as detailed in case of CW operation, the internal conversion efficiency of the SHG process has been estimated as 2.89 %. This compares well with that reported for $ZnGeP_2$, albeit, it is for SHG of the emission of TEA CO_2 laser near 9 µm region and for shorter pulse duration [3.22].

Helium free operation of the TEA CO_2 laser allowed wide variation of molecular gas composition in the laser gas mixture resulting in significant variation in the duration of its

emission. For instance, by increasing CO_2 concentration from 20% to 90%, the pulse duration can be reduced from several hundreds of nanoseconds to several tens of nanoseconds [3.28]. This enabled us to study the dependence of energy of the pump beam and the second harmonic beam on the duration of the pump pulse that is depicted in the traces of figure 3.14. It would be seen that while pump energy exhibited a maximal behaviour, the SH beam energy showed a monotonous rise with reducing pump pulse duration. This behaviour can be qualitatively explained in the following manner. As the laser gas comprises of only molecular gases, reducing CO_2 concentration results in corresponding increase in the partial pressure of N_2 that contributes towards extending the tail of the pump laser pulse [3.28]. While up to a certain concentration of CO_2, this increases the energy output of the laser, further reduction in the active molecular concentration eventually brings it down thus giving rise to a maximal behaviour, as is evident in figure 3.14. The reduction in CO_2 partial pressure also has the effect of lowering the peak laser gain and, in turn, the gain switched peak power of the emission. As the efficiency of the SHG process is known to directly depend on the intensity of the fundamental beam, it is natural to expect a reduction in the SH output with reducing partial pressure of CO_2 i.e. with increasing pump pulse duration (figure 3.14).

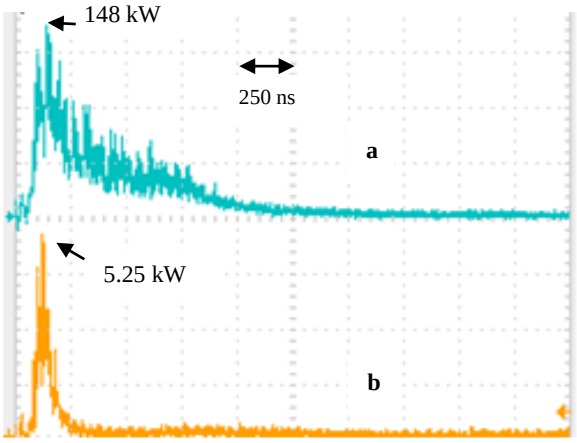

Figure 3.15. Typical temporal profiles of the pump (trace a) and corresponding second harmonic (trace b) pulses.

Towards finding the power conversion efficiency and the detection threshold pump intensity for SHG in case of pulsed operation, we monitored the temporal evolution of both the pump and the generated second harmonic pulse for a gas mixture of CO_2:N_2 :: 2.0:3.5. For this, a tiny fraction of the pump pulse that leaked

through the highly reflective dielectric beam splitter (figure 3.13), and the corresponding SH pulse, were simultaneously detected by placing two fast photo detectors in their respective paths. The oscilloscope traces of these pulses are recorded in figure 3.15. To be noted is that, the time expanded temporal behaviour of both the pump and SH pulses (just the way as elaborated in section 3.3) clearly established beating of the two oscillating longitudinal modes of the pump laser at a period of ~6 nsec that matches with the cavity round trip time for the 88 cm length cavity. The excellent phase and amplitude synchronization of the SH emission with the pump pulse bearing experimental testimony to the instantaneous nature of the SH generation process has been recently reported by us [3.29] and is not being elaborated here. Based on the figure 3.15, the internal peak power conversion efficiency has been estimated as 3.63%.

As can be seen, the peak power conversion efficiency exceeds the energy conversion efficiency. Higher is the coherent field at the fundamental wavelength, better is the SH conversion. Since the peak power always exceeds the average intra-pulse power in case of gain switched pulsed operation, the power conversion efficiency is understandably greater than the energy conversion efficiency of the SH conversion process. This result is in agreement with the findings of several researchers [3.30-3.32]. The intra-pulse average power being much higher as compared to the CW case, the CW SH conversion efficiency is thus understandably much poorer as against that obtained in the pulsed operation. Accurate estimation of the detectable intensity for the onset of SH generation process in this case is error prone owing to the rapid build-up of pump power due to gain-switched lasing. Its fall, on the other hand, is slow and a careful inspection of the temporal profiles of pump and the generated SH pulse reveal that the SH beam ceases to exist even when the incident pump intensity level is ~315 kW/cm^2. This is in sharp contrast with that measured in case of CW operation viz., ~94W/cm^2.

3.5. Conclusions

In conclusion, the operation of a continuously tunable coherent source in the 5 μm region of the mid-infrared based on the frequency doubling of the emission of a multi-atmosphere TE CO_2 laser in $AgGaSe_2$ has been described. The performance of the source has been characterized with regard to its energy and power conversion efficiency. The detection threshold intensity of the radiation at the fundamental wavelength, pre-requisite for the onset of SH generation process and its sustenance, has been measured and found to be ~145 kW/cm^2. Further, the observation of excellent temporal synchronization of the SH pulse with the pump pulse, both in terms of phase and amplitude, bears experimental testimony to the fact that the process of creation of dipole by the pump at frequency ω and its giving out emission at 2ω are indeed instantaneous. Further, the absence of gain switched peak in the emission of the pump laser that stemmed from its operation with a lean CO_2 gas mixture enabled error-free threshold measurement for the detection onset of the second harmonic generation process. Further, the excellent phase and amplitude synchronization of the SH emission with the pump pulse could be observed by studying the temporal profile of the pump and the corresponding SH emission. The mode beating of the pump that is also reflected in the SH emission provides signature of the operation of the pump laser on 2 or 3 longitudinal mode and bears experimental testimony to the instantaneous nature of the SH generation process.

The work with $ZnGeP_2$ crystal clearly establishes its satisfactory performance towards second harmonic conversion of CO_2 laser emission at 10 micron. The literature on SHG in the region of 4.5 μm by $ZnGeP_2$ is quite rich and our observation clearly establishes the utility of this crystal for generation in the 5 μm region of the mid-infrared as well. The significant increase in the conversion efficiency in case of pulsed operation is attributed to the much higher irradiating intensity to which the crystal is subjected here as against the CW case. Of

particular interest is the finding that, in case of CW operation, the pump intensity below which the detection of second harmonic output is no longer possible is lower by three orders of magnitude than the case with pulsed operation. The efficiency of the frequency doubling process in the pulsed operation case has been studied as a function of the duration of the pump pulse and the observation qualitatively explained.

3.6. References

3.1. SHG in doped GaSe: In crystals, Z. Feng, Z. Kang, F. Wu, J. Gao, Y. Jiang, H. Zhang, Y. M. Andreev, G. V. Lanskii, V. V. Atuchin and T. A. Gavrilova, Optics Express,16, 9978 (2008).

3.2. Experiments with second harmonic generation output in pulsed TEA CO_2 laser, Guo. Ruhai and Li. Dianjun, High-Power Lasers and Applications, Edited by Singh, Upendra N, Fan Dianyuan, Yao Jianquan, Walter Robert F, Proceedings of the SPIE, 7843, Article Id. 78430E, 5 (2010).

3.3. CO_2 laser frequency doubling in $ZnGeP_2$, P. D. Mason, D. J. Jackson, E. K. Gorton,Opt.Commun.110, 163 (1994).

3.4. Temperature and Pulse-Duration Dependence of Second-Harmonic Generation in $CdGeAs_2$, A. Zakel, J. L. Blackshire, P. G. Schunemann, S. D. Setzler, J. Goldstein, and S. Guha, Appl. Opt 41, 2299 (2002).

3.5. Frequency doubling of CO_2 laser radiation at 10.6 μm in the highly non-linear chalcopyrite $LiGaTe_2$, J. Zondy, F. Bielsa, A. Douillet, L. Hilico, O. Acef, V. Petrov, A Yelisseyev, L. Isaenko and P. Krinitsin,Opt. Lett., 32, 1722 (2007).

3.6. Second harmonic generation of TEA CO_2 laser radiation in $LiInSe_2$, Y. Andreev, V. Badikov, P. Geiko, S. Grechin, V. Efimenko, T. Efimenko, V. Panyutin, A. Tikhomirov, A. Shaiduko, Atmos. Oceanic. Opt.70, 115 (2004).

3.7. New Nonlinear Optical Materials: Theoretical Research, Ji-Ping Huang, Nova Scientific Publishers, Inc., New York (2007).

3.8. Second Harmonic Generation in $CdSiP_2$, Leonel P. Gonzalez, et al, in Non-linear Frequency Generation and Conversion: Materials, Devices, and Applications VIII, Edited by Peter E. Powers, Proc. of SPIE 7197, 71970N (2009).

3.9. Tittel F K, Richter D and Fried A, Topics in Appl. Phys., 89, 458–529 (2003).

3.10. Kung A H, Proc. SPIE 2379, 163 (1995).

3.11. Mirov S B et al, Proc. SPIE 3491, 1082–88 (1998).

3.12. Herbst R L, US Patent 4200808 (1980).

3.13. Lu Q Y, Bai Y, Bandyopadhyay N, Slivken S and Razeghi M, Appl. Phys. Lett. 98, 181106 (2011).

3.14. Patel C K N Patel, Phys. Rev., 141, 71 (1966).

3.15. V. G. Dmitriev, G. G. Gurzadyan, D. N. Nikogosyan, Hand book of Non-linear Optical Crystals, Springer series in Optical Sciences, Berlin (1991).

3.16. Patel C K N, Lasers, a Series of Advances, volume 2, Ed. A K Levine (NewYork: Marcel Dekker) (1968).

3.17. Petukhov V O, Gorobets V A, Tochitsky S Y and Kozlov K V, Proc. SPIE, 4351, 171 (2001).

3.18. Eckardt R C, Fan Y X, Byer R L, Route R K, Feigelson R S and van der Laan J Appl. Phys. Lett., 47, 786 (1985).

3.19. Russel D A and Ebert R, Appl. Opt. 32, 6638 (1993).

3.20. Jean-Jacques Zondy, Optics Communications, 119, 320 (1995).

3.21. D. J. Biswas, J. P. Nilaya and A. Kumar, Opt Communications, 248, 541 (2005).

3.22. Generation of the second harmonic of pulsed CO_2 laser radiation in $AgGaSe_2$ and $ZnGeP_2$ single crystals, Yu. M. Andreev, V. V. Butuzov, G. A. Verozub, A. I. Gribenyukov, S. V. Davydov, and V. P. Zakharov, Laser Physics,5, 1014 (1995).

3.23. CO_2 laser frequency doubling in $ZnGeP_2$, Mason P D, Jackson D J and Gorton E K, Opt. Communications, 110, 163 (1994).

3.24. Development of coherent tunable source in 2-16 μm region using nonlinear frequency mixing processes, Chatterjee U, Pramana J. Phys., 82, 29 (2014).

3.25. Experimental investigation of single and twin $AgGaSe_2$ crystals for CW 10.2 μm SHG, Zondy J J, Opt. Communications, 119, 320 (1995).

3.26. High power 4.65 μm single-wavelength laser by second-harmonic generation of pulsed TEA CO_2 laser in $AgGaSe_2$ and $ZnGeP_2$, Li D J et al, Laser Phys., 22, 725 (2012).

3.27. Enhanced output power for phase-matched second-harmonic generation at 10.6 μm in a $ZnGeP_2$ crystal, Jiang Y and Ding Y J, Opt. Express, 15, 12699 (2007).

3.28. Operation of a helium-free TEA CO_2 laser, Biswas D J, Nilaya J P and Kumar A, Opt. Communications, 248, 521 (2005).

3.29. Generation of continuously tunable 5 μm coherent radiation by second harmonic conversion of the emission of a multi-atmosphere TE CO_2 laser in $AgGaSe_2$, Nilaya J P, Sai Prasad M B and Biswas D J, Laser Physics, 24, 085401 (2014).

3.30. Efficient generation and heterodyne detection of 4.75 μm light with second-harmonic generation, Russel D A and Ebert R, Appl. Opt., 32, 6638 (1993).

3.31. Andreev Yu M et al CO laser frequency conversion in nonlinear crystals $ZnGeP_2$ and GaSe, Sov. J. Quantum. Electron., 17, 1435 (1987).

3.32. Efficient intra-cavity frequency doubling of CO_2 laser in nonlinear crystals, Petukhov V O, Gorobets V A, Tochitsky S Ya, Kozlov K V, Proc. SPIE, 4351, 171 (2001).

Chapter 4: Development of a Cryo-cooled CW Electric Discharge CO laser by Employing CO_2 Laser Gas Mixture

4.1. Introduction

As discussed in chapter 2, CO_2 laser is the most powerful coherent source providing discretely tunable emission over the 9-11 μm region of the electromagnetic spectrum [4.1]. Discovered in 1964 by C. K. N. Patel [4.1], it is one of the most well researched lasers and has found its way into numerous review papers [4.2-4.5] and textbooks [4.6-4.7], besides the countless research papers published worldwide. Its laser dynamics is therefore well understood and active research is now confined to its application in various disciplines. However, one aspect of CO_2 laser that has hitherto remained experimentally unexplored is its emission spectrum when the gain cell is subjected to liquid nitrogen (LN_2) temperature (77 K) conditions, understandably, owing to the freezing of the CO_2 gas at such low temperatures. However, the operation of this laser at sub-zero temperatures (~200 K) has been explored and an improvement in power and efficiency has been reported [4.4]. We report here, for the first time, the operation of a free running CW-CO_2 laser when its gain cell is cooled to LN_2 (77 K) temperature. Of particular interest is the observation of rich multi-line emission spectrum spanning over 4.95 μm to 5.49 μm. These findings are very significant, as they establish, for the first time, the laser emission in 5 μm region originating from CO molecules that are formed inherently in CO_2 gas discharge due to electron impact dissociation [4.8]. This has rendered the utilization of highly toxic extraneous CO gas source for obtaining lasing in the 5 micron region redundant.

Ever since the discovery of CO laser, also by C K N patel, in 1964 [4.9], it has been recognized as an important coherent source owing to its unique wavelength and very high quantum efficiency (~100%) [4.10] that has applications in areas covering overtone

spectroscopy [4.11], laser chemistry [4.11], industry [4.12] and medicine [4.13-4.15]. Further, the overlap of the CO laser emission with the absorption features of certain heavy molecules viz., MoF_6, WF_6, UF_6 etc., is of importance with regard to isotope harvesting of these molecules [4.16]. Also, CO laser can excite these heavy molecules to higher vibrational levels causing accelerated chemical reactions through Laser Isotope Separation Employing Condensation Repression (CRISLA) [4.17, 4.18], another method, that has been attempted successfully for enriching strategic isotopes.

Laser emission at both 5 and 10 μm wavelengths independently and simultaneously have been previously reported [4.19-4.21] from discharge struck in gas mixture comprising of CO, air and Helium. These results were either achieved in a sealed-off tube or in flowing condition. One such work wherein simultaneous lasing action at both 5 and 10 micron region has been reported [4.21] was from a segmented laser cavity wherein DC discharge was struck in both the segments simultaneously with the first segment cooled by LN_2 and the second by flowing water. Lasing in the 5 micron region occurred from the CO gain medium while CO_2 gain medium formed in the second segment of the discharge tube (as air was used in lieu of N_2, CO_2 formation was facilitated through the dissociation of CO followed by its oxidation in the presence of O_2), contributed to lasing in the 10 micron region. In this chapter, the multi-line emission obtained in the 5 μm region from a LN_2 cooled CO_2-N_2-He gas discharge in non-dispersive configuration shall be discussed. To be noted, in contrast to the earlier reported works by various authors on CO laser [4.19-4.21], the gas mixture here does not include CO at all. Lasing action originated from the CO gain medium that was formed due to dissociation of CO_2 in the discharge owing to electron impact. Lasing action on several lines with their wavelengths ranging from 4.95 to 5.49 μm with a cumulative CW power of 8 W has been obtained at an electro-optic efficiency of 8%. Before we discuss the development of this laser, some aspects of CO laser shall be dwelled upon.

4.2. An overview of CO Laser & its Operational Characteristics

Molecular CO lasers are an important class of gas lasers in the mid-IR region, owing to their output wavelengths being in the atmospheric transmission window around 5 μm region. These lasers are capable of delivering high powers and possess high working efficiencies. Owing to CO being diatomic, it has only one single vibrational mode (in contrast to CO_2 which has 3 modes). Therefore it is possible to achieve 100% quantum efficiency, which is defined as the ratio of the energy of the emitted photon to its excitation energy. However, one problem that exists for certain diatomic molecules (e.g., HF, HBr, NO etc.,) is the very fast V-T collisional relaxation processes that cause them to lose vibrational energy quickly as heat. CO is unique in that respect since its V-T relaxation times are relatively long; typically 10, 4 x 10^{-3}, 10^3 atm-sec for CO-CO, CO-He, CO-Ar collisions, respectively, for relaxation from υ =1 to υ = 0 at 300 K. In terms of number of V-T relaxations, this corresponds to ~10^{-4}/mbar/sec (or 1 V-T relaxation/torr in 10000 sec) between CO-CO, 0.25 /mbar/sec (or 1 V-T relaxation/1 mbar in 4 sec) between CO-He and 10^{-6}/mbar/sec (or 1 V-T relaxation/mbar in 10^6 sec) between CO-Ar.

4.2.1. Laser action in CO molecule

For a diatomic molecule like CO, the ladder of vibrational levels has energy spacings that are nearly resonant, if not for the anharmonic defect, and thus efficient vibrational cross-relaxation processes (V-V) are possible. Pumping of CO vibrational levels is achieved by e-impact excitation. Like N_2, CO has unusually large cross-section for e^- impact excitation of its vibrational levels. Nearly 90% of electron energy in a discharge can be converted into vibrational energy of CO molecules.

$CO + e^-(E) \rightarrow CO^-$ (complex ion state)

CO^- lives for time τ during which its energy is redistributed among various energy modes.

$CO^- \rightarrow CO\ (\upsilon = 1) + e^-(E')$

$CO^- \rightarrow CO\ (\upsilon = n) + e^-(E)$ (less energy)

Having possessed a permanent dipole moment, CO has low rate of V-T and high rate of V-V relaxation. In fact, for a CO laser, it is these rapid near-resonant V-V exchange collisions that dominate the molecular kinetics and decide the structure of vibrational population distribution. A consequence of this is a build-up of non-Boltzmann population in higher vibrational levels, by a process known as anharmonic pumping (figure 4.1), that plays a very important role. Although this phenomenon does not allow total inversion in the vibrational population of a CO molecule, a situation known as partial inversion (figure 4.2) may occur. Under condition of partial inversion, laser action can take place and a new phenomenon

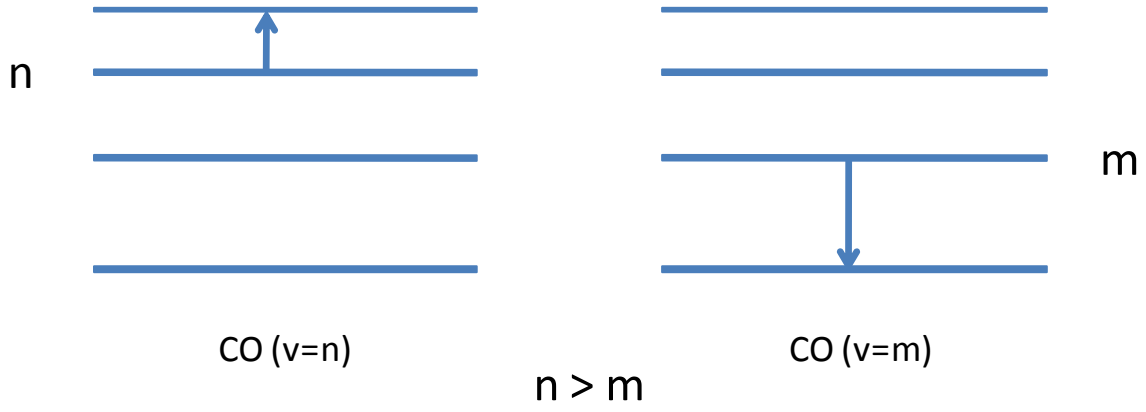

$$CO\ (\upsilon = n) + CO\ (\upsilon = m) \rightarrow CO\ (\upsilon = n+1) + CO\ (\upsilon = m - 1) + \Delta E$$

Figure 4.1. Mechanism of anharmonic pumping

called cascading, can then play a dominating role in lasing action. Laser action, in fact depopulates a rotational level of upper vibrational state and populates a rotational level of the lower vibrational state. The latter level then accumulates enough population to result in population inversion with respect to a rotational level of a still lower vibrational state. At the same time, the rotational level of the upper state may become sufficiently depopulated to result in population inversion with respect to a rotational level of a still higher virbational

state. This cascading action coupled with a very-low V-T rate results in most of the vibration energy being extracted as laser output energy.

4.2.2. Why Cooling is Critical ?

The low temperature requirement arises from the need for very efficient anharmonic pumping. Infact, the population in higher vibrational levels increases rapidly with decreasing translational temperature due to anharmonic pumping. Owing to the anharmonic pumping, the total energy of the two CO molecules after collision is somewhat smaller than that before the collision.

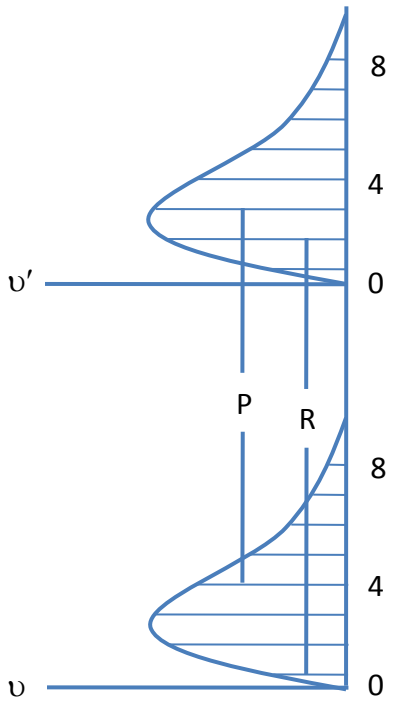

Figure 4.2. Partial inversion between rotational levels corresponding to two different vibrational transitions (v and v′) with the same total population.

$$CO\ (\upsilon=n) + CO\ (\upsilon=m) \rightarrow CO\ (\upsilon=n+1) + CO\ (\upsilon=m-1) + \Delta E \quad (\text{for } n > m)$$

According to the principle of detailed balancing, the forward & reverse reactions are related by,

$$P_{\upsilon(n \rightarrow n+1,\ m \rightarrow m-1)} = e^{\Delta E/KT} P_{\upsilon(n \rightarrow n-1,\ m \rightarrow m+1)}$$

The collision process therefore has greater probability of proceeding in the forward direction than reverse direction if $\Delta E > kT$.

I.e., $P_{\upsilon(n \rightarrow n+1,\ m \rightarrow m-1)} > P_{\upsilon(n \rightarrow n-1,\ m \rightarrow m+1)}$ for $\Delta E > kT$.

So for CO, gain is inversely proportional to temperature. I.e., the pump process is more effective at low gas temperature. Hence, cooling is critical.

4.2.3. Role of different gases used in the operation of CO laser

- **Helium:** He helps in cooling the molecular kinetic translational temperature i.e., the heat of the discharge by V-T process.
- **Xenon:** Since xenon has lowest ionization potential, of any of the constituents used in the CO laser mixture, it is useful for preventing CO decomposition due to collisions with high energy electrons. Further, xenon alters the average e^- energy thereby increasing the fractional electrical power transfer to molecular vibrational levels.

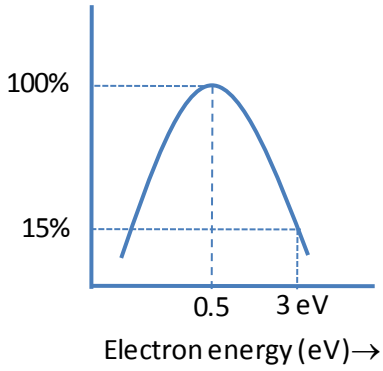

Figure 4. 3. Excitation of CO versus electron energy.

- **Nitrogen:** N_2 is homonuclear molecule and hence has zero dipole moment. So selection rules do not allow ro-vibrational transitions (forbidden). This means its vibrational energy can go be lost either through V-V or V-T relaxations during inter-molecular collisions. Vibrationally excited levels of N_2 are very long lived (τ ~msec) under discharge conditions. As V-V cross-sections are higher than V-T, N_2 efficiently transfers the excitation energy by V-V to CO. Further, it lowers the average electron energy as some energy is lost in exciting N_2 (υ=0) to N_2 (υ=1) through N_2^- (or, equivalently, the E/N of the plasma is altered). So both N_2 and Xe alter the plasma characteristics, resulting in improved fractional conversion of electrical to vibrational energy.

- **Oxygen:** Addition of judicious (small) quantities of oxygen prevents the CO decomposition by driving the reaction backwards and prohibits carbon deposits.

  $CO \Leftrightarrow C + O$

Further, addition of O_2 removes CN radicals believed to be deleterious for CO lasing. The excited states of CO can be undesireably transferred to excited electronic states of CN which dissipates through fluorescence.

4.2.4. Druvestian not Boltzmann

The typical electron densities, N, in the low pressure CO discharge are of the order of ~10^9 /cc, energy ~1 ev, the rate of excitation by electron-molecule collision to form complex ion states (CO^-, N_2^-) are 55/sec and 3/sec for υ=0 to υ=1 and υ=0 to υ=6 respectively. Compared to CO-CO rates ($P_{10\ to\ 01}$) of 10^3 /sec/torr for P_{CO} ~ 0.2 torr, the electron pumping rates are much slower than those for vibrational cross-relaxation. So for higher vibrational states, the near V-V transfer rates become even greater and thus dominate the vibrational distribution for higher energy levels. Figure 4.3 shows the rate of excitation of CO as a function of electron energy. The maximum excitation transfer as shown in figure 4.4 occurs for 0.5 ev of the electron energy in the discharge where the effective cross-section is ~$3x10^{-16}$ cm^2.

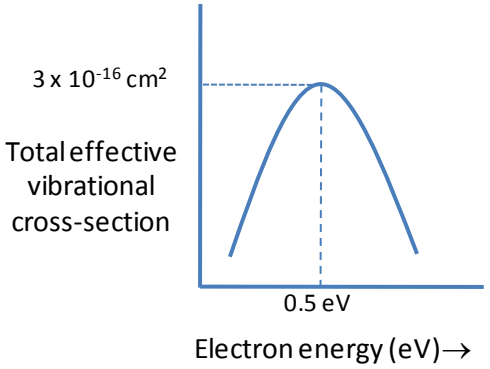

Figure 4. 4. Excitation cross-section of CO versus electron energy.

Knowledge of electron energy distribution as a function of E/N and gas composition makes it possible to calculate the fractional amount of electrical energy input that is deposited into each of the electron-molecule excitation. The electron energy distribution is infact Druvestian. Since electrons in such low-energy weakly ionized plasma (like CO discharge) have no

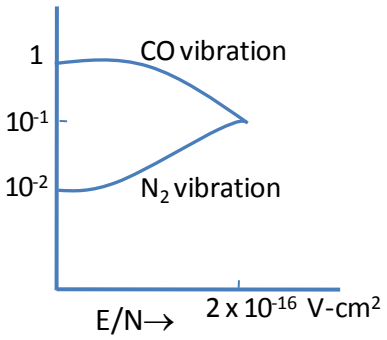

Figure 4.5. Fractional electrical power transfer in CO-N_2-Xe-He.

mechanism for complete thermalization, a departure from Boltzmann is expected. The fractional electrical power transfer for a particular CO-N_2-Xe-He ::1.05:0.05:0.05:0.85 is as shown in figure 4.5.

4.3. Development of a LN_2 cooled CW-CO laser

The importance of CO laser in separation of certain isotopes of strategic interest by laser assisted aerodynamic separation route has been brought out by Eerkens [4.17] and in a more recent work by Baranov et al [4.18]. The second overtone of ν_3 fundamental vibration for certain molecules of strategic interest lies in the region between 1860 and 1880 cm^{-1} that can be accessed by the output of CO laser in the 5 μm region.

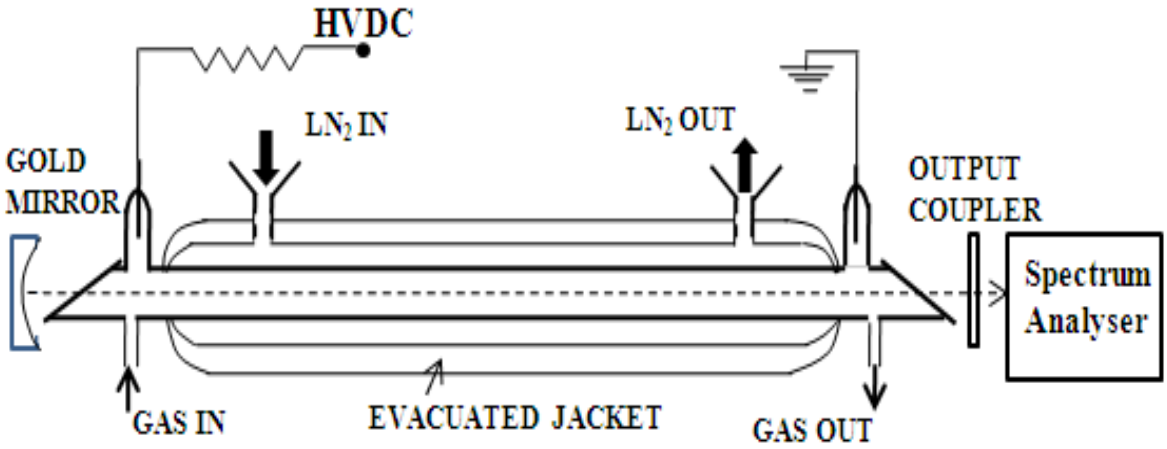

Figure 4.6. Schematic diagram of the CO_2-N_2-He discharge subjected to LN_2 conditions towards obtaining lasing action in the 5 μm region originating from CO molecules formed in the discharge.

Indigenously development of a multi-line CW-CO laser under cryogenic cooled conditions and capable of delivering up to 8 W output under free-running conditions has been accomplished. The schematic of the experimental setup is shown in figure 4.6. The Auto-CAD drawing used for the fabrication of the discharge tube is shown figure 4.7. Discharge was effected in a flowing gas mixture of CO_2:N_2:He::1:1:3 at a total pressure of ~10 mbar,

enclosed in a double jacketed quartz tube (inner diameter 17 mm and active length ~100 cm) that is vacuum sealed at both ends by ZnSe Brewster plates. The outer jacket of 80 mm diameter was evacuated and heat sealed, while the inner jacket of 50 mm diameter served to maintain the walls of the discharge tube at the desired temperature of LN_2. A concave gold mirror, 6 m radius of curvature (ROC), in conjunction with an appropriate flat output coupler that resulted in a high Q value for the 5 micron wavelength, separated by a distance of 145 cm defined the optical cavity. A resistively ballasted DC discharge, with a controllable operating voltage created the required excitation of the active species. The power emitted by the laser was monitored by power meter (OPHIR make, model AN/2), while its emission spectrum was recorded using 5 micron spectrum analyzer (Macken Instruments Inc., CA respectively). The laser was initially operated at room temperature when the lasing, understandably occurred, on the 10P(20) line of CO_2 molecule that has the highest gain at ambient temperature. Following this, LN_2 was poured into the inner jacket until the discharge tube was completely immersed in it. During the process of filling, efforts were expended to maintain the glow discharge on, by maintaining suitable voltage across the electrodes. Sustaining the glow discharge at such low temperatures is essential as the heat of discharge then prevents the complete freezing of the CO_2 gas and its bulk condensation on the walls of

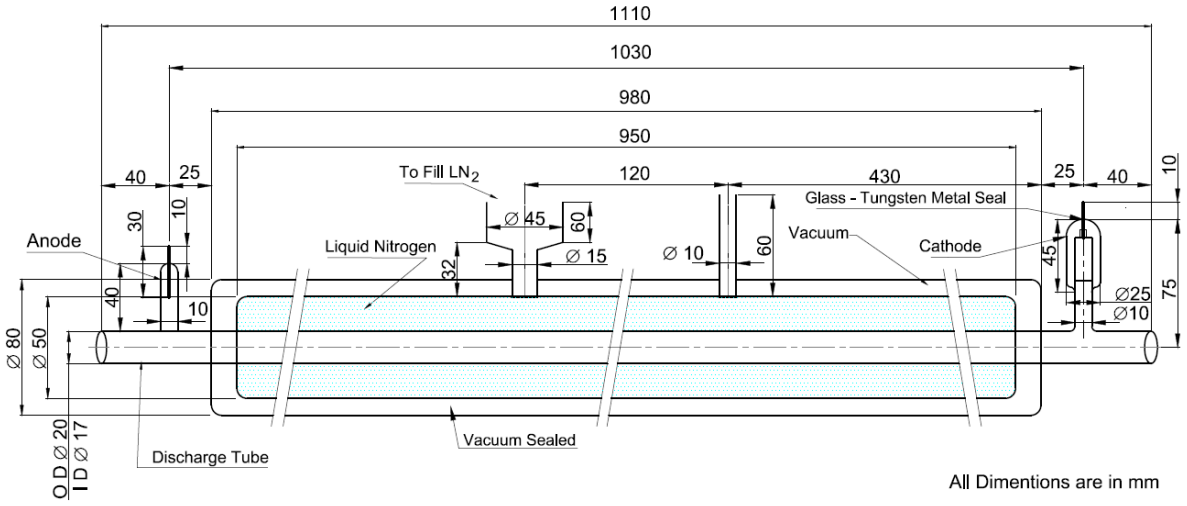

Figure 4.7. Auto CAD drawing used in fabrication of the CW-CO laser tube.

the tube. Under these conditions, the CO formed in the discharge following the dissociation of the CO_2 along with N_2 and He results in the formation of appropriate gain medium conducive for lasing in the 5 micron region.

4.4. Results & Discussion

The screen shots of the CO laser emission spectrum obtained under LN_2 cooled operating conditions as recorded with a CO spectrum analyzer for different output couplers of 85%, 90% & 95% reflectivities coated for 5 μm are shown in figure 4.8. For the three different reflectivities used, cascade lasing on multiple lines in the 5 μm region can be observed under varying conditions of voltage and current. The cascade lasing was observed on several rotational-vibrational lines of P branch of CO molecule, $\upsilon \rightarrow \upsilon$-1 starting from υ=5 and climbing all the way up to υ=12. These corresponding lines could be identified by matching the transitions with the known emission lines of CO that are well documented in the literature [5] and are enumerated in table 4.1. The laser yielded a maximum of 8 Watt power for a current of 5 mA at 20 KV discharge voltage under free-running conditions following optimization of the gas mixture and output coupler. Varying the discharge current changes the gas temperature, that, in turn, alters the CO_2 partial pressure due to change in condensation rate of CO_2. This greatly alters the partial pressure of CO in the gas mixture that can even lead to cessation of lasing. In spite of such sensitive dependence of the discharge on various experimental parameters, lasing over wavelength region from 4.95 to 5.49 μm as is tabulated [table 4.1] could be successfully accomplished.

The observed cascading nature of the output is a well known signature of lasing originating from CO [4.22]. That the emission is only seen on P-branch lines indicates the absence of total vibrational inversion in the CO molecule and the lasing action being entirely due to partial inversion [4.22, 4.23]. While only a few spectrum screenshots have been shown as

part of figure 4.8, lasing, in general, was observed over widely varying discharge current and voltage values ranging from 4-10 mA and 15-20 kV respectively, thereby covering a major portion of the vast vibrational ladder possible from the CO molecule.

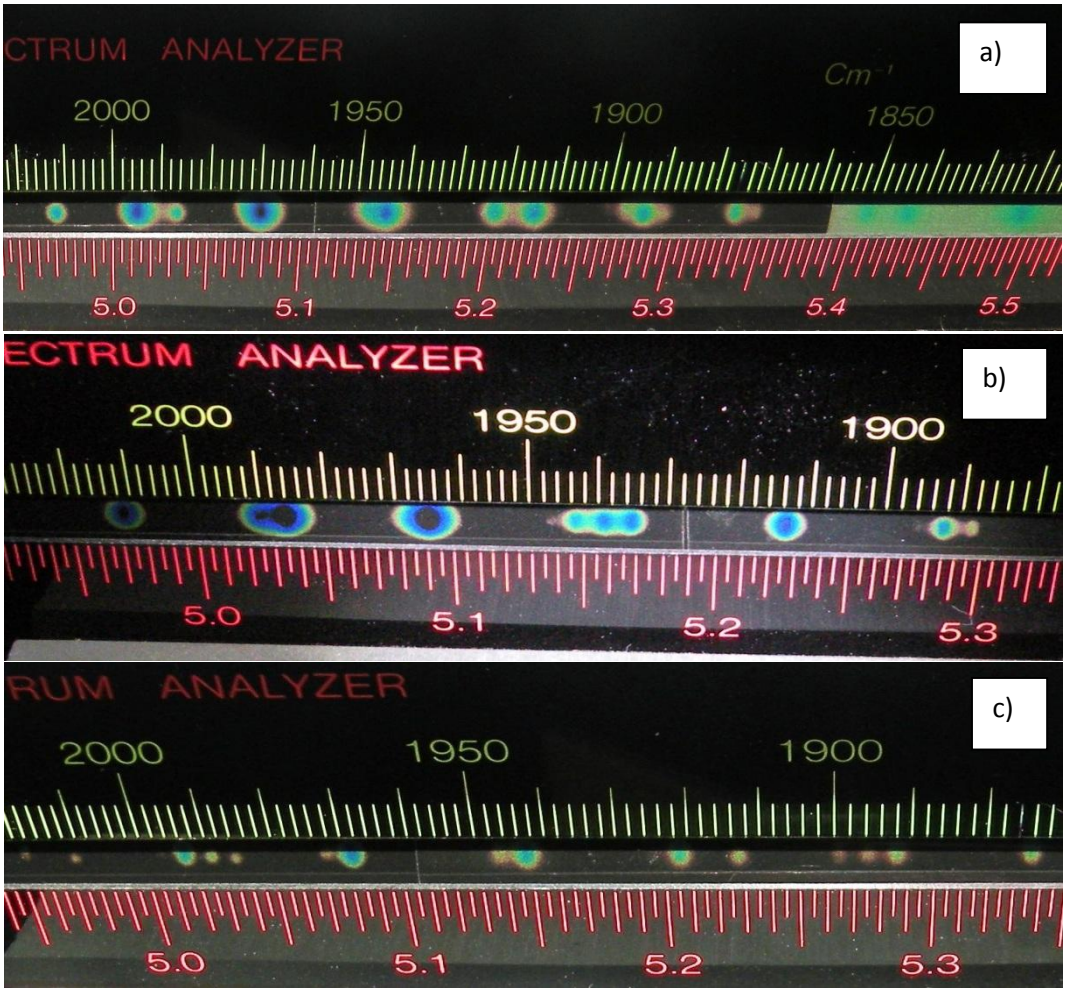

Figure 4.8. CO spectrum analyzer screen shots of the emission spectra in the 5 micron region from the LN_2 cooled CO_2-N_2-He gas discharge for a) 85%, b) 90% & c) 95% output couplers.

To be noted here that, under liquid nitrogen cooled conditions, lasing cannot occur in CO_2 molecules due to the following considerations. Given the freezing points of CO (68 K) and CO_2 (216 K) (to be noted, the freezing points of these gases are much lower at the actual operating pressures of ~few mbar owing to the phenomenon of 'depression in freezing point'), it is obvious that CO escapes condensation at the LN_2 temperature while most of the

CO_2 freezes on the walls of the discharge tube thus making the conditions unfavorable for laser emission from CO_2 gain medium while facilitating inversion in the CO medium. That the emission could be transmitted through a sapphire window bears testimony to the fact that lasing in the 5 micron region indeed occurred from CO gain medium. As mentioned, the frequencies at which lasing was experimentally observed and the corresponding known CO transitions are recorded in table 4.1.

Sl.no.	**Observed wavenumber (υ in cm^{-1}) from the spectrum analyzer screenshots of fig. 2**	**Corresponding wavelength (in µm) from the spectrum analyzer screenshots of fig. 2**	**1/ υ (µm)**	**Nearest corresponding CO Transition [4.5]**
85% OC				
1	2012	4.97	4.9702	5-4 P(7) [4.9724]
2	1995	5.0125	5.0125	5-4 P(11) [5.0123]
3	1986.5	5.033	5.0340	5-4 P(13) [5.0329]
4	1970	5.078	5.0761	6-5 P(11) [5.0780]
5	1948	5.135	5.1335l	7-6 P(10) [5.1348]
6	1944	5.145	5.144	7-6 P(11) [5.1452]
7	1922	5.2025	5.203	8-7 P(10) [5.2034]
8	1914	5.224	5.225	8-7 P(12) [5.2250]
9	1896	5.275	5.2743	9-8 P(10) [5.2738]
10	1892.5	5.2825	5.2840	9-8 P(11) [5.2847]

11	1889.5	5.2925	5.292	9-8 P(12) [5.2957]
12	1875	5.3325	5.3333	10-9 P(9) [5.3349]
13	1871.8	5.3425	5.3425	10-9 P(10) [5.3458]
14	1850	5.404	5.4054	11-10 P(9) [5.4085]
15	1842	5.4275	5.4259	11-10 P(11) [5.4309]
16	1820.5	5.4925	5.493	12-11 P(10) [5.4953]
90% OC				
1	2012	4.97	4.9702	5-4 P(7) [4.9724]
2	1990	5.026	5.0251	5-4 P(12) [5.023]
3	1986.5	5.035	5.0346	5-4 P(13) [5.033]
4	1965.1	5.091	5.0888	6-5 P(12) [5.0884]
5	1944	5.145	5.144	7-6 P(11) [5.1452]
6	1939	5.157	5.1573	7-6 P(12) [5.156]
7	1935	5.1675	5.1680	7-6 P(13) [5.167]
8	1922	5.206	5.203	8-7 P(10) [5.2034]
9	1914	5.226	5.225	8-7 P(12) [5.225]
10	1892.1	5.285	5.2851	9-8 P(11) [5.285]
11	1888.25	5.295	5.2959	9-8 P(12) [5.2957]
95% OC				
1	2018.5	4.953	4.9542	5-4 P(5) [4.9532]
2	2010.5	4.973	4.9739	5-4 P(7) [4.9724]
3	1993.2	5.017	5.0171	6-5 P(5) [5.0179]
4	1989.2	5.028	5.0271	6-5 P(6) [5.0276]
5	1985.6	5.036	5.0363	6-5 P(7) [5.0374]

6	1972	5.073	5.071	7-6 P(4) [5.0744]
7	1968.5	5.0825	5.080	7-6 P(5) [5.0840]
8	1946.5	5.139	5.137	7-6 P(10) [5.142]
9	1943	5.149	5.147	7-6 P(11) [5.145]
10	1921.5	5.205	5.204	8-7 P(10) [5.203]
11	1913	5.2275	5.2274	8-7 P(12) [5.225]
12	1899.5	5.264	5.2645	9-8 P(9) [5.263]
13	1895.6	5.275	5.2750	9-8 P(10) [5.273]
14	1892	5.286	5.2854	9-8 P(11) [5.285]
15	1874.2	5.3365	5.3356	10-9 P(9) [5.335]

Table 4. 1. Laser transitions observed in CO molecule as recorded by the CO spectrum analyzer.

4.5. Conclusions

The emission spectrum of a CW electric discharge CO laser operated with CO_2 laser mixture maintained at LN_2 temperature revealed cascaded lasing over 5 micron region that originated from the active CO species, formed in the discharge due to dissociation of CO_2 by electron impact. This presents a relatively clean and safe alternative method of generation of a coherent light in the 5 micron region as against a conventional CO laser that invariably makes use of toxic and hazardous CO gas. That the handling of the CO gas had been dispensed here assumes significance and we believe should be of interest to the community working in the field of gas lasers at large.

4.6. References

4.1. C. K. N. Patel, Interpretation of CO_2 Optical Maser Experiments, Phys. Rev. Lett., 12, 588 (1964).

4.2. C. K. N. Patel, Gas Lasers in Lasers, A series of Advances, Ed. A. K. Levine, Vol 2, Marcel Dekker Inc., New York (1968).

4.3. D. C. Tyte, Carbon Dioxide Laser, in Advances in Quantum Electronics, Ed. D. W. Goodwin, Vol 1, Academic Press, NewYork (1970).

4.4. A. J. Demaria, Review of CW High Power CO_2 Lasers, Proc. IEEE, 61, 731 (1973).

4.5. P. K. Cheo, Emission Spectra Of Molecular Lasers, in Hand book of Molecular Lasers, Ed. P. K. Cheo, Marcel Dekker Inc., New York (1987).

4.6. W. W. Duley, CO_2 lasers: Effects and Applications, Academic Press, New York (1976).

4.7. W. J. Witteman, The CO_2 Laser, Springer Series in Optical Sciences, Springer-Verlag (1987).

4.8. Robert S. Freund, Dissociation of CO_2 by Electron Impact with the Formation of Metastable CO($a^3\Pi$) and O(^5S), The Journal of Chemical Physics, 55, 3569 (1971).

4.9. C. K. N. Patel and R. J. Kerl, Laser Oscillation on X1Σ+ Vibrational-Rotational Transitions of CO, Appl. Phys. Lett., 5, 81 (1964).

4.10. Mani L Bhaumik, Characteristics of a CO Laser, IEEE Journal of Qunatum Electronics, QE-8, No. 52 (1972).

4.11. Physics and spectroscopic applications of carbon monoxide lasers, a review, Wolfgang Urban, Infrared Physics and Technology, 36 (1), 465-473 (1995).

4.12. https://www.laserfocusworld.com/articles/print/volume-51/issue-06/world-news/gas lasers-carbon-monoxide-laser-aims-at-high-power-applications.html.

4.13. Applications of a carbon monoxide laser in surgery, V. S. Aleinikov et al, Sov. J. Quantum Electron. 13(10), 1304 (1983).

4.14. Laser coronary angioplasty using carbon monoxide lasers, T. Arai, M. Nakagawa, M. Kikuchi, K. Mizuno, K. Arakawa, T. Shibuya, K. Satomura, Proceedings of the Annual International Conference of the IEEE Engineering in Medicine and Biology Society, New Orleans, LA, USA, USA (1988).

4.15. https://www.laserfocusworld.com/articles/print/volume-53/issue08/worldnews/medical-lasers-carbon-monoxide-laser-shows-surgical-potential.html.

4.16. Jeff W Eerkens, Separation of Isotopes by Laser-Assisted Retardation of Condensation (SILARC), Laser and Particel Beams, 16, 295-316 (1998).

4.17. J W Eerkens, Spectral Considerations in the Laser Isotope Separation of Uranium Hexafluoride, Applied Physics, 10, 15-31 (1976).

4.18. Igor Y Baranov et. al., Mode-Locked CO Laser for Isotope Separation of Uranium Employing Condensation Repression, Advances in Optical Technologies, Article ID 693530, Volume 2010 (2010).

4.19. H. J. Seguin et. al., Sealed Room Temperature CO-CO_2 Laser Operating at 5 or 10 μm, App. Phys. Lett., 20, 435-438 (1972).

4.20. W. E. Boney et. al., CO and CO_2 laser action by organic molecule oxidation, IEEE J. Quantum Electron., QE-6, 246-247 (1973).

4.21. J. D. Barry et. al., Simultaneous CO and CO_2 laser, IEEE Journal of Quantum Electronics, QE-6, No. 7 (1973).

4.22. C. K. N. Patel, Vibrational-Rotational Laser Action in CO Molecule, Physical Review, 141 (No. 1), 71-83 (1966).

4.23. Wolfgang Urban, Physics and Spectroscopic Applications of Carbon Monoxide Lasers: A Review, Infrared Phys. Technology, 36 (No. 1) 465-473 (1995).

Chapter 5: Development of a 10 μm Coherent Source and its Application in Sulfur Isotope Enrichment by Laser Assisted Aerodynamic Process

5.1. Introduction

As has been described in chapter 1, laser assisted aerodynamic separation process has been elegantly demonstrated in the separation of sulfur isotopes [5.1-5.3], wherein, the emission from a line tunable CO_2 laser caused vibrational excitation of one of the isotopes in the SF_6 gas. The unexcited isotopic species condenses in the supersonically cooled jet while vibrationally excited species is prevented from forming clusters leading to an increased relative mass difference. The intrinsic advantage derived from the repression of condensation of the laser excited isotopic molecule in the expanding gas jet makes it compatible for enriching both heavier and lighter masses [5.4-5.7] and has therefore gained recent attention [5.8-5.9]. Also as discussed in the introductory chapter, the gas mixture is diluted with an inert gas e.g., Argon, to prevent the transfer of excitation from the resonant to the non-resonant species that can otherwise lead to scrambling of selectivity. The advantage of this scheme over the conventional molecular laser isotope separation processes stems from the fact that a single-step vibrational excitation is enough to inhibit cluster formation. The requirement on the laser power is therefore not stringent here as is in case of MLIS based on classical multi-photon dissociation route.

As a precursor to demonstrating and characterizing Sulfur enrichment in our lab, computational modeling of the supersonic flow for determination of various parameters in the jet has been carried out. The existing analytical expressions for isentropic fluid flow facilitate estimation of various flow parameters along the jet axis. Estimation of these parameters in the radial direction however is not straightforward. CFD simulations help overcome these

limitations. To be noted, CFD modeling is valid only in the collision dominated continuum regime of the flow, and, in free-jet expansion, the flow near the nozzle is in the continuum regime and hence collision dominated. To this end, computation of the axial and radial jet parameters following the nozzle expansion from a circular orifice of 100 μm diameter has been attempted. Further, during supersonic nozzle expansion, the random thermal energy of the flow is converted to directional kinetic energy. The resulting low temperature environment facilitates cluster formation. To characterize the cluster formation, a low pressure environment where the interference with the background gas is minimal is desired. To circumvent the pumping constraints of such systems, it becomes necessary to work with micro jets. However, their small size makes experimental investigation challenging. Computational methods here too work as a guide for such investigations and can be of immense help in understanding the processes as well as for generating the data for process optimization [5.10-5.16]. We studied the extent of clustering in the case of SF_6-Argon jet experimentally by measuring the absorption at different downstream distances and comparing it with the values obtained computationally. Following this, the demonstration and characterization of Sulfur enrichment in SF_6-Ar binary gas mixture by laser assisted aerodynamic separation route employing a CW-CO_2 laser has been discussed. The separation efficiency has been studied as a function of the molar concentration of SF_6 in the gas mixture and the stagnation pressure by employing a single longitudinal mode (SLM), line tunable CW-CO_2 laser, developed in-house, capable of delivering output power up to 14 W. The working principles and operational characteristics of this laser have been discussed in detail in this chapter. It is of interest to note that, we made use of 10P(20) line of CO_2 laser emitting on 944.2 cm^{-1} for the selective excitation of $^{32}SF_6$ even though it is red-shifted with respect to its absorption centre by ~3.5 cm^{-1} [5.17]. The efficient multi-photon excitation observed in this case has been attributed to the red-shifted nature of the incident radiation that facilitates

enhancement in the obtainable separation factor. Also, towards estimation of separation factor, a novel method based on optical absorption technique has been conceived and demonstrated, wherein, the knowledge of the absorption cross-sections of the molecule for the incident laser line is rendered unessential. The separation factor obtained by this technique corroborates well with that obtained by mass spectrometric measurements.

5.2. Development of a Longitudinally Excited, Continuous Wave, Tunable CO_2 Laser

Lasing action from a CO_2 molecule has been deliberated in detail in section 2.2 of chapter 2. The setup of the CW-CO_2 laser comprises of a double-walled cylindrical glass tube (length 112 mm, thickness 2 mm) filled with the lasing gas mixture, usually a mixture of CO_2, N_2 and

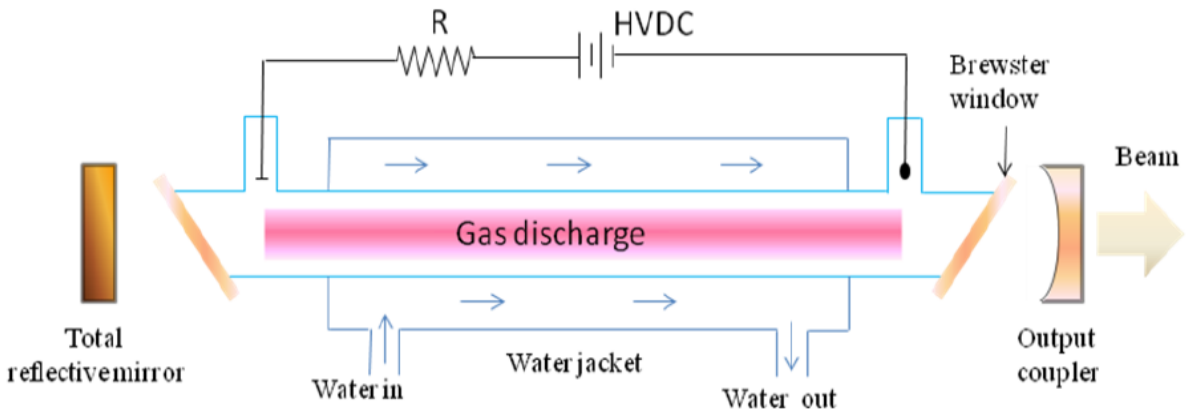

Figure 5.1. Schematic of a CW CO_2 laser.

He in the ratio 2:2:8 at an operating pressure of ~10 mbar. The schematic of the experimental set-up is shown in figure 5.1. The electrodes for energizing the gas medium are located in the side arms. The active medium is pumped by a steady electrical glow discharge along the length of the optical axis with water circulating in the outer jacket for removing the heat of the discharge. The CO_2, N_2 molecules are excited by collisions with free electrons formed in the discharge giving rise to optical gain (population inversion). The desired pressure was maintained in the discharge tube by means of controlling the gas flow employing rotameters in conjunction with a rotary pump. The typical required DC voltages are ~15 kV per meter of the discharge tube length with the DC current being few tens of milli-amperes. In order to

maintain a stable discharge inside the tube, a ballast resistor is connected in series with the high voltage power supply. This compensates for the differential negative impedance characteristics of gas discharge and limits the discharge current thereby preventing arcing. AR coated ZnSe window seals one end of the discharge tube while a Brewster window seals the other end. A simple plano-concave optical resonator with two mirrors located on either ends of the discharge tube is used to provide continuous laser oscillation on various ro-vibrational lines [5.17].

5.2.1. Experimental Work

The AutoCAD drawing used for fabrication of the CW-CO_2 laser is shown in figure 5.2. The gain medium is energized by means of a glow discharge generated by a high voltage DC power supply (60 KV, 30 mA). As discussed, water circulating in the outer cylindrical region

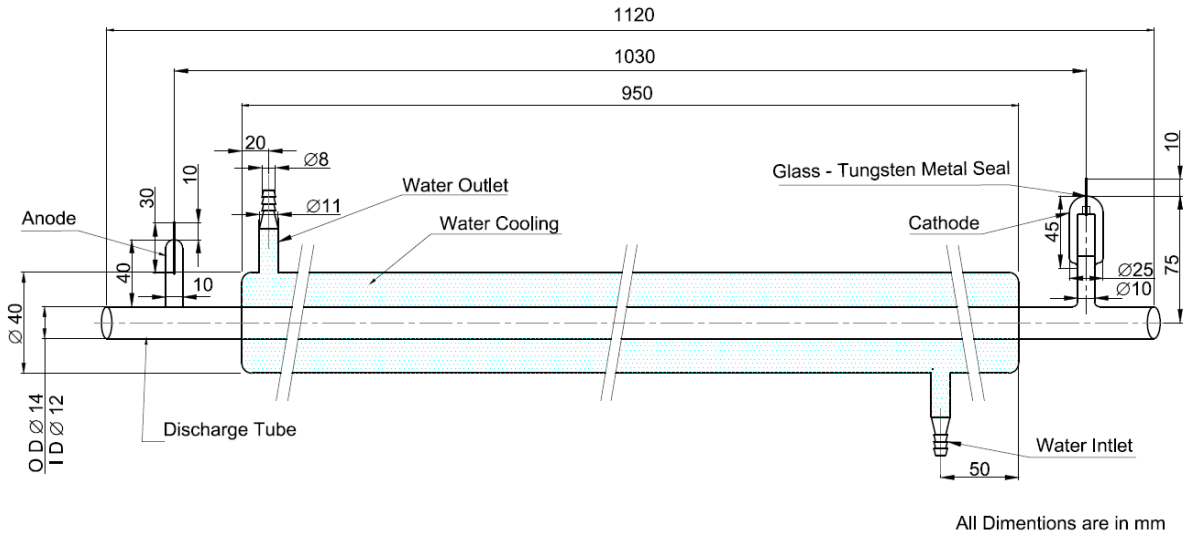

Figure 5.2. Auto CAD drawing used in fabrication of CW CO_2 laser tube.

(outer diameter ~40 mm) cools the heated gas mixture and facilitates efficient laser action. The laser resonator, the crucial device that provides the necessary feedback, comprises of a 100% reflective diffraction grating (blazed for 9 μm) placed at one end of the discharge tube and a 10 m ROC, 70% reflective AR coated ZnSe mirror as the output coupler forms the other extreme that eventually couples the laser beam output. The grating enables selective

tuning over the desired laser lines on P and R branches of the 9 to 11 μm bands. The invar stabilized cavity was placed on a vibration isolation table to ensure stable, uniform power output. A photograph of the CW-CO_2 laser in operation is shown in figure 5.3.

The operational characteristics of the laser have been studied in detail towards optimizing its performance by way of varying the discharge current, total pressure and partial pressures of the gas mixture. The results of these studies detailed as below facilitated obtaining optimum laser output power.

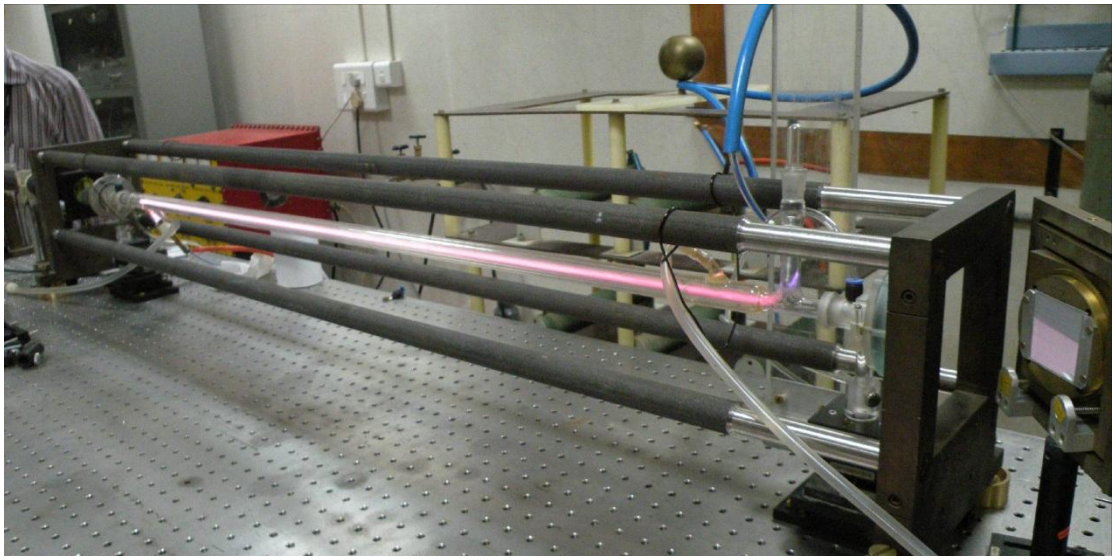

Figure 5.3. Experimental Setup of the CW-CO_2 laser.

5.2.1.1. Variation of the Laser Output with the Discharge Current

The discharge striking voltage depends on the inter-electrode distance, the pressure and the gas composition that in turn also influences the laser output power. Figure 5.4 shows the variation of laser output power as a function of discharge current for different total pressures. Also shown in figures 5.4 a, b, c & d, is the power output obtained for different partial pressures (composition) of the CO_2, N_2, He gases for the same total pressure. The power output here is seen to increase, stabilize and eventually fall with increasing current. The initial rise is due to an increasing number density of the electrons that result in increased excitation and hence higher population inversion. Followed by this, the laser power remains

flat over a significant range of the current, because of the rise in excitation due to the increase in electron number density being negated by a comparable loss of power due to heating of the gas mixture. Beyond this, heating starts dominating and laser output power eventually drops with increasing current.

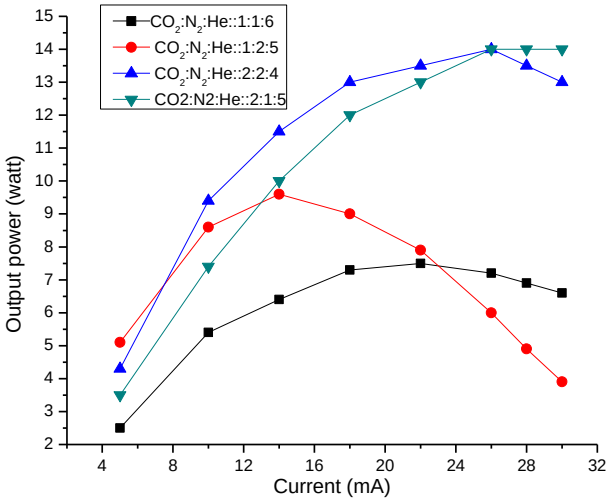

(a) Laser output vs. Current at 8 mbar.

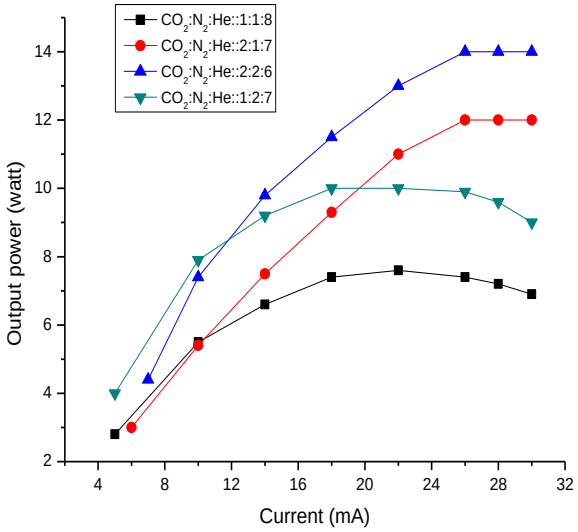

(b) Laser output vs. Current at 10 mbar

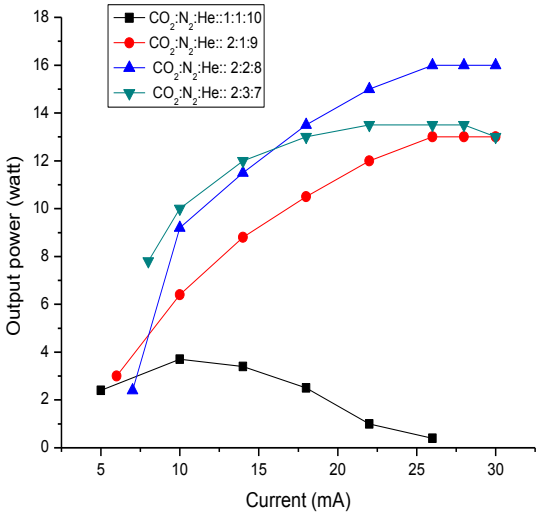

(c) Laser output vs. Current at 12 mbar.

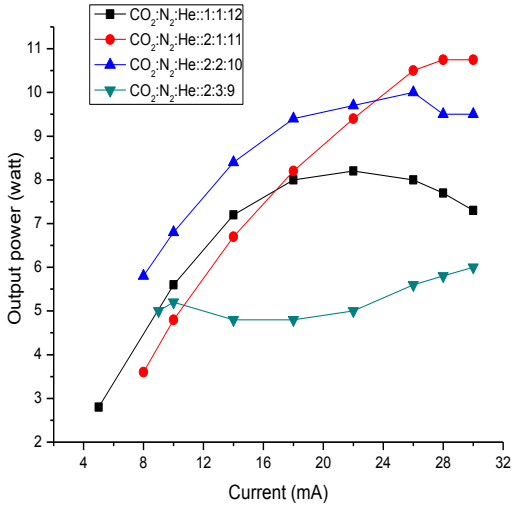

(d) Laser output vs. Current at 14 mbar.

Figure 5.4. Plots of variation of laser output power vs. current for different operating pressures.

5.2.1.2. V-I Characteristics

The basic operational characteristic of a gas discharge is its V-I characteristic for a given operating pressure and composition of the gas. This variation of the voltage across the discharge versus current in the active medium for a certain gas composition of $CO_2 : N_2 : He :: 2 : 2 : 8$ is shown in figure 5.5. The negative dynamic impedance of the discharge, i.e., reduction in voltage across the discharge with increase in the discharge current is apparent from the figure and is found to be 83.3 KΩ. In the absence of a current limiting device in series with the discharge, any instability leading to increase in current would re-generatively convert the glow discharge into an arc characterized by very large currents, excessive heating and ionization, that would inhibit laser action. Thus a ballast resistor, R (figure 1.1) is normally employed in the operation of a CW-CO_2 laser as a current limiter.

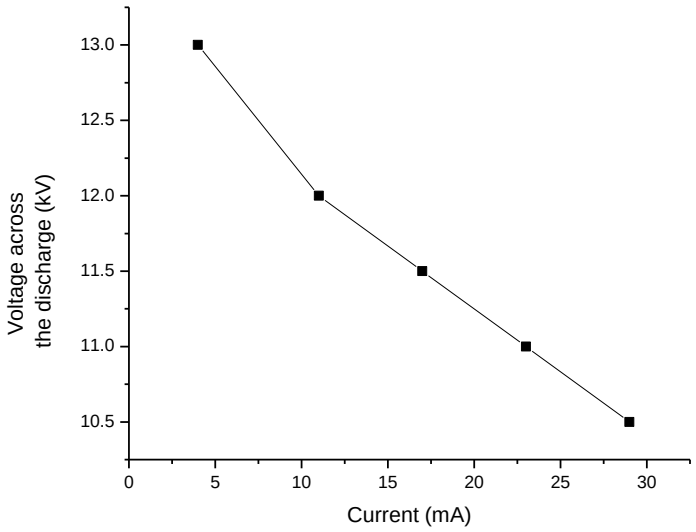

Figure 5.5. Voltage across the discharge versus current.

The voltage across the discharge is given by, $V_{discharge} = V_o - I R$.

5.2.1.3. Line tuning of the CW-CO_2 Laser

It is well-known that, laser action on a selected ro-vibrational transition, out of the broad mid-IR emission spectra of CO_2 is useful in spectroscopy, pumping other molecular gas lasers, photo-chemistry and numerous other applications. The CW-CO_2 laser described here can deliver output powers typically ~few Watts on SLM (single longitudinal mode), TEM_{00} mode when grating tuned over various ro-vibrational transitions spanning over the CO_2 emission

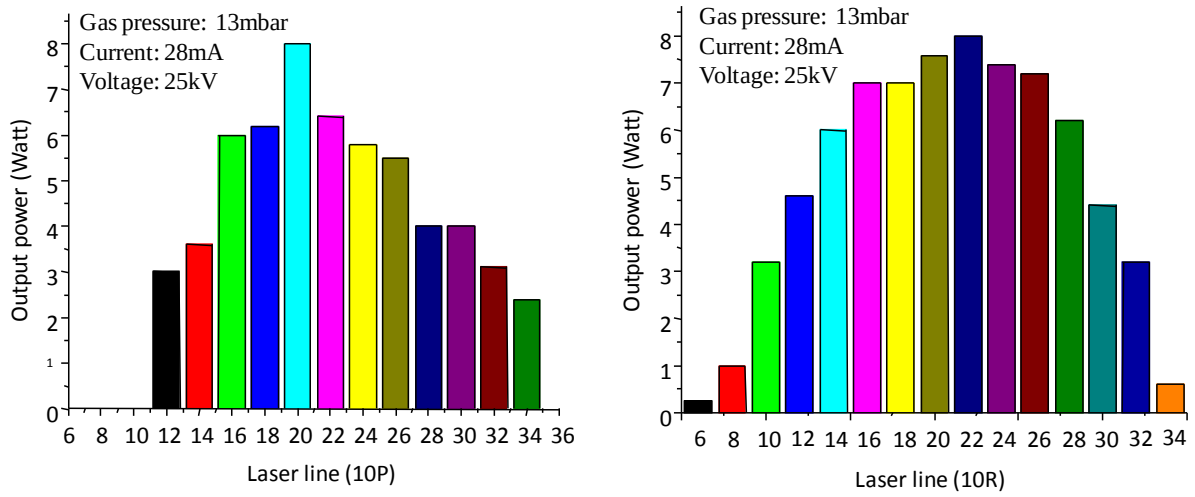

Figure 5.6. Output Power of different laser lines of 10P and 10R branch of the CO_2 line spectrum.

spectrum. A ruled diffraction grating (110 lines/mm), blazed for 9 µm in first order mounted in Littrow configuration and a concave output coupler (10 m ROC, 70% R) formed the resonator cavity. Lasing on a number of lines in the P and R branches of 10.6 µm transitions were obtained as the grating was tuned, and, the measured output powers are depicted graphically in figure 5.6. The grating being blazed for 9 µm, the diffraction efficiency is understandably higher for 10R lines as compared to the 10P lines.

5.3. Characterization of SF_6-Ar Binary Gas Jet by the Line Tunable CW-CO_2 laser

As discussed in the introductory chapter, polyatomic molecules seeded in an inert carrier gas subjected to supersonic nozzle expansion communicate with the low temperature bath provided by the monatomic carrier gas via two body collisions resulting in the relaxation of

their translational, vibrational and rotational degrees of freedom. The extremely low temperature bath promotes formation of weakly bound Van der Waals clusters in the jet. Selective condensation repression of a desired isotope in such dynamically cooled jets by infrared vibrational excitation forms the basis for realizing isotope enrichment [1-4]. Estimation of the onset point of cluster formation downstream the nozzle and cluster densities itself is crucial to the success of laser assisted aerodynamic separation. To this end, we have undertaken the study of cluster characterization of SF_6-Ar gas jet by way of conducting absorption measurements across the jet with a line tunable narrow spectral width CW-CO_2 laser tuned to selectively excite the abundant species. This allowed the determination of molecular number densities in the jet at various nozzle downstream distances in the free-jet. The same were compared with the number densities obtained computationally using isentropic relations of compressible fluid flow that basically do not take into consideration the clustering in the jet. The departure in the results of the number densities, arrived at experimentally, from that obtained computationally was attributed to clusterization/condensation in the jet.

Prior to the jet characterization experiments, CFD simulations towards predicting the axial variation of jet parameters viz., Mach number, temperature, pressure, number density, velocity etc., in the supersonic free-jet of pure Argon gas expanding from a circular orifice of 100 μm have been undertaken. The same have been compared with those evaluated analytically from relations of compressible fluid flow and the results validated. We first begin with the CFD simulations of nozzle flow for case of pure Argon, presented in the following section.

5.3.1. CFD Simulations of Nozzle flow for case of Pure Argon

CFD simulations towards computing various jet parameters in the free-jet expansion of pure Argon have been undertaken. The meshing of the source chamber containing the gas mixture, the nozzle region and the jet chamber into which the gas expands has been carried out using GAMBIT 6.0 as shown in figure 5.7. The magnified view of the same with a zoomed view of the nozzle can be seen in figure 5.8. FLUENT 13.0 has been used for the simulation studies.

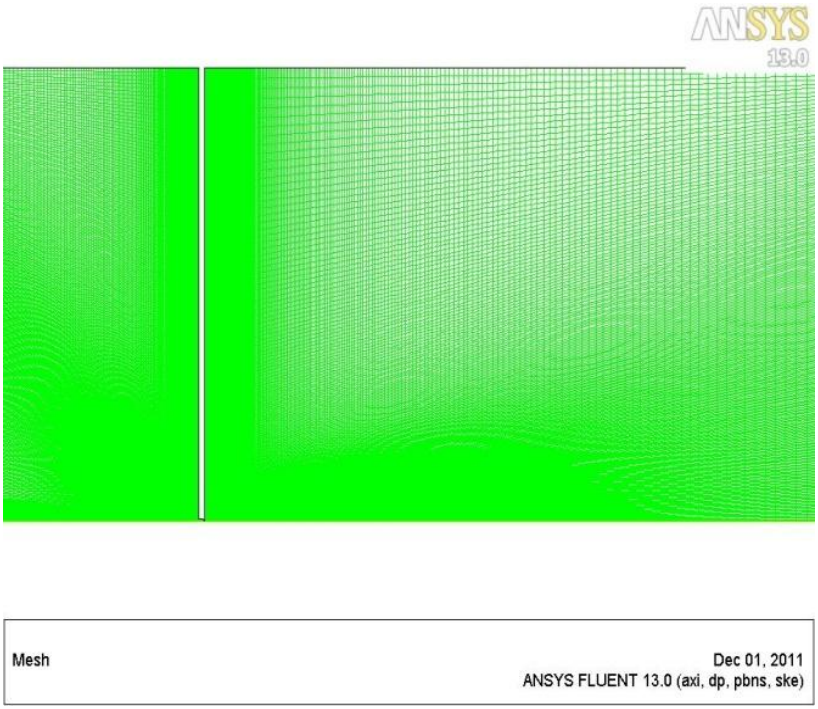

Figure 5.7. Meshing of the 75 µm nozzle, the stagnation and the expansion chamber.

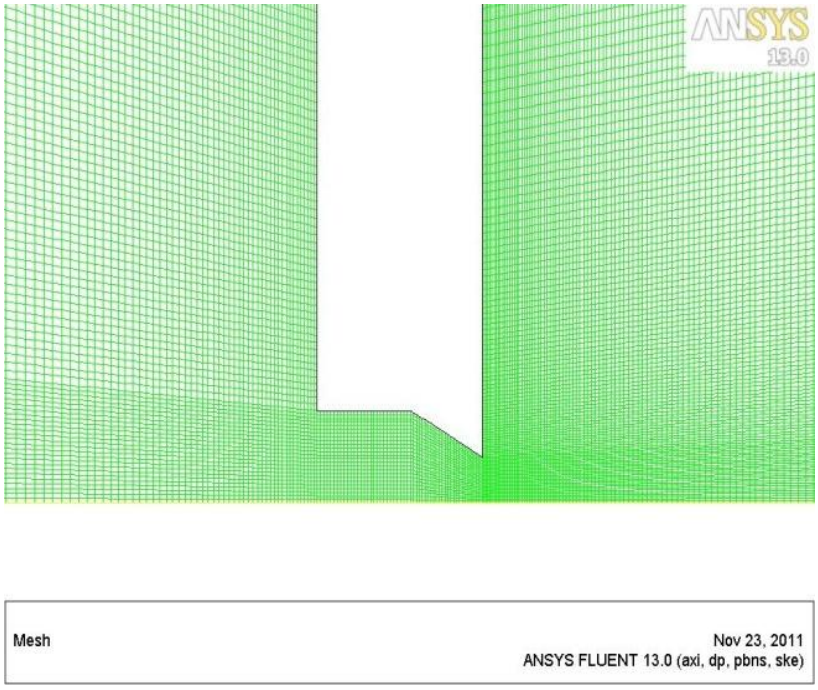

Figure 5.8. Magnified view of the meshing near the nozzle.

Argon gas at 3 bar (abs), 300 K stagnation conditions, was made to expand isentropically from

a 100 μm orifice into a vacuum of 10^{-2} mbar. Figures 5.9 to 5.14 show the plots of the axial variation of flow parameters along the nozzle jet centerline while the radial variation is shown in the form of contours in figures 5.15 to 5.18.

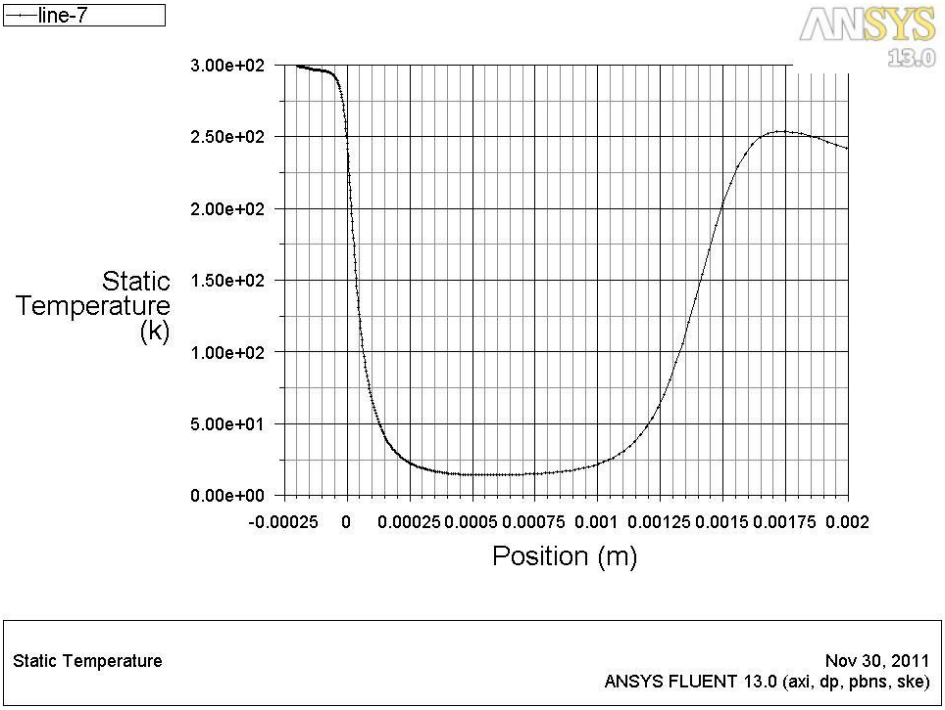

Figure 5.9. Plot of static temperature along the nozzle axial downstream distance.

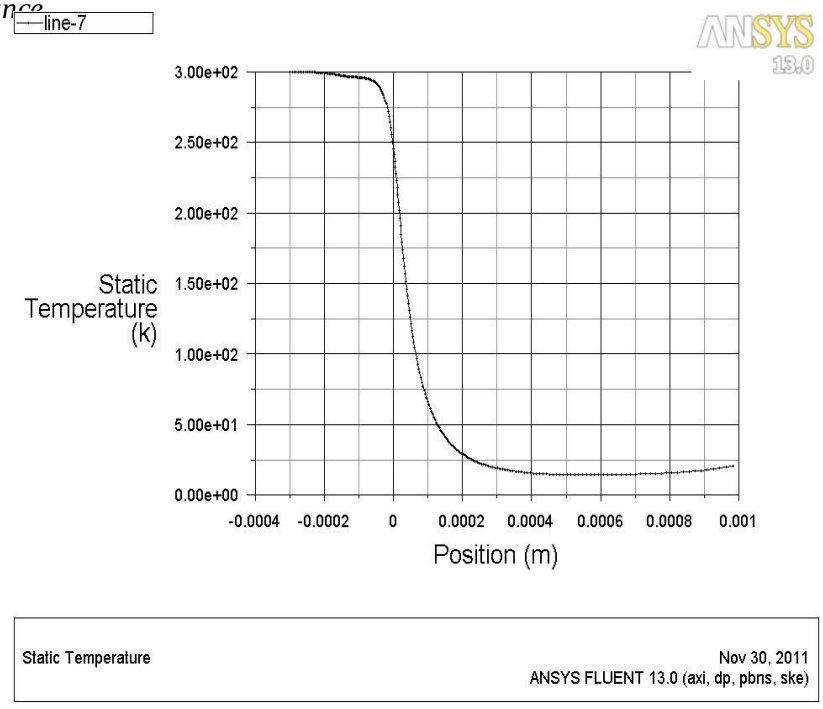

Figure 5.10. Magnified view of plot of static temperature along the nozzle axial downstream distance.

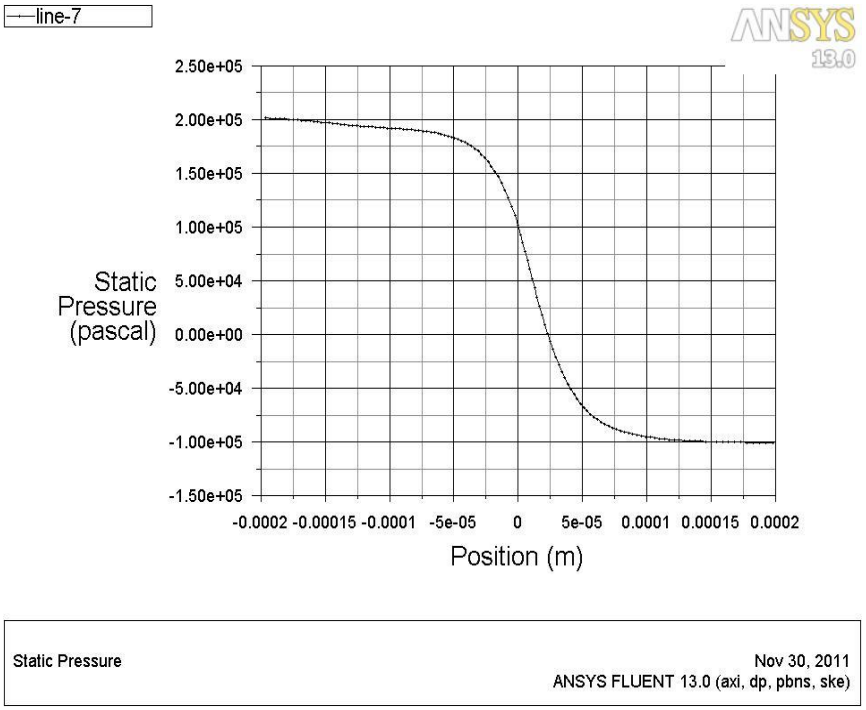

Figure 5.11. Plot of static pressure along the nozzle axial downstream distance. To be noted, the static pressure shown is the gauge pressure and not the absolute pressure ($P_{absolute} = P_{gauge} + 1\ Atm$).

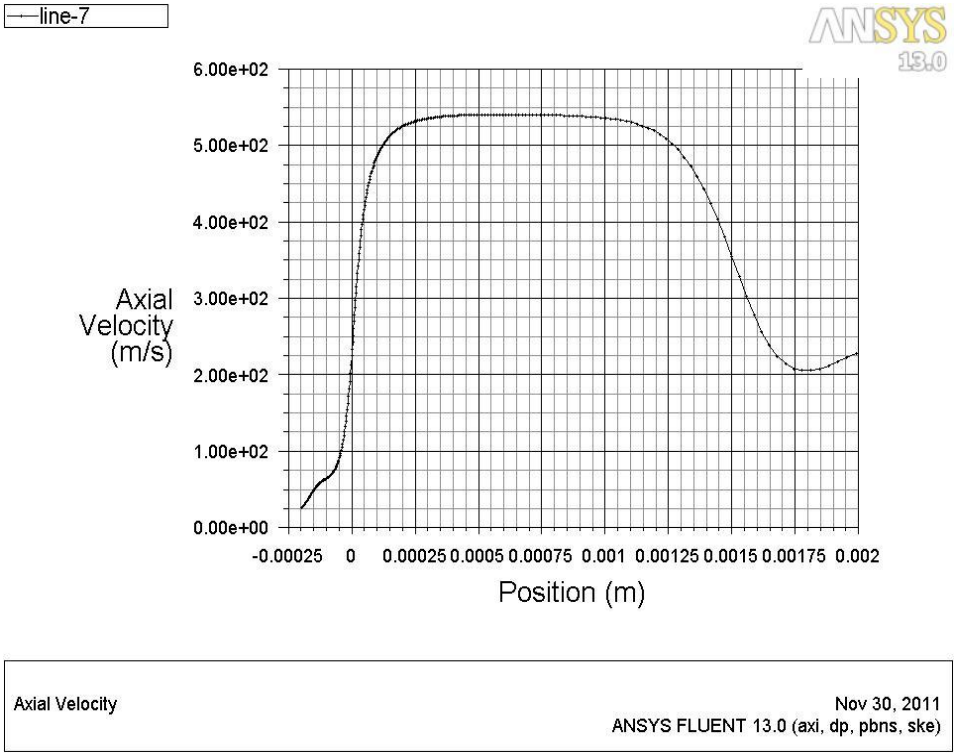

Figure 5.12. Plot of axial velocity along the nozzle axial downstream distance.

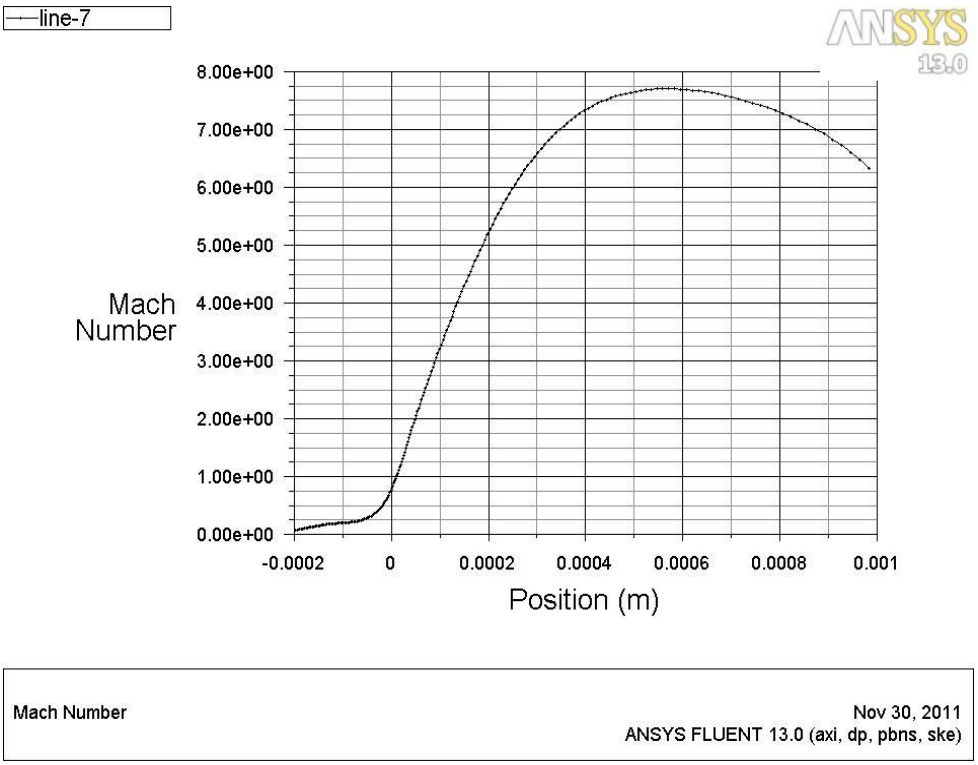

Figure 5.13. Plot of Mach number along the nozzle axial downstream distance.

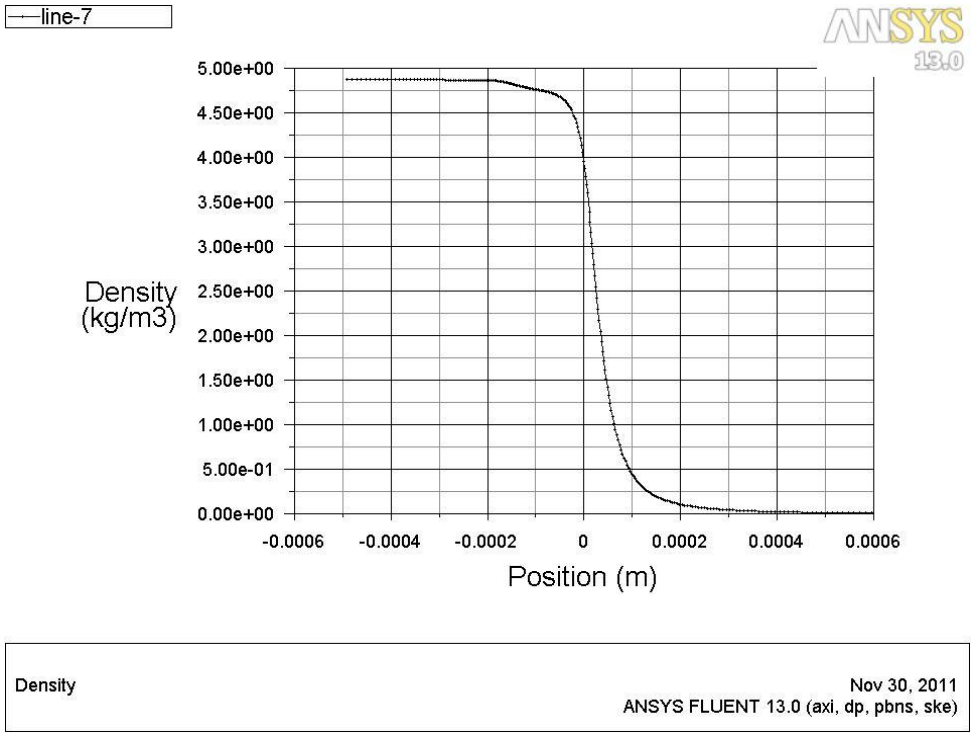

Figure 5.14. Plot of density along the nozzle axial downstream distance.

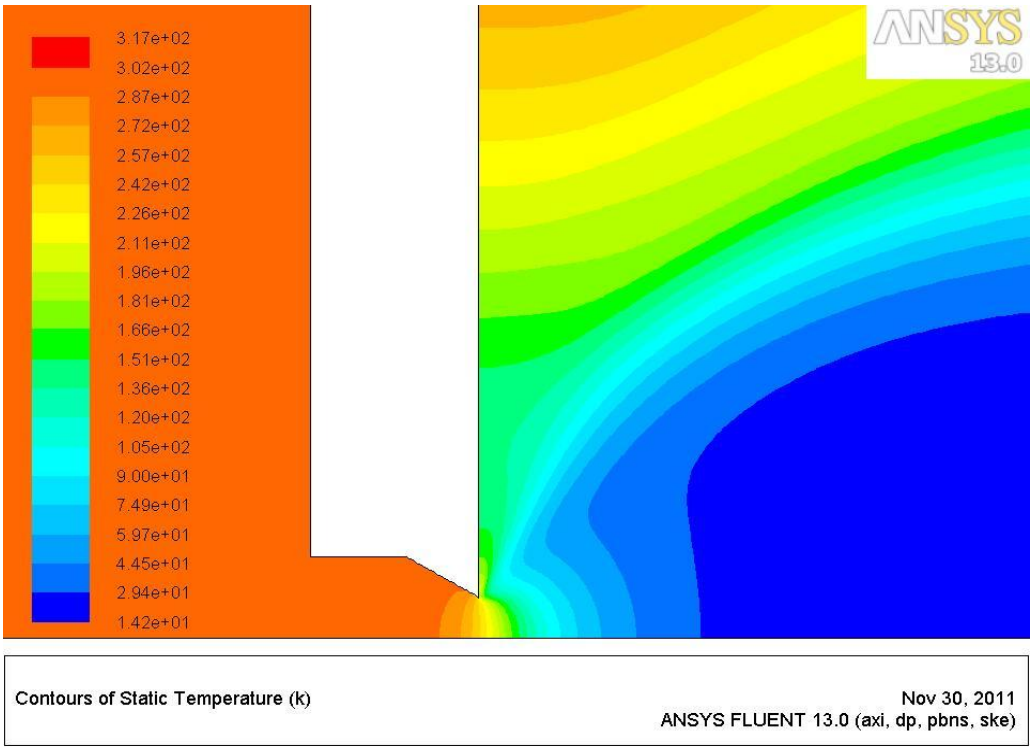

Fig 5.15. Contour of static temperature along the nozzle axial downstream distance and radial direction.

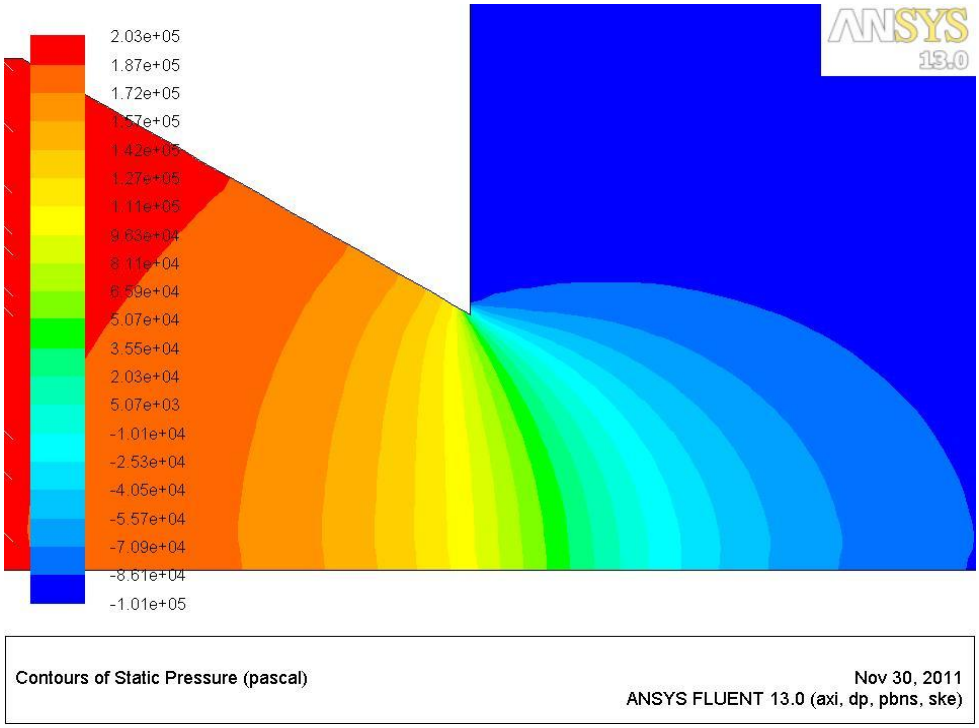

Figure 5.16. Contour of static pressure along the nozzle axial downstream distance and radial direction.

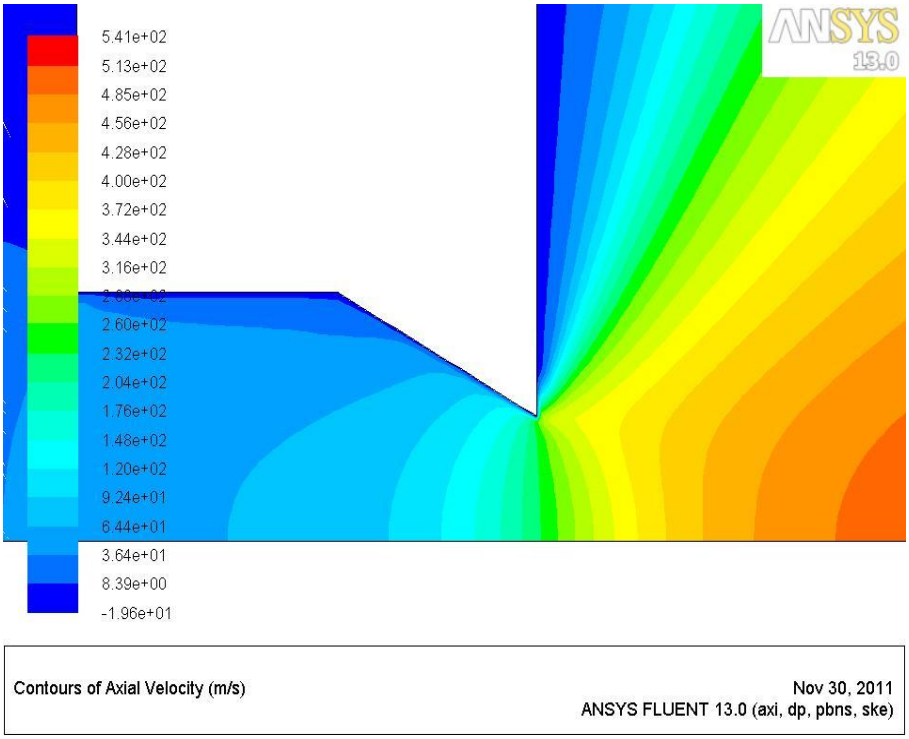

Figure 5.17. Contour of axial velocity along the axial nozzle downstream distance and radial direction.

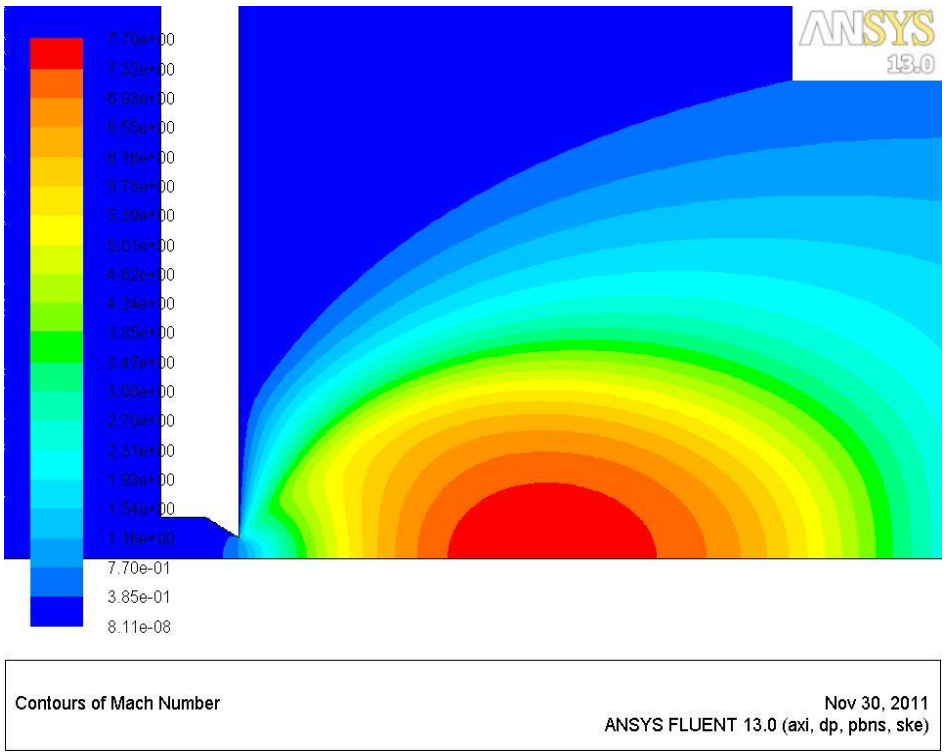

Fig 5.18. Contour of Mach number along the nozzle axial downstream distance and radial direction.

5.3.2. Evaluation of Nozzle Flow Parameters using Analytical Expressions of Compressible Fluid Flow for case of Pure Argon

By employing the isentropic relations for compressible fluid flow as elaborated in section 1.6.2 of chapter 1, the variation of Mach number, temperature, pressure, number density and velocity have been arrived at analytically for case of flow of pure Argon. In the region of free-jet expansion, the variation of Mach number, M, as a function of distance from the orifice, along the flow axis, can be computed from the formulae discussed in section 1.6.5 of chapter 1. Once M is known, all other flow parameters in the supersonic jet can be computed. The various input parameters required towards arriving at these are as shown in table 5.1. Table 5.2 enumerates the different flow parameters arrived at analytically.

T_0	300 K
P_0	3000 torr
n_0	9.53×10^{19}/cc
Gamma, γ	1.67
T*	224.72 K
P*	1460.006 torr
n*	6.19×10^{19} /cc
V*	279.2767 m/s
$V_{Terminal}$	557.5341 m/s

Table 5.1. Input parameters for evaluating the various flow parameters following a supersonic expansion from a 100 μm nozzle for case of pure Argon.

5.3.3. Validation of the Results Obtained by CFD with those obtained by Analytical methods for case of Argon

From sections 5.3.1 and 5.3.2, it is clear that the results predicted by CFD simulations in the jet upstream of Mach disk (figures 5.9 to 5.18) are in excellent agreement with those predicted analytically. That the pressure at the nozzle exit equals $P_o/2$ by both computational and analytical methods is a testimony to the accuracy of the results predicted by CFD. Analytical formulae assume absence of shock and thus beyond the region of Mach disk location, values predicted by them cannot be compared with CFD values. The randomization of the flow properties owing to the onset of shock in the supersonic jet beyond a certain

nozzle downstream distance (0.001 m = 1000 micron), thus frittering the advantages of the supersonic jet properties, is obvious from the CFD simulations plots of temperature (figures 5.9) and Mach number (figure 5.13).

x/D	D(mm)	x(mm)	M	T(K)	P(torr)	n(#percc)	v(m/s)
0.001	0.1	0.0001	1.000003	224.7187	1459.999	6.19E+19	279.2893
0.005	0.1	0.0005	1.000083	224.7097	1459.854	6.19E+19	279.306
0.01	0.1	0.001	1.000332	224.6816	1459.399	6.19E+19	279.3581
0.02	0.1	0.002	1.001322	224.57	1457.591	6.19E+19	279.5652
0.03	0.1	0.003	1.002962	224.3851	1454.602	6.18E+19	279.9075
0.05	0.1	0.005	1.00815	223.8	1445.167	6.15E+19	280.9884
0.08	0.1	0.008	1.020568	222.3998	1422.735	6.1E+19	283.5583
0.09	0.1	0.009	1.025906	221.798	1413.159	6.07E+19	284.6556
0.1	0.1	0.01	1.031829	221.1305	1402.583	6.04E+19	285.8679
0.15	0.1	0.015	1.069882	216.8481	1335.855	5.87E+19	293.5262
0.2	0.1	0.02	1.121152	211.1057	1249.416	5.64E+19	303.4924
0.25	0.1	0.025	1.184484	204.0808	1148.344	5.36E+19	315.2562
0.3	0.1	0.03	1.258723	195.98	1038.072	5.05E+19	328.2988
0.35	0.1	0.035	1.342712	187.0367	923.9882	4.71E+19	342.1209
0.4	0.1	0.04	1.435296	177.5017	811.0079	4.35E+19	356.2673
0.45	0.1	0.045	1.535319	167.6293	703.2006	4E+19	370.3453
0.5	0.1	0.05	1.641625	157.6622	603.5622	3.65E+19	384.0352
0.55	0.1	0.055	1.822421	142.0046	465.0484	3.12E+19	404.6067
0.6	0.1	0.06	1.937063	132.9203	394.398	2.83E+19	416.076
0.65	0.1	0.065	2.0492	124.65	336.0433	2.57E+19	426.2494
0.7	0.1	0.07	2.159549	117.0813	287.4657	2.34E+19	435.3514
0.75	0.1	0.075	2.268486	110.1354	246.8218	2.14E+19	443.54
0.8	0.1	0.08	2.376209	103.7511	212.6873	1.95E+19	450.9355
0.85	0.1	0.085	2.482826	97.87664	183.9272	1.79E+19	457.6349
0.9	0.1	0.09	2.588394	92.46625	159.6213	1.65E+19	463.7193
0.95	0.1	0.095	2.692945	87.47877	139.0173	1.51E+19	469.2584
1	0.1	0.1	2.7965	82.87663	121.4976	1.4E+19	474.312
1.1	0.1	0.11	3.000683	74.69427	93.76539	1.2E+19	483.1667
1.2	0.1	0.12	3.201052	67.67953	73.33094	1.03E+19	490.6306
1.3	0.1	0.13	3.397724	61.63434	58.07698	8.98E+18	496.9729
1.4	0.1	0.14	3.590831	56.39614	46.54344	7.87E+18	502.4038
1.5	0.1	0.15	3.780517	51.83206	37.71419	6.93E+18	507.0884
1.6	0.1	0.16	3.96693	47.83363	30.87465	6.15E+18	511.1571
1.7	0.1	0.17	4.150219	44.31219	25.5167	5.49E+18	514.7139
1.8	0.1	0.18	4.330531	41.19508	21.27484	4.92E+18	517.8418
1.9	0.1	0.19	4.508009	38.42254	17.88315	4.44E+18	520.6082
2	0.1	0.2	4.682786	35.94518	15.14595	4.02E+18	523.0677
2.1	0.1	0.21	4.854993	33.722	12.9177	3.65E+18	525.265
2.2	0.1	0.22	5.024749	31.7188	11.08899	3.33E+18	527.2371
2.3	0.1	0.23	5.192169	29.90688	9.576758	3.05E+18	529.0145

2.4	0.1	0.24	5.35736	28.26206	8.317326	2.8E+18	530.6229
2.5	0.1	0.25	5.520422	26.76386	7.26144	2.59E+18	532.0837
2.6	0.1	0.26	5.735026	24.96188	6.103374	2.33E+18	533.8353
2.65	0.1	0.265	5.819502	24.30072	5.708362	2.24E+18	534.4766
2.7	0.1	0.27	5.90333	23.66954	5.345935	2.15E+18	535.088
2.75	0.1	0.275	5.986528	23.06645	5.012848	2.07E+18	535.6716
2.8	0.1	0.28	6.069115	22.48969	4.706234	1.99E+18	536.2291
2.85	0.1	0.285	6.15111	21.93766	4.423552	1.92E+18	536.7622
2.9	0.1	0.29	6.232529	21.40887	4.162544	1.85E+18	537.2723
2.95	0.1	0.295	6.313389	20.90196	3.921203	1.79E+18	537.7609
3	0.1	0.3	6.393704	20.41564	3.697736	1.73E+18	538.2292
3.05	0.1	0.305	6.473489	19.94876	3.490542	1.67E+18	538.6784
3.1	0.1	0.31	6.552759	19.50021	3.298188	1.61E+18	539.1097
3.15	0.1	0.315	6.631526	19.069	3.119387	1.56E+18	539.5239
3.2	0.1	0.32	6.709803	18.65418	2.952983	1.51E+18	539.9221
3.25	0.1	0.325	6.787603	18.25487	2.797936	1.46E+18	540.3051
3.3	0.1	0.33	6.864937	17.87026	2.653306	1.41E+18	540.6737
3.35	0.1	0.335	6.941816	17.4996	2.518245	1.37E+18	541.0288
3.4	0.1	0.34	7.018251	17.14216	2.391986	1.33E+18	541.371
3.45	0.1	0.345	7.094253	16.79729	2.273834	1.29E+18	541.7009
3.5	0.1	0.35	7.16983	16.46437	2.163158	1.25E+18	542.0192
3.55	0.1	0.355	7.244993	16.14281	2.059383	1.22E+18	542.3265
3.6	0.1	0.36	7.319751	15.83207	1.961988	1.18E+18	542.6232
3.65	0.1	0.365	7.394113	15.53163	1.870497	1.15E+18	542.91
3.7	0.1	0.37	7.468086	15.24102	1.784475	1.12E+18	543.1872
3.75	0.1	0.375	7.54168	14.95978	1.703527	1.09E+18	543.4554
3.8	0.1	0.38	7.614901	14.68749	1.627287	1.06E+18	543.7149
3.85	0.1	0.385	7.687758	14.42374	1.555425	1.03E+18	543.9662
3.9	0.1	0.39	7.760258	14.16816	1.487633	1E+18	544.2095
3.95	0.1	0.395	7.832407	13.92039	1.423634	9.75E+17	544.4454
4	0.1	0.4	7.904214	13.6801	1.363168	9.5E+17	544.674
4.05	0.1	0.405	7.975683	13.44697	1.305998	9.26E+17	544.8957
4.1	0.1	0.41	8.046822	13.22069	1.251907	9.02E+17	545.1108
4.15	0.1	0.415	8.117637	13.00099	1.200693	8.8E+17	545.3195
4.2	0.1	0.42	8.188133	12.78759	1.152169	8.59E+17	545.5222
4.25	0.1	0.425	8.258317	12.58024	1.106164	8.38E+17	545.7191
4.3	0.1	0.43	8.328193	12.37869	1.062518	8.18E+17	545.9104
4.35	0.1	0.435	8.397769	12.18272	1.021086	7.99E+17	546.0964
4.4	0.1	0.44	8.467047	11.99211	0.981729	7.8E+17	546.2772
4.45	0.1	0.445	8.536035	11.80665	0.944322	7.62E+17	546.453
4.5	0.1	0.45	8.604736	11.62615	0.908747	7.45E+17	546.6241
4.55	0.1	0.455	8.673156	11.45042	0.874895	7.28E+17	546.7906
4.6	0.1	0.46	8.741299	11.27928	0.842664	7.12E+17	546.9528
4.65	0.1	0.465	8.80917	11.11255	0.811959	6.96E+17	547.1107
4.7	0.1	0.47	8.876772	10.95009	0.782694	6.81E+17	547.2645
4.75	0.1	0.475	8.944111	10.79174	0.754785	6.67E+17	547.4144

4.8	0.1	0.48	9.01119	10.63735	0.728156	6.52E+17	547.5605
4.85	0.1	0.485	9.078014	10.48677	0.702736	6.39E+17	547.7029
4.9	0.1	0.49	9.144587	10.33989	0.678457	6.25E+17	547.8418
4.95	0.1	0.495	9.210911	10.19656	0.655258	6.12E+17	547.9774
5	0.1	0.5	9.276991	10.05667	0.633079	6E+17	548.1096
5	0.1	0.5	9.276991	10.05667	0.633079	6E+17	548.1096
5.5	0.1	0.55	9.925126	8.823471	0.456926	4.94E+17	549.274
6	0.1	0.6	10.55232	7.832331	0.339517	4.13E+17	550.208
6.5	0.1	0.65	11.1611	7.020667	0.258484	3.51E+17	550.9718
7	0.1	0.7	11.75347	6.345412	0.200893	3.02E+17	551.6063
8	0.1	0.8	12.89539	5.290306	0.127675	2.3E+17	552.5964
9	0.1	0.9	13.98843	4.507789	0.085671	1.81E+17	553.3296
10	0.1	1	15.04011	3.907335	0.059991	1.46E+17	553.8915

Table 5.2. Various nozzle flow parameters obtained using analytical expressions of compressible fluid flow for case of pure Argon.

5.3.4. Cluster Characterization in SF_6-Ar gas Binary Gas Jet following Free-jet Expansion from a 100 μm Orifice

We next attempted cluster characterization of the SF_6-Ar gas jet following its expansion from the 100 micron orifice by way of studying the extent of clustering occurring in it. To this end,

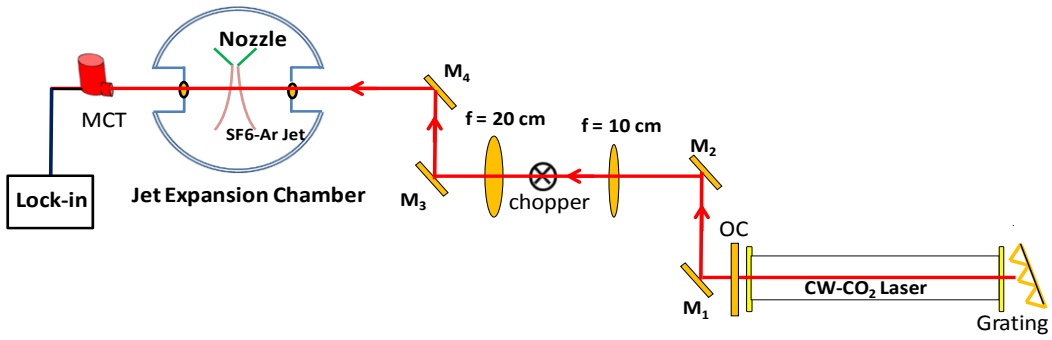

Figure 5.19. Schematic of the experimental setup comprising the expansion chamber and a line-tunable CW- CO_2 laser for carrying out the absorption studies in SF_6-Ar binary gas mixture.

absorption measurement in the jet by way of selective excitation of the ν_3 band of SF_6 has been carried out by employing the CW-CO_2 laser delivering ~2 Watt power on 10P(20) line on SLM TEM_{00} mode. The schematic of the experimental setup towards cluster

characterization is shown in figure 5.19. The laser was made to lase on the well-defined TEM_{00} mode by the use of an intra-cavity aperture. The narrow line width (~few 10's of MHz) laser operating on 944.19 cm^{-1} is resonant to the ro-vibrational transition of the abundant isotopic species of sulfur, viz., $^{32}SF_6$ monomers and the measured absorbance is thus proportional to the $^{32}SF_6$ monomer density. The highly sensitive liquid N_2 cooled HgCdTe (MCT) detector used here required a pulsed beam for its operation and therefore a chopper operating at ~200 Hz was made use of.

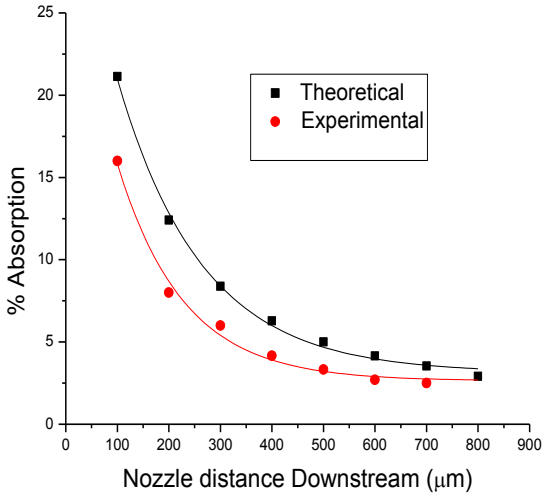

Figure 5.20. Theoretical & experimentally calculated variation of % absorption in SF_6 vs. nozzle distance downstream for 3 bar stagnation, 20% SF_6 in Ar.

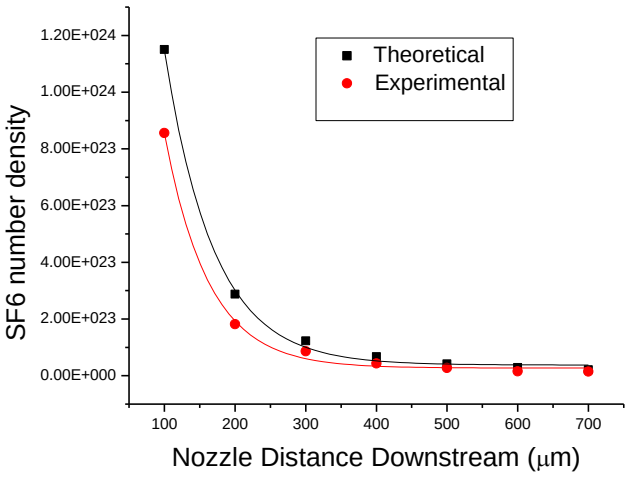

Figure 5.21. Theoretical and experimental variation of SF_6 monomer density vs. nozzle distance downstream for 3 bar stagnation, 20% SF_6 in Ar.

The jet expansion chamber was maintained at a background pressure of ~10^{-4} mbar by employing a diffusion pump of 2000 l/s capacity. Pre-mixed SF_6-Ar gas mixture (20% SF_6 in Argon) at room temperature was fed to the 100 μm diameter at a stagnation pressure of 3 bar (abs), P_oD ~22 torr-cm. The chopped laser beam is focused by a combination of lenses as shown in

figure 5.19 to a spot of ~300 μm diameter on the axis jet and could be transported in and out of the jet expansion chamber through the BaF_2 windows. A jig (hollow cylindrical disc of 5 mm length, with a 1 mm slot in it) held concentric to the nozzle (figure 5.24) facilitated the alignment of the laser beam with the nozzle jet centerline. Translation of M_4 by means of a high resolution micrometer stage (least count = 10 μm) allowed scanning of the jet downstream the nozzle exit along the jet centerline and the corresponding absorption in $^{32}SF_6$ at different downstream location was monitored by making use of the LN_2 cooled HgCdTe detector placed at the exit end of the chamber. Usage of a Lock-in amplifier enhanced the S/N ratio facilitating the detection of absorption in $^{32}SF_6$.

5.3.4.1. Results & Discussion

Figure 5.20 shows the percentage absorption of the CO_2 laser emission in the SF_6-Ar gas mixture at various axial distances from the throat of the nozzle. The knowledge of number densities in the jet in both the axial, radial directions and the absorption cross-section for

Distance from nozzle exit (μm)	**% Absorption (Theory)[1]**	**% Absorption (Experimental) [2]**	**% of molecules in cluster form ($\Delta_{1\text{-}2}$)**	**Percentage of SF_6 clustering**
100	21.14	16.0	5.14	24.3
200	12.41	8.0	3.59	28.9
300	8.39	6.0	2.61	31.1
400	6.28	4.17	2.11	33.6
500	5.0	3.33	1.67	33.4
600	4.15	2.7	1.45	34.9
700	3.54	2.5	1.04	29.4

Table 5.3. Determination of percentage of clustering (fractional condensation) of SF_6 arrived at from both experimental and theoretical considerations.

$^{32}SF_6$ allows theoretical computation of absorption occurring in the jet and is also plotted in the same figure. To be noted the theoretical computation does not take into consideration the formation of clusters in the jet. As can be seen from figure 5.20, absorption in SF_6 decreases asymptotically with increasing axial distance. Further, the absorption in the jet arrived at experimentally at different axial distances is found to be less as compared to that predicted by theory. The difference between the experimental and the theoretical values is attributed to the formation of clusters in the jet. From the absorption data, the number densities of SF_6 molecules along the jet centerline were arrived at for both the experimental and theoretical cases as depicted in figure 5.21. To be noted here, SF_6 homo-clusters have absorption spectra centered on 935 cm^{-1} in the low frequency side and from 955-975 cm^{-1} in the high frequency side [5.16, 5.18]. Similarly, the SF_6-$(Ar)_1$ exhibits a red frequency shift of 3 cm^{-1} with respect to the absorption line centre of SF_6 monomer [5.16, 5.18]. This red-shift increases with increasing Argon atoms in the cluster being formed, reaching as much as 10 cm^{-1} for case of SF_6-$(Ar)_9$ [5.16, 5.18]. On the other hand, the line-width of the laser source used is only few 100's of MHz (0.003 cm^{-1}). Therefore, absorption in both hetero and homo clusters can be neglected in comparison to the monomer absorption.

5.4. Demonstration and characterization of Sulfur enrichment in SF_6-Ar binary gas mixture by Laser Assisted Aerodynamic Separation Process by employing the CW-CO_2 laser.

We present, the experimental results demonstrating the enhancement of enrichment of $^{34}SF_6$ through laser assisted aerodynamic process when the emission of a CW-CO_2 laser is made to interact with a supersonically cooled SF_6-Ar binary gas jet. Selective excitation of $^{32}SF_6$ inhibited its cluster formation thereby enriching the central stream with both homo and hetero clusters of $^{34}SF_6$ and Argon. To this end, the dependence of the separation efficiency as a

function of the molar concentration of SF_6 in the gas mixture and the stagnation pressure has been studied.

5.4.1. Experimental work

The schematic diagram of the experimental setup to enrich Sulfur isotopes [^{32}S (95.02%), ^{33}S (0.75%), ^{34}S (4.21%)] through laser assisted aerodynamic separation is depicted in figure 5.22. SF_6 (commercial grade, purity, 99.8%) and Argon gas, pre-mixed in a desired ratio, at a stagnation pressure, P_o, is made to expand into the chamber maintained at pressure, ~10^{-2} mbar through a 100 micron circular orifice. The photograph of the nozzle-skimmer assembly is shown in figure 5.23. The emission from the indigenous CW-CO_2 laser is steered into the chamber after its appropriate focusing.

Nozzle dimaeter	*100µm*
Skimmer diameter	*500µm*
Nozzle-skimmer distance	*10 mm*
Laser wavelength	*10P(16)*
Focal spot	*300 µm*
Laser Power	*10 W; TEM_{00}*
Laser spot centre from nozzle exit	*150 µm*
Stagnation Pressure, P_o (atm)	*1-3 atm*
SF_6 mole fraction in the SF_6-Ar gas mixture	*0.5% - 10%*

Table 5.4. The pertinent laser and gas mixture parameters used in the experimental work.

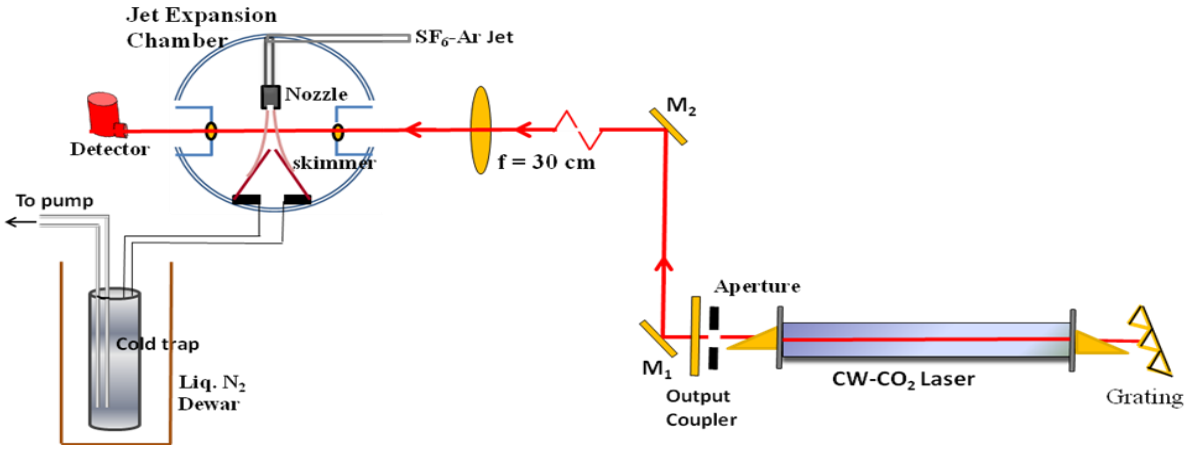

Figure 5.22. Schematic of the experimental setup comprising the expansion chamber and the line-tunable CW-CO_2 laser for carrying out isotope enrichment studies in SF_6. A cold trap for collecting the skimmer contents too is shown.

The laser is tuned to 10P(16) line and made to intersect the jet orthogonally at an appropriate downstream location causing selective vibrational excitation of the abundant species viz., $^{32}SF_6$. A conical skimmer of diameter 500 μm, placed at a distance of ~7 mm from the nozzle exit along the jet centerline, allowed the collection of the core stream of the jet. The other end of the skimmer is connected to a vacuum pump through a container (cold trap) immersed in LN_2 bath. While SF_6 (boiling point: -64 $^{\circ}$C) gets efficiently trapped in the container, the benign Argon (boiling point: -186 $^{\circ}$C) is pumped out. After appropriate experimentation time, the contents of the cold trap were transferred into a sample cell and investigated for the

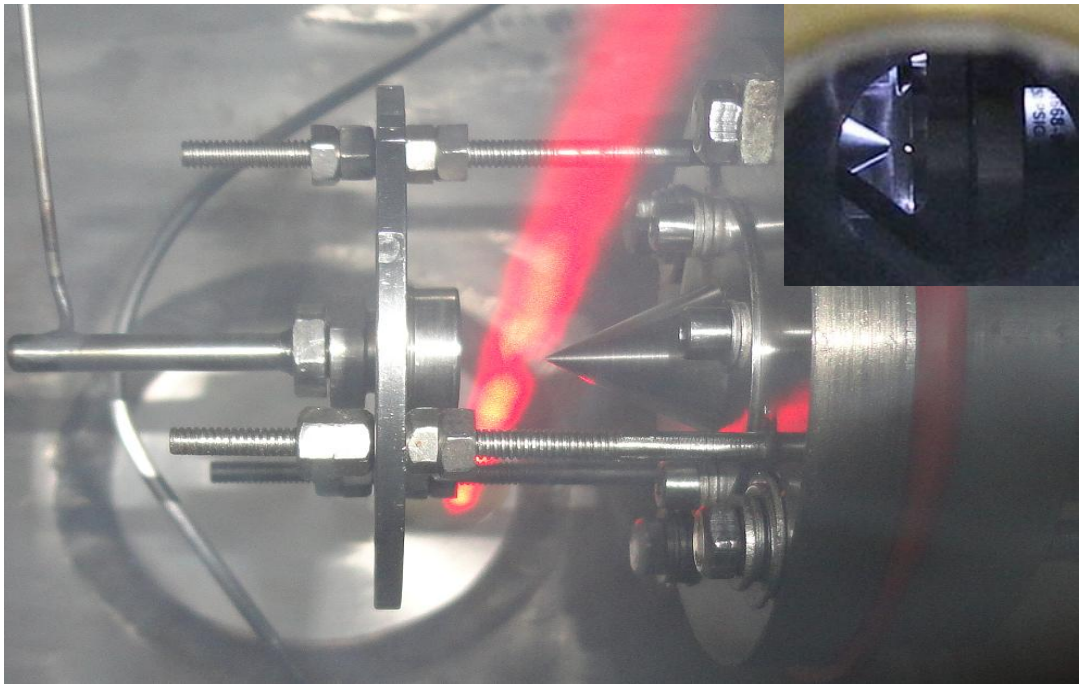

Figure 5.23. A snap shot of the nozzle-skimmer assembly. To the left is the nozzle/orifice. Gas is fed to the nozzle from the source chamber through the 1/4th inch piping brazed to a 1/16th inch SS tube as can be seen. The skimmer on the right separates the jet/expansion chamber from the beam chamber and skims the central heavier stream of the jet that is collected in the cold trap for analysis. A paper strip placed immediate to the nozzle exit for laser focussing along the jet centreline too can be seen. In the inset is shown the focussed laser spot along the nozzle axial downstream distance.

isotopic concentration by Quadruple mass spectrometer as well as by a novel optical based absorption technique (the methodology of this technique is detailed in section 5.5). The results obtained by the absorption technique follow those obtained by the conventional mass spectrometry. The various experimental parameters are as indicated in table 5.4.

5.4.2. Results and Discussion

The CW-CO_2 laser tuned to emit on 10P(16) line, is known to have a strong overlap with the absorption feature of $^{32}SF_6$. Selective excitation of $^{32}SF_6$ (isotope shift (17 cm^{-1}) ≫ emission width of the laser (< 0.003 cm^{-1})) inhibits its cluster formation while the non-resonant isotope viz., $^{34}SF_6$ continues to form clusters, predominantly with Argon. The increased relative mass difference between the resonant and the non-resonant species leads to enhanced concentration of the heavier species in central stream of the jet.

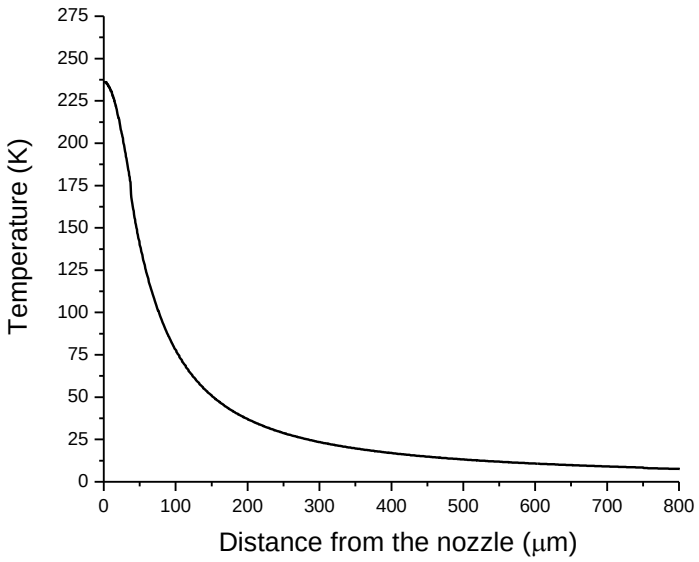

Figure 5.24. Plot of temperature in the jet as a function of nozzle downstream distance.

$^{34}SF_6 + Ar \rightarrow {}^{34}SF_6Ar$

$^{34}SF_6Ar_{n-1} + Ar \rightarrow {}^{34}SF_6Ar_n$

In the first set of experiments, the stagnation pressure was fixed at 3 atm (abs). At this pressure, for the nozzle used, the onset of clustering is expected to occur within 100 μm from the nozzle exit. Figure 5.24 shows the variation of static temperature in the jet as a function

of nozzle distance. This can be understood from the Lennard-Jones parameters for the two gases [5.19, 5.20] involved.

ϵ/k (SF_6) = 222.1 K, where, ϵ is the binding energy (in eV), and, k, the Boltzmann constant, and, ϵ/k (Ar) = 93.3 K. The binding energy, ϵ/k (K), for different clusters are,

$$\epsilon/k\,(SF_6 - SF_6) = \sqrt{\left(\epsilon/_k\,(SF_6) * \epsilon/_k\,(SF_6)\right)} = 222.1\ \text{K}$$

$$\epsilon/k\,(SF_6 - Ar) = \sqrt{\left(\epsilon/_k\,(SF_6) * \epsilon/_k\,(Ar)\right)} = 143.95\ \text{K}$$

$$\epsilon/k\,(Ar - Ar) = \sqrt{\left(\epsilon/_k\,(Ar) * \epsilon/_k\,(Ar)\right)} = 93.3\ \text{K}$$

The focal spot diameter being ~300 μm, the laser beam was made to graze the nozzle exit to derive maximum advantage. It is evident from figure 5.24, showing the variation of temperature along the nozzle downstream distance, that, the critical temperature for onset of clustering occurs for, x/D < 100 μm, where, x, is the number of nozzle diameters. For our case of 100 μm orifice, x/D = 1. From the plot, at x/D = 1 or x= 100 μm, T = 75 K.

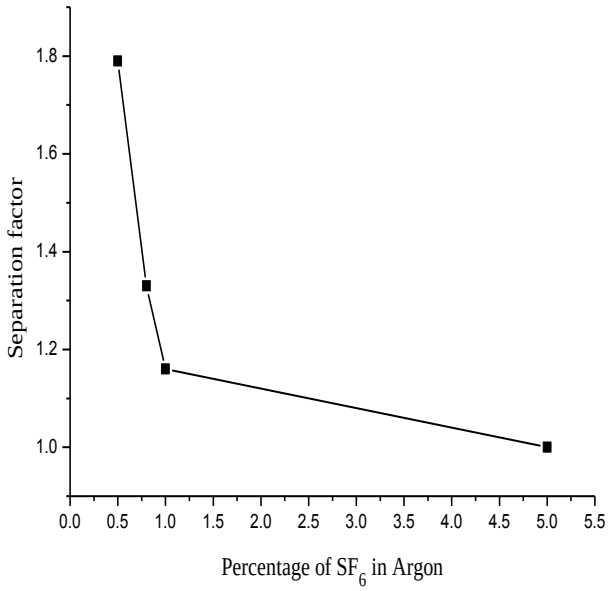

Figure 5.25. Separation factor as a function of percentage of mole fraction of SF_6 in Argon for P_o = 3 atm.

The separation factor, α, defined as $\alpha = (^{34}SF_6/^{32}SF_6)_{\text{enriched stream}} / (^{34}SF_6/^{32}SF_6)_{\text{natural}}$ was studied as a function of the molar concentration of SF_6 and the dependence is as shown in figure 5.25. It

would be seen that the separation efficiency monotonically increases with reducing SF_6 partial pressure. This can be understood in the following manner. Higher concentration of SF_6 results in increased collision rate between its two isotopes leading to transfer of excitation from the resonant to the non-resonant isotopes. This leads to scrambling of selectivity and in turn, reduced separation factor. As can be seen from figure 5.25, the separation efficiency increases with reduced SF_6 concentration. The throughput understandably, reduces in this case as the mole fraction of SF_6 is less here. A judicious balance between the two is thus needed for an actual process application.

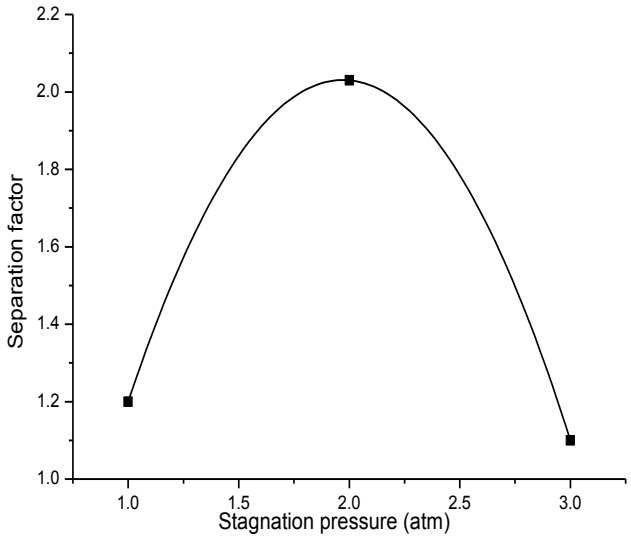

Figure 5.26. Separation factor as a function of stagnation pressure for 0.8% SF_6 in Argon.

In the next set of experiments, the separation efficiency was studied as a function of the stagnation pressure and the dependence is as shown in figure 5.26. To be noted here that, for this measurement, the position of interaction of the laser beam with the jet was maintained as in the previous experiment.

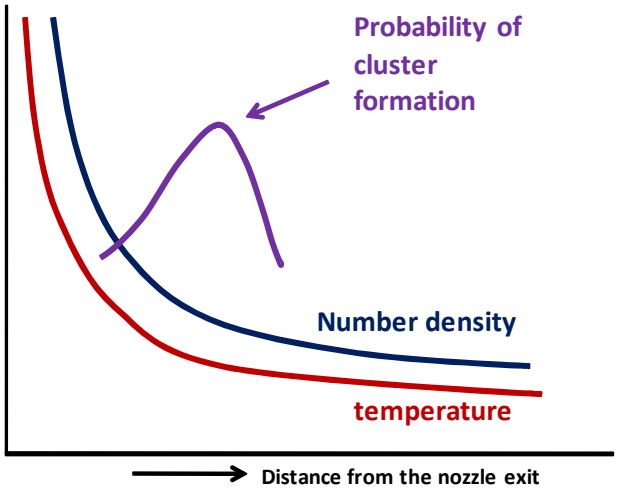

Figure 5.27. Probability of cluster formation, a function of number density and temperature versus nozzle downstream distance.

The separation factor exhibits a maximal behavior with stagnation pressure. This can be understood in the following manner. Following expansion from the nozzle, as the gas cools, both its number density and temperature drops. At a particular distance downstream, the collisional environment and the extent of cooling are just right for the onset of van der Waals clusters. With further increasing distance, the probability of cluster formation gradually drops as the collision becomes much too less even though the gas continues to cool as depicted in figure 5.27. Thus, while the temperature downstream the nozzle is independent of the stagnation pressure, cluster formation is strongly dependent on the collisional environment in the jet. At low stagnation pressures, though the temperature is conducive for onset of condensation of the unexcited isotopomer with the buffer gas (143.95 K for case of SF_6-Ar clusters), the number density in the jet, however, is insufficiently low, thus hampering the extent of clustering (of SF_6 with Argon). Hence, the probability of cluster formation is low in the jet resulting thereby in lower separation factor for case of P_o = 1 atm. On the other hand, for higher stagnation pressures (3 atm), owing to larger number densities, and, therefore more number of collisions, the probability of onset of clustering shifts closer to the nozzle and clustering begins immediately at the nozzle exit. Thus, for the case of 3 atm stagnation pressure, majority of photons (beam diameter ~300 μm) stay unabsorbed, as clustering has already begun thus resulting in poorer separation efficiency as the absorption feature of the clusters is red-shifted with respect to the monomer absorption [5.18]. The higher separation factor obtained for case of P_o = 2 atm points to the fact that, here, the number densities are most optimum for onset of clustering leading to efficient spatial separation. Separation factors exceeding '2' have been obtained for this case of pressure.

5.5. Estimation of Separation factor by a novel Absorption method.

Conventionally, estimation of relative concentration of isotopic species in a sample is carried out by mass spectrometric methods while optical methods e.g., FTIR are not uncommon.

However, optical methods require the knowledge of isotope specific absorption cross-sections which are not readily available for many isotopes. Herein, a novel method of estimation of the relative concentration of the isotopes in the enriched central stream of SF_6-Ar jet following laser irradiation has been proposed, wherein, the knowledge of absorption cross-sections of the molecule under study is rendered irrelevant. The method exploits the selective absorption of the emission of CO_2 laser on 10P(36) and 10P(20) lines by $^{34}SF_6$ and $^{32}SF_6$ respectively. Comparison of the absorption measurements in a photo-chemical cell containing the enriched sample with that of the natural sample renders the knowledge of absorption cross-sections irrelevant and facilitates precise measurement of the separation factor. The details of the methodology are as follows.

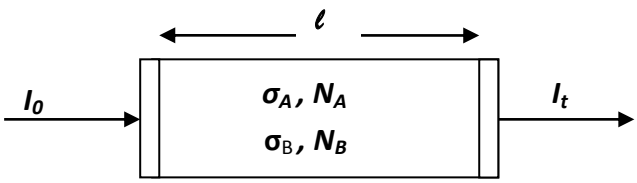

Figure 5.28: Schematic of the experimental cell used for collection and measurement of the separation factor by absorption method. BaF_2 end windows were used for coupling in and out the incident and the transmitted CO_2 laser beam.

Consider a photochemical cell (figure 5.28) of length, *l*, containing a mixture of two isotopes A and B with concentrations and absorption cross-sections N_A, σ_A and N_B, σ_B respectively. Let a coherent beam of Intensity I_{0A}, resonant with isotope A, shine on to it. The transmitted intensity (I_{tA}) is then given by

$$I_{tA} = I_{0A} e^{-N_A \sigma_A \ell}$$

$$\Rightarrow \quad N_A = \frac{\ln\left[\frac{I_{0A}}{I_{tA}}\right]}{\sigma_A \ell} \qquad [5.1]$$

Similarly, when a coherent beam of intensity, I_{0B}, resonant with isotope B is incident on the photo chemical cell, the transmitted intensity, I_{tB}, is given by,

$$I_{tB} = I_{0B} e^{-N_B \sigma_B \ell}$$

$$\Rightarrow \quad N_B = \frac{ln\left[\frac{I_{0B}}{I_{tB}}\right]}{\sigma_B \ell} \qquad [5.2]$$

The ratio of the concentration of the isotopes in the mixture is therefore,

$$\frac{N_B}{N_A} = \frac{\sigma_A}{\sigma_B} \frac{\log\left[\frac{I_{0B}}{I_{tB}}\right]}{\log\left[\frac{I_{0A}}{I_{tA}}\right]} \qquad [5.3]$$

This ratio can therefore be estimated from the above equation provided the absorption cross-sections for the two isotopes are accurately known. If this data is not available, one can still estimate the separation factor '**α**' by measuring the transmission through the photochemical cell filled with the enriched sample in one case, and the natural sample in the other case. Usage of equation 5.3 would readily yield,

$$\alpha = \frac{[N_B/N_A]_{enriched}}{[N_B/N_A]_{natural}} = \frac{\left[\frac{\log\left[\frac{I_{0B}}{I_{tB}}\right]}{\log\left[\frac{I_{0A}}{I_{tA}}\right]}\right]_{\mathbf{enriched}}}{\left[\frac{\log\left[\frac{I_{0B}}{I_{tB}}\right]}{\log\left[\frac{I_{0A}}{I_{tA}}\right]}\right]_{\mathbf{natural}}} \qquad [5.4]$$

R.H.S. of the above equation contains incident and transmitted intensities for the enriched and natural samples, all experimentally measurable quantities. The knowledge of absorption cross-sections is therefore rendered unessential in this method of estimation of separation factor.

By employing equation 5.4, we have experimentally determined the separation efficiency of sulfur isotopes carried out by the laser assisted aerodynamic separation process. The details of the experimental work have been discussed in the earlier section (5.4). The judiciously designed cold trap was used to collect the enriched species in the central stream following the experimentation. The contents of the cold trap were subsequently transferred into the photo-

chemical cell (length = 11 cm and diameter = 2.5 cm) (figure 5.28) and the transmission through it was experimentally measured. The schematic of the experimental set-up employed for measuring I_{0A}, I_{0B}, I_{tA}, and I_{tB} is shown in figure 5.29. The actual setup showing the photo-chemical cell and the laser is shown in figure 5.30. The intra-cavity aperture ensured operation of the CO_2 laser on TEM_{00} mode. Reflection of the incident beam off BS_1 was used to monitor the emission wavelength with the help of a CO_2 spectrum analyzer (Opt. Engg., USA) while that off BS_2 allowed the estimation of the incident power onto the photochemical cell by means of Detector D_1 (Ophir make). The transmission of BS_1 and BS_2 were so chosen as to allow measurements always in the small signal regime. The power transmitted through the cell was monitored by detector D_2 (Ophir).

Experimental conditions (% SF_6 in Ar, P_{stag} (bar))	Enrichment factor		% enhancement in the obtained enrichment factor
	10P(16)	10P(20)	
0.8%, 2 bar	1.31	1.61	22.9%
0.8%, 2 bar	1.28	1.59	24.2%
0.8%, 2 bar	1.345	1.63	21.1%

Table 5.5: Enrichment factor obtained by absorption method under different experimental conditions.

The first set of experiments was performed with the cell containing the enriched sample. CO_2 laser was first tuned to 10P(20) that is resonantly absorbed by the ν_3 = 0 to 1 vibrational

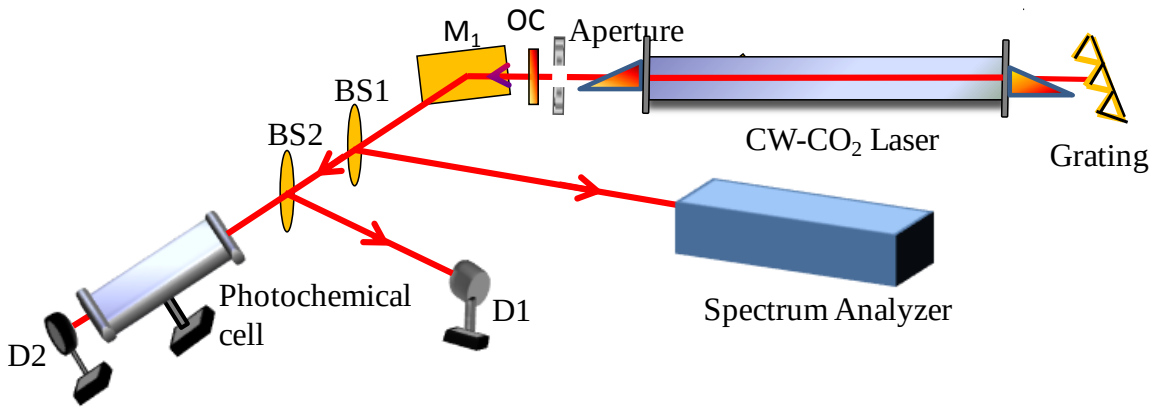

Figure 5.29. Schematic of the experimental setup for carrying out absorption measurements in irradiated and natural samples towards estimating the enrichment factor.

transition of the abundant species $^{32}SF_6$. The incident $(I_{0A})_{enriched}$ and corresponding transmitted $(I_{tA})_{enriched}$ powers were noted. The laser was then tuned to 10P(36) line that is resonant with $^{34}SF_6$ on ν_3 = 0 to 1 vibrational transition and the incident $(I_{0B})_{enriched}$ and corresponding transmitted $(I_{tB})_{enriched}$ were recorded. The next set of experiments were performed with the cell containing natural sample and the corresponding $(I_{0A})_{natural}$, $(I_{tA})_{natural}$, $(I_{0B})_{natural}$ and $(I_{tB})_{natural}$ were recorded by tuning the laser alternately to 10P(20) and 10P(36) as before. Plugging in these values into equation 5.4 allowed us to readily estimate the separation factor for $^{34}SF_6$ enrichment achieved through laser assisted aerodynamic separation process. The separation factors estimated by this technique under different experimental conditions for the 10P(16) and 10P(20) lines are as tabulated in table 5.5. The separation factors have been measured for both the cases by Quadruple Mass Spectrometry (QMS) too as shall be discussed in the following section (section 5.6). The consistency in the general trend of separation efficiency as measured by both QMS and absorption techniques is apparent. The accuracy of this technique is largely dependent on the frequency stability of the laser, its spatial mode quality, stability and the sensitivity of the detectors used for the power measurements.

Aside this, care has been taken to keep the experimental conditions similar during irradiation with the 10P(16) and 10P(20) lines in all the six runs. However, slight variation can creep in, in particular, the partial pressure of SF_6 in Ar, the stagnation pressure itself and hence the slight variation in the values enumerated in table 5.5.

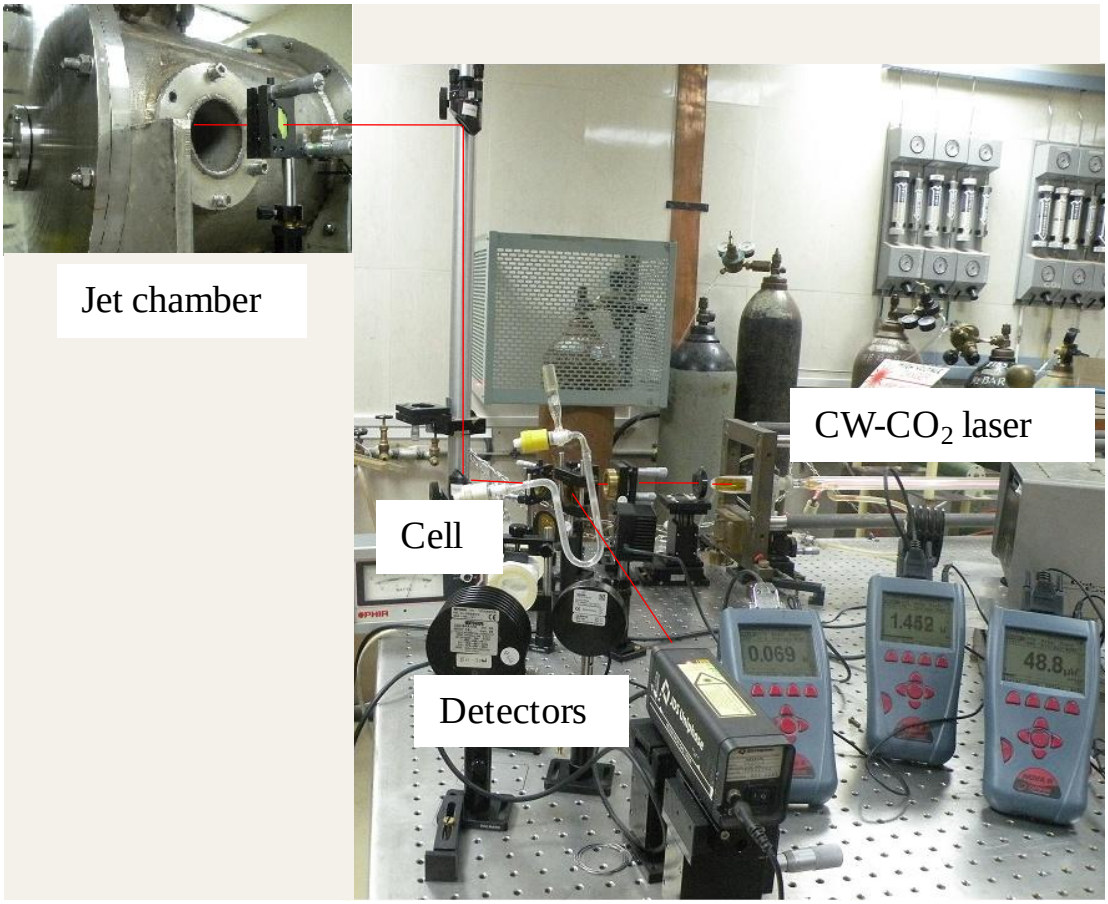

Figure 5.30. The experimental setup comprising the CW-CO_2 laser, photo-chemical cell and the detectors used in conducting the absorption measurements in SF_6 gas by way of measuring I_{0A}, I_{0B}, I_{tA} and I_{tB} in the collected sampled stream towards estimating the isotope separation factor following enrichment by laser assisted aerodynamic expansion process. The beam steering optics and the jet expansion chamber (inset) are also seen.

5.6. Advantage of Multi-step Vibrational Excitation in Laser Assisted Aerodynamic Separation of Sulfur Isotopes

During the course of the experimentation, the advantage of a red-shifted excitation source in furthering the obtainable enrichment efficiency of laser assisted aerodynamic separation process has also been investigated. The enhancement in the enrichment factor owes its origin to the efficient multi-photon excitation possible here due to the red-shifted nature of the incident radiation. This has been experimentally validated in Sulfur isotope separation through laser assisted aerodynamic process wherein the emission of an indigenous line tunable CW-CO_2 laser interacted with SF_6-Ar binary jet. Anharmonic splitting (AS) of the vibrational levels coupled with Coriolis rotational splitting facilitates such multi-photon up-pumping leading to the observed enhancement in the separation factor. It is of interest to note here that van den Berg et al [5.1-5.3], made use of 10P(20) line of CO_2 laser for the selective excitation of $^{32}SF_6$ even though it is red-shifted with respect to its absorption centre by ~3.5 cm^{-1} [5.21]. A qualitative explanation for this has been offered by Jeff Eerkens in a more recent paper [5.22] by invoking the possibility of multi-step

Anharmonic constants of the ν_3 mode of SF_6	
Equilibrium harmonic frequency, ω_e	951.61 cm^{-1} [this work]
Fundamental absorption	947.97cm^{-1}
Anharmonic defect = $-2\omega_e\chi_e$	-3.64 cm^{-1} [this work] -3.48 cm^{-1} [5.30, 5.31]
Anharmonicity constant, χ_e	1.91 x 10^{-3} cm^{-1} [this work]
Second-order Tensor coefficient, T_{33}	-0.246 [5.31]
Ground rotational constant, B_0	0.0910 cm^{-1} [5.30]
B'-B_0, where B' is the excited vibrational state rotational constant.	-1.31x10^{-4} cm^{-1}
Coriolis constant, ξ	0.693 [5.30]

Table 5.6. Spectroscopic constants of the ν_3 mode of SF_6

vibrational excitation [5.21, 5.23] when irradiated by 10P(20) line that is red-shifted with respect to the fundamental absorption frequency of $^{32}SF_6$. We demonstrated for the first time, the experimental evidence of the advantage of such a red-shifted coherent excitation source in furthering the enrichment efficiency of a laser assisted aerodynamic separation process. This was possible by comparing the efficiency of sulfur isotope separation by laser assisted aerodynamic process for the resonant and red-shifted absorption cases. The separation experiments were performed first by tuning the emission of the CO_2 laser to 10P(16) line that offers a near match with the absorption centre of $^{32}SF_6$ and then to 10P(20) line that is red-shifted with respect to the corresponding absorption centre, maintaining all other conditions identical. A quantitative analysis of the extent of resonant up-pumping of the initial vibrational levels occurring in both the two cases has been studied to corroborate the observed experimental result.

5.6.1. Experimental Work

The schematic of the experimental setup to enrich ^{34}S isotope through laser assisted aerodynamic separation process is depicted in figure 5.26. Pre-mixed SF_6-Ar gas mixture (0.8% SF_6 (commercial grade SF_6, purity 99.8%) in Ar,) was made to undergo supersonic expansion through a 100 μm circular orifice into a chamber maintained at a moderate vacuum of 10^{-2} torr. The stagnation temperature and pressure of the gas mixture were maintained at 300 K and 2 atm (abs) respectively. The emission of an indigenously developed CW-CO_2 laser, capable of delivering 10W on TEM_{00} mode, tuned to the desired line, was made to interact orthogonally at the jet centerline immediately after the nozzle exit, where the focused spot size was ~300 μm. In the dynamically cooled jet near the nozzle exit (within 100 micron), the static temperature can reach to ~140 K as discussed in section 5.4.2, evaluated by the standard isentropic relations. The abundant isotope viz., $^{32}SF_6$ that also happens to be the lighter species, was selectively excited. The heavier unexcited species, that stays closer to

the jet centerline aided further by its process of clusterization, forms the core gas, while, the lighter excited species forms the rim gas. The conical skimmer (500 μm diameter) was positioned at an appropriate downstream location to allow the passage of the central core stream that is enriched in $^{34}SF_6$. A LN_2 cooled trap was used to selectively condense this $^{34}SF_6$ while Argon gas was pumped out. After adequate experimentation time, the contents of the cold trap were transferred into a photochemical cell and analyzed by both mass spectrometry and optical absorption methods.

In the first set of experiments the CW-CO_2 laser was tuned to emit on 10P(16) line that is known to have a strong overlap with the υ_3 absorption feature of $^{32}SF_6$ (cross-section, σ, at 947.7 cm^{-1} is ~3.072 x 10^{-17} cm^2) [5.24] and the separation factor α, defined as $\alpha = [(^{34}SF_6/^{32}SF_6)_{\text{enriched stream}}] / [(^{34}SF_6/^{32}SF_6)_{\text{natural}}]$ was measured to be ~1.46 (±0.04) by mass spectrometry method. In the next set of experiments, the laser beam was tuned to the 10P(20) line (cross-section σ ~2 x 10^{-18} cm^2 at 944.2 cm^{-1}) [5.22], and the corresponding separation factor was found to be ~1.63 (±0.06). The enrichment factor was measured by the optical absorption based method, the basic principle of which is discussed in section 5.5. The separation factor measured this way had a close match with that obtained by the mass spectrometric method. The experiment was repeated three times under identical operating conditions and the results are summarized in table 5.5. As would be seen, there is a clear improvement of ~20% in the separation efficiency when the laser was tuned to 10P(20) line as against 10P(16) line. The observed increase in the efficiency is attributable to the multiple vibrational excitation of the desired isotope when the laser is tuned to 10P(20) line which inhibits cluster formation to a higher degree [5.22]. Towards quantitative substantiation of this claim, we invoke anharmonic splitting of the vibrational levels coupled with Coriolis rotational splitting to analyze the possibility and extent of multiple vibrational excitations under the two irradiation conditions.

Among the CO_2 laser lines, 10P(16), is the closest to the absorption line centre of the ν_3 fundamental mode of $^{32}SF_6$ while 10P(20) line is shifted by ~3.5 cm^{-1} to its red [5.17]. Ever-since the first isotopically-selective excitation and dissociation of SF_6 upon irradiation with a strong pulsed CO_2 laser [5.25, 5.26], the fundamental problem was to explain how a large number of photons of equal energy can be absorbed in the υ_3 mode of the molecule despite the fact that its anharmonicity tends to make all but the first transition non-resonant. Various theoretical models have been proposed [5.24, 5.27-5.31] aimed at explaining the resonant nature of the absorption in the first few levels before quasi-continuum takes over to continue the pumping and eventually dissociate the molecule. Given the molecules' anharmonic defect, $-2\omega_e\chi_e$ (~ -3.48 cm^{-1}) [5.31], where 'ω_e' is the equilibrium harmonic frequency and 'χ_e' is the anharmonicity constant, the annulling of the offset due to simple field broadening is not possible (the Stark broadening is only ~10^{-2} cm^{-1} at intensities of ~few 10's of kW/cm^2) [5.32]. Cantrell et al [5.28, 5.29] proposed splitting of the degenerate vibrational modes and shifting due to their coupling, in addition to Coriolis splitting of the rotational levels, as the primary mechanism responsible for compensating the vibrational anharmonicity and in turn permitting near-resonant absorption of CO_2 laser photons. One major advantage of laser assisted aerodynamic separation process, as also discussed earlier, is that the scheme itself is not photon-intensive and excitation of only initial few levels would further enhance the separation factor. We therefore limit our discussion to levels up to, say, υ=8. The $\upsilon\nu_3$ anharmonic levels of the triply degenerate υ_3 mode of SF_6 and the splitting of these states into different vibrational energy levels is shown schematically in figure 5.34. The (n_x n_y n_z) values pertaining to different quanta in the three-fold degenerate υ_3 vibrational mode for various levels up to υ = 4 along with their conventional spectroscopic notations and Eigen values are enumerated in table 5.7 [5.31] (to be noted, say, the 'υ' in the representation (0,0,υ,0,0,0) corresponding to the quanta in different normal modes of vibration of the molecule is

different from (n_x n_y n_z) corresponding to the quanta in the triply degenerate ν_3 mode). The splitting of the rotational level of a vibrational state, into sub-levels that are characterized by the quantum number, 'R' (R = J-1, J, J+1, for a given J) as a result of Coriolis interaction [5.33] too is shown in figure 5.31 for case of υ=1. Each single 'J' in a particular 'υ' is split into a complex manifold as shown. The selection rules governing the transitions are $\Delta\upsilon = \pm1, \pm2, \pm3\ldots$, $\Delta J = 0, \pm1$, $\Delta R = 0$ [5.33].

In order to understand the resonant nature of the red-shifted excitation, it is important to look into the vibrational and the associated rotational broadenings corresponding to these various $\upsilon\nu_3$ states. The same have been evaluated analytically as detailed below. Following this, a possible multi-photon excitation route has been proposed.

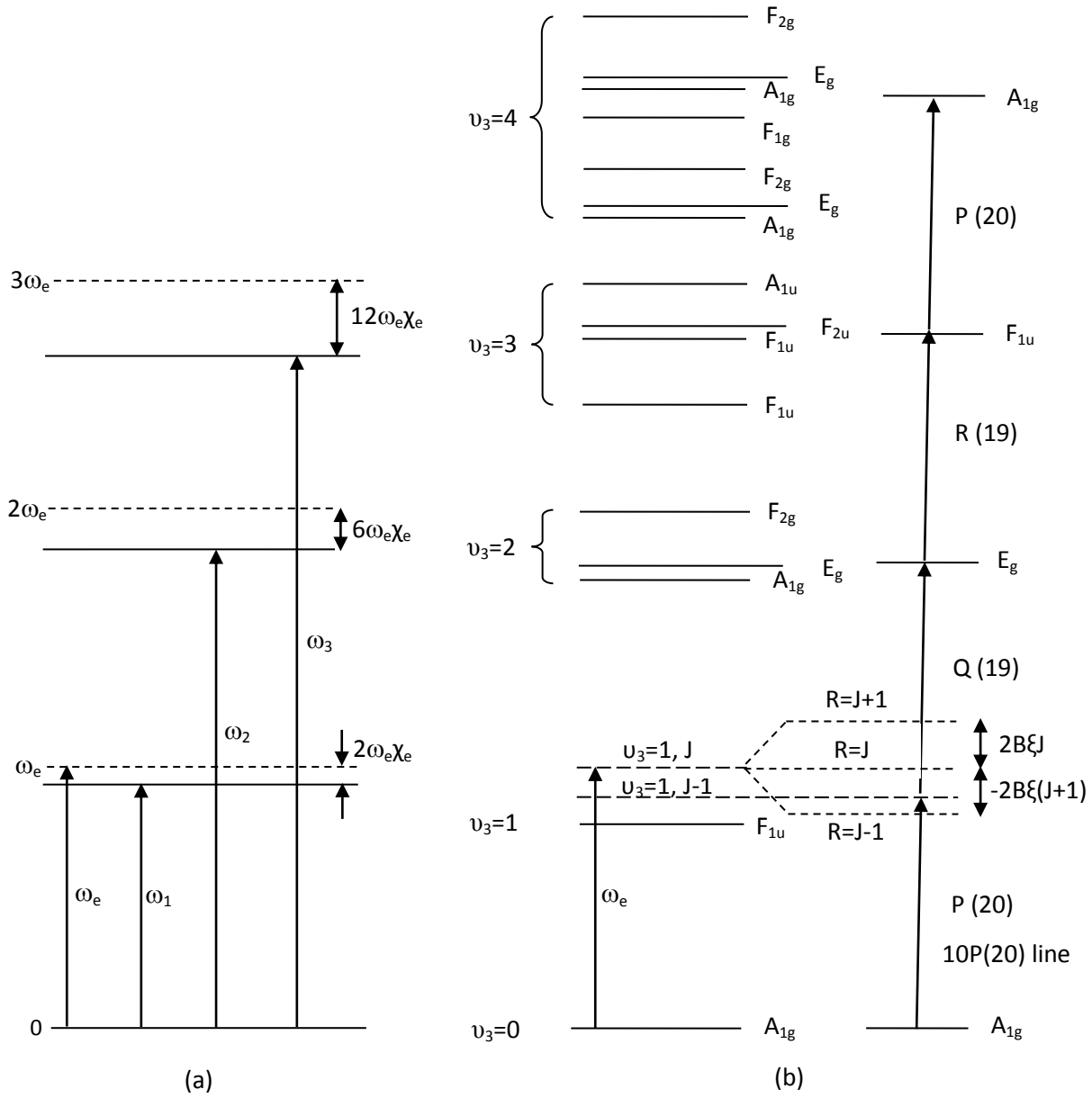

Figure 5.31. a) Schematic of the υv_3 levels in SF_6 with the equilibrium harmonic frequency (ω_e = 951.61 cm^{-1}), the fundamental (ω_1 = 947.97 cm^{-1}), first overtone (ω_2 = 1982.31 cm^{-1}) and second overtone (ω_3 = 2833.02 cm^{-1}) levels along with the anharmonic defects. Dashed lines show the harmonic ladder. b) Schematic of the anharmonic splitting of pure vibrational levels upon laser irradiation into their possible octahedral sub-levels indicated by their respective designations up to v=4. Coriolis splitting of a particular J level into R=J-1, J, J+1 sub-levels is shown for the case of υ_3=1(dashed lines). Also shown to the right is the possible multi-photon scheme involving excitation of four successive vibrational levels of the υ_3 ladder of SF_6 with 10P(20) laser line. Various ro-vibrational states of the molecule in resonance with this laser line starting with P(20) transition (ΔJ=-1) via Q(19), R(19) up to P(20) enable the molecule undergo the multi-step excitation up to υ=4.

The broadening of vibrational levels is given by the expression, $\Delta\nu_{anh} = 20/3T_{33}\upsilon^2$ [5.29], 'T_{33}' being the second order tensor anharmonic coefficient (some anharmonic constants specific to the ν_3 mode of SF_6 used for evaluating these parameters are as shown in table 5.6 for ready reference). The broadening corresponding to the various υ_3 levels evaluated is enumerated in table 5.8. Likewise, the rotational broadening [5.34] corresponding to a particular J level is given by, $2B\xi$ (2J+1), where B is the rotational constant (table 2), ξ is the Coriolis constant. As shown in figure 5.34, the red-shifted contribution is [$-2B\xi$ (J+1)] (separation between R=J level and R=J-1 level). The $(\Delta\nu_{rot})_{max}$ = 5.68 cm^{-1} for J_{max} = 22 occurs for T=140 K, where J_{max}, = $(kT/2hcB)^{1/2} - 1$. The contribution from $(\Delta\nu_{rot})_{max}$ for different levels are enumerated in table 5.8. The extent to which the influence of rotational splitting can compensate the defect has always been a matter of debate and various authors have arrived at these values from the diode laser spectra of the J manifolds at different P & R branches in the ν3 mode of SF_6. [5.28, 5.34]. Cantrell [5.28] proposed a modest value of 2.43 cm^{-1} $(\Delta\nu_{rot})_{max}$.

Table 5.7. Anharmonic split vibrational energy levels in ν_3 ladder of SF_6 (in cm^{-1}) up to υ=4 [5.31].

υ=0		
(000)	A_{1g}	0.0
υ=1		
(100)	F_{1u}	947.97
υ =2		
(200)	A_{1g}	889.05
	E_g	891.60
(110)	F_{2g}	896.53
υ=3		
(300)	F_{1u}	2827.55
(210)	F_{1u}	2839.04
	F_{2u}	2840.35
(111)	A_{2u}	2845.25
υ =4		
(400)	A_{1g}	3758.89
	E_g	3759.49
(310)	F_{2g}	3774.15
	F_{1g}	3779.57
(220)	A_{1g}	3781.87
	E_g	3783.82
(211)	F_{2g}	3788.87

υ	Degeneracy in υ_3 ladder due to anharmonic splitting $(\upsilon+1)(\upsilon+2)/2$	Final degeneracy of states	Broadening due to Anharmonic Splitting $\Delta\nu_{anh} = 20/3T_{33}\upsilon^2$ (cm^{-1})	Rotational broadening due to Coriolis Splitting $\Delta\nu_{rot} = 2B\xi\,(2J_{max}+1)$ (cm^{-1})
0	1	0	0	5.68
1	3	1	-1.67	5.68
2	6	3	-6.56	5.68
3	10	4	-14.76	5.68
4	15	7	-26.25	5.68

Table 5.8. The degeneracies of different $\upsilon\nu_3$ levels of SF_6 and the associated broadenings.

υ	10P(16) line			10P(20) line		
	Harmonic ladder of 10P(16) line[1] (947.74 cm^{-1}) (in cm^{-1})	Nearest Anharmonic Split level[2] (cm^{-1}) [5.31]	Δ_{1-2} (cm^1)	Harmonic ladder of 10P(20) line[1] (944.2 cm^{-1}) (in cm^{-1})	Nearest Anharmonic Split level[2] (cm^{-1}) [5.31]	Δ_{1-2} (cm^{-1})
0	0	0	0	0	0	0
1	947.74	947.97 (A_1)	-0.23	944.2	947.97 (A_1)	-3.77
2	1895.48	1896.53 (F_2)	-1.05	1888.4	1889.05 (A_1)	-0.65
3	2843.23	2845.28 (A_2)	-2.05	2832.6	2833.30 (F)	-0.695
4	3790.97	3788.87 (F_2)	2.10	3776.8	3776.86 (F)	-0.06
5	4738.71	4732.78 (F_1)	5.93	4721.0	4721.8 (F_1)	-0.8
6	5686.44	5677.01 (A_1)	9.43	5665.2	5660.47 (F)	4.73
7	6634.18	6616.58 (F_1)	17.6	6609.4	6608.46 (F_2)	0.94
8	7581.92	7556.23 (F_2)	25.69	7553.6	7553.26 (E)	0.37

Table 5.9. The harmonic ladder of levels of the 10P(16) and 10P(20) lines, their nearest matching anharmonic split levels in the ν_3 ladder of SF_6 and the corresponding differences Δ_{1-2}.

We now look into the effect of anharmonic and rotational broadening on the resonant pumping action with the 10P(20) line. The difference ($\Delta_{1\text{-}2}$) between the harmonic ladder of frequencies corresponding to 10P(16) and 10P(20) laser lines and the nearest anharmonic split level frequencies for different values of $\upsilon\nu_3$ ladder of levels up to υ=8 are shown in table 5.9. It can be seen, both from table 5.8 & 5.9 that, the highest frequency transition near the band centre @ 947.97 cm^{-1} (10P(16) line) will be resonant only up to υ=2 ($2\upsilon_3F_{2g}$), where the vibrational bottleneck occurs. On the other hand, the CO_2 line at 944.2 cm^{-1} (10P(20)) is resonant with the anharmonic split and shifted sub-levels up to υ=8. For this line, the excitation from υ=0 to $1\nu_3$ state can occur owing to the compensation from the aforementioned vibrational and rotational detuning. The transition, $1\nu_3$ to $2\nu_3$, is relatively more straight-forward (1889.05 cm^{-1} which is nearly twice of 944.2 cm^{-1}) while the larger vibrational broadening occurring for υ > 2 owing to splitting, coupled with rotational detuning offers, for this case, a near-resonant pumping all the way up until υ=8, as is evident from table 5.9. To be noted, there is no direct reference in the literature explaining explicitly the selective excitation from υ=0 to υ=1 @ 944.2 cm^{-1} except for a general interpretation as to why the multi-photon excitation occurs in SF_6. It thus is evident that anharmonic splitting of the vibrational levels coupled with the rotational broadening enables the molecule to climb up the vibrational ladder with relative ease upon irradiation with the P(20) line.

Following this, a possible multi-photon excitation that can occur in SF_6 when it is excited by the 10P(20) line has been proposed. The schematic of this up-pumping is shown in figure 5.31. The transitions that drive the molecule up the ladder (up to υ=3) upon excitation with 10P(20) line

(944.2 cm^{-1}) understandably can proceed as,

$$(\upsilon=0, J) \xrightarrow{P(J)} (\upsilon=1, J-1) \xrightarrow{Q(J-1)} (\upsilon=2, J-1) \xrightarrow{R(J-1)} (\upsilon=3, J)$$

The energy terms corresponding to the above ro-vibrational transitions up to υ=3 are,

$\omega_e (1-2\chi_e) - 2BJ = \omega_e (1-4\chi_e) = \omega_e (1-6\chi_e) + 2BJ = 944.2\ cm^{-1}$;

Where J is the resonating rotational quantum number, 'ω_e' is the equilibrium harmonic frequency of the molecule, 'B' and 'χ_e' being the molecule's rotational and anharmonicity constants respectively.

Further, we have for the fundamental excitation (ignoring the cubic and quartic terms in the energy expression),

$\omega_1 = \omega_e (1-2\chi_e) = 947.97\ cm^{-1}$;

Solving the above system of equations, and, plugging in the appropriate value for B (table 5.6), yields $\omega_e = 951.61\ cm^{-1}$, $\omega_e\chi_e = 1.82\ cm^{-1}$ and the resonating J to be 20. The resulting $\chi_e = 1.91 \times 10^{-3}$. The molecule can therefore be excited in its vibrational ladder through the transitions as indicated below.

$$(\upsilon=0, 20) \xrightarrow{P(20)} (\upsilon=1, 19) \xrightarrow{Q(19)} (\upsilon=2, 19) \xrightarrow{R(19)} (\upsilon=3, 20) \xrightarrow{P(20)} (\upsilon=4, 19)$$

Given $J_{max} = 22$ that occurs for T = 140 K, the above transition seems plausible. To be noted here, the value of $-2\omega_e\chi_e$, corresponding to the anharmonic defect, evaluated, matches closely with that reported in literature (table 5.6).

Alternately, we bring to the fore, the possibility of a two-photon resonance to the $2\upsilon_3 A_{1g}$ level upon irradiation with 10P(20) line ($944.2\ cm^{-1}$) that has been reported [5.35] for moderate fields of intensities ~100 kW/cm^2. That, this can be further followed by near-resonant sequential pumping of the vibrational levels of the molecule as elaborated above, only accentuates the fact that pumping with 10P(20) line is indeed advantageous.

5.7. Conclusions

In the beginning of this chapter, the results of the operation, characterization and optimization of a CW-CO_2 laser with output power exceeding 14 Watt on the line with the highest gain, i.e., 10P(20) has been brought out. For this power, the optimum operating pressure was found to be 12 mbar with the partial pressures of constituent gases being CO_2:$N_{2:}$ He:: 2:2:8. Further, the output power of the laser has been studied as a function of the total operating pressure, partial pressure of the gases and the discharge current. The laser was operated in the dispersive cavity configuration and the power on various ro-vibrational transitions spanning 10R and 10P branches were measured.

Characterization of SF_6-Ar gas mixture jet was carried out to ascertain the monomer number densities in the expanding jet from their absorption studies using the above mentioned line tunable CW-CO_2 laser. Percentage of clustering in the seeded supersonic jet has been investigated experimentally. The fractional cluster number density and clustering onset temperature have been determined. Further, enrichment of sulfur isotope in the form of $^{34}SF_6$ has been realized and demonstrated by laser assisted aerodynamic scheme, wherein, the indigenous CW-CO_2 laser tuned to 10P(16) was employed for selective excitation of $^{32}SF_6$. Separation factors exceeding '2' have been achieved when the laser beam interacted with a supersonically cooled SF_6-Ar binary jet under appropriate conditions. Parametric characterization of the separation efficiency has been carried out. Also, we have established the advantage of a red-shifted intense excitation (10P(20) line of the CO_2 laser) source in furthering the enrichment efficiency of laser assisted aerodynamic separation process. This enhancement owes its origin to the efficient multi-photon excitation possible here. This has been experimentally validated in sulfur isotope separation through laser assisted aerodynamic process wherein the emission of an indigenous CO_2 laser, interacting with the SF_6-Ar binary jet, was tuned alternately to match the absorption centers' in a resonant and red-shifted

manner. A novel method based on optical absorption towards estimating the isotope separation efficiency following an enrichment process has been conceived and applied for the case of $^{34}SF_6$ isotopomer. The main advantage of this technique is that the knowledge of absorption cross-sections of different isotopes, that is many a times not so accurately known, is rendered irrelevant.

5.8. References

5.1. H. Van den Bergh, Laser and Optoelectronik, 3, 263 (1985).

5.2. J. M. Zellweger, J. M. Philippoz, P. Melinon, R. Monot, and H. van den Bergh, Physical Rev. Lett., 52, 522 (1984).

5.3. Isotope Separation by Selective Laser-Assisted Repression of Condensation in Supersonic Free Jets, Jeff W Eerkens, Jaewoo Kim, AIChE Journal, 56 (9), 2331-2337 (2010).

5.4. V. M. Apatin, V. N. Lokhman, G. N. Makarov, N.D.D Ogurok, E. A. Ryabov, J. Exptl. and Theoretical Phys. 125, 531 (2017).

5.5. V. M. Apatin, V. N. Lokhman, G. N. Makarov, N. D. Ogurok, E. A. Ryabov, Quant. Electron 48, 157 (2018).

5.6. V. N. Lokhman, G. N. Makarov, A. L. Malinovskii, A. N. Petin, D. G. Poydashev and E. A. Ryabov, Laser Phys. 28, 105703 (2018).

5.7. V. M. Apatin, G. N. Makarov, N. D. Ogurok, A. N. Petin, and E. A. Ryabov, J. Exptl. And theoretical phys. 127, 244 (2018).

5.8. Laser isotope separation: Laser uranium enrichment returns from the dead, Hecht J, Laser Focus World, 47 (10), 18 (2011).

5.9. SILEX Uranium Enrichment, SILEX Annual Report (2014), http://www.silex.com.au.

5.10. Y. Okada, S. Yamaguchi, K. Talkeuchi, Appl. Phys.B, 72, 507-513 (2001).

5.11. Frenkel J, Kinetic Theory of Liquids. Dover, New York (1955).

5.12. Feder, J, Russel K C, Lothe J and Pound G. M. Adu. Phys. 15: 111-178 (1966).

5.13. Andres, R. P. In Nucleation (A. C. Zettlemoyer, ed.), Dekker, New York (1969).

5.14. Dunning, W J, In Nucleation (A. C. Zet-tlemoyer, ed.), Dekker, New York (1969).

5.15. Y. Okada, K. Ashimine, K. Talkeuchi, Appl. Phys.B, 70, 117 (2000).

5.16. J B Anderson, Molecular beams and low density gas dynamics, ed. P P Wegner pp 1-91, (1974).

5.17. The CO_2 laser, W J Witteman, Springer Verlag, New York (1987).

5.18. Molecular beam infrared laser photo-dissociation of van der Waals molecules containing SF_6, T. E. Gough, D. G. Knight, P. A. Rowntree, and G. Scoles, J. Phys. Chem, 90, 4026(1986).

5.19. Molecular Theory of Gases and Liquids, J O Hirschfelder, John Wiley & Sons, Inc. (1954).

5.20. Bird, Stewart, Lightfoot: Transport Phenomena, 2nd edition, John Wiley & Sons, Inc, New York (2002).

5.21. Molecular Laser Isotope Separation, Los Alamos Science No. 4, 3 (1) Winter/spring (1982).

5.22. Separation of Isotopes by Laser-Assisted Retardation of Condensation (SILARC), Jeff W. Eerkens, Laser and Particle Beams, 16 (2), 295-316 (1998).

5.23. Selective Dissociation of Sulfur Hexafluoride by Intense CO_2 Laser Radiation in Pulsed Gas Dynamic Flow, G N Makarov and A N Petin, High Energy Chemistry, 34 (6) 384-388 (2000).

5.24. Explanation of the selective dissociation of the SF_6 molecule in a strong IR laser field, R.V. Ambartzumyan, Yu.A.Gorokhov, V. S. Letokhov, G. N. Makarov, and A. A. Puretskii, JETP Letters, 23, 22 (1976).

5.25. R.V. Ambartzumyan, V. S. Letokhov, E A Ryabov, N V Chekalin JETP Letters, 20, 273 (1974).

5.26. R.V. Ambartzumyan, Yu.A.Gorokhov and G. N. Makarov, JETP Letters, 21, 171 (1975).

5.27. Anharmonic splitting and vibrational energy levels of octahedral molecules: Application to the $n\nu_3$ manifold of $^{32}SF_6$, Craig C Jensen et al, Optics Communications, 20, No.2, 275-279 (1977).

5.28. Towards an explanation of collision-less multiple-photon laser dissociation of SF_6, C D Cantrell et al, Optics Communications, 18, No. 4, 513-516 (1976).

5.29. Effects of anharmonic splitting upon collision-less multi-photon laser excitation of SF_6, C D Cantrell et al, Optics Communications, 374-378 (1977).

5.30. Multi-photon excitation of vibration-rotation states in the ν_3 mode of SF_6, D P Hodgkinson et al, J. Phys. B, At. Mol. Phys., 14, 1803-1814 (1981).

5.31. ν_3 vibrational ladder of SF_6, Chris W Patterson et al, Optics Letters, 6, No.1, 39-41 (1981).

5.32. Molecular reaction dynamics and chemical reactivity, Raphael D Levine, Richard B. Bernstein, Oxford University Press; Revised edition (1987).

5.33. Diode laser spectroscopy of the dynamics of multiphoton excitation of SF_6 molecules by CO_2 laser pulses, Yu A Kuritsyn et al, Laser Chemistry, 8 151-68 (1988).

5.34. The perturbations of line frequencies in high-J manifolds of the ν_3 band of SF_6, Burton J Krohn, Journal of Molecular Spectroscopy, 73, Issue 3, 462-74 (1978).

5.35. Excitation spectrum of SF_6 irradiated by an intense IR laser field, S. S. Alimpiev, N. V. Karlov, E. M. Khokhlov, S. M. Nikiforov, A. M. Prokhorov, B. G. Sartakov, A. L. Shtarkov, Topics in Current Physics, Multiple-Photon Excitation and Dissociation of Polyatomic Molecules, Editor: C D Cantrell, Springer Verlag, 149-58 (1986).

Chapter 6: Application of Continuously Tunable Coherent 5 μm Source in Isotope Selective Studies & Some Important Aspects of Aerodynamic Gas Jets

6.1. Introduction

The importance of ^{124}Sn as detector element in neutrino-less double beta decay experiments [6.1, 6.2] is well recognized for its better sensitivity, and, enrichment of this isotope is therefore, of relevance. A complete knowledge of the spectroscopy of the molecule under consideration is an essential pre-requisite for any laser based isotope separation scheme. Based on the available information in the literature, it was found that Organo-tin compounds [6.3, 6.4] with their Sn-H stretching frequency (fundamental ν_3 mode) lying in the region of 1800-1900 cm^{-1} have good absorption in the 5 μm spectral region that can be reached by frequency doubled emission of a CO_2 laser as discussed in chapter 2. Di-methyl Stannane ($(CH_3)_2SnH_2$), a methyl substituted stannane (SnH_4), was found to be the most appropriate molecule for effecting this scheme as it has a high vapor pressure (530 torr) at ambient temperature in addition to being relatively stable. To this end, we have undertaken isotope selective absorption studies in the Di-Methyl Stannane-Helium binary jet by

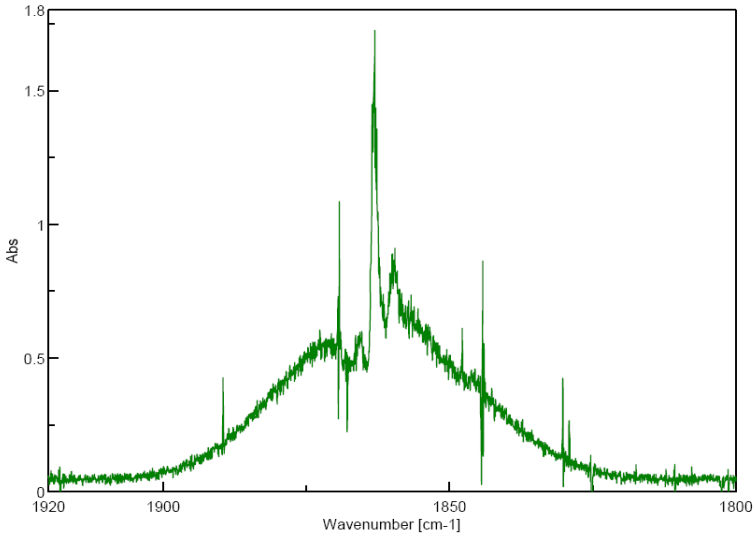

Figure 6.1. Room temperature FTIR spectrum of DMS showing the definite PQR band contour for Sn-H stretching vibrational frequency obtained for 7 torr sample pressure at a resolution of 0.07 cm^{-1}.

employing the continuously tunable 5μm source [6.5]. The shift in the absorption peaks of two of its isotopes could be measured experimentally and was found to be in agreement with the theoretical estimate. The details pertaining to this work are discussed in section 6.2.

In the next part of this chapter, some essential aspects pertaining to aerodynamic separation process have been discussed. As has been described in chapter 1, laser assisted aerodynamic separation process is intrinsically more effective in the separation of dissimilar gases with inherent high relative mass difference [6.6]. Imposing condensation repression by means of isotope selective vibrational excitation by employing an appropriate coherent source makes the scheme amenable to separation of both lighter and heavier isotopes [6.7-6.16] making it a viable alternative to conventional molecular laser isotope separation method that is based on classical multi photon dissociation route [6.17]. However, this scheme, though not photon intensive, suffers from lengthy homogenization time and also dilution of the enriched stream owing to the large mismatch in the nozzle opening duration and the laser pulse duration. A practical method to overcome the former and alleviate the latter by imposing forced circulation of the feed and rim gases shall be discussed at length in this chapter. The forced circulation of the feed gas resulted in drastic reduction in the mixing time of the process and the buffer gases, while recirculation of the rim gas that is mostly unseen by the pulsed laser, back

Temperature	**298K**	**200K**	**150K**	**100K**	**77K**	**50K**	**30K**
Percentage of ground state population of Me_2SnH_2	2.64	10.16	25.44	40.72	56.40	80.32	95.98

Table 6.1. % of total population residing in the ground state of Me_2SnH_2 as a function of temperature.

into the feed vessel allowed its increased interaction with the laser beam reducing the dilution in enrichment to a certain extent. The details of this work are discussed in section 6.3 of this chapter.

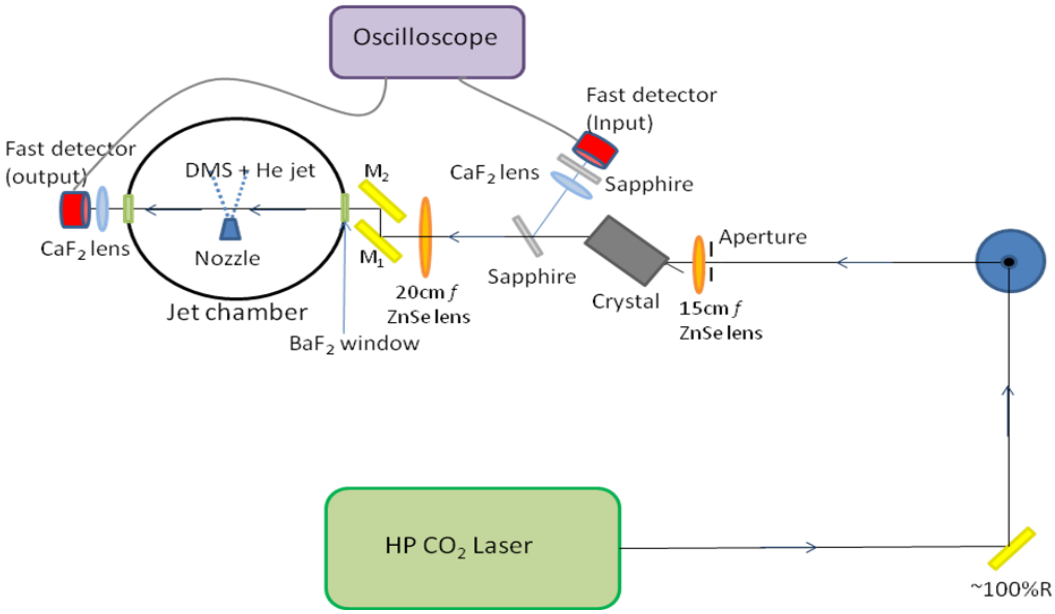

Figure 6.2. Schematic of the experimental set-up comprising the jet expansion chamber, SHG setup involving an $AgGaSe_2$ crystal and the continuously tunable HP-CO_2 laser for carrying out spectroscopy studies in DMS-He binary jet. Sapphire plates were used appropriately to block the 10 μm pump beam while transmitting 5μm output.

6.2. Isotope selective absorption studies in the DMS-He binary jet by employing the continuously tunable coherent 5 μm source

The synthesis and purification [6.18] of the working molecule, DMS, was carried out in-house and the purity of the synthesized compound ascertained by NMR studies [6.18]. FTIR (JASCO/ FTIR-6300) spectrum of DMS at a resolution of 0.07 cm^{-1} was obtained at room temperature for 7 torr sample pressure towards gaining a firsthand knowledge of the rotational structure of the stretching mode (ν_3) and the same is depicted in figure 6.1. The infrared spectrum clearly reveals the fundamental ν_3 band with a sharp peak centered at 1862.9 cm^{-1} corresponding to the Q branch transitions. It is evident that the rotational

structure, however, is totally smeared revealing the typical PQR contour alone. This is due to the fact that, DMS being a heavy, polyatomic molecule, a large number of vibrational levels in the electronic ground state are significantly populated at room temperature at which the FTIR spectrum was taken, with a mere ~3% population in its ground vibrational state. Table 6.1 shows the population in the ground vibrational level as a function of temperature for this molecule that has been obtained by invoking the vibrational partition function. The absorption occurring in the rotational manifold of these vibrational states therefore results in the blurring of the spectrum at ambient temperature. The transitions corresponding to different ro-vibrational transitions of the ν_3 mode of DMS can be resolved if the spectrum of DMS is recorded at a lower temperature where the majority of the population is arrested in the ground vibrational state. However, the absence of any vapor pressure at such low temperatures renders spectroscopic measurements in static cooled conditions totally impossible. We therefore have attempted to carry out the absorption studies in DMS under dynamically cooled conditions by gainfully employing a nozzle based expansion scheme. As discussed in the earlier chapters, polyatomic molecules seeded in an inert carrier gas subjected to supersonic nozzle expansion undergo relaxation of their translational, rotational and vibrational degrees of freedom via two body collisions during their transit in the jet thereby providing ideal cooling conditions for carrying out any spectroscopic studies.

6.2.1. Experimental work

The schematic of the experimental setup towards carrying out absorption studies in the DMS-He binary gas jet at different downstream distances by employing the continuously tunable 5μm source generated by the frequency doubling of the emission of HP-CO_2 laser [6.5] as the excitation source is shown in figure 6.2. DMS exhibits strong absorption in the R branch around 1865 cm^{-1} that is accessible by frequency doubled emission of CO_2 laser on 10P(32)

line. As the emission of the high pressure laser was tuned in steps of 0.1 cm^{-1}, the 5 μm source could also be tuned in steps of 0.1 cm^{-1} across this absorption feature.

The DMS-He gas mixture was fed to a pulse nozzle (diameter: 800 μm, duration: 500 μsec, 5 Hz) at 1.5 bar stagnation pressure and allowed to expand into a volume that is maintained at a background pressure of 10^{-4} torr by means of a diffusion pump (2000 lt/sec). The process of gas mixing involved allowing Helium to bubble through the liquid of DMS (vapor pressure ~530 torr, boiling point ~35°C) contained in a bubbler maintained at room temperature. Helium, owing to its very low boiling point (~4 K), helps the seed DMS to remain in its monomer form by preventing any clustering that might occur otherwise owing to the low temperatures in the expanding supersonic jet thereby facilitating its spectroscopy studies. The partial pressure of DMS in the mixture could be varied by varying the flow rate of helium. The gas mixture being fed to the nozzle was sampled for FTIR studies and the flow rate was such that the partial pressure of DMS in Helium was ~50%. The pump laser was made to lase on a well-defined TEM_{00} mode (line width ~500 MHz) by the use of an intra-cavity aperture. The generated 5 micron beam after its appropriate focusing to a spot diameter of ~300 μm on the axis of the jet was steered into the jet chamber with the help of mirrors M_1, M_2. BaF_2 windows at the entrance and exit ends of the expansion chamber allowed the transport of the laser beam in and out of the chamber. A cylindrical jig concentric to the nozzle assembly with a 1 mm x 10 mm slot in it facilitated the alignment of the laser beam with the jet centerline. Translation of M_2 (figure 6.2) by means of a high resolution micrometer (L.C. = 10 μm) allowed scanning of the jet by the laser beam, along its centerline, downstream the nozzle exit. The absorption of the 5 μm beam in the jet was estimated by monitoring the input power I_o (Fresnel reflection off the sapphire plate) recorded by a fast room temperature MCT detector (PEML3, Vigo Systems) and the corresponding transmitted power (I_t) by a similar detector placed behind the exit port of the chamber (figure 6.2). Short focal length CaF_2

lenses were made use of to accentuate the power on the detector elements. Absorption measurements were carried out for cases of two different downstream distances along the jet centerline, viz., at 1.5 mm and at 3.5 mm, as the laser beam was tuned in steps of 0.1 cm^{-1} spanning over a region of ~0.6 cm^{-1}. Each measurement involved averaging over 124 laser pulses to ensure a good S/N ratio.

6.2.2. Results & Discussion

Figure 6.3 a and 6.3 b show the spectra of DMS obtained from the absorption measurements in the jet at 1.5 mm and 3.5 mm downstream the nozzle respectively. Two distinct absorption peaks separated by ~0.2 cm^{-1} pointing to absorption in two different isotopes for the same vibrational-rotational transitions are clearly observed in figure 6.3 a, for the case of 1.5 mm.

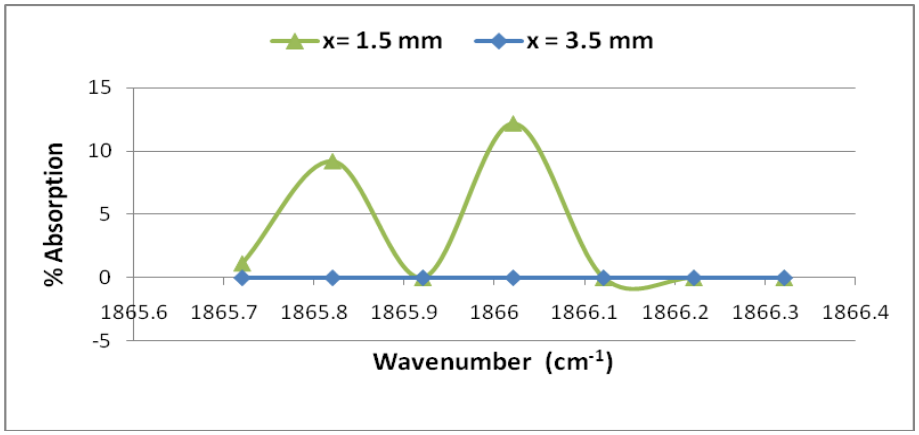

Figure 6.3. Spectrum of DMS at high resolution showing well pronounced structures near the R branch region obtained at a) x = 1.5 mm at 0.1 cm^{-1} resolution, b) at x= 3.5 mm (0.1 cm^{-1} resolution) where no absorption was detected. (800 µm ≡ 1 nozzle diameter).

When the laser beam was scanned at 3.5 mm downstream the nozzle exit (figure 6.3 b), no absorption in DMS was detected probably owing to the low number densities at this distance. It is clear that the dynamic cooling obtained in the jet allowed the resolution of the vibrational-rotational transitions leading to isotope-selective absorption. Studies of estimating the isotopic shifts of fundamental vibrational frequencies of stannanes (SnH_4) have also been carried out using the ab-initio density functional theory (DFT) methods [6.19]. Based on this study, DMS has an estimated isotope shift of ~0.16 cm^{-1} in the Q branch between two

alternate isotopes. The 0.2 cm^{-1} observed experimentally in the R branch is therefore understandable. Towards estimating the temperature in the expanding jet at 1.5 mm from the nozzle exit where isotope-selective absorption was seen, the same was computationally

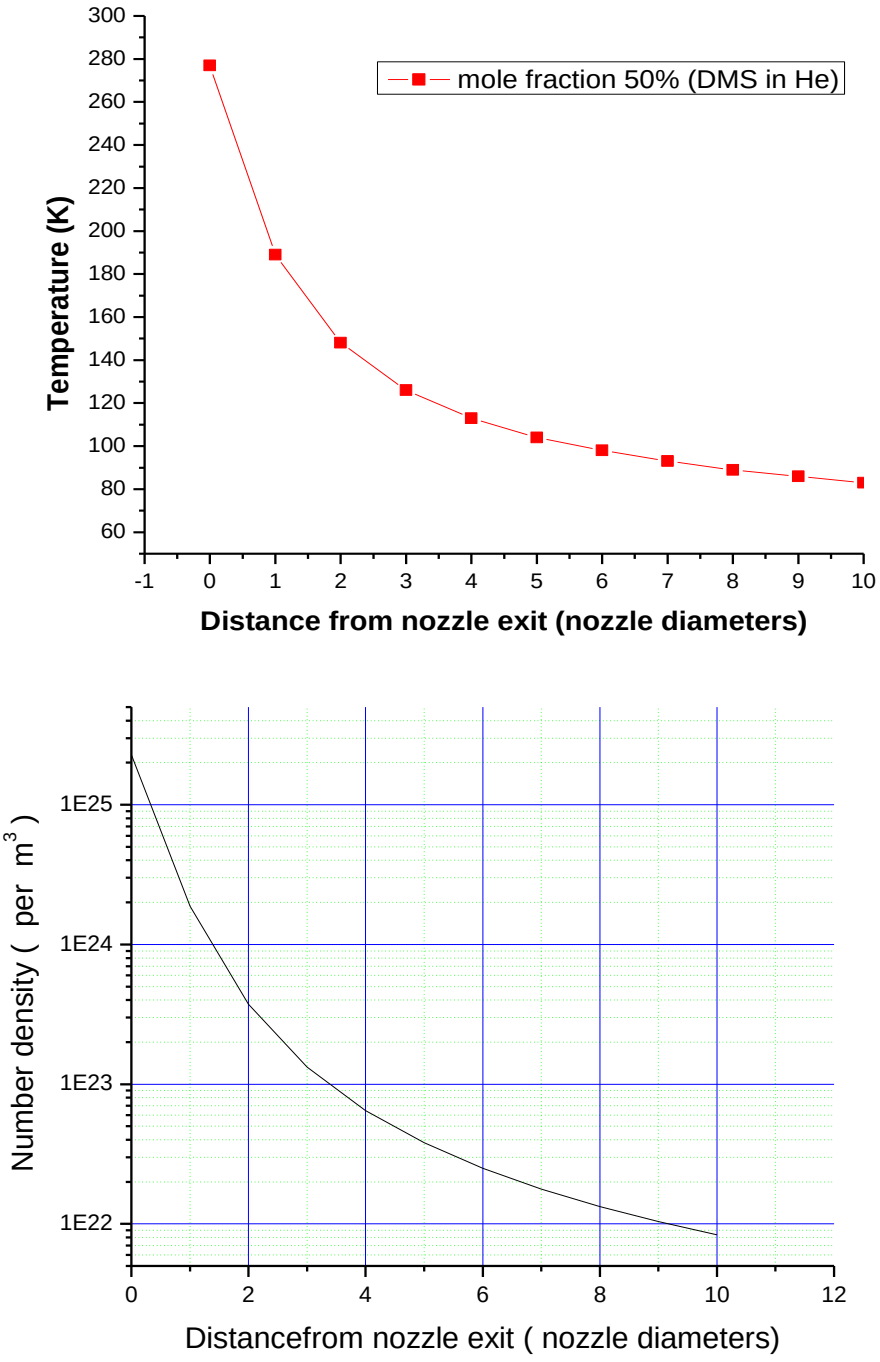

Figure 6.4. Plots of static temperature (top) and number density (bottom) as a function of distance for 50% DMS in He and 1.5 bar stagnation pressure.

calculated and is depicted in figure 6.4 together with the number density variation. It can be seen that, at 1.5 mm downstream the nozzle along the jet centerline, the temperature was ~150K that facilitated resolving the absorption feature of the neighboring isotopes. This experiment clearly established the efficacy of isotope selective spectroscopy of supersonic jets leading to its potential application in isotope separation by aerodynamic process.

6.3. Practical Techniques to Homogenize the Feed Gas Mixture and Enhance the Laser-Jet Interaction Time in Laser Assisted Aerodynamic Separation Studies

We have, in the past [6.20] successfully demonstrated the separation of Sulfur isotopes through laser assisted aerodynamic separation process as discussed in chapter 5 where the CW-CO_2 laser, developed in-house, capable of delivering ~10 W output on 10P(20) transition, was made use of to selectively excite $^{32}SF_6$ in a SF_6-Ar binary CW jet. Usage of a premixed SF_6-Ar gas cylinder ensured homogenized gas feed to the CW nozzle, while usage of a CW laser in conjunction with this CW nozzle assured complete temporal overlap between the laser emission and the gas jet. However, as we moved on to apply this scheme to enrich heavier isotopes, viz., say, Molybdenum (Mo) for which the working molecule is MoF_6, both these issues, i.e., homogenization and dilution became a cause of concern. While safety and cost do not allow us to stock large quantities of the process gas thereby increasing the time taken in homogenizing the process and the buffer gas prior to subjecting it to aerodynamic expansion, the poor excitation cross-section here makes the usage of a pulsed CO_2 laser (for excitation of the combination band, $\nu_3+\nu_5$, band of MoF_6 centered around 1050 cm^{-1}, that can be reached by TE CO_2 laser) as the excitation source mandatory thereby drastically reducing the degree of overlap between the gas stream and the laser emission. The exact nature of these problems and the various measures adopted thereof towards curtailing the same are as discussed below.

The time taken for homogenization of the process and the buffer gas, often, can be too long, in particular, when it involves a heavier process gas [6.21]. The coefficient of diffusion, D_{AB}, of a binary gas mixture is $\propto \frac{1}{P\sqrt{M_{AB}}}$ [6.21], where P is the pressure and M_{AB}, the molecular weight of the gas mixture. This creates an experimental hindrance as the process and the buffer gases cannot be mixed apriori owing to the process gas being radiological/toxic. The necessity to vary the ratio of the mixing during experimentation and the low vapor pressure of the process gas [6.22] can further increase the complexity. It is therefore essential to ensure that the feed gas, as it is fed to the nozzle, is a homogenous mixture. To this end, a novel and practical method of homogenization of feed and buffer gas mixture has been devised and the results are discussed herein. Further, the nozzle & skimmer throughputs for a 150 micron CW nozzle and 1 mm skimmer diameter were measured experimentally; as generally, estimation of skimmer throughput theoretically is not straightforward. An ingenious method of enhancement of the laser-jet interaction time for efficient laser assisted aerodynamic separation has also been demonstrated. This becomes important especially when pulsed laser capable of providing intensities in the range of hundreds of kW/cm^2 to 10's MW/cm^2 is often made use of in case of certain molecules owing to their poor absorption cross-sections for efficient isotope selective photo-excitation [6.23]. Since the laser is pulsed, ideally the nozzle jet stream should also be in the pulsed mode. However, the fastest pulse valves available commercially have typical opening times of several hundreds of microseconds, much too long compared to the duration of the laser emission (typically hundreds of nanoseconds for a pulsed CO_2 laser and mid-infrared lasers pumped by it), resulting in very negligible fraction of the molecules in the jet actually interacting with the laser beam. This thereby results in dilution of any enrichment that might have occurred during the laser-jet interaction period. To this end, a novel method of re-circulating the gas through the nozzle repeatedly so as to enable its interaction with the laser was envisaged, that

eventually led to an increase in the laser-jet interaction time by a factor of '20'.However, the mismatch being much too high, the dilution of the product still remains a cause of concern. We note here that efforts have been expended in the past to reduce dilution by way of illuminating an extended region of the jet [6.24] that, in turn, has the effect of reducing the density of photons in the interaction zone making it applicable only when the absorption cross-sections are high.

6.3.1. Experimental work

Firstly, towards evolving a practical method of homogenization of the process and the buffer gases, we conducted a preliminary experiment to study the natural mixing process of SF_6 and N_2 gases. A feed vessel of volume ~1.5 litres was filled initially with SF_6 at a partial pressure of ~50 mbar followed by flowing N_2 also from the same end to make the total pressure ~500 mbar (figure 6.5). Gas samples were collected at regular intervals from the other end of the feed vessel and analyzed by FTIR to ascertain the SF_6 concentration. The experiment was repeated for a total pressure of 1000 mbar while the partial pressures of the constituent gases were maintained the same. Figure 6.6 shows the change in SF_6 concentration as a function of time in the two cases. Since the order of filling of the feed cell is SF_6 gas first followed by N_2, and given the location from where the sample is drawn (figure 6.5) (to be noted a very small quantity of the sample only was drawn each time for sampling), the measured initial samples are enriched in SF_6. With

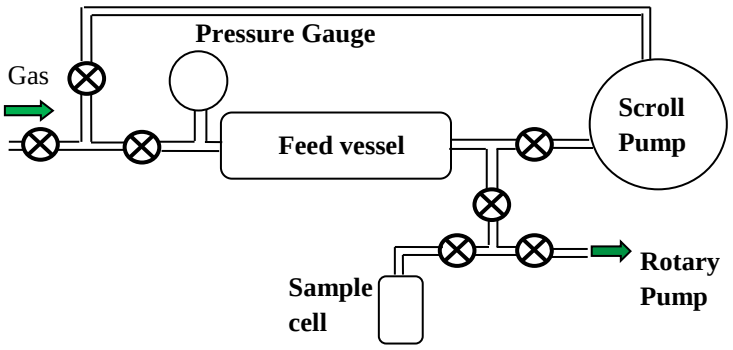

Figure 6.5. Schematic diagram of the set-up used for filling the feed vessel. Forced homogenization required usage of a scroll pump in conjunction with appropriate control valves. Arrangement to collect the sample for analysis is also shown.

time, this slowly approached the concentration at which filling was done. It can be seen that the homogenization time exceeded 24 hours in case of higher filling pressure while it was marginally faster when the total pressure was 500 mbar. This is understandable as greater the pressure, smaller the mean free path [6.21] and hence slower the rate of homogenization. In case of heavier process gases at the same temperature, the homogenization would only take even longer [6.21] making the natural mixing method impractical for studies on laser assisted aerodynamic separation processes for aforementioned reasons.

In the next set of experiments we attempted to expedite the process of homogenization by way of using an oil free scroll pump to re-circulate the gas mixture through the feed vessel (figure 6.5). The SF_6 concentration in the feed sample as a function of time was analyzed and the resulting dependence is as shown in figure 6.7. A dramatic reduction to within minutes in the time taken for homogenization is evident. It was further confirmed that the homogenization time didn't have a strong dependence on the total feed pressure or individual partial pressures. To be noted is that, mass spectrometric measurements also corroborated the FTIR results.

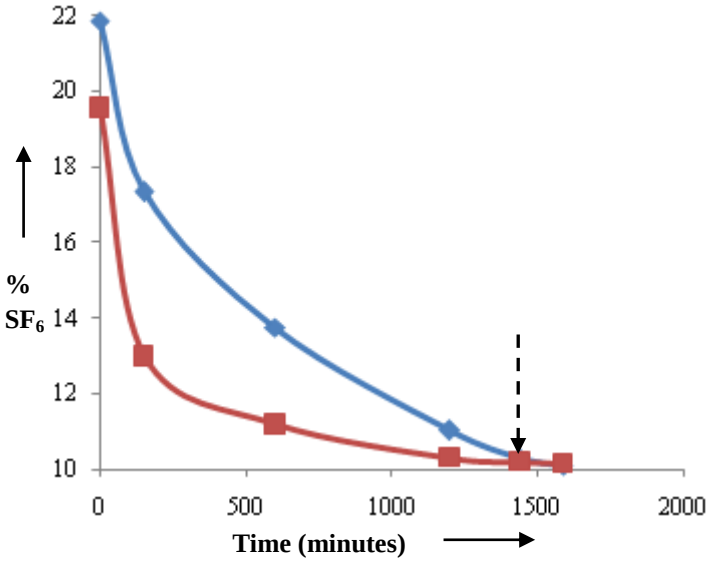

Fig 6.6. Change in the SF_6 concentration in the feed mixture as a function of time for two different initial pressures at 500 mbar (red) and at 1000 mbar (blue) during natural homogenization as estimated by FTIR. The dashed vertical arrow indicates an elapsed time of 24 hours.

6.3.2. Measurement of Nozzle and skimmer throughputs

Schematic diagram of the laser assisted aerodynamic separation experimental set-up used for Sulfur isotope separation [6.20] is as shown in figure 6.8. The schematic of the set-up for nozzle, skimmer throughput measurements is shown in figure 6.9. The AutoCAD drawing of the nozzle-skimmer assembly used for the experimental work is shown in figure 6.10. The 2D view of the same is shown in figure 6.11. The photograph of the CW nozzle-skimmer assembly is shown in figure 6.12. The entire assembly was housed inside the jet chamber as shown in figure 6.13. The binary gas mixture maintained at a pre-determined stagnation pressure is expanded supersonically through the CW nozzle into the evacuated jet chamber. The emission of the CW laser, appropriately focused, interacted with the jet at a desired downstream location resulting in selective excitation of the lighter species. In the present case involving separation of heavier isotopic species, e.g., Mo, wherein a pulsed laser alone can meet the required photon density [6.25-6.27], usage of a pulsed nozzle is unavoidable. This, as stated before, invariably would give rise to dilution of the enriched stream. The skimmer throughput being only a small fraction of the nozzle throughput, a large fraction of process gas, mostly unseen by the laser, also forms part of the rim gas.

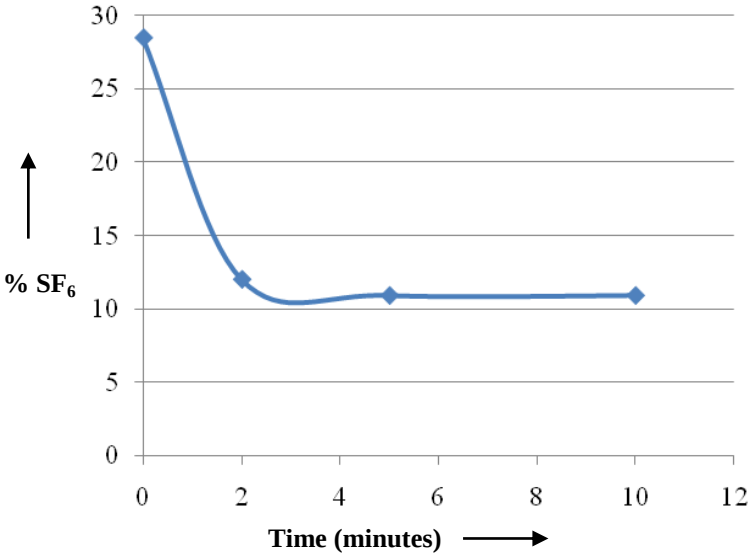

Figure 6.7. The change in SF_6 concentration as a function of time during forced homogenization.

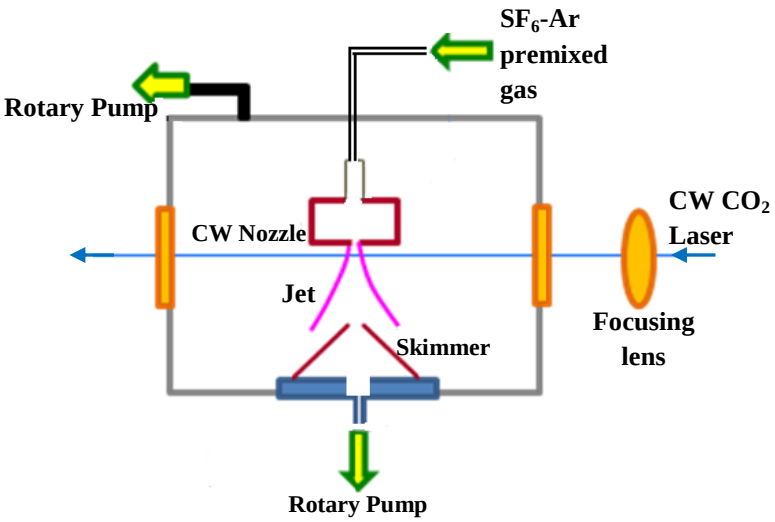

Figure 6.8. Schematic of the experimental set-up used for separation of Sulfur isotopes by laser assisted aerodynamic process.

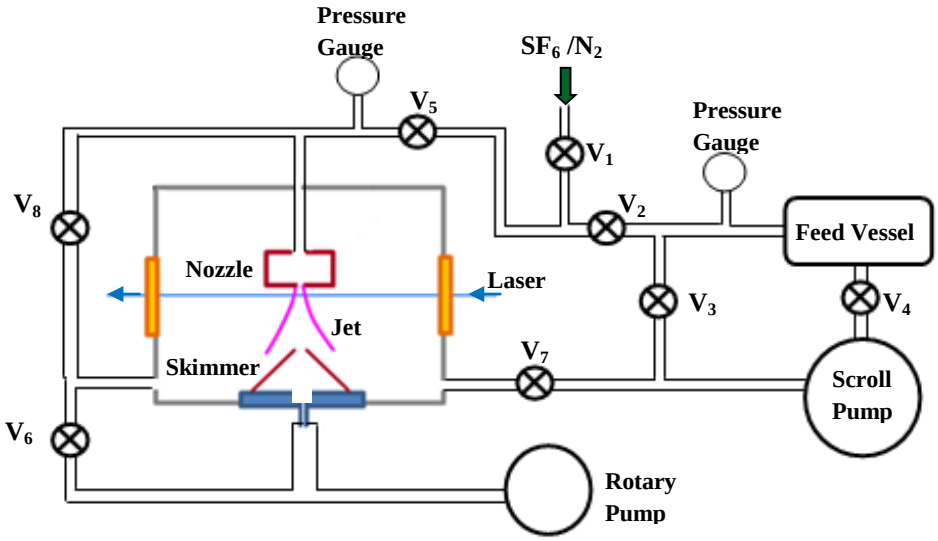

Figure 6.9. Schematic diagram of the experimental set-up used for feed gas homogenization, nozzle and skimmer throughput measurements, and operation in rim gas recirculation mode. The valves V_3 and V_4 were kept open for feed gas homogenization. V_2, V_5, V_6, were in open condition for nozzle throughput measurements while V_2, V_5, V_7 and V_4 were opened for skimmer throughput measurements.

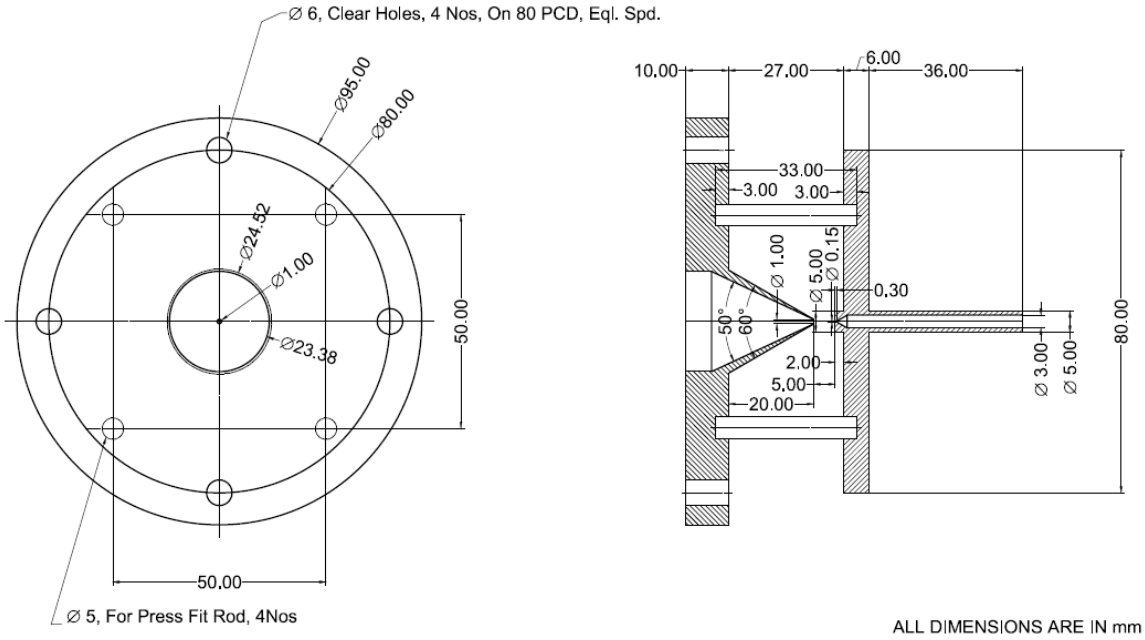

Figure 6.10. AutoCAD drawing of the nozzle-skimmer assembly; nozzle diameter = 150 μm, skimmer diameter 1 mm, spacing between nozzle-skimmer = 5 mm.

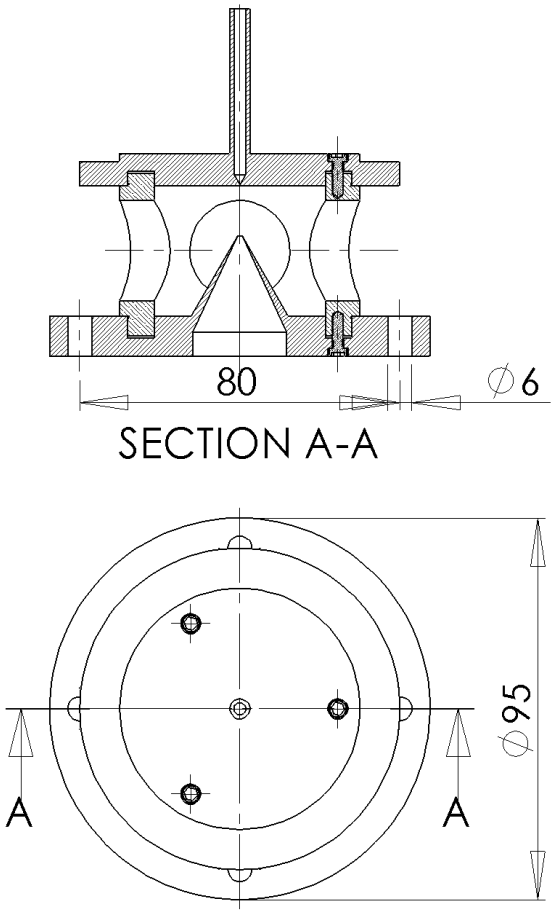

Figure 6.11. The 2-D drawing of the nozzle-skimmer assembly.

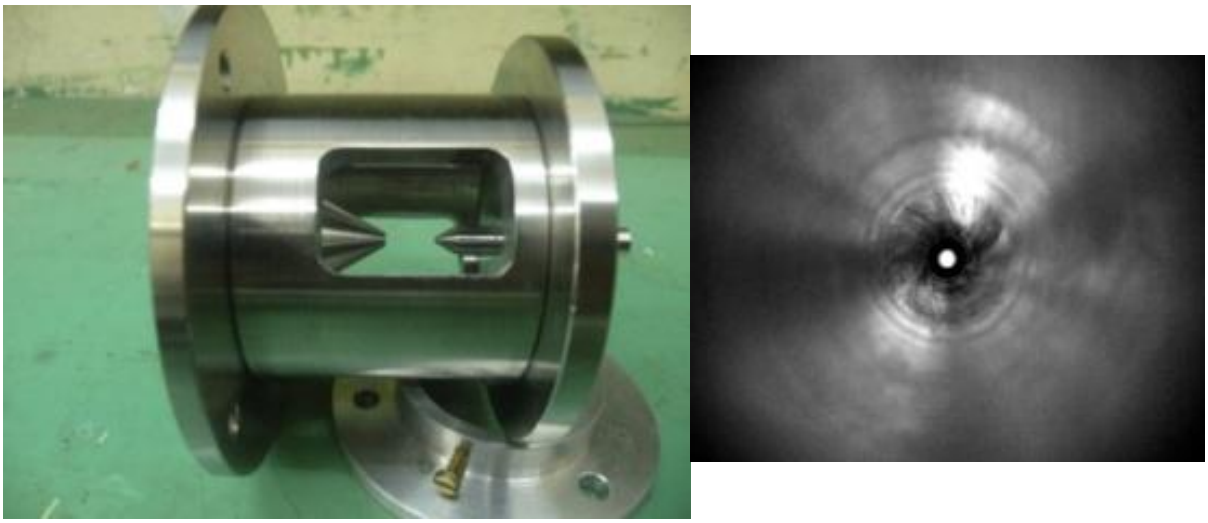

Figure 6.12. The nozzle-skimmer assembly used in the experimental work. The diameter of the exit of the nozzle is 150 μm and that of skimmer is 1 mm. To the right is shown the photomicrograph indicating their co-linearity.

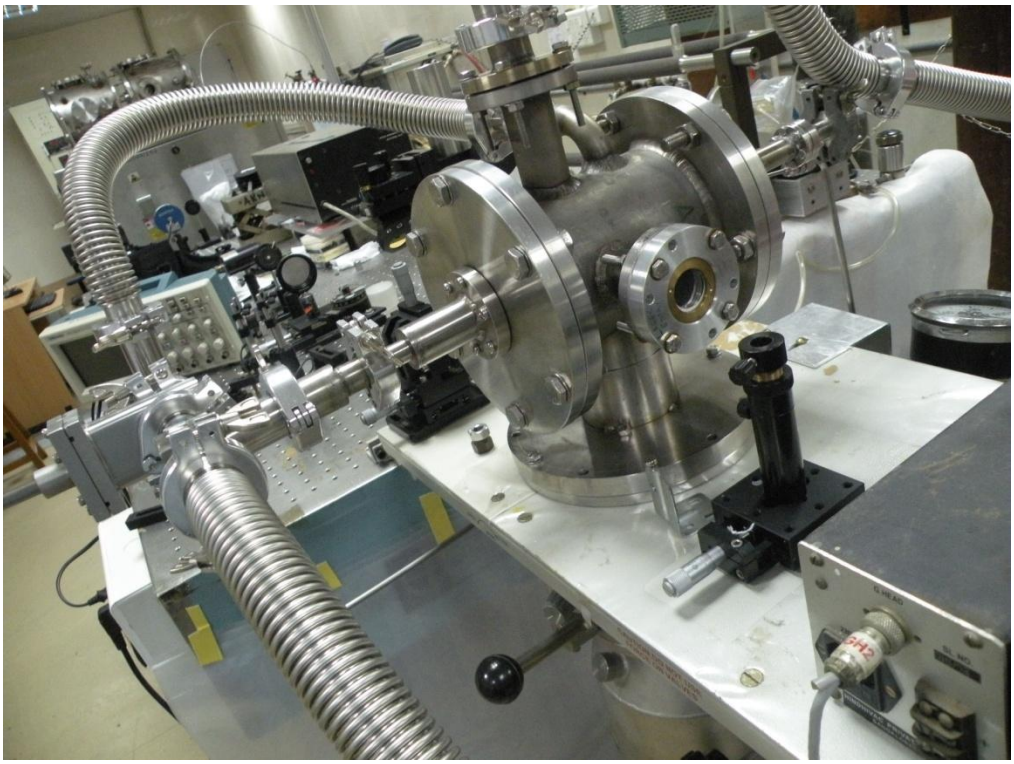

Figure 6.13. Experimental chamber in which the nozzle-skimmer assembly is housed.

It is, therefore, advantageous to reutilize the rim gas by allowing it to pass through the nozzle repeatedly. This is possible by re-circulating the rim gas of the jet chamber back into the feed vessel by means of a dry pump and allowing the same to go through the nozzle. Since the same gas encounters the laser beam repeatedly, it amounts to an increase in the interaction time of the laser beam with the jet, or in other words off-setting the dilution to some extent. We modified the experimental set-up used for Sulfur enrichment experiments by incorporating a dry oil free scroll pump (Edwards make, 35 m^3/hr) to serve the dual purpose of recirculation of the feed gas that hastens the homogenization process and of recirculation of the rim gas that increases the overlap of the laser beam with the expanding jet (figure 6.9).

To experimentally validate the extent of increase in the temporal overlap, we made use of a CW nozzle with a circular orifice of diameter 150 μm (figure 6.12) in conjunction with a pulsed CO_2 laser of emission duration ~1 μsec focused to a spot size of ~300 μm matching with the jet diameter at the nozzle exit. SF_6 diluted in N_2 served as the feed gas. Since the experiment is only to study the effectiveness of recirculation in increasing the interaction between jet and laser beam, a CW nozzle was employed for simplicity. The nozzle and the skimmer throughputs were deduced experimentally without and with recirculation of the rim gas respectively in the following manner.

SF_6-N_2 gases in the ratio of 1:9 were introduced into the feed vessel (volume 1.5 litres) at a total pressure of 800 mbar and homogenized through forced circulation by means of the dry scroll pump. Supersonic expansion of the gas mixture, maintained at a stagnation pressure of 400 mbar by means of fine control needle valve V_5, was achieved through the nozzle into a rotary pump evacuated chamber (figure 6.9). Valve V_6 in the open condition allowed direct evacuation of the jet chamber thereby maintaining the background pressure sufficiently low so as to avoid the formation of any shock [6.8]. For a known volume of the feed vessel, the

rate of change of feed gas pressure as a result of gas flow is a direct measure of the nozzle throughput. We measured a flow rate of 50.5mbar-lit/min that translates into a mass flow rate of 1.45×10^{-6} Kg/sec through the nozzle. The nozzle throughput has also been estimated by isentropic relations for choked flow conditions as below.

Total pressure of the SF_6 +N_2 gas mixture = 800 mbar.

Stagnation pressure =400 mbar.

Ratio of SF_6:N_2 filled in the 1.5 litre feed vessel =1:9

Mole fraction of SF_6 = 0.1 (Partial pressure of SF_6 in the gas mixture =10% of 800 mbar = 80 mbar)

Mole fraction of N_2 = 0.9 (Partial pressure of N_2 in the gas mixture =90% of 800 mbar = 720 mbar)

Molecular mass of the mixture,

$M_{mix} = x_{SF6} * M_{SF6} + x_{N2} * M_{N2}$,

where, x_{SF6}, x_{N2}, corresponds to the mole fractions and M_{SF6}, M_{N2}, their respective masses.

$M_{mix} = 0.1 * 146\ gm/mol + 0.9 * 28\ g/mol$ = 39.8 gm/mol

We know,,

$\frac{1}{\gamma_{mixture}-1} = \frac{x_{SF6}}{\gamma_{SF6}-1} + \frac{x_{N2}}{\gamma_{N2}-1}$, where, $\gamma_{SF6} = 1.09$ and $\gamma_{N2} = 1.4$.

yielding, γ_{mix} = 1.2975.

Recalling equations, 1.20 and 1.21, the isentropic relations for compressible fluid flow under choked flow conditions, as discussed in section 1.6.3 of chapter 1,

$\frac{T^*}{T_o} = \frac{2}{\gamma+1}$

$\Rightarrow T^* = 261.15$ K for a stagnation of $T_o = 300$ K

Using equation 1.13 of section 1.6.3 from chapter 1, for determination of sonic velocity at the throat yields,

$$a^* = \upsilon^* = \sqrt{\frac{\gamma RT}{M}} = 266.05 \text{ m/sec}$$

From equation 1.21, $\frac{P^*}{P_o} = \frac{T^*}{T_o} = \left(\frac{2}{\gamma+1}\right)^{\gamma/\gamma-1}$

Plugging in the necessary values for the gas mixture yields,

$\frac{P^*}{P_o} = 0.546.$

We know that, $\rho^* = \frac{P^* M}{RT^*}$

Plugging in the necessary values yields, one obtains, $\rho^* = 0.4005 \text{ kg/m}^3$

Area at the throat of the nozzle, $A^* = \frac{\pi D^2}{4} = 1.77\text{x}10^{-8} \text{ m}^2$ for D = 150 μm.

The throughput as defined in section 1.6.3 of chapter 1, is given by, $\dot{m} = D.C. * \rho^* * A^* * v^*$; where, ρ^*, A^*, v^* are the density, throat area, velocity of the expanding gas under choked flow conditions respectively and D.C. is the discharge coefficient (=0.82 for high speed flows) as discussed in section 1.6.3 of chapter 1.

Substituting the values for the present experimental conditions evaluated above, yields a throughput of 1.52 $\times 10^{-6}$ kg/sec indicating near match with the experimentally obtained value of 1.45×10^{-6} Kg/sec.

We next measured the skimmer throughput experimentally in the following manner. The valve V_6 was now closed while the rim gas was re-circulated back into the feed vessel by means of the scroll pump

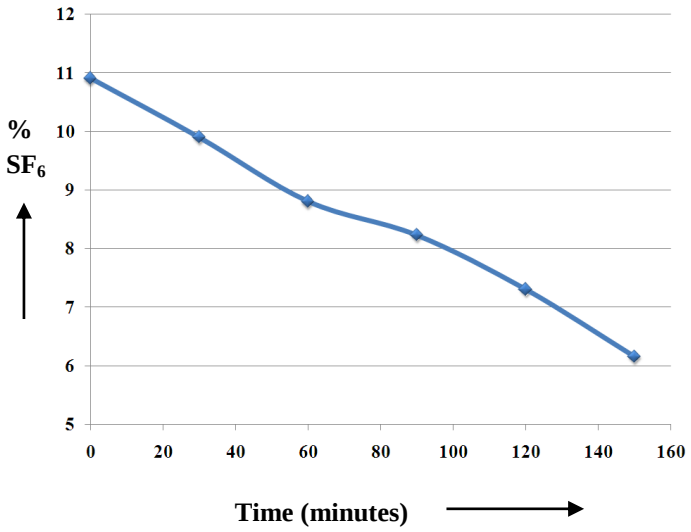

Figure 6.14. Change in SF_6 concentration in the feed gas measured by FTIR as a function of recirculation time.

with valves V_4 and V_7 in open condition (figure 6.9). The central stream of the jet was skimmed by making use of a conical skimmer of 1 mm diameter placed at a distance of 5 mm from the nozzle exit. Differential pressure across the skimmer (between the jet chamber and the beam chamber (post skimmer)) was maintained by a rotary pump of an appropriate pumping speed. The loss of feed material can now occur only through the skimmer and can therefore be quantified from the drop in the feed vessel pressure which was measured in this case to be ~2.68 mbar-lit/min that, in turn, corresponds to ~5.3% of the nozzle throughput.

6.4. Results & Discussion

Having estimated the nozzle throughput for our experimental conditions, it is straightforward to work out the total duration for which an experiment can last maintaining the stagnation pressure of 400 mbar at the nozzle input. At an average gas flow rate of 50.5mbar-lit/min, the flow through the nozzle can be sustained for ~12 minutes beyond which the stagnation pressure cannot be maintained at 400 mbar. For a laser of 1 μsec pulse duration and 10 Hz repetition rate, the interaction time between the laser and the jet in this case can be estimated to be 7.2 ms ($1x10^{-6}$μsec x10 Hz x 12 x 60 sec). In the case of rim gas being re-circulated, the skimmer throughput governs the total experimental time and the same can be worked out to be ~4 hours. The interaction time between the laser and the jet thus extends here up to 144 msec, a ~20 times increase as compared to the conventional flow without any recirculation. The recirculation thus should prove beneficial in reducing the dilution of the enriched sample. Since the rim gas is expected to constitute more of the lighter species including the buffer gas, the recirculation of the rim gas also has an effect of increasing the buffer gas concentration in the feed gas mixture. Knowledge of change in feed gas composition is essential as it has a direct bearing on the efficiency of laser assisted aerodynamic separation process [6.7]. We estimated the change in the feed gas concentration as a function of recirculation time by extracting a small quantity of the feed gas mixture into a sample tube at

regular intervals during recirculation and analyzing it by FTIR to know the change in relative concentration of the process and buffer gases. Figure 6.14 depicts the change in partial pressure of SF_6 as a function of recirculation time in the feed gas. The partial pressure falls from an initial value of ~10.9% to ~ 6% in ~150 minutes of operation here. This clearly shows that there is an upper limit to the time for which recirculation can be carried out as the throughput (quantity of gas being processed) reduces, although, the efficiency of enrichment is enhanced with reducing concentration (partial pressure) of the process gas [6.7]. Furthermore, since the feed gas mixture now gets enriched in the lighter species, the separation factor can now be determined by sampling the feed mixture itself. This is advantageous as the feed mixture is at a higher pressure and the required quantity of sample can be drawn for accurate analysis.

6.5. Conclusions

In the first part, preliminary studies on the isotope selective excitation of Di-Methyl Stannane (DMS) in DMS-He jet using a continuously tunable, narrow emission width, 5 μm source has been carried out. Cooling obtained in the jet allowed resolving the vibrational-rotational transitions leading to isotope selective absorption. The experimentally measured shift in the absorption peaks of two of the isotopes was found to be consistent with the theoretical estimate.

In the second part of the chapter, practical methods of preparation of the feed gas mixture and increasing the temporal overlap between the laser and the gas jet in laser assisted aerodynamic separation process has been demonstrated. Usage of a dry re-circulatory pump has been pivotal towards gaining these advantages. The forced homogenization of the feed gas resulted in drastic reduction in the mixing time of the process and the buffer gas. Recirculation of the rim gas, back to the pulsed nozzle through the feed vessel allowed its

increased interaction with the laser beam thereby reducing the dilution of enrichment. Such dilution is inevitable due to the mismatch between the duration of the laser pulse and the nozzle opening time.

6.6. References

6.1. Dawson J, Nuclear Physics. A, 799, 167 (2008).

6.2. Vandana Nanal, Feasibility study of neutrino-less double beta decay in ^{124}Sn, Proceedings of the DAE Symp. on Nucl. Phys.,55, 114 (2010).

6.3. D.C. McKean, A.R. Morrisson P.W. Clark, Spectrochimica Acta Part A: Molecular Spectroscopy, 41 (12), 1467 (1985).

6.4. H. Kimmel, C. R. Dillard, Spectrochimica Acta Part A: Molecular Spectroscopy 24 (7), 909 (1968).

6.5. J. Padma Nilaya, M. B. Sai Prasad, D. J. Biswas, *Laser Phys.*, 24, 085401 (2014).

6.6. E. Ronander, H.J. Strydom and J. Viljoen, klydongasinternational.com/images/splg.pdf (2010).

6.7. J. M. Zellweger, J. M. Philippoz, P. Melinon, R. Monot, and H. van den Bergh, Phys. Rev. Lett., 52, 522 (1984).

6.8. Jeff W. Eerkens, Jaewoo Kim, American Institute of Chemical Engineers Journal (AIChE J*)* 56, 2331 (2010).

6.9. K. A. Lyakhov, H. J. Lee, Appl. Phys. B, 111, 261 (2013).

6.10. K. Lyakhov, and H. J. Lee, J. Nanoscience and Nanotechnology, 15, 8502 (2015).

6.11. Werner Fuss, https://www.mpq.mpg.de/5178012/MPQ346.pdf (2015).

6.12. G. N. Makarov, Physics Uspekhi, 58, 670 (2015).

6.13. V. M. Apatin, V. N. Lokhman, G. N. Makarov, N.D.D Ogurok, E. A. Ryabov, J. Exptl. and Theoretical Phys. 125, 531 (2017).

6.14. V. M. Apatin, V. N. Lokhman, G. N. Makarov, N. D. Ogurok, E. A. Ryabov, Quant. Electron 48, 157 (2018).

6.15. V. N. Lokhman, G. N. Makarov, A. L. Malinovskii, A. N. Petin, D. G. Poydashev and E. A. Ryabov, Laser Phys., 28, 105703 (2018).

6.16. V. M. Apatin, G. N. Makarov, N. D. Ogurok, A. N. Petin, and E. A. Ryabov, J. Exptl. And theoretical phys., 127, 244 (2018).

6.17. Los Alamos Science, Molecular Laser Isotope Separation, 3, No 1 (1982).

6.18. G. Chakraborty, V. K. Jain, Synthesis of Methyltin hydrides, BARC Internal Report,BARC/2013/I/019 (2013).

6.19. A. Ghosh, T. K. Ghanty, A. K. Nayak, S. K. Ghosh, Theoretical calculation of the Isotopic Shift of fundamental vibrational frequencies of stannane and its alkyl derivatives, NSRP-2013 (2013).

6.20. M. B. Sai Prasad, J. Padma Nilaya, Ayan Ghosh, A. K. Nayak, D. J. Biswas, National Laser Symposium-24, RRCAT, Indore (2015).

6.21. Bird, Stewart, Lightfoot: Transport Phenomena, 2nd edition, John Wiley & Sons, Inc, New York (2002).

6.22. If the partial pressure of the process gas exceeds its vapor pressure, it condenses preventing homogenization.

6.23. John L Lyman, https://fas.org/sgp/othergov/doe/lanl/docs4/silex.pdf (2014).

6.24. Werner Fuss, https://www.mpq.mpg.de/5178012/MPQ346.pdf (2015).

6.25. S. M. Freund and J. L. Lyman, Chemical Physics Letters, 55, 435 (1978).

6.26. Toshiyuki Oyama et al, Laser Chem., 8, 235 (1988).

6.27. Tetsugi Noda et al, J. Nuclear Materials, 307, 715(2002).

General Conclusions

Method of achieving continuous tunability over the 9-11 μm region of the mid-IR by way of eliminating the dark regions in the emission spectrum of a commercially available high pressure transversely exicted CO_2 laser has been realized. Continuous tunability across many of the P and R branch lines of both 9 and 10 μm bands and between any two transitions could be achieved by appropriately altering the charging voltage (from a minimum of 37 kV to a maximum of 43 kV in steps of 1 kV) and therefore the gain of the system, in conjunction with changing the Q value (55% R to 65% R output coupler) of the cavity. As the grating was tuned in a vertical plane, the laser emitted on vertical polarization with output energy that varied depending on the gain above threshold value at that oscillating frequency and lied between a maximum of 400 mJ and a minimum of 100 mJ of energy per pulse. When such a laser source is used as a pump for generating coherent emission in other regions of mid-IR following non-linear routes, its continuous tunability gets automatically translated to the generated coherent radiation.

Synchronized operation of two lasers driven by high voltage discharges is of utmost importance for e.g., in pump-probe experiments. Low-jitter synchronous operation of two spark gaps switches that in turn drive the lasers, has been achieved under optically coupled conditions in addition to being electrically coupled. Under optimized conditions, near 100% improvement in the jitter over their synchronous closure could be achieved. The generation of photoelectrons in the inter-electrode gap facilitated this closure with reduced jitter (1-2 ns). Although the experiments were performed with two switches, the conclusion should stay valid for multiple numbers of switches, a finding that will have bearing in applications where a number of spark gap driven lasers are to be operated in tandem.

Development of coherent sources in the mid-IR region is important in extending the possibility of isotope selective excitation to a wide range of working molecules. The operation of a continuously tunable coherent source in the 5 μm region of the mid-infrared by frequency doubling of the emission of a multi-atmosphere TE CO_2 laser in $AgGaSe_2$ non-linear crystal has been achieved. The performance of this source has been characterized with respect to both its energy and power conversion efficiency. The observation of excellent temporal synchronization of the SH pulse with the pump pulse, both in terms of phase and amplitude, bears experimental testimony to the fact that the process of creation of dipole by the pump at frequency ω and its giving out of emission at 2ω are indeed instantaneous.

Further, second harmonic conversion of the emission of a CO_2 laser (both CW and pulsed) in a $ZnGeP_2$ crystal has been achieved and the performance characterized. In general, the literature on SHG in the region of ~4.5 μm using $ZnGeP_2$ crystal is quite rich while that near 5 μm is rather scarce. To this end, the utility of the ZGP crystal in generation of wavelength ~ 5 μm region is noteworthy. The higher conversion efficiency from this crystal in case of pulsed operation is attributed to the much higher irradiating intensity to which the crystal is subjected here as against the CW case. The efficiency of the frequency doubling process in the pulsed operation case has been studied as a function of the duration of the CO_2 pump pulse and the observations qualitatively explained.

We have obtained lasing on multiple wavelengths in the 5 μm region from a non-selective CW-CO_2 laser cavity when its gain length was maintained at LN_2 temperature. The inversion obtained in the CO medium formed by the dissociation of CO_2 gas in the discharge made this possible. The findings are significant as the handling of the toxic CO gas that is conventionally employed in the generation of wavelength in the 5 μm region has been dispensed with. A maximum CW output power of 8 W at an electro-optic efficiency of 8%

has been reported. The lasing transitions obtained due to the cascading nature of the CO output have been identified and matched with known transitions available in the literature.

A stable and reliable CW-CO_2 laser with power exceeding 18 Watt on the line with the highest gain, i.e., 10P(20) has been developed and optimized. The output power of the laser has been studied as a function of the total operating pressure, partial pressure of the gases and the discharge current. The laser was operated in the dispersive cavity configuration and the power on various ro-vibrational transitions spanning 10R and 10P branches were measured. The operation of the laser is simple, safe, trouble free and economic.

Experimental demonstration of the enrichment of $^{34}SF_6$ when the emission of a CW-CO_2 laser was made to interact with a supersonically cooled SF_6-Argon binary gas jet by laser assisted aerodynamic separation scheme has been realized. In this regard, the advantage of the 10P(20) line as against the resonant 10P(16) line in enhancing the enrichment efficiency has also been experimentally demonstrated. This enhancement owes its origin to the efficient multi-photon excitation possible here due to the red-shifted nature of the incident radiation. Further, a novel way of estimation of separation factor by an absorption method has been elegantly conceived and demonstrated wherein the knowledge of the absorption cross-section of the molecule for the incident laser line is rendered irrelevant. The separation factor obtained by this technique was seen to corroborate with the mass spectrometric measurements.

Studies on the isotope selective excitation of Di-Methyl Stannane (DMS) in DMS-He jet using a continuously tunable, narrow emission line-width, 5 micron source has been carried out. Cooling obtained in the expanding gas jet allowed resolving the vibrational-rotational transitions of DMS leading to isotope selective absorption studies. The experimentally measured shift in the absorption peaks of two of the isotopes was found to be consistent with the theoretical estimate.

Laser assisted aerodynamic separation process has evolved as a viable alternative to molecular laser isotope separation that is based on the classical multi photon dissociation route. However, in case of separation of certain isotopes, this scheme not only suffers from lengthy homogenization times but also dilution of the enriched stream owing to the mismatch between the laser pulse duration and the nozzle opening time. To this end, a practical method to overcome the former and alleviate the latter by imposing forced circulation of the feed and rim gases has been demonstrated. The forced circulation of the feed gas by way of using an oil free scroll pump resulted in drastic reduction in the mixing time of the process and the buffer gases while recirculation of the rim gas, mostly unseen by the pulsed laser, through the feed cell back into the pulsed nozzle repeatedly allowed its increased interaction with the laser beam reducing thereby the dilution in the obtained enrichment to a certain extent. The experimental measurement of the nozzle and the skimmer throughputs, a pre-requisite for such a rim gas recirculation, allowed us to quantify this increase in the temporal overlap of the laser emission with the gas stream. The change in the composition of the feed gas as a result of recirculation has also been experimentally quantified as this has a strong bearing on the overall achievable separation efficiency.

Future Scope of Work

While an attempt has been made successfully to develop coherent sources indigenously in the mid-IR wavelengths and apply the same for isotope separation in laser assisted aerodynamic process, the scope of future work includes accurate modeling of the cluster formation, both homo and hetero, as that gives a deeper insight into the aerodynamic process and effective usage of laser for selective excitation. Development of efficient, high power tunable coherent sources in the mid-IR region and their characterization (operation of CO laser in dispersive configuration) will enable selective excitation and separation of a variety of isotopes of strategic importance or otherwise.